Engineering *in vitro* cellular models through spatial patterning of morphogens

Daniel Boland

Imperial College London

Department of Materials

The Institute of Cancer Research

Division of Cancer Biology

Submitted in accordance with the requirements for the degree of Doctor of Philosophy

March 2022

Declaration of originality

I declare that the content of this thesis is my own, unless otherwise stated and referenced. All work presented in this thesis was carried out at Imperial College London, The Francis Crick Institute and The Institute of Cancer Research. Data generated or work done by others is acknowledged in the text as appropriate.

Copyright declaration

The copyright of this thesis rests with the author. Unless otherwise indicated, its contents are licensed under a Creative Commons Attribution-Non-Commercial 4.0 International Licence (CC BY-NC). Under this licence, you may copy and redistribute the material in any medium or format. You may also create and distribute modified versions of the work. This is on the condition that: you credit the author and do not use it, or any derivative works, for a commercial purpose. When reusing or sharing this work, ensure you make the licence terms clear to others by naming the licence and linking to the licence text. Where a work has been adapted, you should indicate that the work has been changed and describe those changes. Please seek permission from the copyright holder for uses of this work that are not included in this licence or permitted under UK Copyright Law.

Acknowledgements

First and foremost, I am extremely grateful to Professor Molly Stevens, for giving me the opportunity to carry out my PhD in such a diverse, interdisciplinary and exceptional group. Thank you for your unending support, advice and enthusiasm, which have helped me to develop as a scientist over the course of my PhD.

Thank you also to my assistant supervisor, Dr Stuart Higgins. Since I joined the group, his mentorship and friendship have always provided direction and motivation, in particular through challenging times. Without his insights and advice, this PhD would not have been the same, and I will always be thankful to have had him as a mentor.

Thank you, Professor Chris Bakal, for taking me in to your group, and giving me the opportunity to learn so much about the field of cancer biology. Thank you to Dr Tomo Higo and Dr Lucas Dent, for their assistance in multiple experiments, and also in offering their guidance and patience as I explored a field that was entirely new to me.

Thank you Dr Daniel Hachim Diaz, for assistance with the development of the layer-by-layer method, and also for kindly carrying out XPS and AFM measurements that were used herein. Thank you to Raya El Laham for her assistance in capturing SEM images. Thank you Dr Vernon Lalone, Dr Isaac Pence and Dr Jelle Penders for assisting in carrying out Raman spectroscopy. The entire Stevens group has been a pleasure to work with, and I know I have made friends here that will last a lifetime. In particular, the newbies of 2017 – I feel very lucky to have taken this PhD journey with you all.

I would also like to thank Professor James Briscoe, and his group members, for their invaluable contributions and collaboration over the last number of years. It has been a pleasure to work with and learn from such a talented group of developmental biologists. In particular, I would like to thank Dr Despina Stamataki, for the collaboration and friendship over the last 3 years. Our work together presented many challenges, but her enthusiasm, determination and optimism were vital in keeping the

project moving in the right direction. The mentorship and help provided will always be appreciated.

To my partner Danielle Manlutac, for being with me through the trials and tribulations that a PhD, a thesis and a global pandemic presented. There certainly were plenty of stressful moments, but your love and support have been some of my main strengths through the whole process - I think we make a pretty great team Akin, and I know I am lucky to have you. Also to Kaze, who has enjoyed having me around a lot more while I was writing!

To my grandparents - Tom and Elizabeth Boland, Peter and Bridie Gough - who always encouraged education and celebrated every achievement along this journey. Their cards and messages of support and love were a source of strength and connection to home in challenging times. None of this would have been possible without their sacrifices and compromises to support both my siblings and I, and also my parents, and I could not be more grateful for that. They are all dearly missed.

To my siblings (and doctors before) JB and Lisa, for forging ahead and paving for me this path that I have taken. I have the benefit of being the youngest of us three, and so received a lot of help from you both. I could not ask for a more supportive brother and sister, and I am so thankful for the guidance and advice you have always given me. I really am thankful to have you both.

Finally, to my parents. Thank you for the opportunities you have given me, and the sacrifices and efforts you have made. You have always been the anchor for me through difficult times, and our regular chats have been a real bright spot for me. Although I am a bit further from home now, I have never felt closer to you as a result of the love and care that you have always provided. Thank you for encouraging me to spread my wings, to persevere and to take chances. No matter where life takes me, I know I will always have the warmth and comfort of Baylin waiting when I return.

Abstract

Spatial patterns of biomolecules play a central role in a range of biological processes, from embryogenesis to cancer development. Although some progress has been made in recent years, most current engineered platforms lack the spatial resolution to accurately model these systems. The ability to exert control over the local activation of signalling pathways that cells experience *in vitro* could facilitate investigations into developmental processes, as well as disease and cancer progression, and could lessen the burden of animal research. To this end, this thesis describes efforts to manufacture a novel material system that can present a spatially patterned interface to cells in culture. By leveraging inkjet printing on nanotopographical substrates, the behaviour of cells can be influenced both biochemically and physically. A range of bio-inks were investigated in this work, from proteins to small molecule pathway activators and inhibitors.

Through the printing of Shh protein gradients, a spinal cord-on-a-chip model was developed, with motor neuron and other progenitor cell types being generated from mouse embryonic stem cells. A range of transcription factors verified the presence of specific ventral subtypes from the neural tube, and quantitative analysis of microscopy images was used to visualise the reproducibility of the differentiation induced in cells on printed patterns.

The platform was also utilised in preliminary studies into targeted Wnt pathway activation for cancer investigations. A number of candidate cell lines were screened, with similar image analysis methods being utilised to visualise the role that printed bio-inks played in a range of cell behaviours. The printed Wnt gradients were seen to influence cell density considerably, and also showed location-dependent levels of pathway activation.

It is hoped that this approach may encourage more emphasis on spatial patterning in materials design in the future, to enhance the capabilities of bioengineered systems for cell interfacing applications.

Scope of the thesis

Chapter 1 introduces the current approaches for engineering bioactive material systems. The literature described within this chapter details techniques from 2D coating materials to complex microfluidic device architectures, and the applications they have been utilised for. This chapter highlights the need for more controlled methods to generate materials that present spatially patterned biochemical cues to cells.

Chapter 2 describes the bottom-up approach used in this work to generate a spatially patterned cell interfacing material. This method builds on the silicon nanoneedle substrates previously developed in the Stevens group, with the addition of an electrostatic protein binding mechanism. The generation of morphogen patterns via inkjet printing is then described, with two different printer devices being explored. Throughout the chapter, the characterisation of each step of the material design process is detailed.

Chapter 3 begins with a discussion of the current literature in developmental neural biology, and the potential for a novel neural engineering technique for the modelling of spinal cord development. The application of the material system described in Chapter 2 is then demonstrated, via the seeding of mouse embryonic stem cells on printed protein gradients. Through the controlled differentiation of these cells, a model of the early ventral spinal cord is generated, with an image analysis pipeline being used to better understand the capabilities of the platform.

To further demonstrate the capabilities of the biomaterial developed in this work, Chapter 4 details preliminary studies into its application in cancer modelling *in vitro*. Before the presentation of the data, literature describing the role of signalling pathways in cancer is summarised. Following this, the influence of protein bio-inks on various cancer cell lines is investigated. These data demonstrate the modular nature of the substrates designed here, and highlight the potential for the system to be utilised

across a range of biological disciplines in the future, including in the exploration of novel therapeutic approaches for cancer.

Finally, Chapter 5 summarises the data presented within this thesis, and also the conclusions that were drawn from those data. Potential future works are discussed, along with some opportunities to increase the reliability and reproducibility of the system.

Contents

Chapter 1: Introduction **18**

1.1 2D surface modification for cell culture applications 18

1.2 Hydrogels and scaffolds 22

1.2.1 3D scaffolds from natural materials 24

1.2.2 3D scaffolds from synthetic materials 28

1.3 Microfluidic devices 33

1.3.1 Microfluidic devices for neural engineering 35

1.3.2 Microfluidic devices for cancer biology 38

1.4 Inkjet printing and its applications 41

1.4.1 Background 41

1.4.2 Applications 43

1.5 Nanostructured substrates 45

1.5.1 Nanopillars and nanowires 45

1.5.2 Nanoneedles 47

1.6 Conclusions and aims 50

Chapter 2: Materials fabrication and characterisation **53**

2.1 Summary of experimental approach 54

2.2 Nanoneedle substrate fabrication 55

2.3 Layer-by-layer coating development for silicon substrates 57

2.3.1 Motivation for the use of layer-by-layer coatings for protein binding 57

2.3.2 Method to generate layer-by-layer coatings 58

2.3.3 Initial investigations into alginate/chitosan bilayers for SAG binding 60

2.3.4 Investigating heparin/chitosan coatings for binding of Shh/Wnt3a 64

2.4 Optimisation of inkjet-printed morphogen gradients on nanoneedles 74

2.4.1 Shh ELISA release assay 75

2.4.2 Shh gradient generation with Canon inkjet printer 76

2.4.3 Characterisation of Shh gradients generated using the Canon inkjet printer 78

2.4.4 Shh gradient generation with the BioDot AD3220 80

2.5 Conclusions and discussion 84

Chapter 3: In vitro replication of the neural tube using inkjet printing 87

3.1 Literature Review 88

3.1.1 Embryogenesis – formation of the germ layers 88

3.1.2 Neural tube formation, neurogenesis, and the role of morphogens 89

3.1.3 Defects in the neural tube and spinal cord 94

3.1.4 Isolating stem cells for interrogating developmental processes 97

3.1.5 *In vivo* methods for investigating the developing spinal cord 98

3.1.6 *In vitro* methods for modelling the developing spinal cord 100

3.1.7 Neural organoids 103

3.1.8 Ex vivo approaches 107

3.1.9 Opportunity for a novel neural engineering material platform 110

3.2 Materials and Methods 112

3.2.1 Cell culture 112

3.2.2 Imaging 113

3.2.3 Immunostaining 114

3.2.4 Image analysis 114

3.2.5 Summary of experimental approach 116

3.3 Results 118

3.3.1 Initial differentiation of mESCs on substrates 118

3.3.2 First inkjet-printed morphogen tests 123

3.3.3 Changing the seeding timepoint 127

3.3.4 Printer Change, Linear vs. Exponential gradients 132

3.3.5 Imaging pipeline analysis for exponential Shh gradients 135

3.4 Preliminary experiments 148

3.4.1 Dorsal neural tube modelling 148

3.4.2 Time-dependent ventral response 153

3.4.3 Axonal guidance with nanostructured surfaces 155

3.5 Discussions and conclusions 158

Chapter 4: Spatial patterning of Wnt ligands for cancer investigations 160

4.1 Introduction 162

4.1.1 Cancer and signalling pathways 162

4.1.2 Wnt signalling in cancer 165

4.1.3 Hedgehog signalling in cancer 171

4.2 Materials and methods 174

4.2.1 Substrate preparation and inkjet printing of Wnt3a 174

4.2.2 Cell culture 174

4.2.3 Imaging 175

4.2.4 Image analysis 175

4.3 Results 175

4.3.1 Characterisation of Wnt activators/inhibitors via Raman spectroscopy 176

4.3.2 Finding the optimal candidate cell lines to investigate Wnt signalling 178

4.3.3 A new candidate cell line for spatially resolved Wnt3a response. 191

4.3.4 Initial investigations and pipeline development 193

4.3.5 β-catenin response at higher printed Wnt3a concentrations 198

4.4 Discussions and future work 204

Chapter 5: Conclusions and future work 207

5.1 Material system development 209

5.2 Inkjet printing for the modelling of developing neural systems 211

5.3 Inkjet printing for investigating cancer development and progression 213

5.4 Perspective 215

Chapter 6: Appendix **220**

References **220**

List of Figures

Figure 1.1: Glycosaminoglycan molecule subtypes 20
Figure 1.2: Layer-by-layer method 22
Figure 1.3: IKVAV-modified silk hydrogels for neural stem cell culture 25
Figure 1.4: Scaffold materials for neurite outgrowth 26
Figure 1.5: Hyaluronic acid hydrogel structure 28
Figure 1.6: PLLA scaffolds for neurite outgrowth 29
Figure 1.7: Osteochondral tissue constructs 32
Figure 1.8: Perfusible microfluidic device for modelling kidney function 34
Figure 1.9: Microfluidic device for modelling rostral-caudal neural development 37
Figure 1.10: Microfluidic device for modelling melanoma and immune cell interactions 39
Figure 1.11: Inkjet printhead types 43
Figure 1.12: Nanocolumns used to direct neurite outgrowth 46
Figure 1.13: Silicon nanoneedles 48
Figure 1.14: Diamond nanoneedles 49

Figure 2.1: Summary of experimental approach 54
Figure 2.2: Nanoneedle fabrication method 56
Figure 2.3: Layer-by-layer protocol 59
Figure 2.4: Alginate layer-by-layer coatings 61
Figure 2.5: Raman and FTIR spectra for SAG coatings 63
Figure 2.6: Heparin/chitosan layer-by-layer coatings 64
Figure 2.7: Contact angle measurements of coated substrates 66
Figure 2.8: Safranin-O staining on coated substrates 68
Figure 2.9: XPS spectra of coated substrates 72
Figure 2.10: AFM analysis of coated substrates 73
Figure 2.11: Shh ELISA release assays 76
Figure 2.12: Canon inkjet printing apparatus 77
Figure 2.13: Inkjet printed Shh gradient 79
Figure 2.14: Canon and BioDot inkjet printers 81
Figure 2.15: Shh gradients printed with the Canon and BioDot printers 83

Figure 3.1: Neural tube patterning by morphogen gradients 91
Figure 3.2: Hedgehog signalling pathway 92
Figure 3.3: Development of neural tube zones 93
Figure 3.4: Formation of germ layer cells *in vitro* 98

Figure 3.5: Timepoints of mouse neural tube formation 99
Figure 3.6: Generation of neuromesodermal progenitors 101
Figure 3.7: Generation of neural organoids 104
Figure 3.8: Neural tube organoid modelling 105
Figure 3.9: Spinal cord explant culturing 108
Figure 3.10: PLLA scaffolds for spinal cord explant culturing 109
Figure 3.11: Overview of image analysis method 116
Figure 3.12: Transcription factor network of the neural tube dorsal-ventral axis 118
Figure 3.13: Representative image of mESC colonies 119
Figure 3.14: Initial mESC differentiation tests on nanoneedle substrates 120
Figure 3.15: Shh coating concentration tests 122
Figure 3.16: First printed Shh gradient differentiation of mESCs 124
Figure 3.17: Nkx6.1 as a ventral marker for gradient differentiations 126
Figure 3.18: Revised Shh protocol 128
Figure 3.19: Shh Gradient response of mESCs at Day 7 130
Figure 3.20: Tiled image of Nkx6.1 signal in response to Shh gradient 132
Figure 3.21: Overview of mESC response to printed Shh gradient 133
Figure 3.22: Overview of substrates to be processed with image analysis pipeline 135
Figure 3.23: Pixel probability masks from ilastik 136
Figure 3.24: Data cleaning and rotation 137
Figure 3.25: Model of mean Olig2 intensity across all printed substrates 138
Figure 3.26: Background subtraction for Olig2 mean intensity model 139
Figure 3.27: Model of mean Nkx6.1 intensity across all printed substrates 140
Figure 3.28: Pooled mean intensity heatmaps for Nkx6.1 and Olig2 142
Figure 3.29: Individual mean intensity heatmaps for Nkx6.1 and Olig2 143
Figure 3.30: Individual mean intensity heatmaps for Nkx6.1 and Olig2, universal scale 144
Figure 3.31: Individual mean intensity heatmaps for Nkx6.1 and Olig2, controls 145
Figure 3.32: Model of mean Nkx6.1 intensity with feature number threshold 147
Figure 3.33: Generation of dorsal subtypes with BMP4 treatment 150
Figure 3.34: BMP4 coating concentration tests 151
Figure 3.35: Dbx1 and Pax7 antibody tests 153
Figure 3.36: Time-dependent ventral response of mESCs 154
Figure 3.37: Nanomohawk substrate 156
Figure 3.38: Axonal guidance of mature neurons on nanomohawks 157

Figure 4.1: Schematic of the MAPK signalling pathway 164
Figure 4.2: Schematic of the canonical Wnt signalling pathway 167
Figure 4.3: Concentration-dependent response to Wnt3a in hESCs 170
Figure 4.4: Shh pathway in cancer 172
Figure 4.5: Raman spectra of small molecule Wnt activators and inhibitors 177
Figure 4.6: MEL10 cells seeded on nanoneedles with a Wnt3a printed gradient 179
Figure 4.7: Directionality of MEL10 cells seeded on a Wnt3a printed gradient 180
Figure 4.8: MEL10 cells seeded on nanoneedles with soluble Wnt3a 181
Figure 4.9: Directionality of MEL10 cells, with soluble Wnt3a 182
Figure 4.10: MEL10 cells seeded on a Wnt3a gradient, with soluble IFNG 183
Figure 4.11: Directionality of MEL10 cells, on a Wnt3a gradient with soluble IFNG 184
Figure 4.12: 19398 cells seeded on a Wnt3a gradient 185
Figure 4.13: Directionality of 19398 cells seeded on a Wnt3a gradient 186
Figure 4.14: 19398 cells seeded on nanoneedles with soluble Wnt3a 187
Figure 4.15: Directionality of 19398 cells seeded with soluble Wnt3a 188
Figure 4.16: 19398 cells seeded on a Wnt3a gradient with soluble IFNG 189
Figure 4.17: Directionality of 19398 cells on a Wnt3a gradient with soluble IFNG 190
Figure 4.18: Characteristic shape of WM266.4 cells 191
Figure 4.19: Change in the shape of WM266.4 cells with Wnt3a treatment 192
Figure 4.20: Schematic of the image analysis pipeline 193
Figure 4.21: Boxplot of mean nuclear β-catenin signal, 1 µg/mL Wnt3a gradient 194
Figure 4.22: Boxplot of mean nuclear β-catenin signal at 48 h, 1 µg/mL Wnt3a gradient 196
Figure 4.23: Nuclear translocation of β-catenin on a 4 µg/mL Wnt3a gradient 198
Figure 4.24: Heatmap of mean nuclear β-catenin, 1 µg/mL Wnt3a gradient 200
Figure 4.25: Boxplot of mean nuclear β-catenin, 1 µg/mL Wnt3a gradient 200
Figure 4.26: Boxplot of mean nuclear/cytoplasmic β-catenin, 1 µg/mL Wnt3a gradient 202
Figure 4.27: Boxplot of mean nuclear β-catenin, no response to Wnt3a gradient 203
Figure 4.28: Boxplot of mean nuclear/cytoplasmic β-catenin, no response to Wnt3a 204

Figure 6.1: Cell capture for spatially resolved transcriptome analysis 218

List of Tables

Table 1: Elemental composition of layer-by-layer coatings via XPS 70
Table 2 (a)/(b): Raman peak assignments for Figure 4.5 (a)/(b) 219

List of abbreviations

AFM	Atomic force microscopy
ALS	Amyotrophic lateral sclerosis
AP	Anterior-posterior
BMP	Bone morphogenetic protein
BSA	Bovine serum albumin
CIJ	Continuous inkjet
DAPI	4',6-diamidino-2-phenylindole
DCIS	Ductal carcinoma in situ
DMSO	Dimethyl sulfoxide
DNA	Deoxyribonucleic acid
DOD	Drop-on-demand
DRIE	Deep reactive ion etching
DV	Dorsal-ventral
ECM	Extracellular matrix
ELISA	Enzyme-linked immunosorbent assay
ERK	Extracellular signal-regulated kinase
ESC	Embryonic stem cell
FGF	Fibroblast growth factor
FP	Floor plate
FTIR	Fourier transform infrared spectroscopy
FZD	Frizzled
GAG	Glycosaminoglycan
GTP	Guanosine triphosphate
HA	Hyaluronic acid
Hh	Hedgehog
hPSC	Human pluripotent stem cell
HUVEC	Human umbilical vein endothelial cells
IFNG	Interferon-gamma

IQR	Interquartile range
LbL	Layer-by-layer
MAPK	Mitogen-activated protein kinase
MN	Motor neuron
MS	Multiple sclerosis
mTOR	Mammalian target of rapamycin
NMP	Neuromesodermal progenitor
OCT	Optimal cutting temperature compound
PBS	Phosphate-buffered saline
PCP	Planar cell polarity
PDK1	Phosphoinositide-dependent kinase 1
PEG	Poly(ethylene glycol)
PFA	Paraformaldehyde
PI3K	Phosphatidylinositol-3-kinase
PLA	Poly(lactic acid)
PLGA	Poly(lactic-co-glycolic acid)
PMEF	Primary mouse embryonic fibroblast
PORCN	Porcupine
PTCH	Patched1
RA	Retinoic acid
RIE	Reactive ion etching
RP	Roof plate
SAG	Smoothened agonist
SEM	Scanning electron microscopy
Shh	Sonic hedgehog
siRNA	Small interfering ribonucleic acid
Smo	Smoothened
TGFβ	Transforming growth factor beta
XPS	X-ray photoelectron spectroscopy

Chapter 1

Introduction

Chapter 1: Introduction

Cell culture experiments offer a window into the inner workings of biological systems as they occur *in vivo*. However, while useful for exploratory investigations, culturing cells on 2D plastic surfaces alone offers limited insight into their true behaviour, as a result of the drastic differences between the culture conditions and those experienced by cells in their parent tissue. In recent decades, bioengineered systems have been developed in efforts to overcome these limitations, and to explore in greater detail the biological machinery underpinning the interactions between cells and their environment. These efforts have ranged from simple 2D surface coatings to complex 3D scaffold architectures and materials systems such as microfluidics and nanotopographical substrates. Advances in fabrication techniques have enabled more sophisticated devices to be manufactured, to exert greater physical and biochemical control over the behaviour of cells *in vitro*. The ultimate goal of these investigations is to expand the understanding of biological systems, and to offer novel insights into potential therapeutic avenues for a myriad of conditions.

This chapter discusses current engineering approaches for investigating biological systems *in vitro*, from simple 2D coatings to complex microfluidic device architectures. Through the discussion of these engineering approaches, the opportunity for a high throughput, biochemically patterned, and modifiable materials platform for the modelling of complex biological systems becomes clear.

1.1 2D surface modification for cell culture applications

Approaches involving the seeding of cells in well plates are the current standard for modelling biological systems *in vitro*. This method allows relatively quick and cheap experiments to be carried out, that can generate specific cell populations and systems. 2D cell culture is especially powerful in fields where a single cell type is needed, and so entire populations of cells can be treated with the same conditions. It allows for fine control over this process, and also is amenable to imaging through the use of clear

plastic well plates. All immunostaining or treatments can be carried out in the well, and no mounting or extra handling are needed.

Despite this, the limitations of current *in vitro* methods persist. One challenge that is continuously highlighted is the fact that standard culture platforms maintain the cells in 2D environments. While this is suitable for some applications, the natural environments of cells in the body are almost uniquely 3D (excluding some cases such as early-stage developmental systems). The complex architecture that surrounds cells in the body is known as the extracellular matrix (ECM). This network of biomolecules is made up of, among other things, proteins, enzymes and glycosaminoglycan molecules. These components provide structural support for cell networks within the body, as well as providing signalling and biochemical cues to enable processes such as adhesion, proliferation and the inflammation response to occur. In recent decades, researchers have made attempts to recapitulate this effect in 2D culture systems through the use of ECM components (such as collagen and gelatin) as coatings in their well plates.[1,2] These coatings make the surface more amenable to cell adhesion, and can promote proliferation and intercell signalling. A collection of ECM proteins known as Matrigel was identified as an interface coating material to carry out this role.[3] This mixture presents a number of biological cues to cells that have been seeded on it, allowing for more accurate representation of the environments that they would grow in *in vivo*.

As well as proteins, the ECM contains a number of glycosaminoglycan (GAG) molecules. These are long chain polysaccharide molecules, made up of repeating double sugar units. Some common examples include heparin and dermatan sulfate, with most being made up of similar structured backbones, differentiated by their branches and side chains. These macromolecules play a number of different roles in the body.[4] They are known to participate in structurally supporting the cells as components of the ECM, but have recently also been discovered to influence cell signalling, directing processes such as cell growth, proliferation and the wound

response.[5] This involvement across a range of biological processes is as a result of their charged nature, allowing the GAG molecules to interact with various proteins, growth factors, chemokines and other biomolecules. They can be broken down into four subclasses, based on their underlying structure, linkages and degree of sulfation: heparin/heparan sulfate; chondroitin sulfate and dermatan sulfate; hyaluronan; and keratan sulfate.[5]

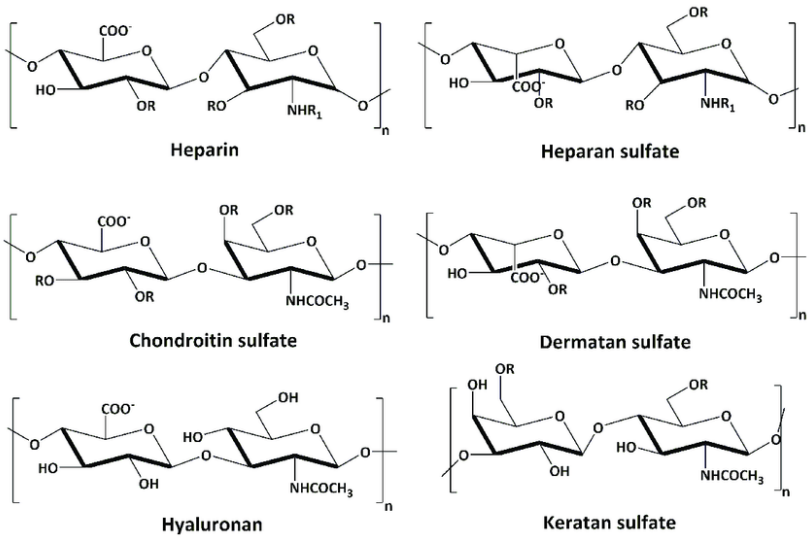


Fig. 1.1: *The four different GAG molecule subtypes: heparin/heparan sulfate; chondroitin sulfate and dermatan sulfate; hyaluronan; and keratan sulfate. Reproduced from Morla.*[5]

Particularly for materials that would otherwise not be hospitable for cell growth, the enhanced adhesion these macromolecules offer as a coating can be invaluable. The negative charge and hydrogen bonding capabilities GAG molecules possess enable their use as a coating or functionalisation method for engineering applications. Combined with their ability to improve adhesion and proliferation of cells, they can be used as an electrostatic binding mechanism for the attaching of molecules to surfaces.[6] Electrostatic binding can still provide robust interactions in the right conditions (pH, GAG and protein choice), while allowing the structure of the biomolecule to remain unchanged.

In any application where surface functionalisation is required, the mechanism of binding must be considered. Chemically modifying the surface offers a means to ensure that the desired molecule is maintained for sufficient time to carry out its intended purpose, but must do so in a manner that does not negatively impact the end application of the material. Covalent bonding involves the donation of electrons to form chemical bonds, and so creates extremely strong connections between the surface and the loading molecule. When the substrate is silicon-based, silane chemistries are the most common choice for this, as a range of different silanes with various functionalities are available.[7,8] However, as the covalent bonds formed are extremely strong, the bonds are not easily broken to release the molecule to be delivered, without some form of external chemical or physical cue. Also, in forming new chemical bonds, the structure of the payload may be modified irreversibly, which can affect the properties and so the intended application of the system (e.g. protein or peptide activity). In contrast, electrostatic binding does not usually require any sort of external release cue, and as the interaction is purely based on oppositely charged materials, does not involve any permanent altering of the molecular structure. This is usually achieved through some form of charged surface coating, such as the glycosaminoglycans mentioned above, or with a charged polymer.[9,10] These electrostatic interactions, although not as robust as the binding via covalent chemistry, can be sufficient to maintain the cargo at the interface for multiple days in cell culture conditions, before being released into the media. For systems requiring longer cell interfacing, the electrostatic binding and release kinetics can be tailored through the materials used as the charged layers. This is important in cell delivery applications, where the slightly weaker electrostatic interactions enable both the presentation and release of biomolecules in a controlled manner. In particular, the layer-by-layer (LbL) technique is extremely useful for generating uniform, nanometre-scale coatings of charged materials at the substrate surface that can then be used for the binding of biomolecules such as proteins and peptides, as well as electrostatically charged small molecules.[11,12] A schematic of the layer-by-layer method is shown in Figure 1.2.

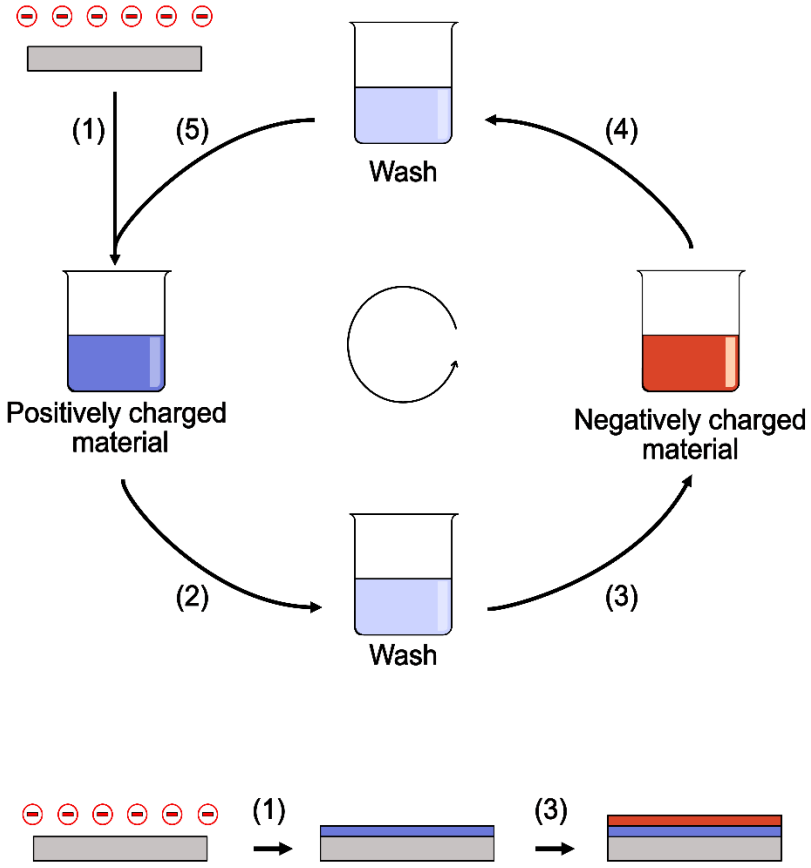


Fig. 1.2: *Schematic of the layer-by-layer technique for generating uniform surface coatings of charged materials. Initially, a negative charge must be induced at the material surface. The substrate is subsequently submerged in the positively charged material, followed by the negatively charged solution. Repeating this cycle generates more stacked bilayers, increasing the thickness and uniformity of the coating.*

Coatings such as Matrigel and GAG molecules can undoubtedly enhance the *in vitro* approach, although there is still the challenge of replicating *in vivo* processes in a 2D architecture. The networks and structures formed in the body are complex, with structures arising that enable directed growth and support of cells and tissues.

1.2 Hydrogels and scaffolds

Where 2D surfaces and coatings are not sufficient, scaffolds can be utilised to generate 3D cell architectures *in vitro*. In recent decades, efforts have been made to generate a

range of platform types, primarily through the use of hydrogel systems.[13] Hydrogels can be defined as a 3D crosslinked gel structure, often made up of hydrophilic polymers, that contains a large portion of water. While useful as scaffolds, the applications of these materials in literature can also inform design choices for coatings or materials for cell interfacing, where their 3D structure is not required.

Gelation is induced by a physical or chemical cue (e.g. pH, temperature, chemical reaction), and usually provides mechanical stiffness that is comparable to those found in some *in vivo* systems. The inherently porous nature of hydrogel scaffolds enables diffusion of nutrients to cells across the entire material, allowing for true 3D growth of cultures *in vitro*. Hydrogels can be formed from both natural and synthetic polymers, and as such their applications are widespread.[14] Modifications can be made to the component polymers to allow for custom chemistries and functionalities to be added, enabling the binding of peptides and growth factors to further enhance their capabilities in a biological capacity. They can be comprised of ECM components (collagen gels have been used repeatedly) or GAG molecules (heparin and heparan sulfate are the most common, although chondroitin sulfate and hyaluronic acid hydrogels have also been described).[15]

A number of scaffolds have been designed in attempts to recapitulate various aspects of development and for regeneration purposes. The strength of these structures lies in their ability to mimic somewhat the environment of biological systems *in vivo*. This is of particular importance for scaffold materials that are to be implanted, where it is vital that the platform enables the growth and movement of cells and creation of connections between them, but also the formation of new vascular systems. In order to achieve this, any implantable material system should offer similar mechanical and physical properties to those present in the tissue being modelled, depending on the intended application. The material should also offer the ability to either be pre-functionalised, or to recruit proteins and other biomolecules that will support the developing cells and systems. Finally, if the material is to be implanted, it should be

biocompatible and biodegradable to prevent adverse host reactions over time, which would inevitably cause inflammation and other more serious side effects.

1.2.1 3D scaffolds from natural materials

Many natural materials have previously been used to create supporting gels for biological applications. Perhaps the most common material used to generate these scaffolds is collagen, a naturally occurring biopolymer that can readily be functionalised to enhance the attachment and proliferation of cells. Sargeant *et al.* demonstrated the use of collagen/poly(ethylene glycol) (PEG) hydrogels for tissue engineering applications, culturing fibroblast cells to confluence over a period of seven days.[16] The degradation characteristics of the gels could also be tuned based on the size of the PEG used, which is extremely valuable for potential implantation applications.

The stiffness of collagen scaffolds can be tuned based on the requirements of the application in question, by varying the amount of water contained in the scaffold. Hadjipanayi *et al.* achieved this by applying a compression to their scaffolds, effectively forcing liquid out of the material.[17] By varying the water composition of their scaffolds, the authors investigated the role that the matrix stiffness played in the proliferation of fibroblast cells. Otherwise, the stiffness can be tuned by changing the concentration of collagen used in making the scaffold, as shown by Kuntz Willits *et al.*[18] By varying the concentration of collagen during scaffold formation from 0.4 to 2.0 mg/mL, they could increase the stiffness of the scaffold and in turn investigate the role that stiffness played in neurite outgrowth of dissociated chick dorsal root ganglia. These collagen scaffolds can also readily be modified by other biomolecules to enhance their viability and effectiveness at influencing cell behaviour. One common method to achieve this is to add a targeted peptide to the scaffold, to enhance adhesion and proliferation. Hosseinkhani *et al.* employed the IKVAV peptide for this purpose, which was attached covalently to the carboxyl groups on the collagen scaffold.[19] This peptide, and others

derived from laminin (a protein that is abundant in the ECM), can be used to mimic the environment cells would experience *in vivo*. The IKVAV peptide has been used extensively in the past to enhance the adhesion and differentiation of cells on surfaces and substrates[20–22], while other laminin peptides or their synthetic analogues have been used to achieve similar results.[23,24]

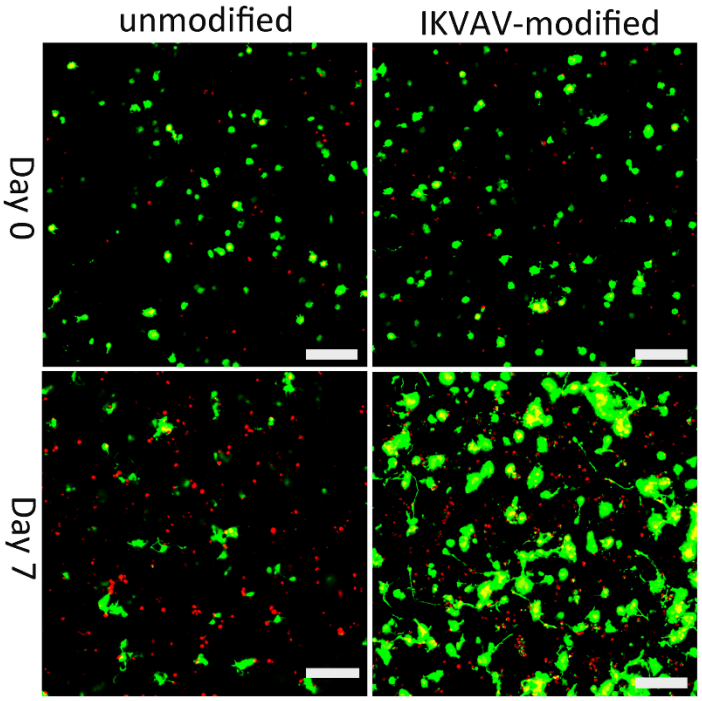


Fig. 1.3: *The enhanced adhesion and proliferation of human neural stem cells when seeded on silk hydrogels that were functionalised with the IKVAV peptide. Scale bars = 100 µm. Adapted from Sun et al.*[22]

These reports further emphasise however that in these collagen-based materials, some type of additional bioactive molecule is most likely required in order to achieve the functionality and complexity that is needed. While the addition of peptides certainly offers an extra degree of control over the functionality of scaffold systems, it does somewhat complicate the synthesis and manufacturing process, and so this factor should also be considered when deciding on a suitable material for biomedical applications. Similar functionalisation requirements would also be present if collagen were to be used as a 2D coating material.

Mixtures of biomolecules such as Matrigel can also be used to generate scaffolds, with the advantage of not requiring the addition of other bioactive peptides or molecules to achieve many of the same adhesion- and proliferation-enhancing effects.[3] They can effectively mimic the ECM, and so can readily be used to model neural and other biological systems. Kaiser *et al.* showed the effectiveness of Matrigel not only in allowing human neural progenitor cells to survive *in vitro*, but also to support the differentiation of those stem cells into mature neurons, for potential cell replacement therapies.[25] Cavo *et al.* utilised a Matrigel/alginate composite hydrogel to develop a breast cancer model *in vitro,* and to investigate the invasiveness of cancer cells.[26] It was noted that by varying the Matrigel to alginate ratio in the gel, the cell morphology, viability and invasiveness could be influenced. This suggested that systems such as this could be utilised to effectively recapitulate the behaviour of cancer cells *in vivo*. Matrigel is also suitable for direct transplantation, with Uemura *et al.* demonstrating its ability to outperform collagen, laminin and other materials as a means to facilitate graft neural precursor cell survival, outgrowth and proliferation.[27]

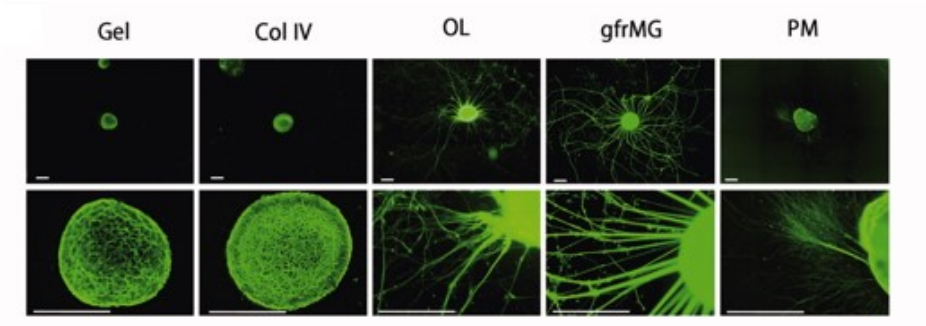


Fig. 1.4: *The effect of different scaffold materials on neurite outgrowth in embryonic stem cell-derived neural progenitor cells. Growth-factor reduced Matrigel (grfMG) was seen to perform favourably relative to the other materials used, with a larger number of neurites observed. Scale bars = 200 µm. Reproduced from Uemura et al.*[27]

The above investigations did not require any added functionalisation or modification of the scaffold from the material as purchased, which is a significant advantage compared to the collagen scaffolds described previously that mostly require some

biofunctionalization. However, it should be noted that in the study carried out by Uemura *et al.,* the Matrigel system did not prevent or significantly decrease the amount of inflammation that was observed at the graft site, indicating that modifications may still be required to minimise the adverse response to the transplanted cells.

Another class of materials that can be leveraged for cell culture systems are GAGs and proteoglycans. Proteoglycans are proteins that contain covalently bound GAG groups. They are ubiquitous across biological systems, and are a major component of the ECM and tissues of the body. In the same way they are used in 2D culture coatings as described above, these molecules can be used to recruit proteins and other growth factors that could play a beneficial role in any 3D bioengineered system.[28,29] Their biodegradability makes these materials a powerful scaffold candidate for implantation, where they can carry their encapsulated cells to the target location before being degraded by the body, which would limit any long term inflammation.[30,31] Karumbaiah *et al*. demonstrated their use as a scaffold for neurite outgrowth through their design of a chondroitin sulfate hydrogel.[32] The scaffold successfully encapsulated neural stem cells, maintaining their viability and, through the binding of growth factors such as FGF-2, also demonstrated higher self-renewal of the stem cells than in unconditioned hydrogel systems. Another GAG that has been used extensively in a range of engineering applications is hyaluronic acid (HA).[33–35] The porous nature of the scaffolds formed by HA means that cell proliferation and growth will not be hindered by the architecture of the scaffold, while also allowing nutrients and signalling molecules to be readily transported throughout the scaffold.[36] It is also a principal component of the neural ECM, meaning that it can aid in attempts at generating engineered neural environments.

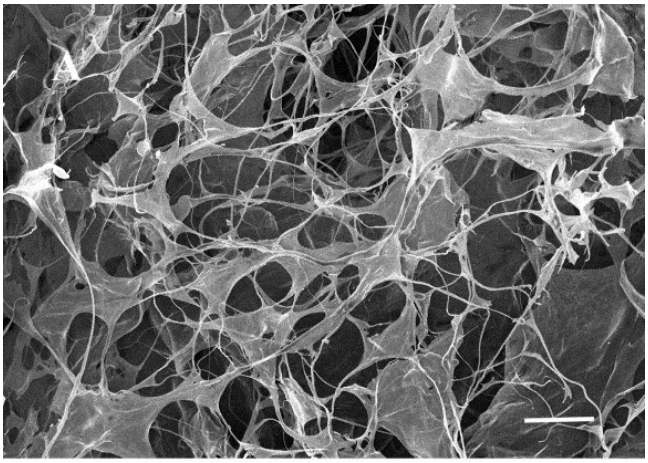


Fig. 1.5: *The porous structure formed in hyaluronic acid hydrogels, which enables cell proliferation and nutrient transport. Scale bar = 50 µm. Reproduced from Hou et al.*[36]

Along with being used to generate scaffolds for tissue engineering applications, GAG molecules can also be added as a coating to scaffolds as a means to electrostatically attach further bioactive components, or to make a substrate surface more amenable for cell adhesion and proliferation.[37–39] Heparan sulfate is a common GAG coating for biomaterial substrates, due to its high affinity for the binding of growth factors and proteins.[40,41] By utilising the charged nature of these molecules, a binding mechanism for proteins or other bioactive molecules could readily be added to a substrate surface. This has various applications in cell interfacing, where the presentation of proteins can be used to direct cell behaviour. In particular, a controlled patterning of proteins could be used to influence the local environment experienced by cells on a single substrate. In this instance, a 2D coating configuration might be more beneficial than a scaffold structure, which could prove challenging to spatially pattern with the biomolecules of choice.

1.2.2 3D scaffolds from synthetic materials

When natural biopolymers are not suitable for specific biological systems, or when higher control over functionality is required, synthetic polymer scaffolds can also be

designed. These materials offer enhanced tailoring of the gel composition, by means of controlled reactions to add side groups and, in doing so, further functionality. This allows the material system to be designed from the bottom up, specifically for the application in question. As well as controlled functionality, the gelation kinetics and physical properties can more readily be modified if the entire gel composition is controlled. This allows for the generation of bespoke systems that can more accurately represent biological environments. Along with controlled functionality, these materials have the advantage of being tailored to specific cell types or applications, with control over physical properties such as elasticity, stiffness and degradation characteristics. Many options have been presented in this area, but some of the most common materials used are poly(lactic acid) (PLA), poly(lactic-co-glycolic acid) (PLGA), and poly(ethylene glycol) (PEG).[42,43] The added control over functionality that these materials provide enables more flexibility towards using the scaffolds for cell interfacing. Growth factors, proteins and other biomolecules can be added to enhance the adhesion of cells to scaffolds, or to direct differentiation of stem cells.

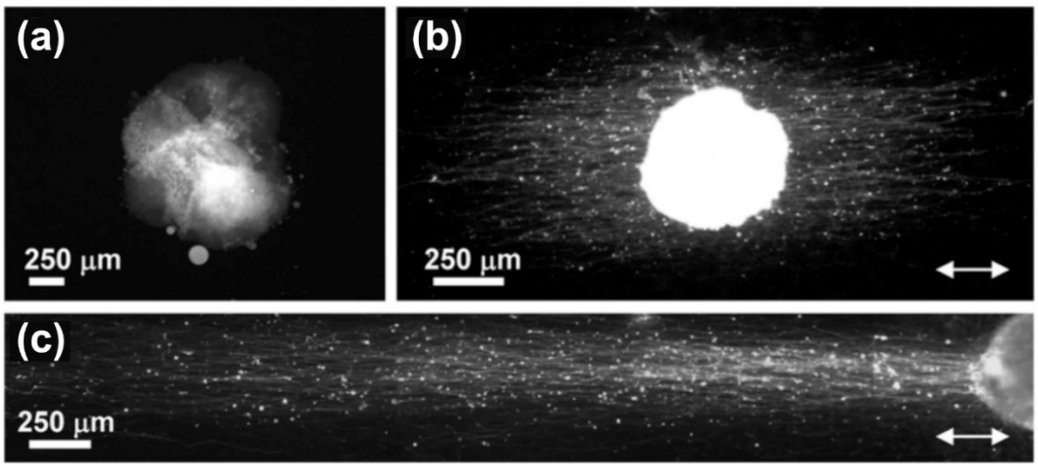


Fig. 1.6: *Neurite outgrowth from dorsal root ganglion tissue on synthetic PLLA nanofibers. (a) shows growth on a randomly aligned scaffold, while (b) shows the enhanced directionality of outgrowth on aligned fibres. (c) shows the neurite growth when aligned fibres in the scaffold are also functionalised with bFGF. Adapted from Patel et al.*[44]

PLA was used by Farzamfar *et al.* to adhere Schwann cells, and to promote growth and elongation of their axons.[45] The system was generated using electrospinning, and cells were enriched with platelet-rich plasma to aid in the axon elongation. While this is an exciting proof-of-concept for neural regeneration studies, it should be noted that as a fabrication method, electrospinning does not always offer control over the alignment or directionality of the individual fibres, but rather creates an overlaid mesh of random orientation (although alignment can be obtained in some cases by controlling rotation speed). This is a limiting factor in any directed growth or regeneration application for the spinal cord or brain. It also required platelet-rich plasma in order to obtain significant changes in cell behaviour. Perhaps a more promising use of PLA as a nerve conduit for regeneration was demonstrated by Zeng *et al.,* who generated channels of controlled dimensions and directionality using phase separation and injection molding.[46] The topography of the material also played a role here, with the nanofibrous nature of this material enabling the controlled differentiation of nerve stem cells into mature neurons.

Relative to the above-mentioned polymers, PLGA offers an increase in the tunability of its various properties, based on the formulation used (since the ratio of PLA and PGA can be varied). This means that factors such as its stiffness and degradation characteristics can be modified to fit specific applications. Kuriakose *et al.* demonstrated the use of PLGA microparticles as a scaffold for lung cancer cell culture.[47] The authors showed that the method of forming pores in the gel influenced the amenability of the material for cell adhesion and proliferation, highlighting the importance of pore structure in the effectiveness of scaffolds. The ability to culture cancer cells in high densities enabled preliminary drug treatment studies to be carried out for therapeutic investigations. It should be noted however that the particles required a fibronectin coating to enable cells to adhere to the polymer. Nune *et al.* utilised the mechanical properties of PLGA, along with self-assembling peptide modifications, to direct Schwann cell elongation and growth, indicating the potential of these synthetic polymer materials as nerve conduits.[48] Electrospinning was again

utilised here, however, giving a random orientation of cell elongation and so limiting the applications until further directional control could be exerted. Hwang *et al.* exhibited this directional control by using a rotating microfluidic system, and used their spun PLGA fibres to seed neural progenitor cells, which had been differentiated from human embryonic stem cells.[49] The progenitor cells were further differentiated while on the scaffold, and behaved as would be expected in tissue culture plastic, but with an increased directionality in their growth.

PEG is a common anti-fouling component of many synthetic biological systems due to its resistance to protein absorption. It is also easily modifiable, with PEGs including various different chemical handles commercially available to facilitate functionalisation. It has been used across a range of biological applications, including in osteochondral, cancer and neural engineering.[50–52] Lampe *et al.* demonstrated that the stiffness of PEG systems can be modified by varying the weight percent of PEG used in the formulation, with lower weight percent compositions enhancing proliferation of neurons and neural precursor cells.[52] The authors did however note that their PEG material only influenced cell behaviour in a 3D configuration. When used as a 2D coating, the material was not seen to have any noticeable effect. Like many synthetic polymers, PEG is not biologically active without the addition of functional groups, and so usually must be incorporated as a mix with other materials (as in the case of some of the above-mentioned natural polymers). However, when used in this way, it has significant potential as a scaffold material for cell interfacing. These materials can also be used as a delivery mechanism, to enhance their effectiveness at directing cell behaviour. Lampe *et al.* loaded PLGA microparticles with a PEG hydrogel and neurotrophic factors. By leveraging the biodegradable nature of PLGA, and the functionalisation of PEG, the authors were able to administer the payload in a controlled manner over a period of 56 days, effectively decreasing the immune response after surgery on animals.[53]

However, as with all platforms, there exists some drawbacks to the use of hydrogels. Functionalisation is not always straightforward, particularly in situations where patterned systems are required, such as the applications to be described in the following chapters. Pre-functionalisation of polymer sidechains can be carried out before gelation, but this can further complicate the optimization of gelation kinetics and mechanical properties. In the case of patterned gels, osteochondral gradient systems have been described in the past, showing significant results.[54] However, this approach could be enhanced by a high throughput technique in parallel, that allows for more rapid prototyping of *in vitro* conditions. By combining 2D and 3D architectures, future experiments and investigations can be better informed.

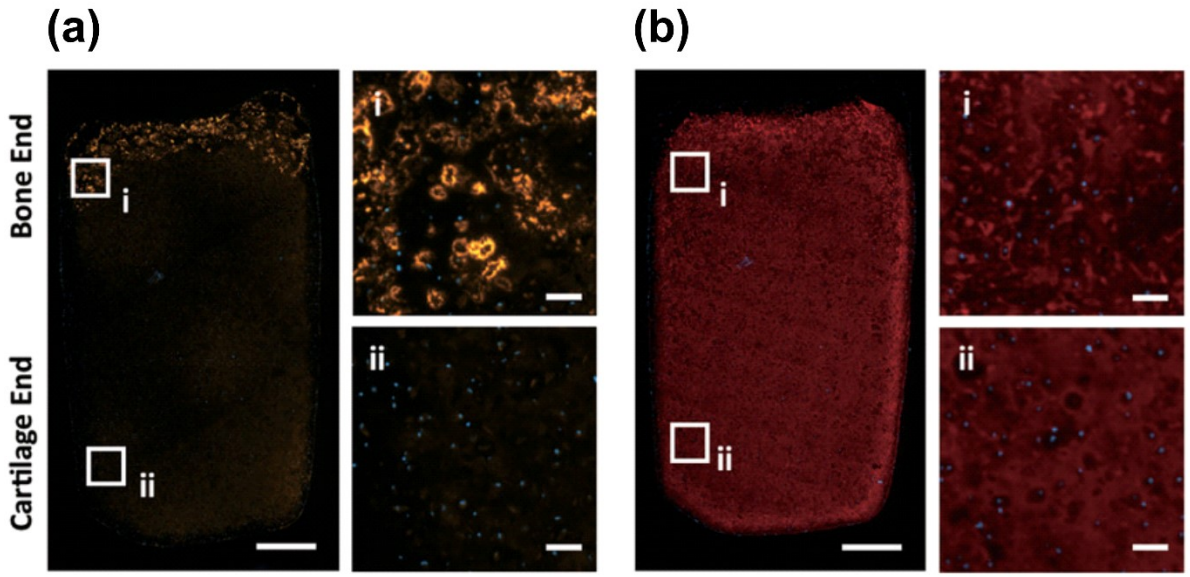


Fig. 1.7: *Osteochondral tissue constructs formed as a result of the presence of a BMP2 gradient (decreasing from top to bottom in above images) in a gel. (a) The bone-specific marker osteopontin was only present in the high growth factor concentration region, while in (b), the cartilage marker type-II collagen was present across the entire construct. Scale bars = 1 mm in low magnification images, 100 µm in high magnification images. Reproduced from Li et al.*[54]

1.3 Microfluidic devices

Many of these *in vitro* approaches have proven quite powerful in advancing the understanding of basic biology, and also in developing new therapeutic methods and tissue engineering strategies. One technique that remains a challenge, however, is the ability to present spatially resolved biochemical cues at the material-cell interface, in order to influence cell behaviour in some way. A controlled exposure to morphogens or small molecules could have profound impact on fields such as stem cell therapy, where controlled subpopulations of cells could be generated. Many attempts have been made with materials systems to recapitulate some of the spatial patterns that arise *in vivo*, in the hope of better modelling biological processes. For example, attempts have been made to replicate the spatial differentiation of cells in the neural tube.[55,56] These studies highlight the potential of a spatially patterned material system for neural engineering applications. The ability to present morphogens at the cell interface in a controlled manner has applications across a range of biological systems, and is an approach that remains underexplored.

The precision of modern techniques such as photolithography enables the generation of materials that present chemical and morphological cues to cells on bio-relevant scales. For applications where dynamic gradients and other patterns are required, microfluidic devices have emerged in recent decades as one of the most potent engineering approaches available. Platforms that use diffusion-based systems can readily generate controlled gradients or patterns, that can be modelled accurately using Fick's diffusion equations. Through a bespoke inlet and flow system, complex local environments of morphogens, nutrients and small molecules can be generated to exert fine control over cellular processes.[55,57] This also enables the modelling of vasculature and perfusion-based systems, which is vital in many tissue engineering applications.

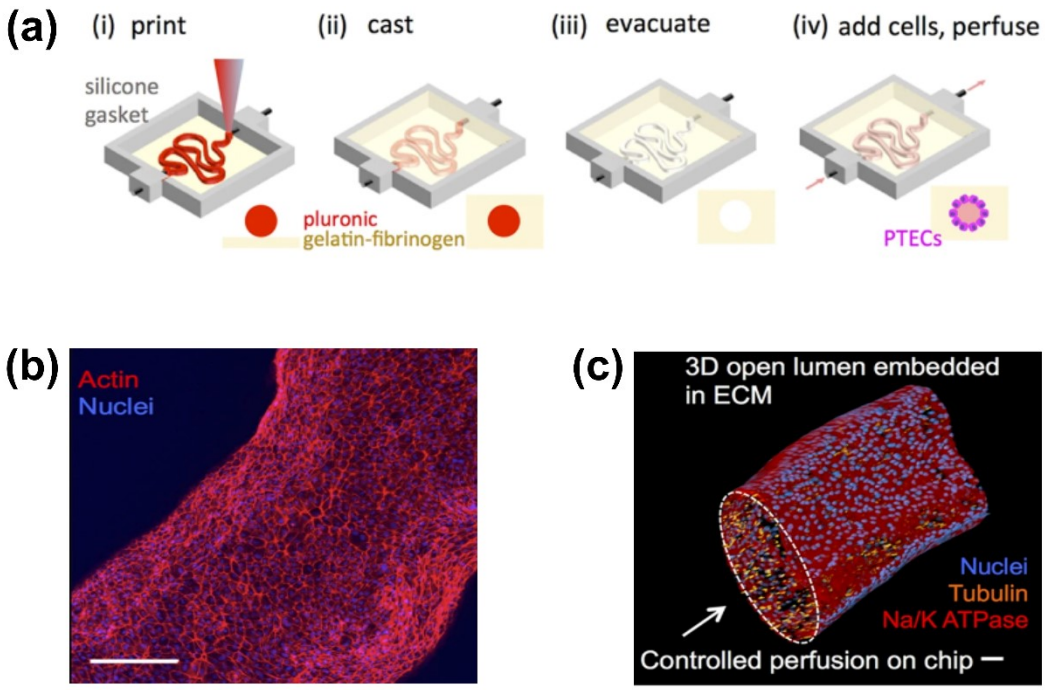


Fig. 1.8: *The design and fabrication of perfusion-based systems for the modelling of kidney function. (a) 3D printing and casting with ECM molecules created a device with a tube-like structure, that was then filled with proximal tube cells and perfused with cell media. (b) Fluorescence image showing the presence of cells in the device chamber. Scale bar = 200 µm. (c) 3D render of the same tube structure seen in (b). Scale bars = 50 µm. Adapted from Homan et al.*[58]

The microfluidic approach enables the recapitulation of systems that occur *in vivo*, and also for the screening of drugs in a manner that more accurately models how they might interact with cells in the body.[59,60] These systems can be made from a range of different materials, with some of the most common being fashioned from silicon and glass using standard microfabrication techniques.[61,62] While these techniques offer fine control over feature dimensions, they employ complicated, time-consuming fabrication methods, and are relatively costly to produce. As such, if a static gradient were required, this might better be achieved through controlled spatial functionalisation of a substrate surface. As the microfluidics field has advanced, polymer-based systems have mostly replaced silicon/glass devices. These offer more

options in terms of material choice, and retain much of the accuracy and robustness of the silicon/glass combination systems, while being cheaper and easier to generate.[63] However, the challenges of throughput and device modification remain.

1.3.1 Microfluidic devices for neural engineering

Microfluidic systems have shown significant promise as a means to generate neural systems *in vitro*, and indeed to model the neural tube itself. Their ability to create dynamic liquid gradients enables the exposure of cells to continuously refreshing nutrients and growth factors, which can be used to differentiate or maintain neural cells in culture for as long as the application requires. Device architectures can also be designed to obtain more complex morphogen patterns, allowing for a range of biological processes to be modelled. As many developmental neural interactions are controlled by gradient signalling systems, these are an exciting candidate for further exploring the frontiers of neural engineering. These systems can also serve to inform researchers on other possible engineering approaches to generate morphogen gradients *in vitro*.

A number of different approaches have been used in attempts to leverage the power of microfluidic devices for neural engineering. Chung *et al.* used a microfluidic device to generate a gradient of a growth factor cocktail that was used to both maintain and differentiate neural stem cells *in vitro*.[64] A significant graded increase in density was observed in the cell chambers that were exposed to a gradient of growth factors relative to the control chambers. The authors also demonstrated controlled differentiation of the neural stem cells into astrocytes, with an inverse relationship observed between number of astrocytes and growth factor concentration. This was consistent with the data obtained from parallel experiments carried out in standard cell culture conditions, demonstrating the effectiveness of this platform at generating graded differentiation responses. Park *et al.* observed a similar trend when they seeded embryonic stem cells in an opposing gradient of sonic hedgehog (Shh) and fibroblast

growth factor 8 (FGF8).[65] There was a sharp decrease in cell density as the Shh concentration decreased and FGF8 increased. The authors also showed preliminary data on the differentiation of the stem cells into neurons, with the number of neuron bodies and neurite bundles showing the same concentration dependency. Choi *et al.* utilised Wnt5a in their microfluidic device to induce differentiation of adipose tissue-derived stem cells into neurons.[66] The authors also noted that they could transplant the cells cultured in their devices into mouse spinal cord injuries, and obtained similar effectiveness of differentiation in cells cultured in both the microfluidic device and on tissue culture plastic controls.

Efforts have also been made to model neural tube development *in vitro* using microfluidics. Demers *et al.* utilised a silicon/glass chip design to expose embryonic stem cells (ESCs) to gradients of the Shh agonist purmorphamine, and bone morphogenetic protein 4 (BMP4).[55] By controlling the concentrations of both the ventral and dorsal inducing signals, the authors were able to specify in which region of their devices mature motor neurons emerged. They also demonstrated the role that the time over which signalling molecules act plays, by observing the Pax6 signal regressing towards the dorsal end of the chip as the time under exposure to the Shh agonist increased. By exposing the cells to a gradient for a week and carrying out live imaging, directed growth of axons along the gradient was observed by day 7. Although the initial device had two input channels, the authors carried out simulations to model the behaviour of a device with four inlets. They hypothesised that this would allow greater influence over the microenvironment that stem cells would experience in the chamber, and so would allow for finer control over the differentiation process.

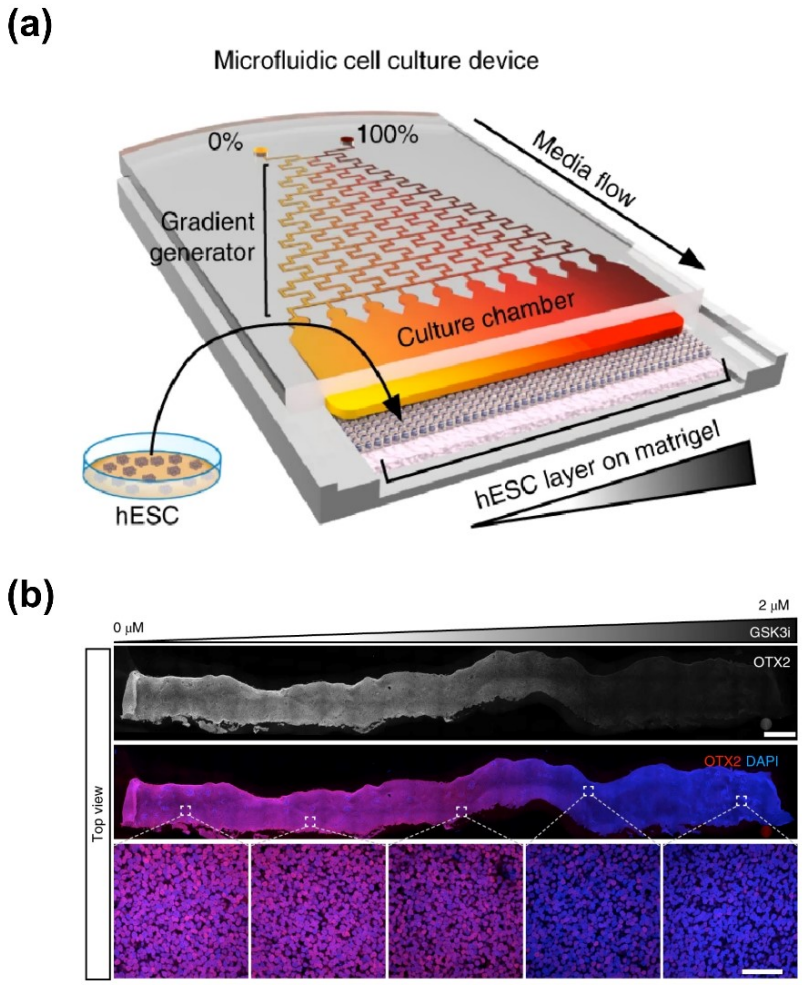


Fig. 1.9: *(a) The microfluidic device design used by Rifes et al. to model the developing rostral-caudal axis of the neural tube.*[56] *(b) The resulting tissue pattern generated from the embryonic stem cells by the Wnt-activating gradient. The rostral marker OTX2 was seen to decrease as Wnt activation (via GSK3i exposure) increases, as would be expected in the neural tube in vivo. Scale bars = 1 mm (top) and 100 μm (bottom). Adapted from Rifes et al.*[56]

While the work from Demers *et al.* focussed on the dorsal-ventral axis of the neural tube (and so the spinal cord), Rifes *et al.* utilised their microfluidic platform to model the rostral-caudal axis of the developing nervous system, and specifically the brain (see Figure 1.9).[56] They employed Wnt-activating gradients to differentiate ESCs into regions that resembled the forebrain, midbrain and hindbrain. Their cells formed tissue

within the seeding chamber, and after 24 h of exposure to their gradient, was shown via single cell transcriptomics to have formed a rostral-caudal separation. The formation of entire tissue sections patterned in a way similar to that of the neural tube is a promising demonstration of the power of gradient-based engineered systems.

1.3.2 Microfluidic devices for cancer biology

Microfluidics platforms have also been used for investigating cancer *in vitro*. Much like the applications described above, the capability to have a dynamic environment for cells with a constant supply of nutrients and/or therapeutic agents makes them a prime candidate for investigating complex systems such as cancers. The bottom-up design approach of microfluidic devices means that the system can be tailored to a specific cancer type, which is of utmost importance when modelling the tumour microenvironment. Mattei *et al.* demonstrated this through the co-culture of B16.F10 mouse melanoma cells and immune cells from the spleen.[67] The cells were cultured in separate chambers, but were connected by microchannels to allow for the movement and interaction of the two cell types. The authors found that mice deficient in interferon regulatory factor-8 were more amenable to the growth and proliferation of melanoma cells, with their immune cells interacting far less with the cancer cells than those of wild type mice. In doing so, their microfluidic device enabled the identification of a potential therapeutic target for future clinical applications. Businaro *et al.* later utilised the same combination of cell types in a more advanced microfluidic device configuration (see Figure 1.10 below) to track via time lapse the movement of the B16.F10 cells through microchannels in the presence of immunodeficient mouse cells.[68]

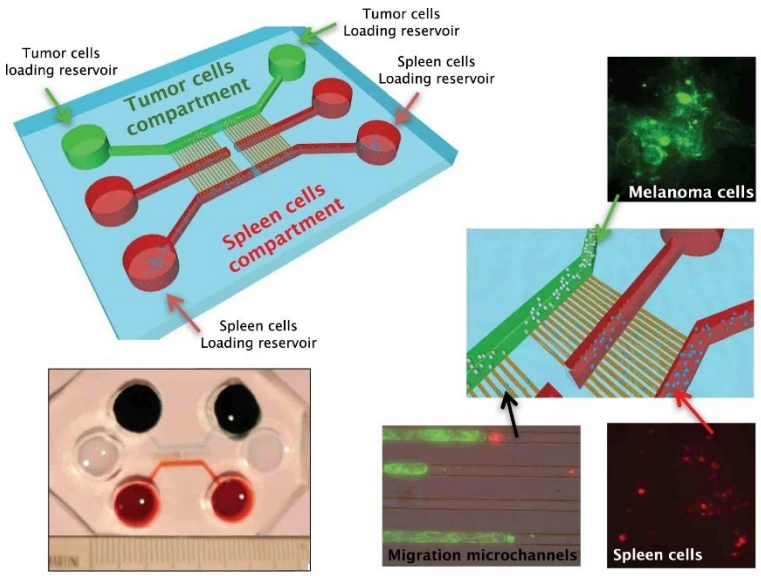


Fig. 1.10: *The microfluidic device used by Businaro et al. to investigate the interaction of melanoma cells with immune cells from both wild type and immunodeficient mice. Melanoma cells were seen to migrate through the microchannels more readily when in the presence of spleen cells from an immunocompromised mouse. Image reproduced from follow-up analysis paper by Agliari et al.*[69]

Bischel *et al.* used their flow-based device to model ductal carcinoma in situ (DCIS), a common precursor to many types of breast cancer.[70] The authors patterned the culture chamber with ECM hydrogel scaffolds that contained lumens lined with epithelial cells. The lumens were then filled with DCIS cells, which were co-cultured with fibroblast cells to recapitulate the tumour microenvironment in a mammary duct, and to investigate the invasiveness of the cancer cells. Their model was seen to accurately generate cell-cell interactions and junctions as would be seen *in vivo* in the mammary duct. When DCIS cells were introduced to the system, a number of invasive lesions were also observed, indicating that this material system could be used in future works to investigate the role that specific factors play in the progression and metastasis of this condition.

Along with the culturing of cancer cells to recapitulate the tumour environment *in vivo,* microfluidic devices can also be used to investigate the interaction of therapeutic

agents with cancer cells. Han *et al*. used their microfluidic device as a means to generate cell types that were resistant to a specific drug, through exposure to a continuous gradient of Vemurafenib (a common inhibitor drug used for cancers containing BRAF mutations).[71] These cells could then be isolated and sequenced, to investigate the mechanisms giving rise to their resistance to treatment. In this study, the microfluidic system offered a means to rapidly generate drug-resistant cell lines that might otherwise have been difficult to obtain from patient samples. Bai *et al*. employed a method similar to that of Bischel *et al.*, co-culturing cancer cell lines with human umbilical vein endothelial cells (HUVECs) in their microfluidic device chambers to better model the tumour microenvironment.[72] Once cultured, the authors then used their flow-based device to expose two different carcinoma cell lines to four common drugs, and to investigate how multiplexing of drugs and the co-culture environment inhibited the dispersion of the cancer cells that might play a role in metastasis in the body. The HUVEC cells were seen to increase dispersion of the cancer cells, which was attributed to the release of growth factors from the HUVECs that influenced the cancer cell behaviour.

The potential of microfluidic devices is apparent from the studies described above. However, there remains a number of challenges to be overcome before their use becomes widespread in cell interfacing applications. The devices in general once manufactured are extremely difficult to alter structurally. Surface chemistry modifications can be introduced, but the general device architecture is not easily modifiable. Although the liquid being introduced can be altered, the pattern being generated is defined by the design and inlet system, and so potential changes in this part of the device are limited. These devices are usually manufactured with one or few target applications, and a new device must be drawn up if the scope of the investigation evolves. This drastically limits the throughput of these materials systems relative to standard *in vitro* well plate approaches. Some of these disadvantages have been somewhat offset since polymer materials have replaced silicon/glass devices.

However, these chips are still time consuming and challenging to manufacture, and may well be expensive relative to other approaches for prototyping.

1.4 Inkjet printing and its applications

If the limitations of microfluidic devices cannot be overcome for a system that requires spatially patterned biomolecules, other approaches must be considered. One technique that has received considerable attention in research settings in recent decades is inkjet printing. The applications of this method are limited for the patterning of 3D scaffold structures (due to the top-down printing approach), but for patterning of 2D surfaces and interfaces, inkjet printing enables the deposition of bio-active inks at a high resolution and accuracy, while enabling rapid modification of the device configuration that would not be possible with microfluidic systems.

1.4.1 Background

As the technology of inkjet printing has advanced, two methods have emerged as the most common printing techniques – continuous inkjet printing and drop-on-demand printing.

In continuous inkjet (CIJ) printing, the ink in question is pumped from a reservoir through a nozzle in a stream, which is then broken up into droplets through the vibrations of a piezoelectric crystal.[73] The droplets are directed by passing electrically charged plates, to deposit onto the substrate. This continuous deposition allows for high speeds of printing, and is less prone to nozzle blockage due to the continuous flow of ink. However, the use of the charged plates to pattern the ink means that charged inks or polar solvents must be used, which can be a limiting factor for many of the research applications to be discussed below. The fact that the majority of the ink is not deflected enough to be printed and is instead recycled to the reservoir can also cause issues where unstable or volatile materials are being used. It is relatively expensive (due to the use of piezoelectric crystals and a recycling circuit) and inefficient

as a technique. Despite this, CIJ printing still finds use in some industrial applications, particularly large-scale printing.

More recently, drop-on-demand (DOD) printers have become widespread, and are the most common type of inkjets used in office and home applications. These systems offer finer control over the patterning of the ink, removing the need for ink recycling and potential wastage. There are two main variations of this technique – thermal and piezoelectric DOD printing.[74] In thermal printing, the ink is contained in a reservoir or cartridge, which contains outlets in the printhead for patterning. These are manufactured using photolithography techniques, to have multiple nozzles that can print simultaneously. The printhead contains a microresistor in the chamber wall which, when a droplet is needed, has a current passed through it. This current causes the resistor to heat up, and in turn vaporises a small amount of the ink. A cavity is created which forces a droplet out of the nozzle, and this process is repeated as needed to release droplets and generate a pattern. It is important to note that the volume of ink heated at the resistor is extremely small, and does not have any lasting impact on the ink content as a whole. This is the cheapest version of inkjet printing in common use. The ink must contain a volatile component in order for cavitation to occur, and so water is often used as the carrier. This somewhat limits the materials that can be printed with this approach.

In the piezoelectric system, a similar process occurs to that of a thermal printer. However, instead of heating a resistor, in this case a voltage is applied to a piezoelectric crystal in the reservoir, causing it to change shape. This creates an increase in pressure in the ink chamber, which forces a droplet out of the nozzle. There is no heating of the ink, and so there is no risk of denaturation or loss of activity in the case of biomolecule printing. However, the piezoelectric systems are somewhat more expensive and difficult to manufacture, due to the use of piezoelectric crystals. This in turn increases the cost of maintenance if needed. Together, these two techniques are utilised in the majority of inkjet printing applications in use today.

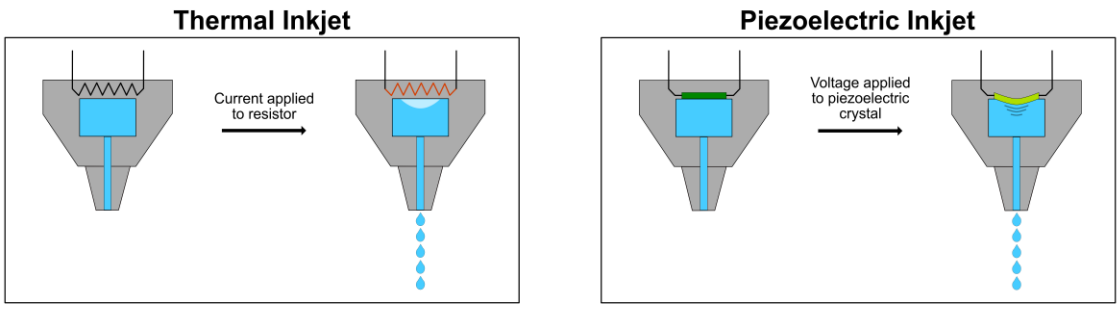


Fig. 1.11: *The two types of drop-on-demand inkjet printing most common in modern machines. Thermal inkjet (left) relies on a microresistor within the printhead. When heated, this creates a cavity within the body of ink in the reservoir, which forces droplets out of the nozzle. In the piezoelectric system (right), a voltage is applied to a crystal within the printhead, causing it to change shape. This in turn creates a pressure wave within the ink reservoir, which forces droplets through the nozzle.*

Other methods of inkjet printing have also emerged in recent years as the applications and commercial opportunities in the field have grown. These range from pressure-based systems (e.g. the I-DOT liquid handling system, Cellink GmbH) to solenoid valve-based apparatuses that are controlled by the application of a current to the valve (e.g. BioJet, BioDot).[75] Most of these modern printing approaches enable fine control over the volume of ink being deposited, and by avoiding the use of thermal perturbations, minimise the risk of any disruption to the bio-ink quality.

1.4.2 Applications

Initially, this technique was used to print inks in office work and industrial labelling. However, in the mid-1990s, researchers began to investigate the potential of spatially patterning biomolecules in applications such as microarray generation, *in vitro* cell culture investigations and in drug screening.[76–80] In standard *in vitro* cell culture, the cells are exposed to their environment through the contents of their media only, or through some form of coating on the substrate they are seeded on. While this is useful

for interrogating the influence of one homogenous condition, it removes any option of variation within a single sample, as all cells will experience the same conditions and so will respond in a similar manner. Through the patterning of molecules such as proteins or peptides, a complex microenvironment can be generated on a substrate surface, wherein cells will be exposed to different local cues that can direct differentiation, proliferation or a host of other biological processes.[81–83] Microarrays of varying molecules can be generated with ease, which can be used for the screening of different small molecule drugs, or as a concentration screen for protein agonists or inhibitors. Directed differentiation of stem cells is of particular interest for many bioengineers, for the potential therapeutic applications it offers. Current stem cell therapies require the generation of various cell types, which is time consuming and expensive when done with standard *in vitro* approaches. Through the printing of patterns such as gradients or competing morphogens, signalling pathways can be activated in a controlled manner, and so the stem cells can be directed with finer control and precision. This has significant applications in osteochondral, cardiac and neural engineering, and as well in blood-related conditions and in cancer.

In particular, printing can potentially offer an effective method for modelling developmental processes. At the early stages of embryogenesis, bodies of stem cells in the various structures are directed along specific paths by patterns of morphogens. These initial components give rise to incredible complexity, and by using inkjet printing, patterns can be generated to potentially emulate this and direct the differentiation of stem cells *in vitro*. The flexibility of the platform, and ease of ink changing means that once developed, the technique can be used across a range of different applications, by modifying or replacing the morphogen and cell type being used.

The method is also high throughput, as a number of substrates can be patterned simultaneously, and the pattern generated is limited only by the number of ink reservoirs present. In theory, with current industrial machines, hundreds of inks can be

printed in parallel to generate complex patterns. As such, concentrations, combinations and mixes of biomolecules can rapidly be prototyped, to optimise for the application in question. As the technology and industry advances, the precision, accuracy and resolution improve dramatically, and the scope for its use continues to expand.

Perhaps the main drawback of inkjet printing is that the pattern generated is 2D, which somewhat limits the fidelity to which *in vivo* systems can be modelled. However, as a complimentary tool with other techniques, or in applications where 3D structure is not required, inkjet printing still has significant potential in biological research and industrial applications.

1.5 Nanostructured substrates

The choice of substrate for any printing application is of utmost importance, since the topography and wetting properties present will determine how efficiently a printed pattern can influence cell behaviour. In recent years, nanostructured substrates have been applied across a range of cell interfacing applications, with various topographies being investigated.[84] These structures have garnered considerable attention due to the increased contact surface area they provide with the basal cell membrane. These substrates enable exertion of finer control over the microenvironment experienced by cells, by presenting both physical and biochemical (through functionalisation) guidance cues. Combining these topographies with the capability to selectively pattern regions of the substrate with bioactive molecules could enable a range of biological applications, from stem cell differentiation to directed cell growth and proliferation.

1.5.1 Nanopillars and nanowires

Advances in manufacturing techniques have allowed for the fabrication of increasingly detailed topographical surfaces, with techniques such as photolithography and nanoimprint lithography enabling feature sizes on the micrometre-scale and

below.[85,86] As the demand for a reliable and non-toxic method to interface with cells has increased in tandem with advances in genetic engineering and cell biology, these material systems have offered a novel approach to influencing cell behaviour. Nanostructured materials offer a complex, modifiable surface that can be interfaced with cells for a range of applications. Previously, silicon nanopillars have been used as a means to physically influence the growth of cells, for electrical sensing within cellular microenvironments, and also as electrical stimulation systems.[87–89]

Kim *et al.* demonstrated the ability of nanopillars (titled nanocolumns here by the authors) to act as a physical guidance cue for neurite growth *in vitro*.[89] By generating silicon structures varying in height from 300 nm to 1.8 µm, the authors demonstrated directed axonal growth along the tops of the nanotopographies. The arrays generated were disordered, but were constrained to a defined region by the fabrication of the cross-shaped patterns on the substrate. The structures did not require any functionalisation or coating to achieve the effect shown in Figure 1.12.

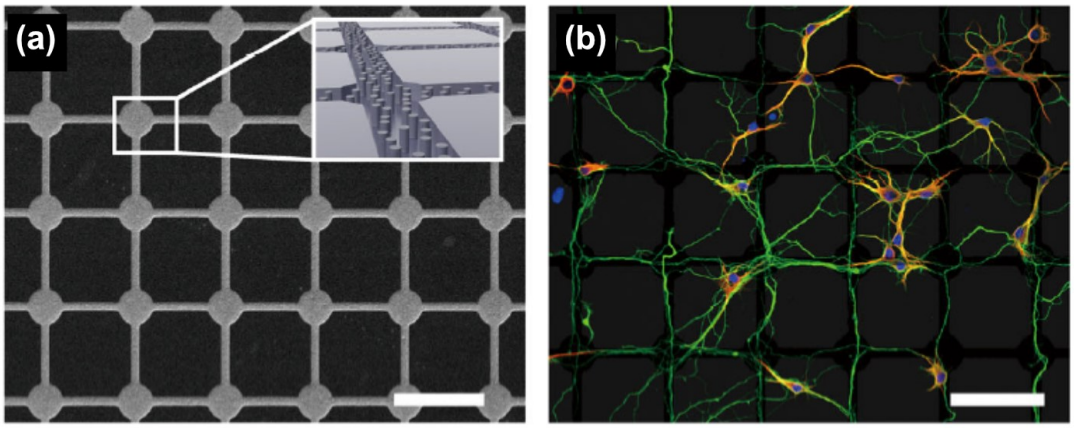


Fig.1.12: *Silicon nanocolumns used to direct neurite outgrowth in vitro. (a) Representative scanning electron microscopy image of the nanocolumn arrays. (b) Neurons growing on the nanotopographical substrate. Scale bars = 100 µm. Reproduced from Kim et al., with permission.*[89]

Shalek *et al.* utilised a similar nanowire system as a delivery mechanism, successfully silencing genes within a range of cell types by delivering siRNA.[90] In doing so, the

authors demonstrated the capability of nanostructured substrates to deliver cargoes to primary immune cells, highlighting the potential of these systems for gene therapy applications. It was noted that the dimensions and properties of the structures needed to be changed based on the cell type in question, with certain cell lines requiring sharper and more dense arrays for successful delivery.

Nanotopographies have also been shown to successfully record action potentials of neural cells, and have similarly demonstrated the ability to influence cell behaviour through electrical stimulation. The enhanced surface area and more intimate contact with the basal cell membrane relative to flat substrates allows for improved sensing and stimulation relative to a flat surface of the same material.

1.5.2 Nanoneedles

Another material system that has shown considerable promise in the interfacing field is the nanoneedle platform, developed in a number of labs around the world.[91,92] Most often, these nanoneedle substrates are made from silicon or diamond, with both systems having their advantages. In general, silicon structures offer finer control over the surface topography, being limited only by the pattern definition in the photolithography step. Ordered arrays can readily be generated, with a controlled pitch and feature size, to ensure homogeneity across the surface and to allow for uniform interfacing with all cells that are seeded on the surface. The size and shape of these silicon structures allows them to interact directly with individual cells without any perceived negative effects, and to deliver a payload to the cell cytosol without permanent membrane disruption.[93] This has included the delivery of quantum dots and nanoparticles, as well as a pH-sensing technique which can be used in cancer diagnostics.[91] In particular, the localised delivery of nucleic acids to cells offers a range of possibilities for gene expression and tissue structure/function studies.[93] These nucleic acids must be delivered directly to the cytosol or cell nucleus to carry out their intended task, which presents a challenge due to their inherent charged nature. This

prevents them from crossing the cell membrane boundary, and as such, nanoneedles offer the ideal candidate to ferry these biomolecules directly into the cell. This also minimises interactions with the endolysosomal system, which could be detrimental to the uptake of the intended molecule. It is still unclear whether the nanoneedles puncture the cell membrane, or simply associate tightly with it, allowing for internalisation through standard pathways. However, as discussed by Gopal *et al.*, the most likely mechanism is an invagination of the cell membrane without penetration, allowing for increased uptake due to the larger contact surface area and endocytosis.[94]

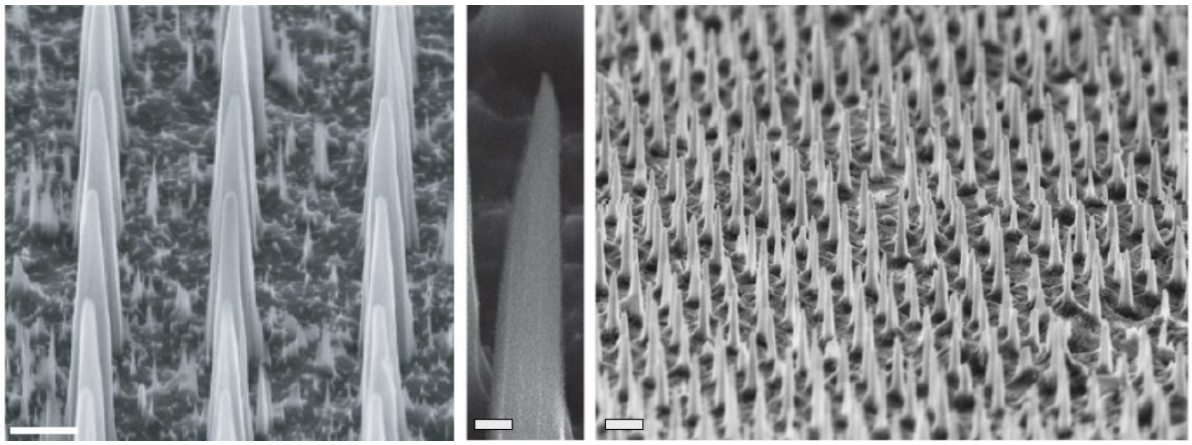


Fig. 1.13: *Silicon nanoneedle structures created by the Stevens group using microfabrication techniques. Scale bars: left = 2 µm, centre = 200 nm, right = 2 µm. Adapted from the work of Chiappini et al.*[91,93]

The Stevens group have reported a delivery efficiency of greater than 90% with their nanoneedle system, which has also included two simultaneous payloads (siRNA and DNA). This transfection ability, which is central to any gene expression or silencing applications of the delivery method, is significantly superior to that reported by other potential approaches.[95,96] In a biosensing capacity, the potential of the nanoneedles was investigated through their use as a pH sensor (using a pH-sensitive fluorophore).[91] Studies have also demonstrated the enhanced delivery to tissue using nanoneedles relative to flat surfaces, showing that these substrates have potential *in vivo* application also.[93]

As well as silicon nanoneedles, diamond nanoneedles have been manufactured for biological interfacing, and have reported competitive delivery efficiencies (eight times more effective than lipofection).[92,96–99] These structures were used to deliver anti-cancer drugs, quantum dots, genes and cell probes in a similar manner to that of the silicon needles described above. However, a centripetal acceleration was required with this system for delivery, which could increase the risk of damage to cells and would not be viable for *in vivo* applications. In general, interfacing with cells from above or below without the need for centrifugation would be the optimal way to apply these substrates.

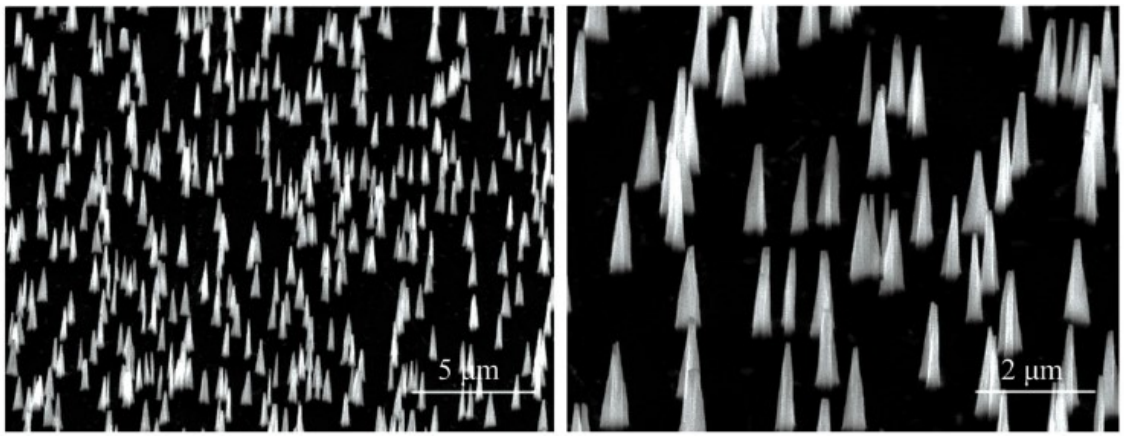


Fig.1.14*: Diamond nanoneedle arrays generated for cell interfacing. The manufacturing method used creates a random array of surface structures, without the order observed in the silicon nanoneedles above. Reproduced from Zhu et al.*[97]

While the mechanisms responsible for the uptake of payloads into cells are debated, its efficacy is obvious from the multiple studies mentioned here. The disruptive nature of the substrates on cell integrity seems minimal, although further studies will no doubt investigate this further. Nanoneedle arrays offer an abundance of potential uses and experiments, with chemical functionalisation and new morphologies now possible. A combination of these surface topographies combined with the technique of surface patterning offers both physical and biochemical control over cell behaviour, and could be a valuable tool for investigating fundamental biological questions.

1.6 Conclusions and aims

Bioengineered material systems have shown significant promise in investigating a range of biological systems both *in vitro* and *in vivo*. While 3D scaffolds are ideal for specific applications, the complexity they introduce to a system is not always required to effectively investigate biological systems. For example, in neural tube modelling or in organoid formation, 3D architectures do not in fact offer a significant advantage over simple surface coatings from the same materials. In many instances, cells are in thin sheets (or often even monolayers), and so a 2D environment with suitable biochemical cues is sufficient to recapitulate the biological processes at work. As organoids grow, they need space to develop and form full functionality. Although the cavity size and porosity can be controlled to some degree in hydrogels, this would still inevitably limit the growth space that the organoid would have. In those cases, growing the cells on coatings of ECM components such as proteins or GAG molecules, with relevant cues attached, would most likely be the most suitable approach. This would also enable electrostatic binding of bioactive molecules to exert control over cell behaviour. For systems requiring patterning of morphogens or proteins, 2D surfaces also offer considerably more facile patterning than the complex structures of scaffold and gel materials.

Ideally, if a new material system were to be presented to offer a realistic alternative to many of the methods mentioned above, a number of criteria would need to be met: the platform would need to be high throughput, allowing for large numbers of tests and conditions to be carried out in parallel; it would need to be easily modifiable, allowing for alterations to the test conditions (e.g. the morphogen or concentration the cells are exposed to) as required; it would need to be relatively simple to use, without the technical complexities of something such as a microfluidic system; it should be biocompatible across different environments, and robust enough to withstand a host of different test conditions and handling. If all of these conditions could be met by a materials system, this could potentially provide a tool that could massively enhance the capabilities of developmental neural engineering, cancer

biology and biological investigations as a whole, by accelerating the rate at which new discoveries and treatments can be realised. If this platform were iterative and relatively easily modifiable, then the system could readily be applied to other systems by changing the morphogen pattern and cell type seeded. For any application in which morphogen patterns play a role, a materials system such as this has potential to become a tool with significant impact across a range of biological fields.

1.6.1 Aims of the thesis

Chapter 2 describes efforts to generate a material platform to realise the requirements for an effective spatially patterned material interface described above. Efforts were made to fabricate a modular system for influencing cell behaviour *in vitro* by leveraging nanotopographies and biochemical surface patterns (via inkjet printing).

Chapter 3 details the utilisation of this material platform in controlling the differentiation of embryonic stem cells into spinal cord progenitor cells. The goal of this project was to leverage the ability to create gradients of protein bio-inks to recapitulate the spatial patterning of the early-stage neural tube. It was hoped that by effectively modelling the emergence of the developing nervous system *in vitro*, novel insights into the mechanisms of neurogenesis (and indeed the occurrence of diseases) could be gained.

In chapter 4, investigations were carried out to apply a modified version of the patterned interface system to cancer cell culture, to elucidate the role of Wnt signalling in cancer progression. It was hoped that by presenting varying local concentrations of relevant ligands to cancer cells, the potential of this platform across a range of biological fields could be demonstrated. Signalling pathways play a central role in cancer emergence and progression, and are the focus of a number of clinical trials towards novel therapeutics. A material system such as this that enables the generation of bespoke local biochemical environments *in vitro* could be a powerful screening tool in accelerating investigations into advanced therapies for cancer.

Chapter 2

Materials fabrication and characterisation

Chapter 2: Materials fabrication and characterisation

This chapter describes the methods used to generate the morphogen-patterned substrates for cell culture experiments in chapters 3 and 4.

Nanoneedle substrates were fabricated by Dr Stuart Higgins. Raman spectroscopy was carried out by Dr Isaac Pence. X-ray photoelectron spectroscopy and atomic force microscopy were carried out by Dr Daniel Hachim Diaz. Scanning electron microscope images were captured by Raya El Laham. Dr James Armstrong assisted in Safranin-O staining protocols. All other experimental data, data interpretation and analysis were carried out by the author.

2.1 Summary of experimental approach

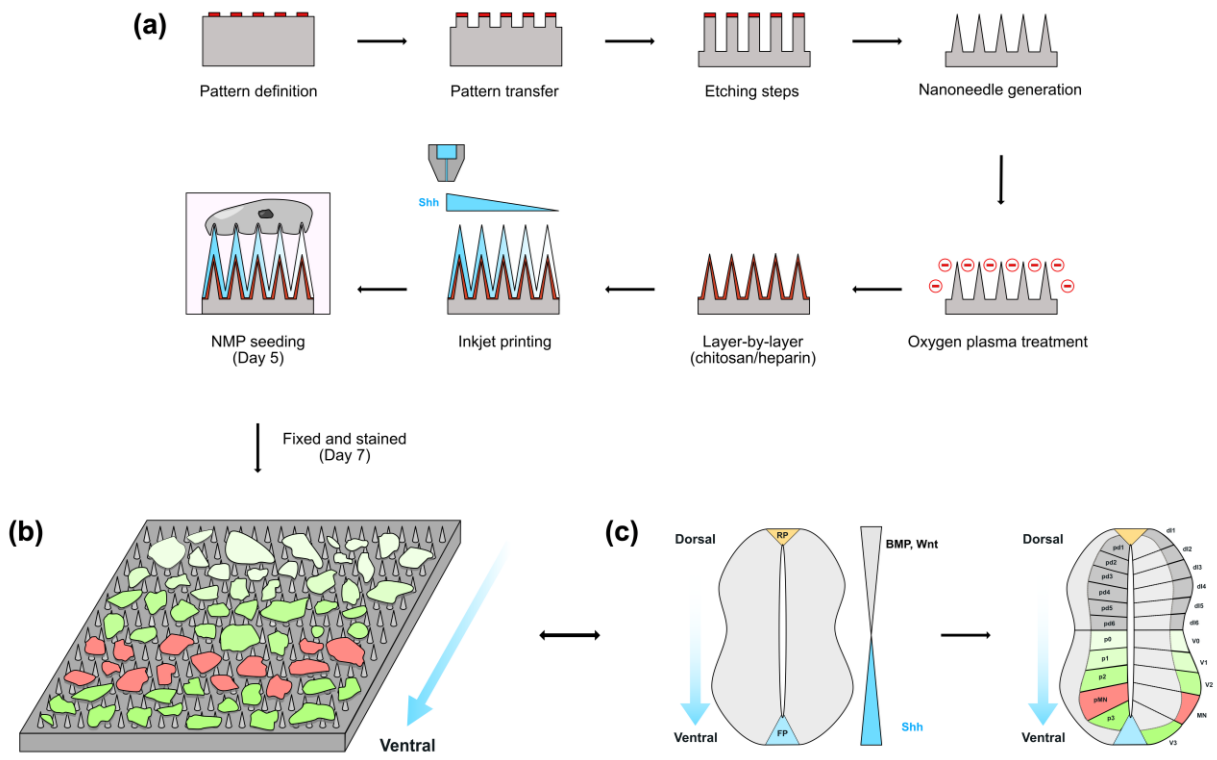


Fig. 2.1: *A schematic of the experimental approach across the various projects in this piece of work. (a) Microfabrication techniques were used to define and etch high aspect ratio nanoneedle structures onto the silicon substrate. These substrates were then coated in electrostatic material through the use of the layer-by-layer method, which enabled the binding of inkjet-printed protein gradients. (b) When cells were seeded onto the gradient substrates, the printed pattern could then be used to direct their behaviour. In the case of neuromesodermal progenitor cells shown here as an example, gradients were used to recapitulate, on a single substrate, the delimited regions of neural cell types generated in the ventral neural tube (shown in (c)).*

The defining piece of this work is a materials platform that directs cell behaviour *in vitro* via physical and biochemical surface cues. This is achieved through the use of nanotopographical silicon substrates and inkjet-printed morphogen gradients.

Figure 2.1 above depicts the methods that were employed to generate this material system. Microfabrication techniques were used to generate high aspect ratio silicon nanoneedles, with a tip sharpness of less than 50 nm. These topographical substrates have previously been shown to provide physical guidance cues to cells, and also are an efficient means of biomolecule delivery, due to their increased contact surface area with the cell basal membrane.[91,93,94,100,101] Their hydrophobic nature (as a result of their high aspect ratio) also makes them an attractive candidate as a printing substrate.

Nanoneedles were coated in electrostatic bilayers via the layer-by-layer process, before being patterned with bioactive molecules in order to influence cell behaviour *in vitro*. In the above schematic, the ventral patterning of the developing spinal cord is used as an example, where printed Shh gradients directed the differentiation of mouse embryonic stem cells from neuromesodermal progenitors (NMPs) into spinal cord progenitors.

The platform has also been utilised as a means to investigate Wnt signalling pathways, and their role in cancer progression. This chapter describes the steps taken to fabricate this material system.

2.2 Nanoneedle substrate fabrication

In the Stevens group, there are two versions of nanoneedle substrates that have been utilised for cell interfacing applications. The first is a porous, degradable nanoneedle substrate that has been used primarily for delivery applications.[91,94,100] The second nanoneedle substrate type is made from a non-degradable, non-porous silicon. The motivation behind the fabrication of this substrate type is to enable longer cell interfacing studies, to better understand the role that these topographies could play in influencing cell behaviour.[101] This second type is used throughout this work.

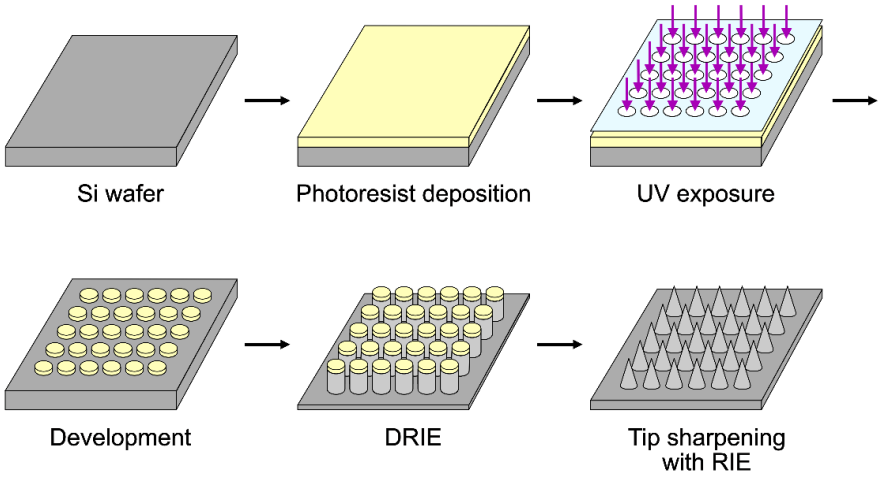


Fig. 2.2: *The fabrication process for the generation of nanoneedle substrates from a silicon wafer. Through the use of a photoresist and UV exposure in the presence of a photomask, the positions at which the nanoneedles were to be generated were defined. Plasma etching steps (DRIE and RIE) were then utilised to generate high aspect ratio nanoneedles. Note: schematic not to scale.*

Silicon nanoneedle substrates were generated from boron doped p-type wafers. Firstly, a negative photoresist (NR7-250P, Futurrex) was spin coated onto the surface in a three-stage process: an initial 5 s at 500 rpm, followed by 40 s at 4000 rpm, and finally 5 s at 0 rpm. This gave a photoresist layer with a thickness of approximately 175 nm. The wafer was soft baked on a hot plate at 135°C for 60 s, before being placed on a room temperature metal surface to cool.

The wafer was loaded into a mask aligner (MA-6, Karl Süss, fitted with a 320 nm UV filter) to perform photolithographic pattern definition. The lamp was set at 400 W in the constant power mode, and the wafer was exposed for 2.9 s, yielding a dose of 8 mJ/cm^2, before being post-baked on a hotplate at 100°C for 60 s. The UV-exposed substrate was then subjected to a development step (RD6 developer, Futurrex, made up in 3:1 ratio with deionised water) for 12 s with agitation, before being submerged in deionised water for 1 min, and dried. At this point, the array of nanoneedle positions had been defined on the surface, and the substrate was ready for further etching steps.

A deep reactive ion etching step was needed to etch the defined points on the surface into pillar-like structures, via the Bosch process (sequential deposition and etching, using C_4F_8 and SF_6 respectively. The C_4F_8 acts as a protective element, ensuring that the SF_6 etching occurs in an anisotropic manner). This resulted in deeply etched features with minimal etching of the walls of the structures, increasing the height of the pillars left behind. In this instance, 45 deposition/etch cycles were carried out to generate nanopillars with a height of 5-10 µm. Reactive ion etching (RIE) was used to sharpen the pillars into needle shapes (PlasmaPro NGP80 RIE, Oxford Instruments, again with SF_6). After a ten minute cycle (two minute stabilisation, eight minute etching), the pillars had been sufficiently sharpened. Post-sharpening, wafers were diced into 8 x 8 mm substrates.

2.3 Layer-by-layer coating development for silicon substrates

2.3.1 Motivation for the use of layer-by-layer coatings for protein binding

In order to influence the behaviour of cells via printed bio-ink patterns, a method would be needed to maintain the chosen morphogen at the substrate surface. This binding method would need to be robust enough to be preserved in culture media, to effectively initiate the target signalling cascades. One option would be to carry out a covalent chemical coupling of the patterned protein to the surface. However, for this work, this approach was disregarded because of the possibility of interfering with protein activity, which is central to the cell signalling and differentiation processes. Covalent bonds would irreversibly alter the structure of the protein being functionalised on the surface, which could prevent it from carrying out the intended purpose. Electrostatic binding was instead chosen as a more suitable means to achieve this goal, due to the non-permanent nature of the interactions formed. The layer-by-layer (LbL) technique was selected, which involved the deposition of alternating layers of oppositely charged materials in nanometre-scale coatings on the substrate surface. As the coating process is repeated, multiple stacked bilayers are created, generating a

robust coating with one charged material as the outer layer. This outer layer can then be used to electrostatically bind the protein of choice. Heparin and alginate were chosen here as candidates for the outer, negatively charged layer for the platform. A negative material can be used to bind a range of positively charged biomolecules, enhancing the flexibility and utility of the system for other applications (provided the biomolecule maintains this positive charge in the printing conditions). Through the use of an electrostatic interaction, the structure and activity of the morphogen is maintained, while the binding is strong enough to anchor the molecule at the surface sufficiently to allow interactions with cells to occur.

2.3.2 Method to generate layer-by-layer coatings

As the LbL coating is quite a time-consuming technique, efforts were made to automate the process. A desktop 3D printer (MeCreator 2) was modified with extra printed parts, with a bespoke holder designed to contain up to three nanoneedle substrates. A script was written by Dr Liliang Ouyang to move the holder from well to well in a 24-well plate to carry out the coating. The substrates were washed in a 1:1 mixture of acetone and isopropyl alcohol to remove any debris or contaminants. After drying, substrates were treated with an oxygen plasma to induce a negative charge (100 W, 20 min. Plasma Prep, GaLa Instrumente GmbH) before the coating process could be initiated.

Solutions of heparin (Sigma-Aldrich, cat. no: H3393) were made up at 2 mg/mL in HPLC grade water, while chitosan (low molecular weight, Sigma-Aldrich cat. no: 448869) solutions were made up at 2 mg/mL in water/acetic acid (0.5% v/v). A schematic of the well plate layout is shown in Figure 2.3 (d) below. By submerging the substrate in well A1, a layer of chitosan was first added onto the negatively charged substrate surface, followed by three water washes (A2-4), before a subsequent heparin coating was carried out (B4). After three more washes (B3-B1), the first bilayer was completed, and the steps could then be repeated to generate the required number of bilayers.

Previous internal studies by Dr Daniel Hachim Diaz had indicated that ten bilayers were sufficient to give total coating of the silicon substrates used here. The presence of the heparin/chitosan on the substrate surface was verified using scanning electron microscopy, contact angle measurements, Safranin-O staining, X-ray photoelectron spectroscopy and atomic force microscopy.

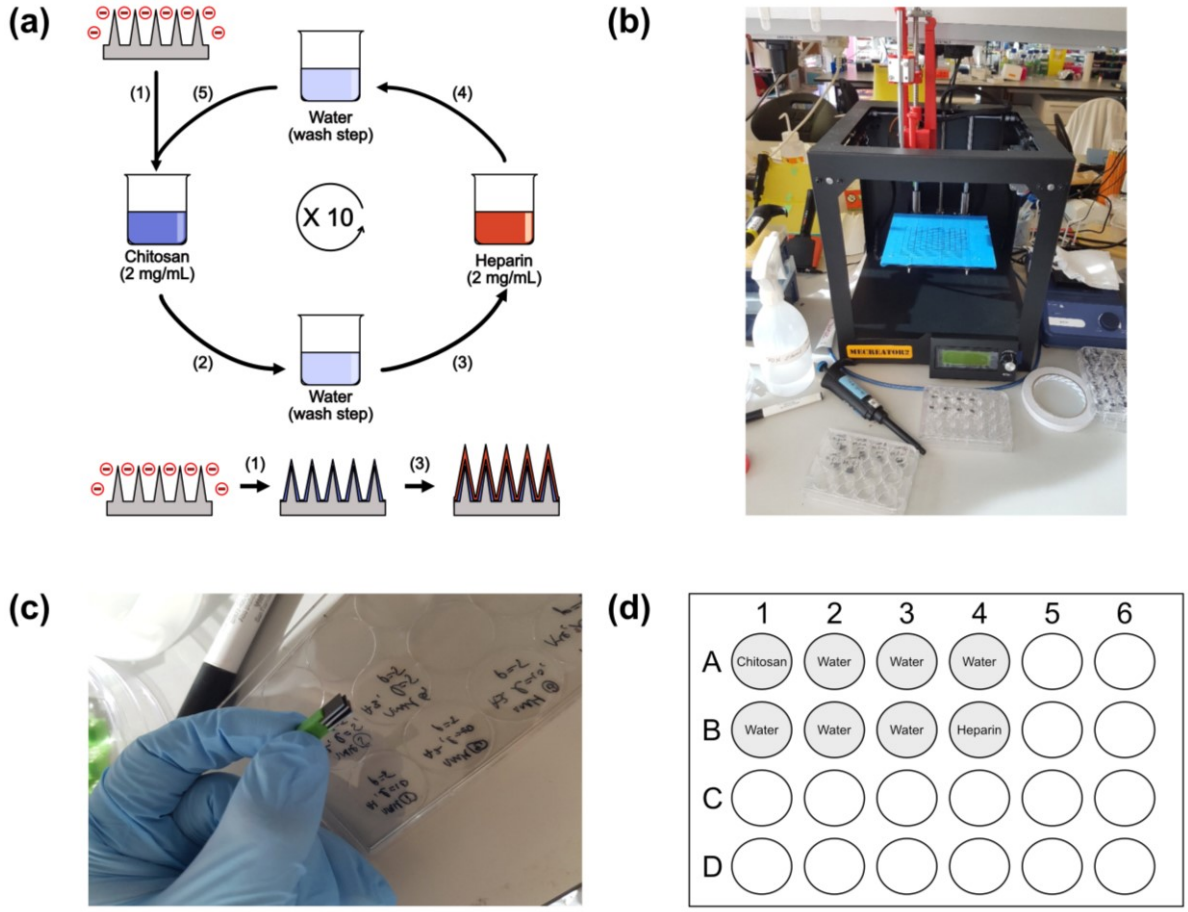


Fig. 2.3: *The layer-by-layer coating method. (a) A schematic of the process used to generate heparin/chitosan bilayers. (b) A modified 3D printer was used to automate the coating process. (c) Extra holder parts were printed to secure the substrates during coating. (d) A schematic of the 24-well plate used to carry out the LbL coating, with heparin/chitosan being shown here as the representative bilayer materials.*

2.3.3 Initial investigations into alginate/chitosan bilayers for SAG binding

In developmental neural labs, smoothened agonist (SAG, Cayman Chemical, cat. no: 9125451-86-9) is primarily used to create ventral NMP cells, and so ideally this would be viable as a surface coating. As such, this was the first candidate for the directed differentiation of stem cells via printed bio-ink patterns. Alginate was proposed as a LbL material to bind SAG due to it being negatively charged (with SAG being slightly positively charged), and also due to its abundance of hydroxy groups (which could form hydrogen bonds with the SAG molecule).

Using scanning electron microscopy to visualise alginate/chitosan coatings

It was important that the nanotopography of the substrate surface was preserved during the LbL process, since this ensured a higher effective hydrophobicity to improve the consistency of the printed bio-ink pattern, and increased the contact area with seeded cells. Scanning electron microscopy (SEM) was used to visualise the LbL surface coatings, to observe obvious topographical changes that the coatings might introduce to the substrates (Auriga Cross Beam, Zeiss).

Substrates were mounted on SEM sample holders using carbon tape (double sided). Samples required a silver sputter coating to prevent charging of the substrate, as this would hinder the image quality. Although this silver coating was expected to be on a similar scale to that of the LbL coating, it would be present on all substrates, including controls. A small amount of silver paint was also placed on the corner of the mounted substrate, to allow for the dissipation of charge.

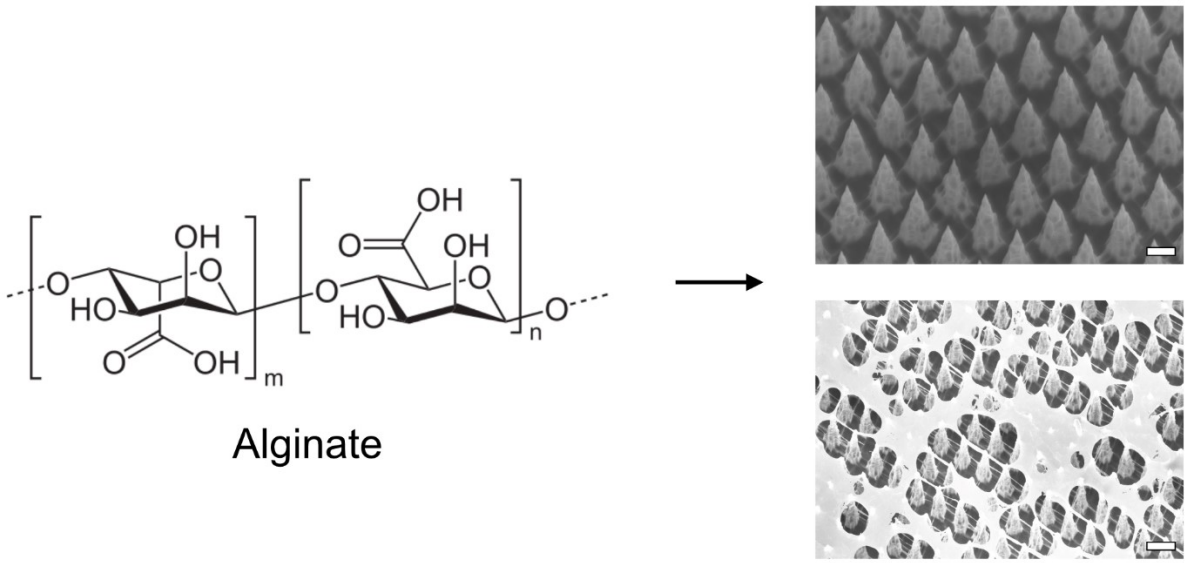


Fig. 2.4: *The surface change introduced by the layer-by-layer coating of alginate/chitosan. SEM images revealed significant differences between the topography of the uncoated (top) and alginate-coated (bottom) substrates. Scale bars = 1 µm.*

The alginate coating was seen to significantly alter the surface topography. Due to the viscous nature of the alginate solution, web-like structures were seen between the needle points, and the areas between the needles were partly covered. This generated an inhomogeneous surface that would be detrimental for the cell culture applications required of this material platform, and would also lead to non-uniform distribution of SAG along the gradient. Despite the discouraging LbL results with the alginate, it may have been possible to optimise treatment conditions and concentrations to account for the viscous nature of the solution. However, this alginate material coating would only be required if characterising the small molecule SAG was possible. As such, attempts were made to detect SAG on the silicon substrate surface.

Raman spectroscopy and Fourier transform infrared spectroscopy for SAG gradient characterisation

Although SAG has been shown to be extremely effective as a soluble factor for creating ventral cell types, it was unclear that the chemical and physical properties of the molecule would make it suitable for printing and binding to the nanoneedles. SAG is only soluble in organic solvents, which are not amenable to printing in an inkjet system such as the Canon printer, as it contains many plastic parts. SAG can be made up in DMSO, and diluted in water immediately before printing to minimise this issue, but this could give rise to aggregation in the bio-ink. Nevertheless, in the early stages of this work, efforts were made to test this molecule as a surface-bound cue on LbL-coated substrates. As SAG is not fluorescent, alternative methods to fluorescence microscopy were needed. Both Raman spectroscopy and Fourier transform infrared (FTIR) spectroscopy were used in attempts to detect SAG on the substrates, with the hope of utilising these techniques later for gradient analysis.

Raman spectra of samples were captured (alpha 300 R+ Raman confocal microspectrometer, WITec) at a magnification of 10X (EC Epiplan-NEOFLUAR, Zeiss, N.A. = 0.25), with a green solid-state excitation laser (λ = 532 nm, 32 mW).

Three FTIR measurements were taken at each region along the gradient (bottom, middle and top) using the FTIR spectrometer (Cary 600, Agilent Technologies).

Ten overprinted gradients of SAG were patterned on flat silicon substrates for each measurement type with the Canon inkjet printer, at an ink concentration of 500 nM. Overprinting refers to the printing of repeated patterns in the same position to increase the amount of material deposited. Flat silicon was used here as a proxy for nanoneedle substrates that would later be used.

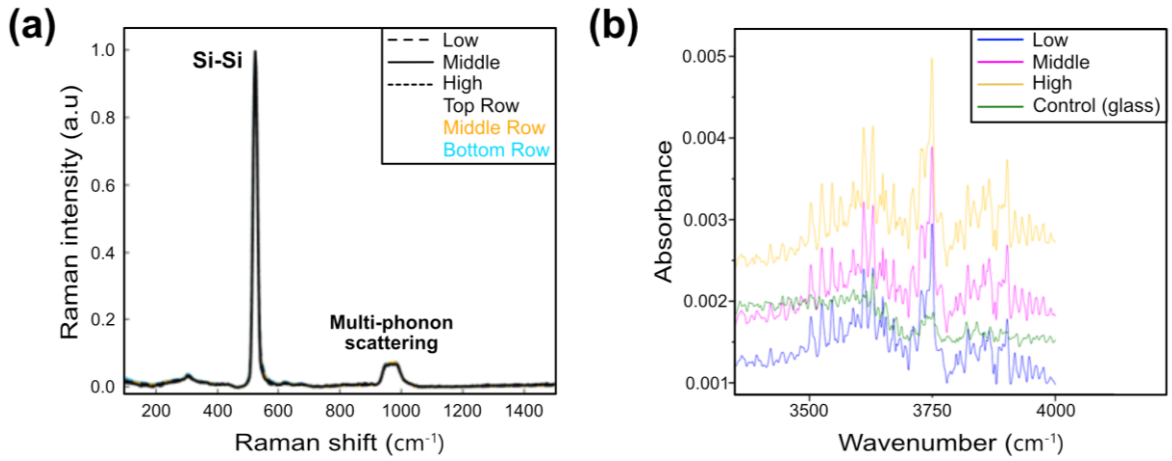


Fig. 2.5: *(a) Raman spectra from measurements taken in a 3 x 3 grid on a silicon substrate, with a 500 nM printed SAG gradient. Low-High and Top-Bottom represent the rows and columns respectively. (b) FTIR spectra taken at the low, middle and high points of a 500 nM printed SAG gradient (three measurements taken in each region and averaged).*

In the case of Raman spectroscopy, only the background silicon signal was seen, across the entire gradient. It was expected that SAG would be Raman-active, due to the presence of aromatic groups in the molecule. The lack of signal was most likely due to the small amount of SAG deposited in the ten overprints used here. However, as this was similar to the conditions that would be used going forward, Raman spectroscopy was evidently not a viable method to characterise gradients of SAG. Higher numbers of prints would not be suitable due to over-wetting of the substrate surface, and also would be extremely time consuming, which would decrease the throughput of the technique. Increasing the concentration was also challenging, as SAG is only soluble in DMSO, and so higher concentrations would risk causing damage to the internal parts of the printer.

FTIR spectroscopy was next used in attempts to characterise the gradient, with measurements taken at the low, middle and high points. Although a slight increase in the signal strength was noted along the gradient (Figure 2.5 (b), low to high) it was extremely noisy and low intensity, barely above that of the glass control. This difficulty

of characterisation, combined with the poor outlook of using alginate as a surface coating, supported the discarding of SAG for the generation of ventral character, and to instead direct focus to the protein Shh. Although this would be a deviation from the protocols using SAG by collaborators in the Briscoe lab, proteins are water soluble, and so would be more suitable bio-ink candidates for the printing protocol going forward.

2.3.4 Investigating heparin/chitosan coatings for binding of Shh/Wnt3a

For the binding of Shh, heparin was chosen as the second LbL material in place of alginate. The interactions between Shh and heparin have previously been described in literature.[102,103] It was also likely that the heparin coating would make the silicon surface more amenable for adhesion and proliferation of certain cell types, assuming it did not form inconsistent coatings as seen with alginate.

Scanning electron microscopy for visualisation of the heparin/chitosan coatings

Both coated and uncoated control samples were again imaged to determine the difference in surface topography caused by the LbL process and the coating materials.

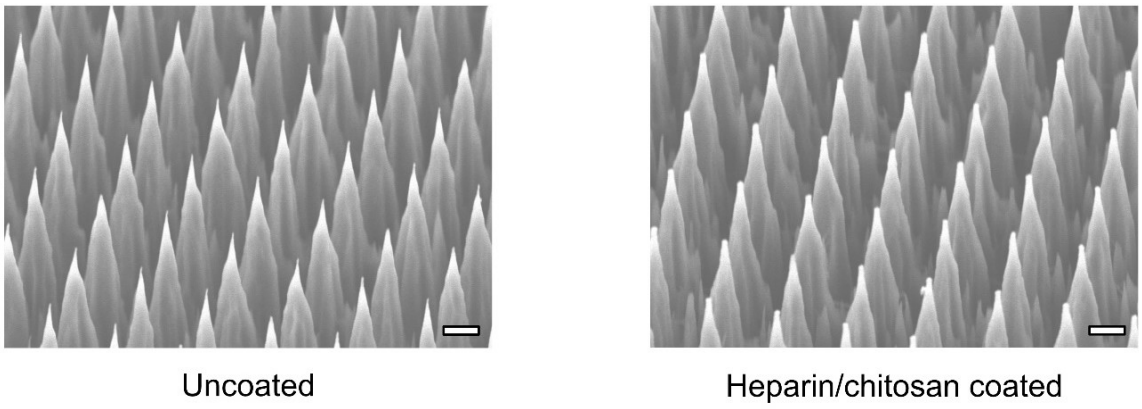


Fig. 2.6: *The surface change observed via scanning electron microscopy after carrying out layer-by-layer coating with heparin/chitosan. The needles on the coated substrate were slightly more blunt than the uncoated needles, but the general topography was maintained. Scale bars = 1 μm.*

In this case, the coating seemed to be much more uniform and conformal to the surface topography, relative to the changes introduced by the alginate coating. A slight decrease in the needle sharpness was noted, but the general pitch and shape of the features were maintained. The areas between the needles were not filled in or covered as they had been in the case of alginate, which suggested that the effectiveness of the needles as a hydrophobic printing substrate would be maintained.

Contact angle measurements to confirm surface modification

Following the encouraging results from the LbL coating process, contact angle measurements were carried out on uncoated substrates and substrates that had been coated with ten heparin/chitosan bilayers. The purpose of this test was to confirm a change in hydrophobicity after the coating process, and also to confirm that there was indeed a significant surface modification occurring during the LbL process (since the coating was not as obvious in the SEM images as it had been with the alginate coatings).

Three coated and uncoated nanoneedle substrates were included for the measurements. A 5 µL droplet of water was placed on a corner of each substrate, and an image was taken immediately after the addition of the droplet to ensure minimum spreading or deformation (Contact angle goniometer, Ossila). This process was repeated for each of the other three corners, to provide four measurements per substrate. Contact angle readings were then calculated via the built-in software script, ensuring that any images taken had the droplet and substrate surface in focus before any calculations were carried out.

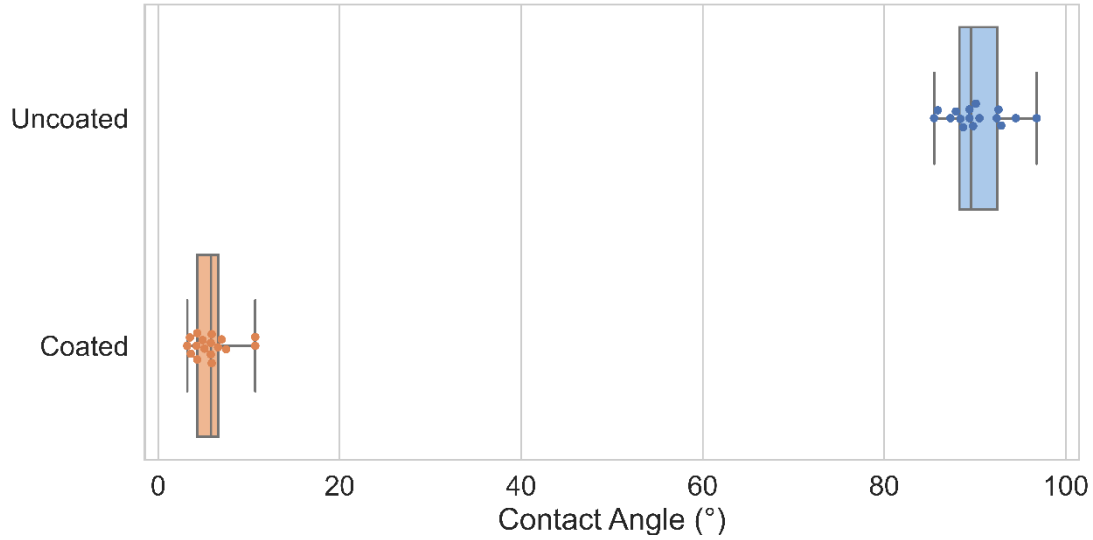


Fig. 2.7: *Contact angle measurements of nanoneedle substrates before and after layer-by-layer coating with heparin/chitosan. A considerable decrease in contact angle was observed with the coated substrate relative to the uncoated nanoneedles.*

The uncoated substrates demonstrated a contact angle close to 90°, which was consistent with previous internal nanoneedle results. However, after coating with ten heparin/chitosan bilayers, this contact angle was seen to fall below 20°, indicating that a surface modification had indeed occurred, and that the surface had become considerably more hydrophilic. These data, combined with the SEM images above, suggested that the LbL coating process was depositing a relatively uniform coating on a nanometre-scale thickness, which did not drastically alter the surface topography and would be suitable for the binding of printed morphogens. The presence of proteins on the surface would also be easier to characterise (via immunostaining and fluorescence) than small molecule activators or inhibitors. Combining this with the significant improvement in coating quality compared to that seen with alginate, the decision was made to focus solely on proteins and heparin/chitosan as the pathway activation method for directing cell behaviour going forward.

Safranin-O staining to visualise the uniformity of heparin/chitosan coating

While SEM can reveal any large changes to the topography of the substrate after coating, it does not provide information on the uniformity of the bilayer coatings, since only a small region of interest can be imaged. To achieve a more substrate-wide description of the coating, a staining would be needed that could treat the entire surface, and be fluorescently imaged to ascertain the quality and uniformity of the functionalisation. The candidate labelling material would need to be reactive with one of the components of the LbL process, to ensure that sufficient labelling at the substrate surface occurred. Safranin-O was chosen for this purpose, which is a common fluorescent stain used in histology applications. It binds strongly to proteoglycans and glycosaminoglycans (such as heparin), and so could be employed to confirm the presence of heparin in the bilayer coatings.

A Safranin-O solution (0.1% v/v) was made up in acetic acid (0.1% v/v, as described by Kovarova[104]). Substrates had previously been coated with ten heparin-chitosan bilayers via the LbL process as described in section 2.3.2. Those substrates, and control nanoneedle substrates, were submerged in the Safranin-O solution for 6 min (ensuring enough solution was used to cover the entire surface), before pouring the excess remaining stain off. Each substrate was then dipped ten times in 95% v/v ethanol, before dipping 20 times in 100% ethanol. Finally, each substrate was left standing in 100% ethanol for 1 min, before drying and storing at 4°C.

The substrates were mounted face down in 8-well plates, with a small amount of mounting media (Fluoromount-G, Thermo Fisher Scientfic, cat. no: 00-4958-02) in each well. They were imaged on the widefield microscope (Axio Observer, Zeiss) at 20X magnification, with the entire substrate being tiled. Safranin-O has an emission maximum at 585 nm when excited at 521 nm (Wan *et al.*[105]), and so no secondary staining was needed for the imaging process. The pixel intensities across the tiled images were grouped into ten bins along the x axis for visualisation purposes, and the

mean intensity for each bin was calculated. Error bars in the plots below represent standard deviation for each mean intensity calculation.

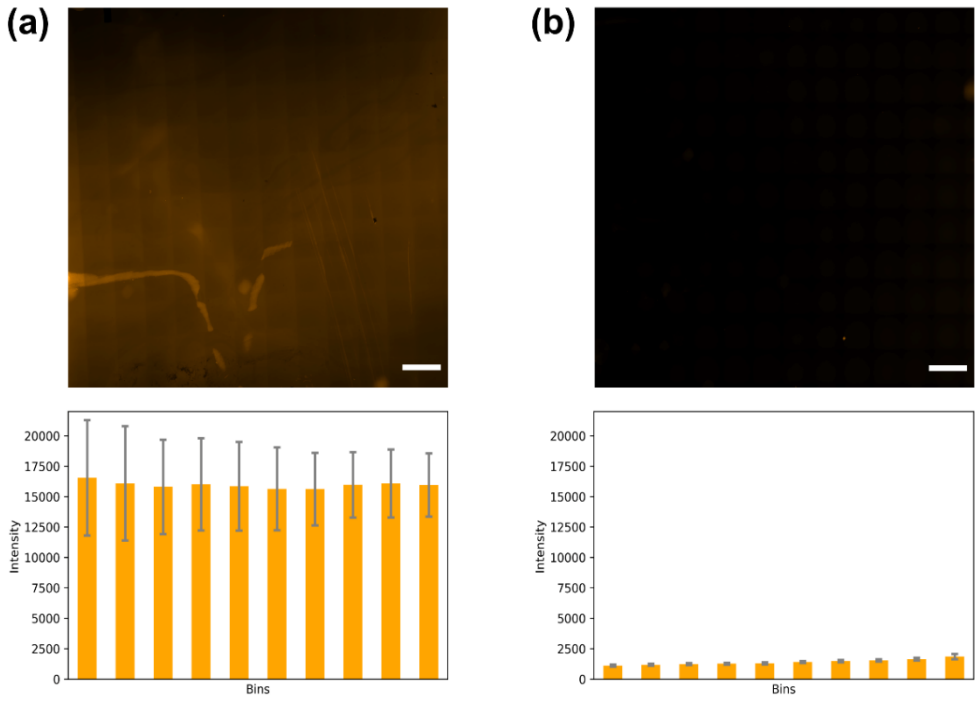


Fig. 2.8: *Tiled images of (a) a representative ten bilayer heparin/chitosan coated substrate and (b) a representative uncoated nanoneedle substrate, both stained with Safranin-O. Corresponding bar charts showing pixel intensities across the substrate surface are shown below each image. There is a clear increase in the intensity of the coated vs. uncoated conditions, showing the presence of heparin across the coated substrates. Scale bars = 1 mm.*

The images of the coated substrates showed a clear increase in signal intensity relative to the uncoated control, indicating that there was indeed heparin present on the surface from the coating process. A small amount of signal was observed on the uncoated control, which may have been as a result of non-specific binding, or background fluorescence from the nanoneedle substrate. This was however still significantly lower than the signal observed on the coated substrate.

While there was indeed clear evidence for the presence of the bilayer coatings, there was significant non-uniformity across the substrate surface. Even accounting for the stitching and shading artefacts that were apparent in the tiled image, the edges of the substrate were lower intensity than the centre. This may have been as a result of the drying of the substrates, or may have been due to their orientation in the holder during the LbL process. Regardless, even in the regions that showed lower intensity, the amount of Safranin-O signal was still considerably higher than any region on the control substrates. These data, when considered along with the contact angle and SEM analysis, further indicated that the LbL process was indeed coating the silicon substrates as intended, and was a suitable candidate going forward for the electrostatic binding of printed proteins. The non-uniformity of the coating, however, is a factor that should be considered in downstream analyses. Edge regions of the substrates often contain defects that may affect surface quality (and so cell culture variation may be introduced). Coupling this with the less uniform coating of heparin/chitosan near the edges observed here, and the damage to the substrate edge caused by the LbL holder, it is apparent that edge regions should not be considered in downstream analysis protocols.

X-ray photoelectron spectroscopy analysis of layer-by-layer coatings

To further confirm the presence of bilayers on the silicon substrates after the LbL process, X-ray photoelectron spectroscopy (XPS) measurements were taken of the various conditions. This provided information on the elemental composition of the surfaces in each treatment, and also approximations on the thickness of the LbL coatings (which could not be inferred from the Safranin-O staining or SEM images).

Measurements were carried out, on uncoated nanoneedle substrates, plasma treated nanoneedles and finally nanoneedle substrates coated with ten heparin/chitosan bilayers (K Alpha XPS system, Thermo Fisher Scientific). Before taking measurements, a survey scan was carried out twice (analyser energy = 200 eV, dwell time = 25 ms,

step size = 0.5 eV, X-ray spot size = 400 mm). After the survey, single element scans were carried out individually (analyser energy = 20 eV, dwell time = 50 ms, step size = 0.1 eV, X-ray spot size = 400 mm, scan number = 10 for Si/C/O, 20 for N/S.) Analysis of the obtained spectra was carried out using Avantage software V5.9925 (Thermo Fisher Scientific).

Table 1: *The elemental composition data from various substrate types obtained via XPS. Elemental composition of measurements taken from (a) an uncoated nanoneedle substrate, (b) an oxygen plasma-treated nanoneedle substrate and (c) a nanoneedle substrate coated with ten heparin/chitosan bilayers in the layer-by-layer process.*

(a)

Uncoated nanoneedles		
Element	Peak BE (eV)	Atomic %
C	285.36	2.48
O	532.6	37.49
Si	98.94	60.03

(b)

Plasma-treated nanoneedles		
Element	Peak BE (eV)	Atomic %
C	285.23	1.9
O	532.85	38.27
Si	99.3	59.83

(c)

LbL-coated nanoneedles		
Element	Peak BE (eV)	Atomic %
C	286.85	33.95
N	402.02	4.19
O	532.79	42.36
S	168.9	4.55
Si	99.39	14.95

In the case of the uncoated nanoneedle substrate, the majority of the atomic composition percentage was made up of silicon (silicon-silicon and silicon-oxygen bonds) and oxygen, which primarily came from the silicon oxides present on the surface. There were small amounts of carbon and other oxygen types on the surface, which were attributed to impurities within the environment of the substrate surface. There was less than 0.01% elemental composition of sulfur or nitrogen present (below the limit of detection).

In the case of the plasma-treated substrate, the composition was again dominated by silicon and oxygen, with a slight increase in the silicon-oxygen bond signal (as a result of the surface being treated with an oxygen plasma).

The LbL-coated substrate contained a larger range of elements and bond types on the surface, as there were now heparin and chitosan molecules present. Sulfur, nitrogen and carbon signals were detected in significant amounts. Heparin contains sulfate and ammonium sulfate groups, which accounted for the presence of sulfur peaks in the spectrum. These ammonium sulfate groups, combined with amine groups from the chitosan, also gave rise to two distinct nitrogen peaks from the coated substrate. Both chitosan and heparin contain a number of oxygen atoms, which contributed to the larger percentage of oxygen being present relative to the non-treated or plasma-treated substrates. The silicon composition was significantly decreased in the coated condition, which was to be expected as the entire surface was most likely coated in the polysaccharide bilayers. The silicon signal did not disappear totally, however, indicating that the ten bilayer coating was of a nanometre-scale thickness (since XPS is a surface sensitive technique). The X-rays do not penetrate further than approximately 10 nm, and so the detection of silicon in significant amounts after the LbL process (almost 15% in this case) supported the observations from the SEM images above that the coating would not drastically alter the surface topography of the substrates. It is however possible that some of the silicon signal emerged as a result of defects in the coating leaving exposed silicon, such as at the edge regions seen in the Safranin-O staining.

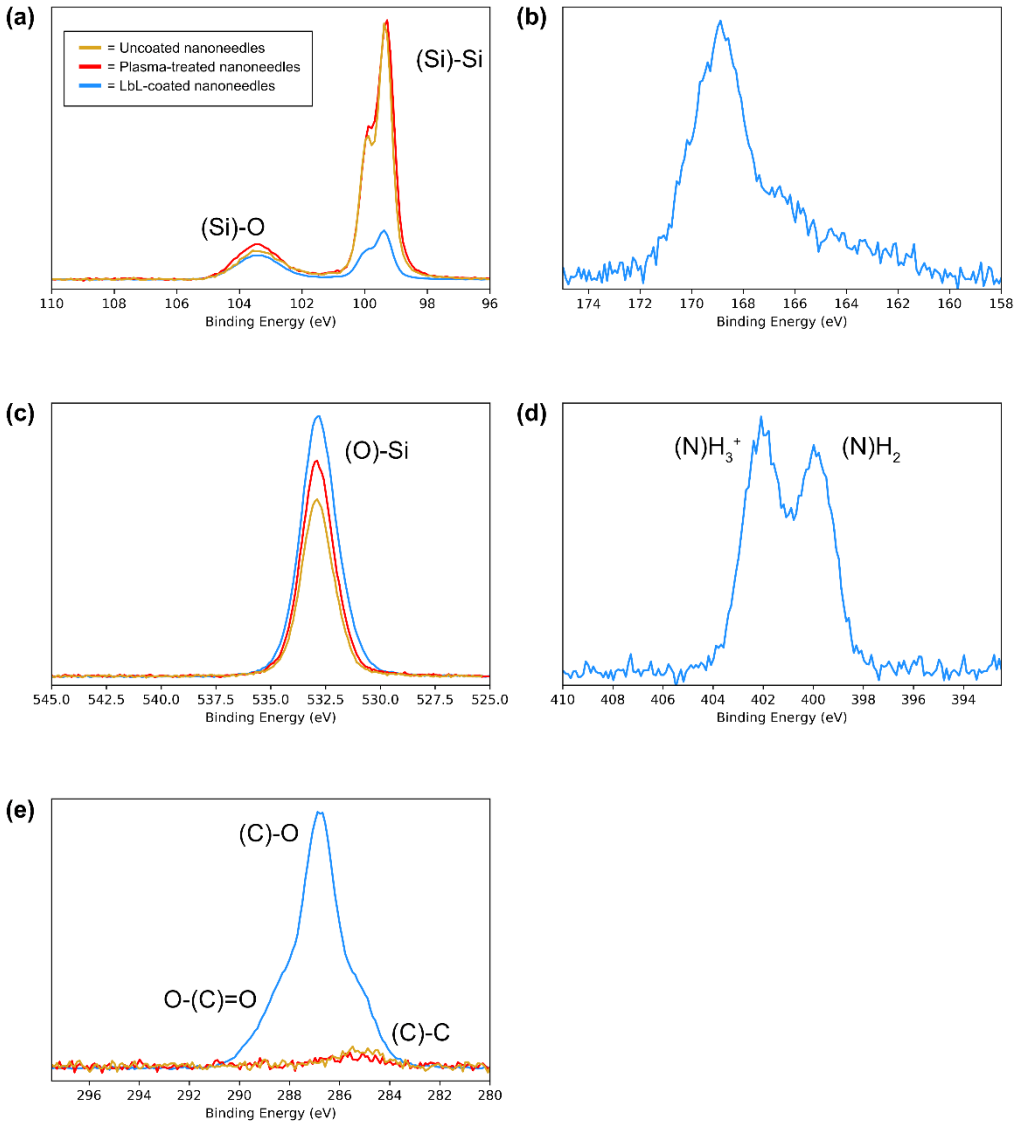


Fig. 2.9: *XPS raw data for the spectra obtained for (a) silicon, (b) sulfur, (c) oxygen, (d) nitrogen and (e) carbon for the uncoated (yellow), plasma-treated (red) and LbL-coated (blue) substrates. Where signal below 0.01% elemental composition was detected (e.g. sulfur for uncoated and plasma-treated substrates), data was not displayed for clarity purposes. In the case of obvious charging errors, spectra were charge corrected to suitable reference peak values.*

Atomic force microscopy analysis of layer-by-layer coatings

As a final method to determine the roughness introduced to the surface by the LbL process, atomic force microscopy (AFM) was carried out on coated substrates. As the nanoneedle structures were not amenable to AFM measurement (due to the topography of the surface, and the size of the features relative to the cantilever), flat silicon substrates were used to investigate the level of modification introduced. As such, this data should only be used as an estimation for changes to the surface, and should not be used as a direct comparison with coated nanoneedles.

Scans was carried out on flat silicon substrates in intermittent contact mode (Agilent 5500 AFM, Agilent Technologies. Silicon nitride cantilever, MikroMasch AFM Tips). The output data from the measurements was processed in Gwyddion V2.49.

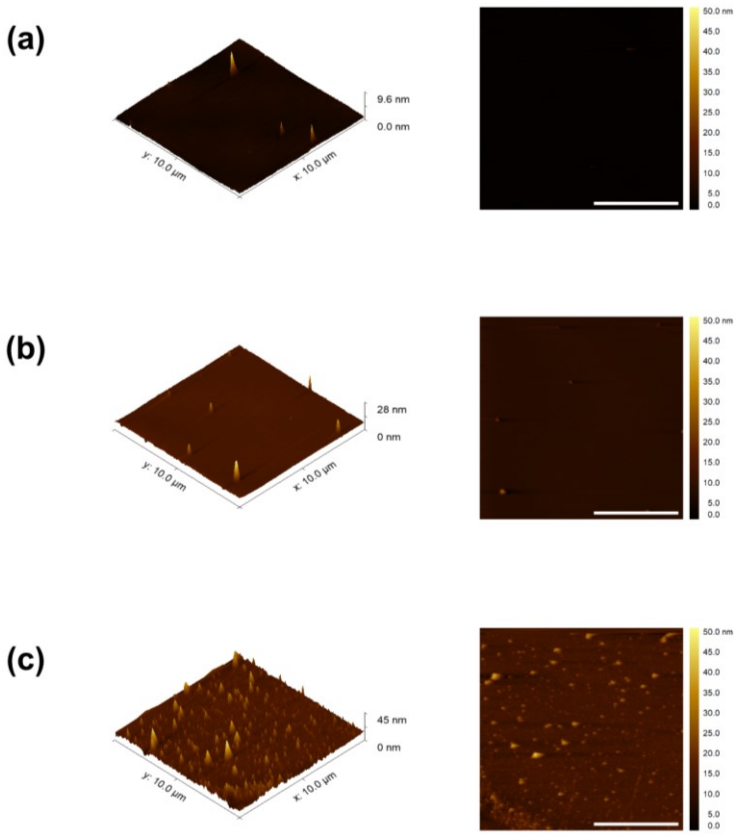


Fig. 2.10: *AFM measurements taken on flat silicon substrates as a proxy for nanoneedle substrates, with three conditions: (a) untreated flat silicon, (b) oxygen plasma treated and (c) ten bilayers of heparin/chitosan. Scale bars = 4 µm*

As with the XPS, three different conditions were measured: uncoated silicon, plasma-treated flat silicon and a LbL-treated substrate coated with ten heparin/chitosan bilayers. The uncoated silicon was seen to be extremely smooth, with little roughness observed beyond some impurities (some small features of sub-10 nm height were detected). The oxygen plasma treatment did not noticeably increase the surface roughness relative to the untreated surface, although slightly larger features were detected. Once coated in heparin/chitosan bilayers, however, a much less smooth surface was observed. Features as large as 45 nm were detected, and the entire surface was seen to be considerably more rough than in the untreated or plasma-treated conditions.

These measurements indicated that the LbL treatment did indeed modify the surface topography of the substrate. However, it should be noted that the flat silicon and nanoneedle substrates may not have behaved in the same manner, and so these sub-50 nm structures may have been slightly different on the nanotopographical substrate. However, these data combined with the SEM and XPS give an approximation for the thickness of the coating introduced and, as the needles are 5-10 μm tall, it can be inferred that the coatings would maintain the shape and structure of the needles (allowing for a slight decrease in sharpness).

2.4 Optimisation of inkjet-printed morphogen gradients on nanoneedles

The techniques described above confirmed that nanometre-scale heparin/chitosan bilayers could be deposited onto the nanoneedle surface. These coatings were seen to be relatively uniform (once edge regions were accounted for) and did not significantly alter the topography of the substrates. Having confirmed the addition of the electrostatic binding method on the surface, the next step was to develop the surface binding efficiency of proteins, and gradients of morphogens for cell interfacing.

2.4.1 Shh ELISA release assay

One factor that needs to be considered when using this platform is the inevitable non-permanent nature of electrostatic protein binding. As the binding being used was not covalent, it was possible that when in culture, Shh or other proteins would be released into the media. This could interfere with the effectiveness of a controlled spatial pattern approach, as the protein released would be free to interact with cells across the entire substrate surface. As such, it was deemed necessary to carry out a release assay on coated substrates to investigate this. Shh was used as a representative protein here. While the general release profile may be similar, the strength of binding for each new protein would vary based on their relative charges, and so Shh should only be used as a guide when considering the release of other bio-inks.

Shh release assays were carried out using a Shh ELISA kit (cat. no: DSHH00, R&D Systems). Three substrates were included for this investigation, and were coated in 200 nM Shh overnight in N2B27 media. The same substrates were then submerged in the N2B27 media for a total of five days, with the media being collected at each timepoint (day 0.5, day 1, day 2, day 3, day 5) and frozen. These media samples were then tested using the ELISA kit with the reagents provided, and the absorbance for each sample was taken (Spectramax plate reader) at 450 nm and 570 nm. Using the given reference materials, a calibration curve was generated that could be used to determine the amount of Shh released at each time point.

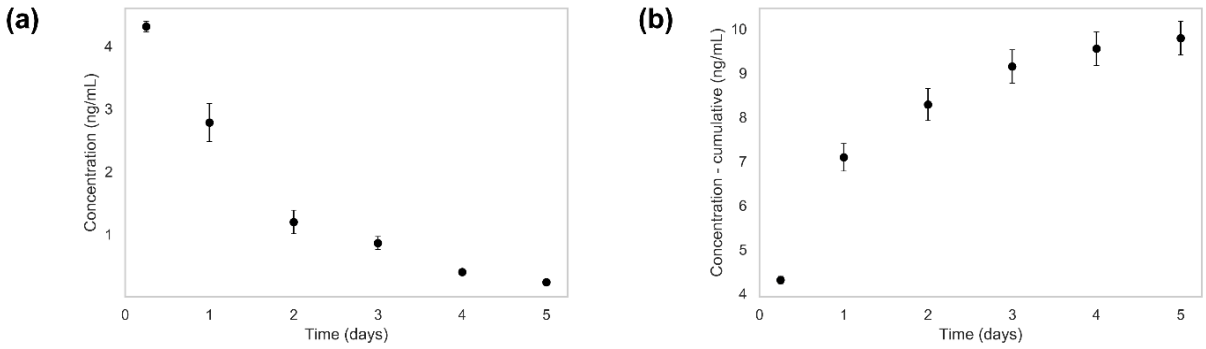


Fig. 2.11: *The ELISA release assay carried out for Shh-coated nanoneedle substrates. The Shh release profile is shown for individual timepoints in (a), while the cumulative Shh release profile is depicted in (b).*

Within the first 12 h and up to a day of incubation for the Shh-coated substrates in N2B27 media, a burst release was noted, that quickly slowed and began to plateau by day 5. While this burst was worth consideration, the amount released (approximately 4.3 ng/mL) was over an order of magnitude lower than the amount that would be added to the media in positive control experiments, in order to induce ventral character. The media would also be changed daily in cell culture experiments, meaning that accumulation of protein in the media was not going to exceed this value. As such, it was unlikely that the amount released would have any significant effect on the cell population as a whole, and so this was seen as validation for this protein binding method.

2.4.2 Shh gradient generation with Canon inkjet printer

Initially, a Canon PIXMA iP7250 thermal inkjet printer was purchased, and modifications were made to allow the printing of custom aqueous bio-inks (in this case, proteins). This printer was chosen due to the ease of access it provided to the ink cartridges, and also due to the compact disc printing capability it possessed, which could be used as a means to mount printing substrates.

The top cover of the printer was removed, in order to allow access to the printhead. The cartridges were opened, cleaned with water/isopropyl alcohol and adapted with a reservoir to hold up to 1 mL of bio-ink if required.

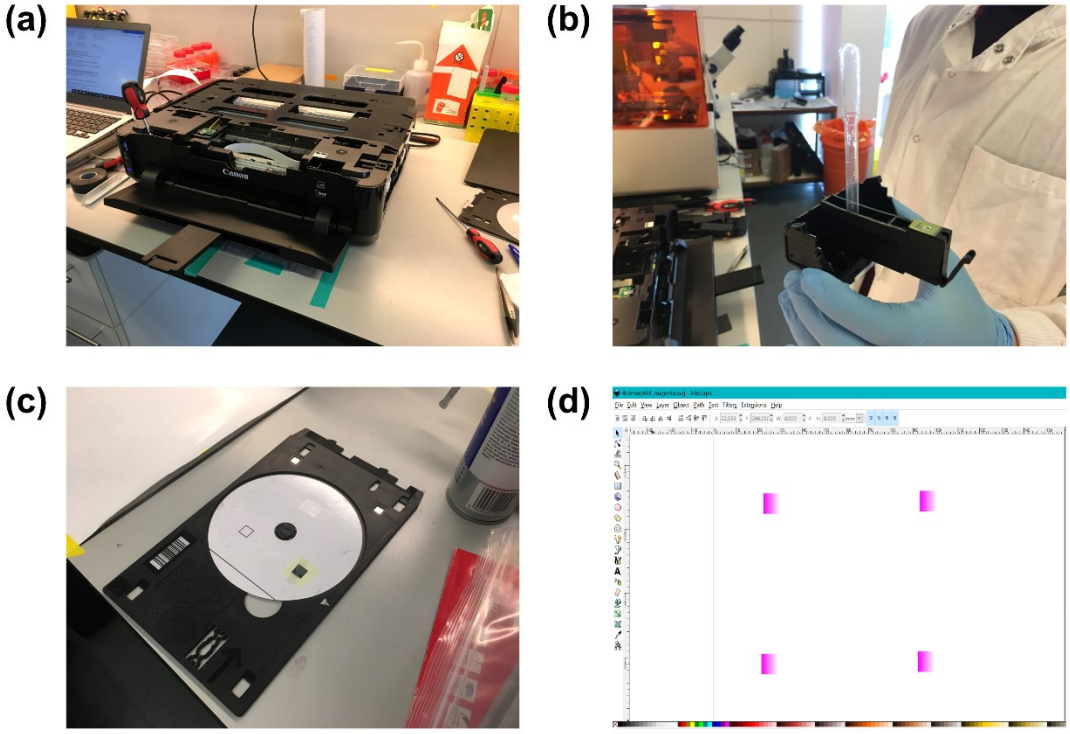


Fig. 2.12: *The initial inkjet printing apparatus used for the generation of morphogen gradients. (a) A modified Canon PIXMA iP7250 printer that was used in this work. (b) The modified ink cartridge for the loading of bio-inks. (c) Disk tray that was used for the mounting of substrates to be printed. (d) Representative gradients drawn in Inkscape.*

The disk tray was covered in a piece of paper and registration marks were printed using standard printer ink (with an older printhead that would not be used for printing of proteins, to prevent any contamination). This ensured that the substrates could be placed in the correct position for gradient printing, since the pattern would not always be visible by eye with colourless inks. Four substrates were printed at once, although this could have been increased dramatically by printing more registration marks if required. These registration marks were printed to match the size of nanoneedle

substrates (8 x 8 mm, see Figure 2.12 (c) above). Inkscape was the software of choice for printing these patterns, as it interfaced well with the Canon printer, and allowed for rapid changing of the pattern to be created as needed (see Figure 2.12 (d) above). A linear gradient was drawn at each registration mark position using the built-in gradient generation in Inkscape, again at a scale of 8 x 8 mm.

2.4.3 Characterisation of Shh gradients generated using the Canon inkjet printer

As SAG had shown little promise as a printing candidate, Shh was to be used for ventral cells, and BMP4 for dorsal cells in modelling the early-stage spinal cord, while Wnt3a would be used as a biochemical cue in the cancer-based work (since this pathway is implicated across a range of cancer types). All of these candidate proteins had isoelectric points that indicated they would bind to heparin, meaning that the surface chemistry would not require modification between applications (Shh isoelectric point = 8.09, BMP4 isoelectric point = 8.97, Wnt3a isoelectric point = 8.52. Isoelectric points found via Phosphosite Plus[106]). The inkjet printing of these proteins provided fine control over the pattern being generated, and also would enable the patterning of multiple surfaces in parallel.

The printing concentrations of the proteins were optimised via uniform surface coating experiments (See section 3.3.1). These proteins were then made up from stock as needed in the buffer of choice on the day of printing, to prevent aggregation or loss of activity. Before carrying out any tests with cells, the efficiency of gradient generation needed to be tested. To investigate this, labelling of Shh with Alexa Fluor 488 was carried out (Alexa Fluor 488 Antibody Labelling Kit, cat. no: A20181, Thermo Fisher Scientific). The fluorescent protein was loaded and printed onto the substrates, for ten overprints at a concentration of 200 nM.

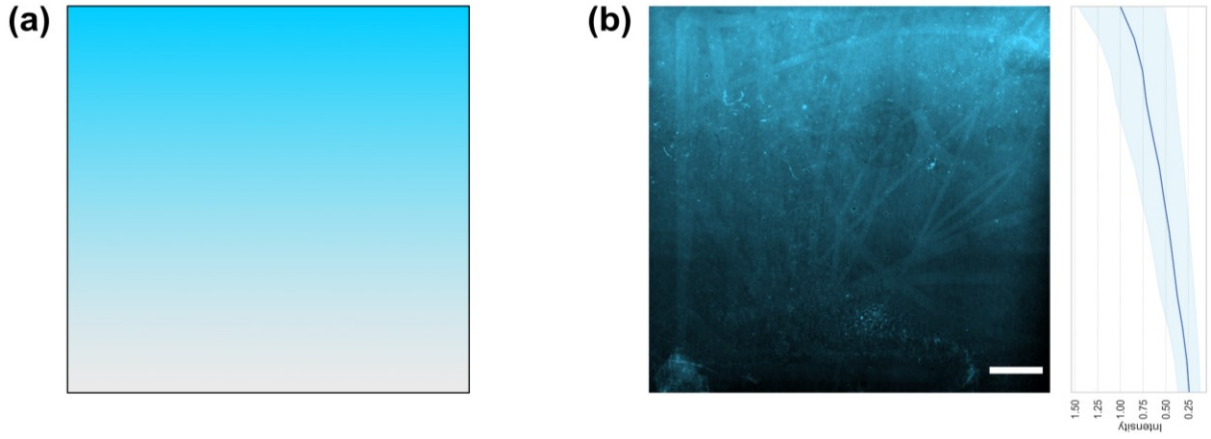


Fig. 2.13: *(a) The input gradient pattern drawn in Inkscape, to be printed on the nanoneedle substrate using the Canon inkjet printer. (b) Representative image of a printed Shh gradient (200 nM), showing an approximately linear increase in Shh signal intensity along the substrate. Shh protein was pre-labelled before being using as a bio-ink. Normalised intensity plot represents the mean intensity across three substrates. Scale bar = 1 mm.*

A linear gradient of Shh was observed across three substrates that was consistent with the input pattern generated in Inkscape. There were minimal disruptions to the pattern, apart from scratches on the surface that were not related to the printing process. This was seen as a success, and showed that gradients of Shh could be printed with relative ease.

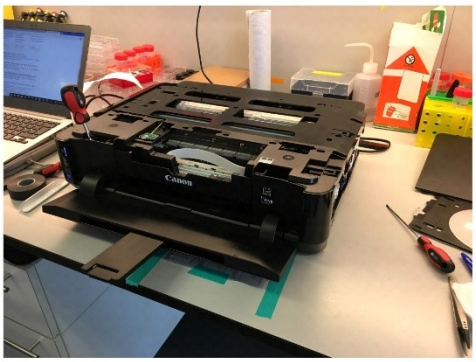
These Shh gradients successfully induced ventral character in seeded NMPs (see initial gradient tests, section 3.3.2). At this point in the project, however, a number of challenges presented themselves as attempts were made to obtain replicates with the Canon-printed gradients seen in Figure 2.13. The reproducibility and reliability of the results became inconsistent, with a large variability being observed in the response of cells to printed gradients across different experiments, and indeed across substrates within the same experiment. A number of factors may have contributed to this. The printhead of the Canon was seen to become blocked after a small number of experiments, with attempts to unblock it using washing and sonication steps often

unsuccessful. These unblocking steps may well also have damaged the printhead, as it would not have been designed to withstand these conditions or treatments. These factors led to inconsistent prints, and increased blockages in subsequent printing attempts. Another factor complicating this situation was the ceasing of production of this specific model of inkjet by Canon. As a result, new printheads had to be bought from third party suppliers, which had variable quality and were often found to be contaminated on arrival, making them unsuitable for cell-interfacing experiments where protein purity and sterility of the parts were of utmost importance. This printer had demonstrated the proof-of-concept for reprogramming spinal cord progenitor cell types using patterned substrates, but was not viable for long term or higher throughput experiments. An alternative printing system was needed that would allow for the rapid manufacturing of multiple gradient-patterned surfaces, and that could generate reproducible data and offer finer control over the bio-ink pattern being created. This would allow for more in-depth studies to be carried out into the effects of the morphogen pattern on cell differentiation, and also would enable faster and higher throughout substrate patterning.

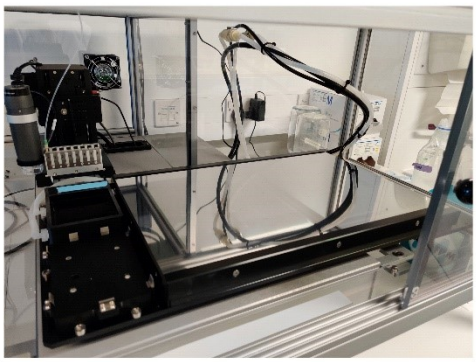
2.4.4 Shh gradient generation with the BioDot AD3220

A new printing platform had recently been obtained by the group – a BioDot AD3220 system. The BioDot printer is a drop-on-demand solenoid valve-based printing system, offering fine control of position and volume of deposition (as low as 1.3 nL per drop). This has significant benefits compared to the Canon printer, which used multiple print heads to pattern simultaneously, and so could not be used for applications that require high degrees of accuracy and control. The BioDot printer also has easily changeable parts, meaning that it was feasible to repair it when issues did arise, unlike in the case of the Canon, which required entirely new printheads (or sometimes whole new printers) to be purchased.

The small volumes and precision of array generation, coupled with the ease of access to the printing components for troubleshooting, made this an ideal candidate to replace the Canon inkjet system. The fact that the BioDot system was operated by a solenoid valve also removed any doubts about damage to the bio-inks that may have been introduced by the thermal system in most standard inkjet printheads.



Canon PIXMA IP7250



BioDot AD3220

Fig. 2.14: *The two inkjet printer models used in this work – the Canon PIXMA iP7250 and BioDot AD3220.*

It should be noted that, although the BioDot printer offers finer control due to the drop-on-demand capabilities, this does bring some challenges that needed to be taken into account when planning experiments. The Canon printhead had rows of nozzles that printed simultaneously and so made precision lower, but allowed for the efficient printing of macro scale patterns. A pattern could be drawn and printed almost immediately without considering drying, droplet volume or substrate position (after initial registration mark printing). However, multiple layers could not easily be generated, and so an overprint approach was required to deposit enough material to interact with cells.

In the case of the BioDot printer, the system is designed to print microarrays of single droplets at designated positions, and so variation across macro scale patterns is possible due to surface wetting and drying times. When building a millimetre-scale

pattern such as the gradients being used here, the array printing through the BioDot Link2020 software can be utilised to generate the required protein concentration by controlling the number of drops that are deposited at each point. Single droplet volumes can be controlled as well as the number of drops, and so fine control over the exact amount of protein deposited was possible (unlike with the Canon, where exact volumes and droplets were unknown).

For gradient characterisation tests with the BioDot printer, the protein was labelled post-printing using a monoclonal mouse anti-Shh antibody (DSHB 5E1, obtained from the Briscoe lab). The antibody was made up at a concentration of 5 µg/mL in PBS/BSA (1% w/v)/Triton X-100 (0.1% v/v), and gradient-printed substrates were treated overnight in the fridge before staining using anti-mouse Alexa Fluor 488 made up in the same buffer, for 2 h at room temperature. The substrates were then again mounted in an 8-well plate with a small amount of mounting media in each well, and imaged on the widefield microscope using the tiling feature at 20X magnification.

The pattern creation method for each printing platform is shown below, along with fluorescence images of the output protein patterns.

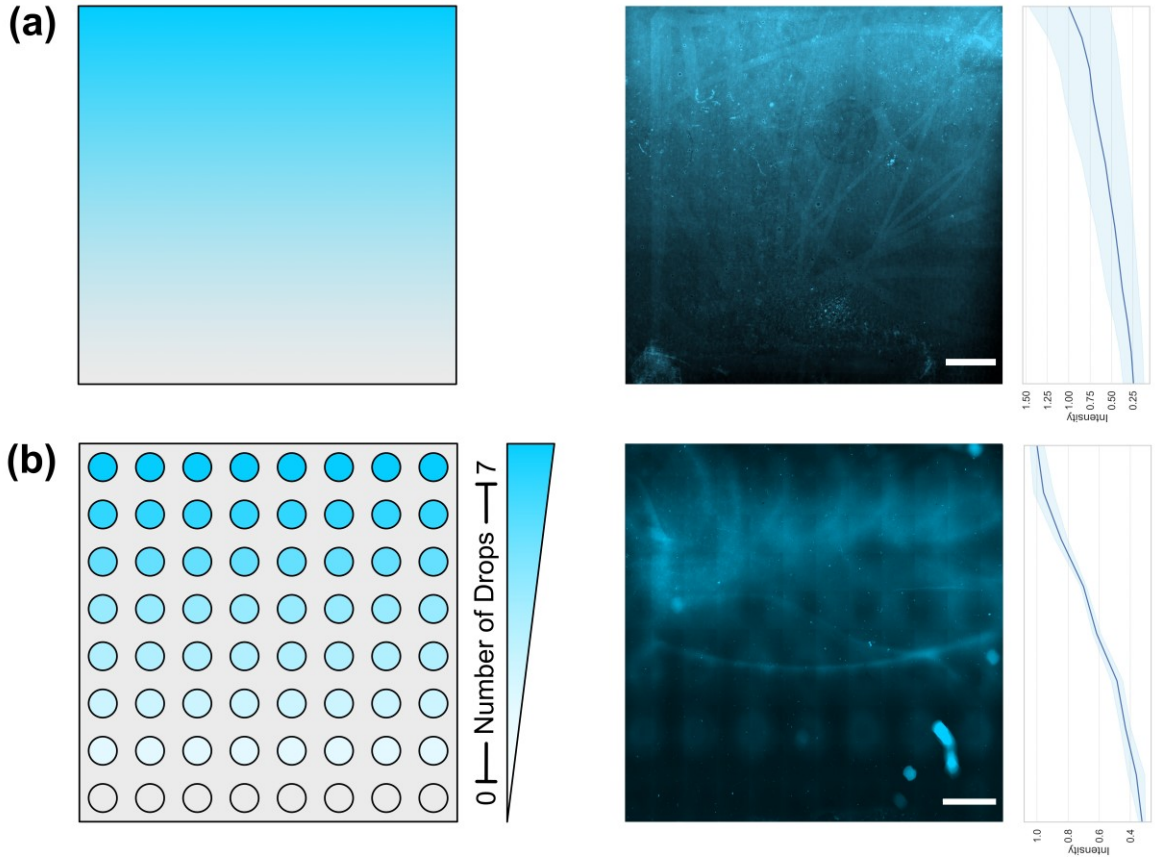


Fig. 2.15: *The different input methods for the two printing platforms, and representative images of the corresponding output gradients. (a) The continuous gradient generated by multiple printheads in the Canon inkjet printer. (b) The microarray drop pattern used to generate a linear gradient using the BioDot printer. Scale bars = 1 mm. Normalised intensity plot represents the mean intensity across three substrates.*

Although the single droplet dispensing does require careful planning when forming patterns, the fine control over droplet position and volume allows for conditions to be generated that would be challenging with more coarse-grained printers such as the Canon (e.g. exponential vs. linear gradients, to be discussed later). Multiple inks can also be printed without the risk of contamination, as washing steps are automatically carried out between deposition and aspiration steps. However, it is more difficult to generate smooth gradients, as seen in Figure 2.15 above. In this instance, darks spots were observed where droplets landed, perhaps due to wetting artefacts or spreading

caused by the impact at the surface. By using the surface wetting of the substrate (and so droplet coalescence), the goal was to cause discrete array points to blend together and form a continuous gradient. Surface treatments and surface topography play a role in the degree to which this will occur, and in this instance, there were some defects in the printed pattern. While the gradient is less smooth than in the case of the Canon printer, it is much more reproducible across multiple experiments, which was the primary limiting factor with the Canon. Also, for population-based responses, this level of printed pattern is sufficient to induce a location-dependent response from cells across the substrate, based on the pattern printed. As such, the BioDot printer was chosen as the printing platform to be utilised going forwards.

2.5 Conclusions and discussion

Within this chapter, the successful generation of a material system for presenting spatially resolved biochemical patterns at the cell-material interface was described.

Electrostatic binding was achieved via the layer-by-layer technique, with heparin/chitosan being identified as the ideal candidate materials for the formation of bilayers on the nanoneedle substrates. Release profiles from ELISA assays indicated that the protein would be maintained at the surface in sufficient amounts to activate target signalling pathways, with the released protein being of too low of a concentration to play a significant role in the cell response. XPS and AFM measurements suggested that the coating thickness was on the nanometre-scale, which would not cause significant changes to the needle surface beyond a slight decrease in sharpness.

Challenges still remained however in the non-uniform edge regions obtained in the coating process. This most likely occurred as a result of drying artefacts during the coating or Safranin-O staining processes. This inconsistency, coupled with the damage caused by the holder during the layer-by-layer process, indicated that edge regions should not be considered when carrying out downstream analyses of cell behaviour.

The capability to generate gradients of bio-inks was also demonstrated, through the use of Shh protein as a representative ink. Both the Canon PIXMA iP7250 inkjet and the BioDot AD3220 were used in the generation of these patterns, with the BioDot printer emerging as the more reliable and promising system for cell interfacing experiments going forward. While the gradients generated were not as continuous as those seen with the Canon, the consistency of printing and ease of access to parts meant that the BioDot system would enable more reproducible and higher throughout device generation. The ease of pattern creation with the Link2020 software ensured that in future works, various gradient types could readily be investigated for their ability to invoke a response in cells seeded on the devices.

Chapter 3

In vitro replication of the neural tube using inkjet printing

Chapter 3: In vitro replication of the neural tube using inkjet printing

This chapter describes the application of the morphogen-patterned substrates in modelling the developing spinal cord.

Cell culture experiments and imaging were carried out by Dr Despina Stamataki and the author. The image analysis pipeline was developed by Dr Stuart Higgins. All other experimental data, data interpretation and analysis were carried out by the author.

3.1 Literature Review

3.1.1 Embryogenesis – formation of the germ layers

In humans, the process of embryogenesis takes approximately eight weeks from conception in total (defined by Carnegie stages).[107] 24 h after fertilisation, the zygote forms. This is a single cell, and is the structure that will give rise to the entire embryo. This cell begins to divide, and eventually forms a spherical structure called the morula. A cavity develops within this morula, and cells inside undergo a morphology change to form the blastocyst, which is the structure that will be implanted to further develop towards the embryo. It is made up of an outer layer (the trophoblast), and an inner population of cells (the embryoblast). The embryoblast then further divides into a bilaminar structure.[108] Once implanted, the cells in the blastocyst divide rapidly, and eventually the process of gastrulation begins. This is the point at which the germ layers begin to emerge. These are the three cell populations from which the various tissues and systems of the organism will arise, and so this is a vital stage in the overall developmental process. The germ layers emerge in the third week after fertilisation, which entails a total reorganisation of the cellular structure of the blastocyst. The cells then undergo a number of changes, governed by a structure called the primitive streak.[109] Differentiation begins at this point, along with migration of cells from the epiblast. Migrating cells form the endoderm and mesoderm, while the cells that do not undergo a migration in the epiblast form the ectoderm. Once this has completed, the three germ layers are present, and the complex tissue formation processes in the embryo can begin.

The endoderm gives rise to the linings of various tissues, including those in the digestive and urinary systems. It is also responsible for the formation of the liver, the pancreas, the lungs, the thyroid, the prostate and the thymus (a vital component of the immune system).[110]

The mesoderm gives rise to early structures such as the notochord and the somites. These play a role in signalling to aid in further restructuring of the embryo (including

in the development of the nervous system). The mesoderm can be divided into a number of parts, including the paraxial mesoderm, the intermediate mesoderm and the lateral plate mesoderm.[111] The paraxial mesoderm gives rise to parts of the musculoskeletal system – bone, cartilage, connective tissues such as ligaments and tendons, skeletal muscle and the dermis layer. The intermediate mesoderm develops into the reproductive system, the kidneys and the urinary tract (which is lined by endodermal cells). Finally, the lateral plate mesoderm is responsible for a number of vital organs – the heart and spleen develop from this body of cells. Smooth muscle and adipose tissue also arise from the lateral plate mesoderm, as well as the blood, lymph nodes and the limbs.

The ectoderm is the germ layer that produces the nervous system, which acts as the centre of the senses and motor command for the entire organism.[112] It is comprised of the central nervous system (the brain and spinal cord), and the peripheral nervous system (nerves and glia). Sensory organs also arise from the ectoderm, and play a central role in the ability of the individual to interact with the world around them.

3.1.2 Neural tube formation, neurogenesis, and the role of morphogens

Approximately three weeks after conception, the process of neural tube formation begins.[113] At this point in the embryo, gastrulation has occurred, and the germ layers have formed. At the onset of neurulation, signalling from the notochord induces thickening in a region of the ectoderm to form the neural plate. Signals from surrounding cells and changes in the neural plate cells themselves cause an invagination to occur, with the edges of the plate meeting to form a cylindrical shape that is known as the neural tube. This structure is vital, as the entire central nervous system (the brain and spinal cord) will eventually arise from the cells contained within. A lumen is also formed in the centre of the tube as it closes, which will form the central channel of the spinal cord and eventually contain the cerebrospinal fluid. The method and timing in which this process occurs varies slightly across species, but the general

mechanisms at work are similar. In humans and other mammals, the tube closes in the middle outwards, in contrast to others that often close across the entire tube simultaneously (e.g. amphibians) or from anterior to posterior (e.g. birds).[114] Neural crest cells are isolated from the rest of the neural tube when it closes, between the dorsal end and epidermis layer. As they mature and migrate, they will give rise to the peripheral nervous system (nerves and connective cells outside the brain and spinal cord). Somites (from mesodermal cells) form in parallel beside the neural tube, and are themselves vital in a signalling role.

In the cranial end of the neural tube, five different ventricles form which will eventually give rise to the different regions of the brain, while the caudal end develops separately. The neuroectodermal cells within this caudal region eventually give rise to the complex circuitry and networks that make up the spinal cord.[115] As in all neural systems, a variety of cell types and connections make up the spinal cord, and so the controlled differentiation of the cells in the neural tube is of utmost importance. This transformation, similar to many developmental processes, is believed to be controlled by signalling molecules called morphogens. These are biochemical cues (often but not always proteins) that induce changes in cell morphology, differentiation and migration, and in the neural tube, they play a vital role in determining the eventual structure of the neural circuits that make up the brain and spinal cord. After closing, the neural tube develops two axes that are used to distinguish the various regions: the anterior-posterior (AP) and the dorsal-ventral (DV) axes. Along the AP axis, Wnt proteins, fibroblast growth factors (FGF) and retinoic acid (RA, a derivative of vitamin A) are believed to govern many of the changes that occur. The AP axis is central to formation of the various brain regions, and these morphogens aid in the segmentation into the different zones and constituent cell types. Along the DV axis, TGFβ/Wnt proteins and Sonic hedgehog (Shh) protein play a similar role, from the dorsal and ventral ends respectively.[116]

After neural tube closure, Shh is secreted from the notochord (and later the floor plate). The exact mechanism of pattern formation is still debated, but the model of a ventral to dorsal Shh gradient is generally accepted. This gradient decreases from a high concentration at the ventral end to extremely low concentrations around the neural tube midline. Similarly, a gradient of the TGFβ signalling molecules, most notably BMP proteins, forms from the roof plate down through the dorsal half of the neural tube. The complex signalling landscape induced by these molecules exposes each region of neuroectodermal cells to varying local concentrations, which in turn causes a cascade of signalling pathways to activate within these cells.

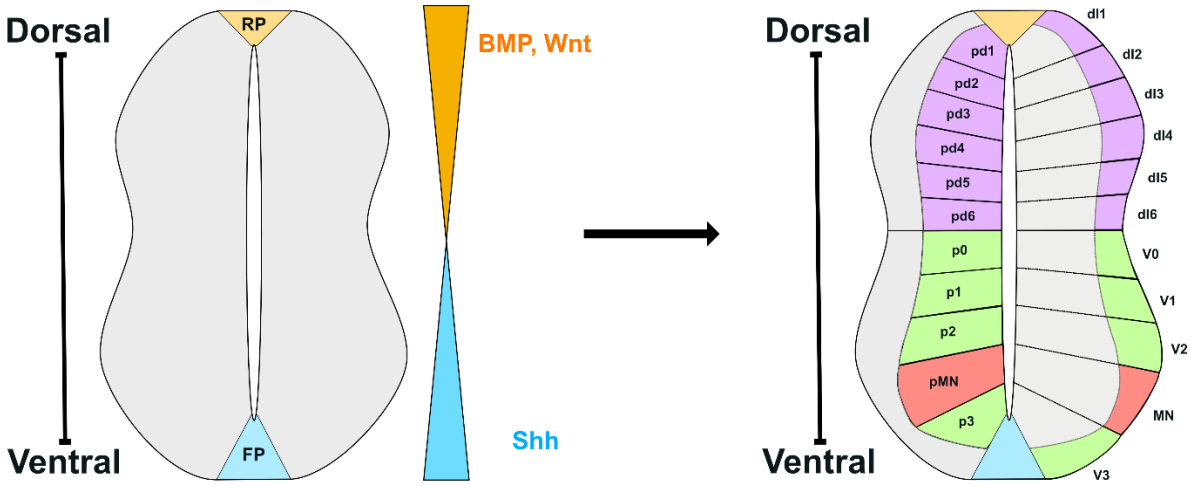


Fig. 3.1: *The patterning of the early-stage neural tube. The neuroectodermal cells are patterned by opposing morphogens at the ventral (Shh) and dorsal (BMP, Wnt) ends, which are released from the floor plate (FP) and roof plate (RP) respectively. The varying local concentrations of these morphogens influence the differentiation of these cells into neural progenitors (right), with six distinct dorsal subtypes (pd1-pd6) and five ventral classes (p0-p2, pMN and p3).*

In the case of Shh and other members of the hedgehog family, the pathway is quite well studied and understood.[117,118] When Shh ligands are absent, the transmembrane protein Patched1 (PTCH) at the cell surface binds to the receptor protein Smoothened (Smo), and in doing so, inhibits its action. This prevents Smo from acting on Gli

transcription factors within the cell, and blocks the signalling cascade from beginning. When an Shh ligand is present, it binds to PTCH, and in doing so prevents the inhibition of Smo. This allows the receptor to act across the membrane on Gli transcription factors, to enable them to act as transcription activators. A schematic is shown in Figure 3.2.

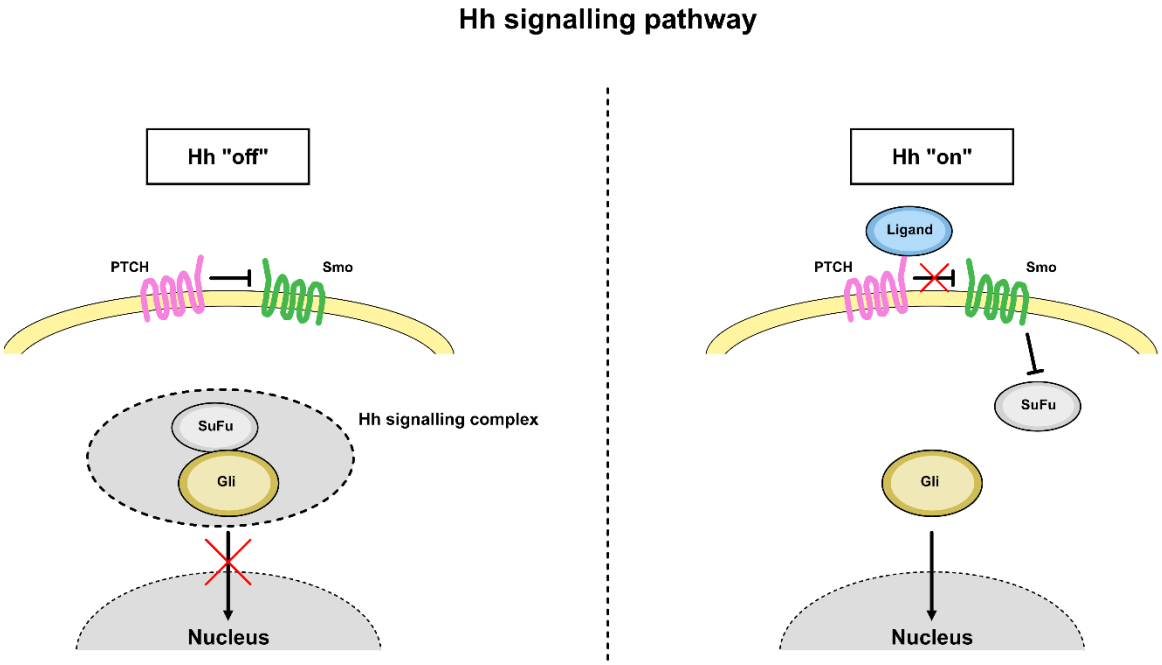


Fig. 3.2: *A schematic of the Hedgehog (Hh) family of signalling pathways. When no ligand is present, the receptor Patched1 (PTCH) inhibits the protein Smoothened (Smo). The Hedgehog signalling complex, a collection of proteins within the cell, prevents the Gli proteins from translocating into the nucleus to act as a transcription activator. When the pathway has been activated by the binding of a ligand to Ptch, the inhibition of Smo is in turn prevented. This then allows Smo to inhibit SuFu, enabling the Gli proteins to move into the nucleus and activate transcription factors there.*

This process plays a significant role in tissue repair, development and transformation, but in the case of the spinal cord, it is vital in differentiating cells towards ventral fates. In the ventral half, this gives rise to five distinct subpopulations of progenitors (see Figure 3.1, p0-p3 and pMN), and eventually mature neural cell types as they migrate

from the ventricular zone to the mantle layer and differentiate (V0-V3, MN), where axons then extend through the marginal zone.

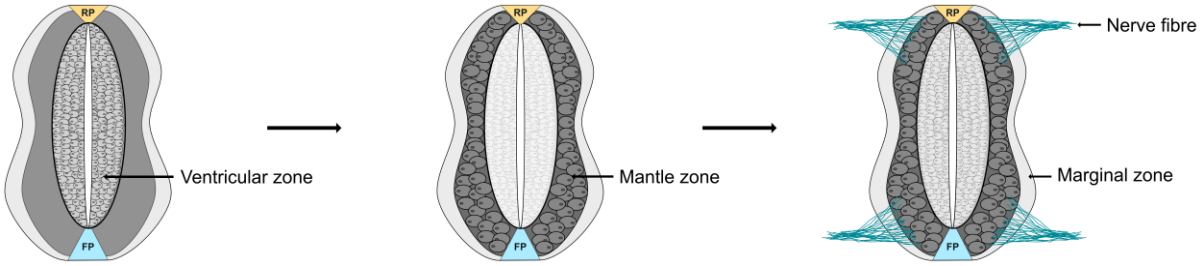


Fig. 3.3: *The development of the neural tube zones. Neuroectodermal cells initially reside in the inner ventricular zone, proximal to the lumen (left). As they differentiate into mature, post-mitotic neurons, they migrate outwards into the mantle zone (middle), and extend axons out across the marginal zone, forming nerve bundles that make up the circuitry of the spinal cord and nervous system (right).*

In particular, the motor neuron progenitors (pMNs) formed in the ventral horn are vital in the formation of the motor neurons (MNs) that will carry signals from the spinal cord to the various muscles, organs and tissues that they innervate. The mature neurons that form from this process in the V0-V3 regions are both excitatory and inhibitory, playing an equally pivotal role in the processing of information from the outside world through our senses, and in turn carrying out responses controlled via action potentials through the neural network from the brain.

Signalling governed by BMP acts in a similar, multi-step process to that of Shh mentioned above, which entails various activation-inhibition interactions.[119] TGFβ signalling in general is governed by the intercellular R-Smad complex (and a co-receptor Smad4). When the TGFβ ligand (BMP protein in the neural tube) is present, binding at cell surface receptors induces R-Smad phosphorylation and complex formation with Smad4. The complex then translocates to the nucleus, where it can act to regulate gene transcription, and so direct cellular processes such as differentiation. In the neural tube, this gives rise to six delimited regions of dorsal progenitor

subclasses (Figure 3.1, pd1-pd6). These in turn migrate to the mantle layer as in the ventral half, and give rise to the six mature classes of interneurons in the dorsal horn, some of which will later act as the sensory neurons to carry signals from the sensory organs to the processing centre that is the brain.

3.1.3 Defects in the neural tube and spinal cord

In general, the formation and closure of the neural tube is a well-controlled and ordered process, giving rise to a healthy and functional central nervous system. However, as in all biological processes, there exists the possibility of defects or complications that may arise, which can have a significant impact on the quality of life of the patient in question. Perhaps the most common condition associated with the neural tube are the family of conditions that come under the name spina bifida. The rates of occurrence vary significantly by country, and can reach as high as five births per 1000 in developed countries.[120]

There are four distinct types of spina bifida, with varying degrees of severity and risk to the patient.[121] Occulta refers to the mildest form of spina bifida, in which one or more vertebrae have failed to form correctly. This is quite a common form of the disease. and often does not have any symptoms. It will have little to no impact on the quality of life of the person in question, and is often missed unless scans or X-rays are taken for other reasons.

The second type of defect is classed under the name closed neural tube defects. This group of defects are normally covered by the skin, and are caused by issues with the formation of the bones, fat or the protective coatings around the spinal cord (known as meninges). In mild cases, this has minimal, if any, impact on the patient. However, in severe cases, it can lead to a dysfunctional urinary system and bowel, or even partial paralysis.

Meningocele refers to the cases of spina bifida in which an abnormal opening in the spine causes the protrusion of the meninges and spinal fluid. As with the closed neural

tube defects, the severity of meningocele varies patient to patient, but in some cases can again lead to issues with the bladder and bowel, or partial paralysis.

The final type of spina bifida is known as myelomeningocele, and is the most severe of the four. In this case, a similar opening is present as in meningocele, but here the spinal cord itself or other neural tissue protrude through the opening. This often leads to partial or complete paralysis from the point of protrusion, and can have significant impact on bladder and bowel function.

While spina bifida is the most common group of defects associated with the neural tube, faults in neural tube formation can lead to issues with the formation of the head, which normally have a much worse prognosis than spina bifida. In the case of anencephaly, the neural tube fails to close at the rostral end, leading to the forebrain not forming correctly. As a result of this region of the brain being absent, the child is normally stillborn, or will die shortly after birth. Rates have been found to be as high as 1 in 1000 in some regions for this defect.[122,123] Encephaloceles are disorders in which a protrusion forms from the brain itself (with the protrusion normally being covered in some form of membrane). One study estimated survival rates to 20 years of age at 67.3 %, although these rates depend on the location of the defect.[124] However, they often occur in conjunction with other defects that can hamper development and quality of life, and so it is difficult to assign a survival rate. Hydranencephaly occurs when the cerebral hemispheres of the brain are absent, and are instead replaced with cerebrospinal fluid. This condition has extremely poor prognosis, with most patients not surviving more than a few days.[125]

With all of these neural tube defects, the exact cause remains unclear. It is likely that they can often be attributed to genetic factors, although this is not always the case. Another factor that has been linked with decreased likelihood of neural tube defect is folate (vitamin B9) intake.[126,127] As such, women are encouraged to take vitamins B9 and B12 during pregnancy to decrease the chances of these defects arising. However, the exact mechanism by which the administration of folates influences the

developmental process is not well understood. There still remains many unanswered questions and challenges in regard to the understanding of the formation of the neural tube and the nervous system.

After the developmental stage, there are also conditions and diseases associated with the mature spinal cord, which is composed of a host of different neural cell types. Perhaps the most well-known of these is multiple sclerosis (MS), which manifests as a degradation of the myelin sheaths coating neurons in the spinal cord and brain, and sometimes damage to the neurons themselves. This causes disruption of their ability to convey information from the brain to the muscles the nerves innervate. The damage to the myelin sheath arises because in certain cases, the immune system invokes a mistaken foreign body response to attack the myelin, damaging or removing them entirely, and often leaving scar tissue in its place. In the UK alone, more than 130,000 people have been diagnosed with MS, which has a drastic impact on all aspects of their lives.[128] Of those 130,000, there are three times as many women as men afflicted by this condition. It is a degenerative disease, that worsens over the course of the patient's life, and cannot be cured at current. The most effective treatment methods offer targeted therapies for the specific symptoms, but cannot tackle the problem at the root of the disease.

Another devastating disease associated with the spinal cord is amyotrophic lateral sclerosis (ALS), also known as Lou Gehrig's disease. This condition causes the death of neurons in the spinal cord, which affects the ability of the patient to control their muscles. Over time, as the disease progresses, the patient loses the ability to carry out voluntary movements, which leads to weakness and muscle atrophy. As with many other nervous system conditions, the exact cause of ALS is not known, but a combination of genetic and environmental factors is most likely. Once the disease has been diagnosed, patients on average live for two to four years.[129]

With this plethora of diseases and conditions affecting the spinal cord remaining without a definitive cure (or in some cases understanding of the mechanisms giving

rise to the condition), it is evident that further neural engineering efforts are needed. Thousands of lives every year depend on better treatments and therapies, which can be informed by further optimisation of cell culture techniques, drug development and novel materials systems.

3.1.4 Isolating stem cells for interrogating developmental processes

The goal of developmental biology in general is to replicate processes that occur within the developing embryo, to further elucidate the systems at work or to investigate potential therapies for the conditions and defects that can arise there. Embryonic stem cells, which are isolated from the inner cell mass of the blastocyst, can be used to generate ectoderm, mesoderm or endoderm cells for further studies.

Insights into the formation and function of the ectoderm and the neural tube can serve to educate researchers on how conditions such as those mentioned above can arise. It can also potentially offer a method to generate controlled populations of neural cell types. These could have wide ranging applications in the treatments of conditions such as ALS, where specific cell types die off preferentially. The ability to generate large quantities of controlled cell populations could enable cell replacement therapies to overcome the loss of neurons in these neurodegenerative diseases. Neural engineering is still in the early stages of its development, and large strides are needed to make clinical applications more widespread, to tackle these conditions that are a burden on so many patients worldwide.

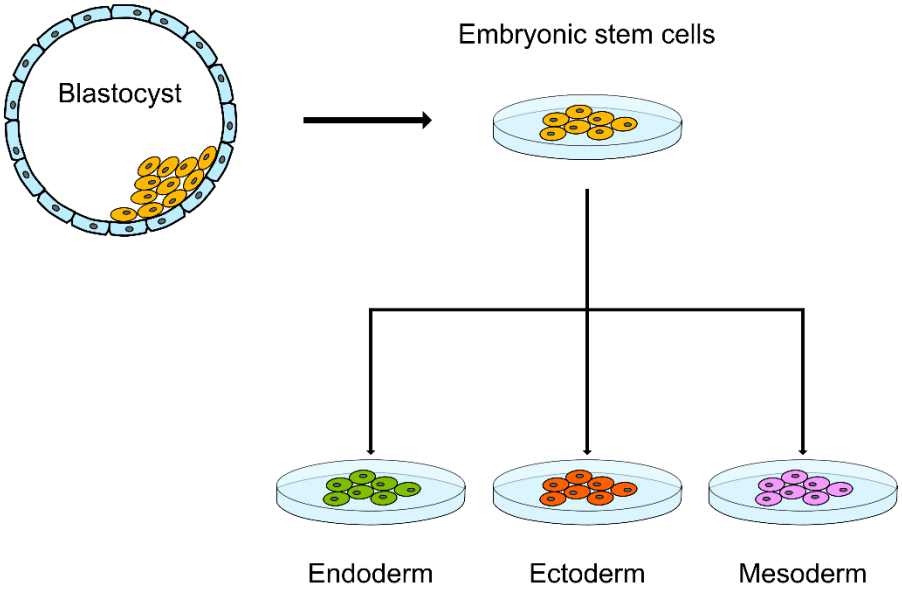


Fig. 3.4: *Formation of germ layer cells in vitro. Embryonic stem cells can be isolated from the early-stage embryo blastocyst (usually in mice). These cells can then be directed to differentiate into any of the germ layer cells, and from there into almost any type of cell required.*

3.1.5 *In vivo* methods for investigating the developing spinal cord

Many features of neural tube formation and development are conserved across all vertebrates. While invertebrates exhibit some differences, parallels and similarities can still be drawn between the two. Indeed, many of the initial discoveries regarding the neural tube were made in comparisons between human, mouse and drosophila embryos, and the genes and pathways active in each.[130] The primary reason for this is the ease of access to embryos, and the lower ethical and moral burden of carrying out research on invertebrates or murine embryos. However, as a result of the similarities between human development and other vertebrates, as well the development of robust ethical guidelines, mouse and chick embryos have become the gold standard in recent years, although drosophila studies can still inform experiments in other species. Certain genes have homologs across species, and so can direct researchers on expected behaviour in other species, and indeed in humans. In particular in regard to the DV axis and the spinal cord, protocols to extract mouse neural tube sections at

specific timepoints have offered a wealth of data, which has confirmed many of the signalling and morphogenic theories in regard to the formation and progression of neural circuitry. The neural tube formation occurs between day 8 and day 10.5 of the mouse embryo (E8-10.5), and explants can be taken along the DV axis at various timepoints to investigate the generation of the specific cell types.[131–133]

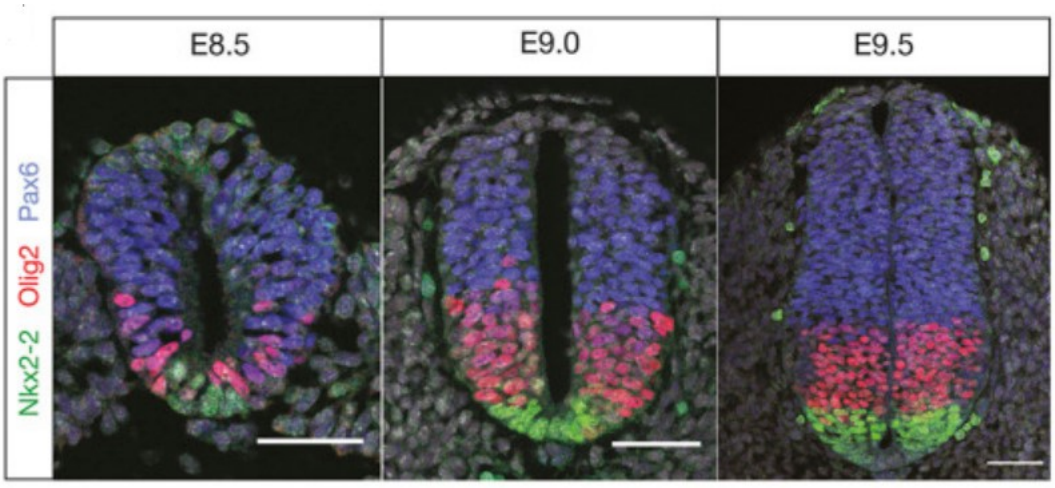


Fig. 3.5: *The formation of the mouse neural tube, captured using immunostaining. As the time progresses from E8.5 to E9.5, delimited regions of neural progenitor subtypes begin to emerge (as can be seen by the presence of the transcription factors Pax6, Olig2 (motor neuron progenitors) and Nkx2.2). Scale bars = 50 µm. Reproduced from Exelby et al.*[134]

Immunofluorescence studies can be carried out, with antibodies targeting specific transcription factors used to label each subtype of progenitor and neuron as needed. Mutant embryos can also be generated, with specific knock-outs or knock-ins, to elucidate the impact of the presence or absence of specific genes and transcription factors in the formation of the spinal cord and nervous system in general. Combining this with *in vitro* cell studies, a platform can be generated that provides a window into the developmental process, and the subsequent formation of the central nervous system. Despite this, there are drawbacks associated with the use of embryos and explants. It is an expensive and time-consuming process, and the surgery required is

technically challenging. Above all, it requires the use of animal studies, which, when possible, should be avoided completely. An ideal investigative *in vitro* method would maintain the complexity and spatial accuracy of the neural circuits *in vivo*, without the need to sacrifice animals in the process.

3.1.6 *In vitro* methods for modelling the developing spinal cord

The standard in most labs currently remains the use of a combination of *in vitro* and, only where necessary, *in vivo* models in mice, chicks and drosophila.[134,135] *In vitro* systems offer a simple, robust method to generate controlled populations of neural subtypes. In regard to the neural tube, protocols have been developed to generate the various neural cell fates from embryonic stem cells through the differentiation process (neuromesodermal progenitors (NMPs), neural progenitors, mature post-mitotic neurons), most often carried out using mouse cell lines (e.g. HM1 cells). For mouse cells, basic fibroblast growth factor (bFGF) is used to generate neural character in the cells, before retinoic acid and further signalling cues (e.g. small molecule activators/inhibitors) are used to direct the cells down specific neural pathways. For example, small molecules such as Smoothened agonist (SAG) and purmorphamine have been developed to specifically activate the Shh pathway and to generate motor neurons and other ventral cell types (based on the concentration used).[136,137] These offer a cheaper alternative to using the protein ligands themselves, and induce a similar level of activation of the various pathways. Likewise, inhibitors such as cyclopamine and robotnikinin can be used to block the pathway, and to generate more dorsal cell lines.[138,139] The TGFβ (BMP in the DV axis) and Wnt pathways can be targeted in a similar manner, with activators and inhibitors now commercially available for most pathways for the generation of dorsal cell types. In this manner, the entire spectrum of cells in the neuroectoderm and neural tube can be recapitulated.

Gouti *et al.* generated NMP cells *in vitro* from both human and mouse pluripotent stem cells through the use of Wnt and FGF signalling pathways.[140]

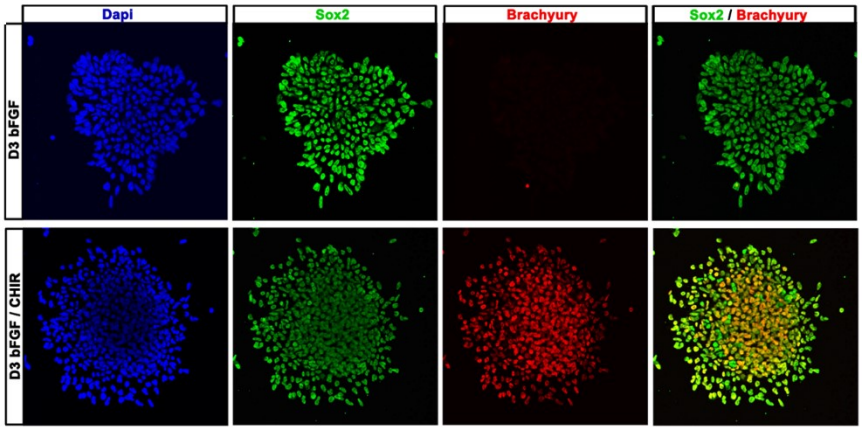


Fig. 3.6: *NMPs generated from mESCs in vitro. Cells treated with bFGF alone exhibited neural character (Sox2 but no Brachyury), while cells that were treated with both bFGF and CHIR exhibited neuromesodermal character (Sox2 and Brachyury). Reproduced from Gouti et al.*[140]

The authors directed the differentiation of the progenitor cells into either spinal cord or mesoderm cell types by treating with retinoic acid/SAG or CHIR. In doing so, they demonstrated the potential to generate the different cell types of the early-stage spinal cord, but also showed the limitation of the approach by losing the spatial control of the differentiation process. As such, while the *in vitro* approach is suitable for investigating the mechanisms and interactions of a single cell type per well, they do not possess many of the finer details that other methods might offer. While useful for exploratory studies, this method requires other complimentary approaches to fully recapitulate neural systems.

Liem *et al*. carried out a similar study to Gouti *et al. in vitro*, to investigate the role that BMP signalling plays in the response on differentiating chick neural cells to Shh from the floor plate.[141] The authors were able to demonstrate the ventral character obtained when only Shh was present, and the dorsal character that appeared when BMP7 was added to the culture media. The same behaviour carried through from progenitors to mature neurons, as expected. Lippmann *et al.* demonstrated the ability to direct the differentiation of hPSC-derived NMP cells into neuroectodermal cell lines based on

treatment with retinoic acid.[142] By controlling CHIR treatment time before exposure to retinoic acid, they could also direct the cells towards different groups of mature spinal cord regions (e.g. thoracic, lumbar) (with different conditions separated across wells).

It should be noted that in the studies carried out by Gouti *et al.* and Liem Jr. *et al.*, the spinal cord dorsal and ventral cells were not generated in specific subtypes, but rather were identified only by being in a larger family of cells (e.g., dorsal or ventral spinal cord, anterior, hindbrain or mesodermal cells). In the case of Lippmann *et al.*, control over the type of spinal cord cell that was generated was shown. However, the differentiation was limited by the cells being contained within well plates, meaning that all cells within a plate differentiated towards the same fate, removing any interaction or control over the various cell types that would ideally be present, as they would *in vivo*. In general, standard *in vitro* screening exposes all cells in a single well to the same conditions, and so there is less fine control over the final fate of the neural cells.[143,144] They do not have the spatial or dynamic cues that would be present in their parent tissues – for example, in the neural tube, the cells in well plates cannot readily be differentiated into the various subtypes of neural cells that would make up the circuits of the spinal cord and brain. The models generated *in vitro* are also less detailed or accurate than other approaches, as the *in vitro* cells are growing in an environment different to that experienced *in vivo*, and so may not behave as expected. These methods will always be a valuable tool in labs around the world due to their low cost, high throughput and relative simplicity. While useful for certain applications when a single neural subtype is needed, or to avoid the need for animal research and sacrifice, the potential of this as a standalone method is limited. As such, it is often necessary to combine these protocols with *in vivo* neural studies or other experimental approaches.

3.1.7 Neural organoids

An alternative that provides a compromise between standard *in vitro* cell culture techniques and the complex neural systems *in vivo* is the area of neural organoids/spheroids. This field has emerged in recent years as a means to grow clusters of cells *in vitro* that develop characteristics of the parent tissue or organ. In doing so, they provide a more accurate model for the target tissue than cells on tissue culture plastic, but do not require as high a burden on animal sacrifice as *in vivo* or *ex vivo* studies (beyond the isolation of the parent cells). They can be considered a 3D culture method, as the cell bodies that form will often be hundreds of micrometres or even millimetres in diameter. The organoids are often grown in or on a supportive structure of some type, usually a fibre mesh or hydrogel scaffold. They have extensive applications in fields such as drug development and screening, since controlled populations of cells can be generated to emulate the response of organs to specific stimuli. In regards to neural organoids, much of the work has focused on the brain, in particular cerebral embryonic bodies.[145,146]

Protocols have been established to generate these over the course of weeks, with cells from the various regions of the brain contained within. The Knoblich group are one of the leading teams in pushing this field forward, demonstrating methods to both generate neural organoid systems, and also to use them in modelling of developmental neural diseases.[147,148]

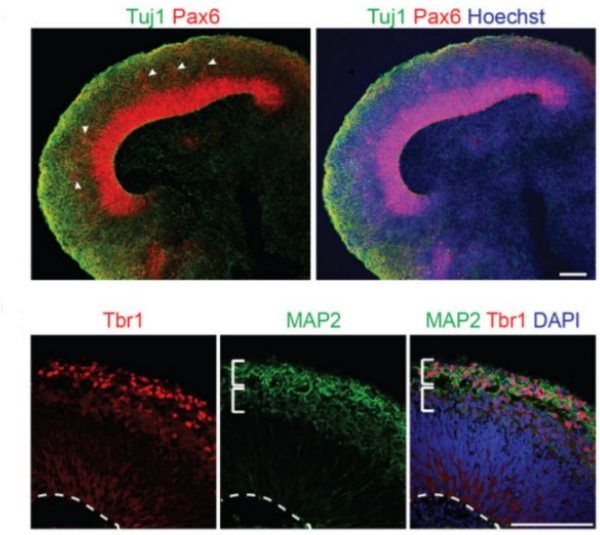


Fig. 3.7: *Neural organoids that exhibit dorsal cortical organisation as would be expected in vivo*. (Top) *Radial glia (Pax6, red) and mature neurons (Tuj1, green) were seen to organise into layers much like the zones present in the brain. (Bottom) Layer formation was further emphasised by the presence of preplate cells (Tbr1, red) and neurons (MAP2, green) on the outer edge of the neural organoid. Scale bars = 100 µm. Reproduced from Lancaster et al.*[147]

The developing neural tube has also been modelled in this way by a number of groups, who see these cell bodies as ideal candidates to recapitulate the spatial organisation and delimited regions of cell types in the developing nervous system. Meinhardt *et al.* established a neural tube model system that generated cell clusters that were responsive to the morphogens that would pattern the developing nervous system *in vivo*.[149] Their cell bodies, formed from mESCs, could be differentiated into the various types of ventral neural progenitor cells by exposing them to the Shh agonist, SAG. Without any treatment, their organoids expressed dorsal character (as shown through the expression of Msx1). A similar treatment using retinoic acid could induce posterior character in the cell bodies, while untreated cells had more anterior character. The treatment with retinoic acid also induced floor plate cells in the bodies, which created some semblance of dorsal-ventral patterning via inter-cell signalling (although this was irregular, and did not have the spatial separation of the dorsal and ventral cell types

that would be present in the neural tube). In this way, the authors successfully created an *in vitro* system that exhibits many of the hallmarks of the developing nervous system, but lacked some of the spatial control required to model the neural tube in an accurate manner.

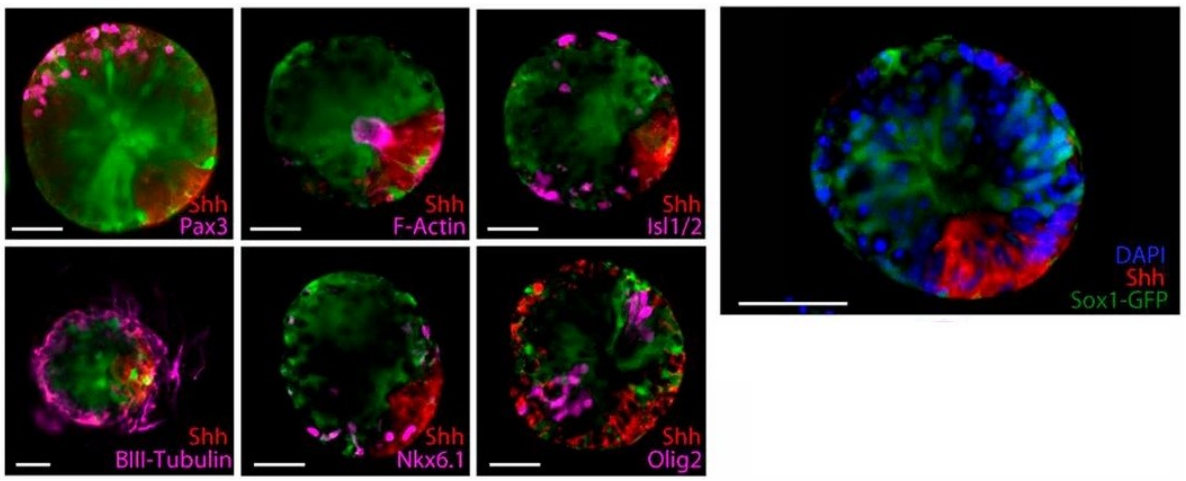


Fig. 3.8: *Representative images of the neuroepithelial cysts obtained by Ranga et al.*[150] *An Shh-positive floor plate region was seen to emerge, along with ventral (Olig2, Nkx6.1) and dorsal (Pax3) regions. Mature motor neurons were also seen at the periphery of the bodies (Isl1/2-positive), which is seen in the neural tube as cells mature and migrate outwards. Scale bars = 50 µm. Reproduced from Ranga et al.*[150]

Ranga *et al.* investigated the role that matrix composition plays in the growth of neuroepithelial cysts for neural tube modelling.[150] When the optimum material was used (PEG tested against Matrigel scaffolds, and was optimised for stiffness), organoid structures were obtained that resembled the developing neural tube. The authors observed a region of Shh-positive cells, as would be expected in the floor plate of the neural tube. They also observed the presence of other ventral transcription factors (Olig2, Nkx6.1) and dorsal markers (Pax3). However, it should be noted that there was again not a clear distinction between the different regions, and the Nkx6.1-positive region was quite narrow. The transcription factor network of the neural tube is complex and dynamic, and so this may have been attributable to the stage of development that

the cysts represented (the authors reported their system to represent the E10.5 timepoint). Regardless, the presence of multiple neural markers and somewhat defined regions of the transcription factor network demonstrates the potential of this platform for investigating development and neural diseases.

It is clear that the organoid platform has significant potential as a means to investigate injury and disease to both the developing and mature central nervous system, and specifically the spinal cord. Organoids in particular offer the capability to model the neural tube accurately and effectively, without the need for the sacrificing of animals. By growing structures that consist of the cell types and transcription factor networks that would be present *in vivo*, the platform can be used to model the effects of specific genes or drugs on the developing nervous system, and could potentially aid in tackling conditions such as spina bifida and cephalic disorders that as yet remain as large burdens on social and health systems worldwide.

However, before they can be seen as the answer to the questions posed by neural biology, further progress in the field is needed. Organoid development as a whole is still in its nascent stage, and so more advances are needed before this can be seen as the answer to many developmental biological questions, with the establishing of standardised methods being of utmost importance. It is an inherently slow approach, since growing mature organoids often takes many weeks. This limits the throughput that the approach offers, and so inevitably slows down any investigation being carried out. There also does not yet exist a consistent method to generate delimited regions of specific cell types that would be expected in the developing spinal cord (although efforts are being made to control cell populations within organoids[151]). The positions and interactions of the various cell types within the nervous system play a pivotal role in the functionality that emerges as the neural circuits form. Until these challenges can be overcome, other complimentary *in vitro* approaches will be needed to support any neural applications of the organoid field. An ideal stand-alone method would offer high throughput, simplicity in carrying out the culture, and also would provide spatial

and temporal control over the emergence of the various neuron types of the spinal cord.

3.1.8 *Ex vivo* approaches

Where standard *in vitro* approaches are not sufficient to achieve the complexity required in neural engineered systems, *ex vivo* approaches may be used. The intricacy of the central and peripheral nervous systems necessitates complex engineering approaches, to not only accurately model healthy growth and development, but also disease and injury of neural tissue. While standard *in vitro* cell culture can offer insights into certain aspects of the nervous system, they are often overly simplified, and do not accurately represent the neural environment that cells would experience *in vivo*. As such, they can only ever serve as proof-of-concept studies for any engineered system that might be implanted or translated to patients in the clinic.

For the generation of an *in vitro* model that would overcome the lack of complexity in 2D culture methods, neural tissue explants can be employed. Tissue sections can be explanted from the source of choice, and cultured in much the same way as cells would be on tissue culture plastic or a material system. This approach maintains the complexity and connectivity of the neural tissue, and so can be used as a more accurate model for the behaviour of neural cells *in vivo*. Bonnici *et al.* took longitudinal slices of a mouse spinal cord, and developed a method to maintain and culture the explanted section to study axonal growth and synapse formation.[152] The section maintained its dorsal-ventral character, and the neurons within the section proceeded to form synapses and myelin sheaths. The authors also induced mechanical lesions into the spinal tissues, and observed the decrease in the number of fibres growing across the lesion over time. This shows that these explanted models can indeed behave in a manner that is consistent with the spinal cord *in vivo*, and so are viable models for spinal cord injury and disease. As well as offering a means to investigate formation of

new connections post-lesion, explanted models can also be applied to lost functionality studies of the spinal cord.

Heidemann *et al.* cultured explanted spinal cord sections on microelectrode arrays, and in doing so were able to monitor the neural activity of the tissues.[153] The authors discovered that, as the time *in vitro* increased, the functionality of the spinal cord sections decreased. The timeline over which this occurred was similar to that observed in *in vivo* models They were also able to investigate the signal transfer between tissue sections that were cultured close to each other, through the formation of new connections between the two sections and synchronisation of neural pulses.

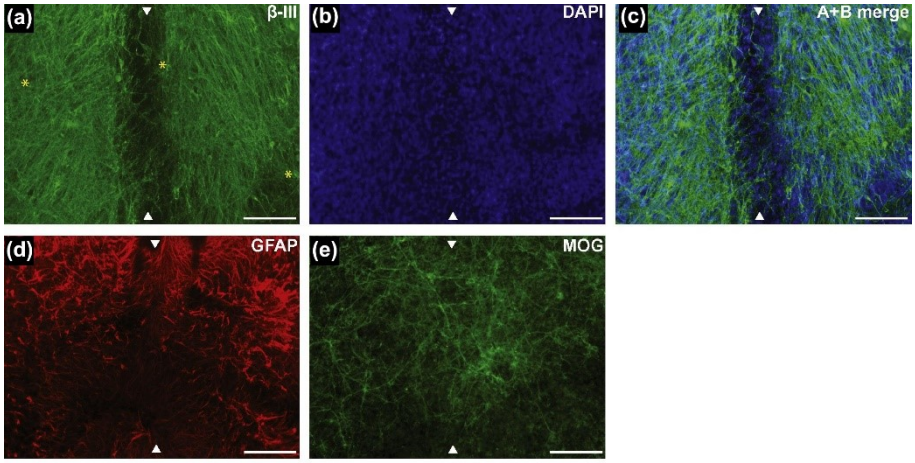


Fig. 3.9: *Separate explanted spinal cord sections grown in culture in close proximity showed some level of interaction. (a-c): Anti-β-III-tubulin staining (green) shows neural fibres and connections forming across the gap between the two spinal cord sections (white arrows indicate point where sections meet). (d) and (e): A small number of astrocytes (GFP, red) and an abundance of myelin/oligodendrocytes (MOG, green) were seen at the fusion site between the two slices. Scale bars a-c, e = 100 µm, d = 200 µm. Adapted from Heidemann et al.*[153]

Ex vivo models can also be a powerful platform for investigating the role that novel materials systems might play if implanted at the site of a nervous system injury. Weightman *et al.* demonstrated this through their spinal cord injury model, by

culturing slices of murine spinal tissue and interfacing them with various types of patterned substrates.[154] PLA nanofibre meshes were interfaced with the tissue sections, and were functionalised with poly-lysine and laminin coatings to investigate their potential regenerative interaction with the tissue. By introducing lesions to these cultured spinal cord explants, the authors could investigate the role that the topography of their aligned nanofibres played in the wound response within the tissue.

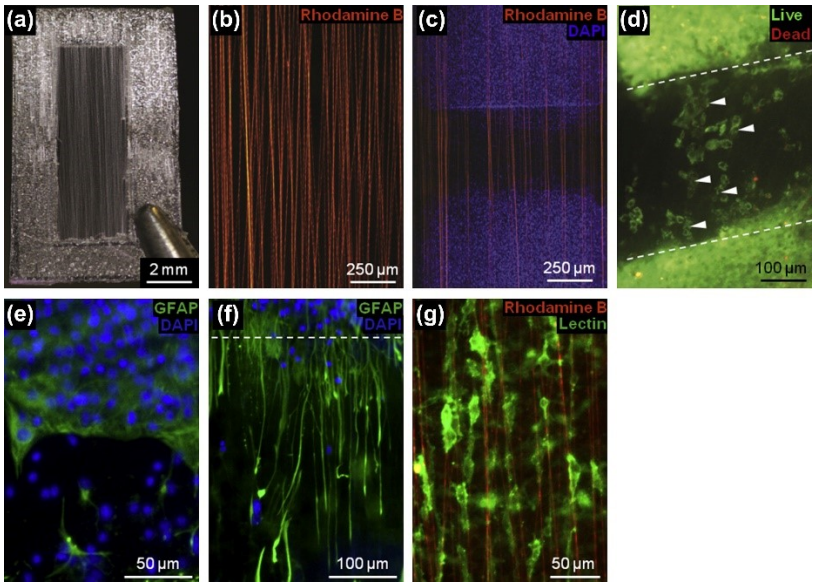


Fig. 3.10: *(a) and (b): Photograph and rhodamine-B-stained image of the PLA nanofibers. (c) Fibres extending across a lesion in the spinal cord explant. (d) a live-dead assay carried out at the lesion site three days after the nanofibers were applied. (e) Astrocyte cells showing little to no interaction with non-coated fibres at the lesion site. (f) Increased interaction of astrocytes with fibres coated with poly-lysine and laminin. (g) Microglia attaching to uncoated nanofibre meshes. Adapted from Weightman et al.*[154]

The scaffolds were found to enhance growth of astrocytes across the lesion site, with the coated fibres showing much higher attachment. Microglia were also seen to attach to all the fibre scaffolds that were applied across the lesion. This study shows the power of *ex vivo* studies for investigating material system applications, where the spinal cord explant here could be used to draw conclusions about how fibre scaffolds might

behave if implanted into a patient, and so could offer valuable insights into future therapies targeting the nervous system.

While the ability to explant tissue sections and culture them is undoubtedly powerful and informative on neural tissue injury and regeneration, as with all methods it has some drawbacks. The acquisition of suitable explants is a task that requires a specific skillset and knowledge, and so would not be readily available in all bioengineering labs. There is also the burden of animal research, as animals must be sacrificed in order to obtain these sections. Ideally, a method that investigates these matters would not require sacrifice of animals, and would be more accessible for engineers and biologists alike.

3.1.9 Opportunity for a novel neural engineering material platform

For a novel materials system to be an effective neural engineering tool in investigating the emerging central nervous system, it would need to offer significant advantages to the already established protocols and techniques. It should maintain the simplicity and throughput of standard *in vitro* methods, while improving on the spatial control that can be exerted over the differentiation into the various neural cell types in organoid systems.

There is a pressing need for alternatives to animal research, and if a materials system could offer this in a more efficient, higher throughput method, while maintaining a comparable spatial resolution to that seen *in vivo*, there could be potential for use across developmental neural biology as a whole.

Currently employed materials systems such as microfluidic devices have shown promise in the modelling of neural systems through the exposure of cell types to dynamic culture conditions. However, low throughput and difficulty of manufacture are hindering their applications considerably. Polymer casting of microfluidics is a promising candidate for the future of the field, as this could remove the need for

cleanroom fabrication steps (beyond perhaps the generation of master devices to cast from), but more progress is needed before their applications are widespread.

It is clear there exists the opportunity for the development of a materials platform that maintains the simplicity, relatively low cost and high throughput of *in vitro* approaches, while offering comparable spatial organisation to that seen in the neural tube. Until organoids and microfluidic devices can be developed to achieve the level of complexity required for the mapping of neural circuitry, inkjet printing emerges as a promising candidate. The rapid generation of printed gradients far exceeds the requirements of microfluidic systems, where dynamic gradients and large amounts of material are needed at a much greater cost. The ease of bio-ink manufacturing and patterning enables rapid modification of the platform for various applications, and the ability to print multiple substrates in parallel increases the potential number of conditions that can be explored in a single investigation relative to organoids or microfluidics, with each substrate having the capability to be a self-contained experiment.

The next sections describe how inkjet printing, when applied to neural systems, can be used to recapitulate many of the aspects of the developing spinal cord, and in doing so can overcome a range of the challenges mentioned above. Mouse embryonic stem cells in their neuromesodermal and neural progenitor states were used in conjunction with these printed morphogen patterns to demonstrate the capability of this platform to recreate the complex map of spinal cord cell types generated across the dorsal-ventral axis of the neural tube. This serves as a proof-of-concept for a novel approach to neural engineering, which could be used in conjunction with other methods or as a stand-alone technique to offer insights into the embryogenesis process, and the development of the central nervous system.

3.2 Materials and Methods

3.2.1 Cell culture

Mouse embryonic stem cells (mESCs) were used for all experiments (unless otherwise stated). Mitotically inactivated primary mouse embryonic fibroblast (PMEF) cells were thawed, and plated in tissue culture plates coated in gelatin (0.1% v/v), in DMEM knockout medium media (cat. no: 21331020, Thermo Fisher Scientific) with ESGRO-LIF (2000 U/mL, cat. no: ESG117, Sigma Aldrich), fetal bovine serum (10% v/v), penicillin/streptomyocin (1% v/v, cat. no: 15140122, Thermo Fisher Scientific) and L-glutamine (2 mM, GIBCO). These were left overnight in the incubator at 37°C, to ensure they had adhered sufficiently.

The mESCs were thawed and seeded onto the plates with PMEFs in the same media, with media being changed every day, and the cells were split every two days. This was carried out by washing with PBS, and detaching using Trypsin (0.05% v/v) before collecting. The cells would then be seeded onto a fresh PMEF-coated plate, at a density of 3×10^6 cells per p10 plate. When the cells were passaged two/three times, they were ready to be differentiated. On day -1, p10 plates were coated in gelatin (0.1% v/v) for the panning process. On the morning of day 0, the media was changed. A minimum of 2 h later, the cells were washed with PBS and removed with Trypsin (0.05% v/v). The cells were transferred to the first panning plate, and left to sit for at least 20 min, or until PMEF cells were seen to start to stick to the surface (since these are larger, heavier cells, they would settle onto the surface first). The cells were collected, and placed in a second panning plate for the same time period. If PMEFs were still seen floating after this, a third panning step could be carried out. The mESCs were then collected, counted, and spun down in a centrifuge. They were washed in PBS, before being centrifuged again. The cells were then resuspended at a concentration of 1×10^6/mL, and plated in gelatinized p35 plates at a density of 50,000-80,000 per plate. These plates were filled with 1.5 mL of N2B27 media, and bFGF (10 ng/mL, cat. no: 100-18B, Peprotech). N2B27 medium contained a 1:1 ratio of DMEM/F12: Neurobasal medium (cat. no: 21331020 and cat. no: 21103049, Thermo Fisher Scientific), 1 x N2 (cat. no:

17502001, Thermo Fisher Scientific), 1 x B27 (cat. no: 17504001, Thermo Fisher Scientific), penicillin/streptomycin (1% v/v, cat. no: 15140122, Thermo Fisher Scientific), L-glutamine (2mM, cat. no: 25030024, Thermo Fisher Scientific), BSA (40 mg/ml, cat. no: A7979, Sigma Aldrich), and 2-mercaptoethanol (0.1 mM, cat. no: 21985023, Thermo Fisher Scientific).

On day 2, the media was changed with N2B27/bFGF (10 ng/mL) and CHIR99021 (5 μM, Axon), replaced by N2B27/RA at day 3 (10 nM, cat. no: R2625, Sigma Aldrich). In the early stages of the project, cells were seeded onto substrates at day 3. However, the protocol was later modified to maintain the cells in N2B27/RA from day 3-5. At day 5, the cells were split and seeded onto substrates. The media was changed on day 6, and the cells were fixed on day 7 (unless otherwise stated).

3.2.2 Imaging

Imaging was carried out on an Axio Imager (Zeiss, fitted with an Apotome 2) or Axio Observer (Zeiss) widefield microscope, which had a motorised stage to allow for tiling of the whole substrate. All exposures were calibrated off the control substrates in each experiment, and were maintained at the same values for each set of substrates. Up to four channels were imaged in each case, with the final configuration of stains for ventral experiments being CF430 (Pax7), Alexa Fluor 488 (Sox2), Alexa Fluor 568 (Olig2), and Alexa Fluor 647 (Nkx6.1) (unless otherwise stated). The substrates were imaged at 20X magnification, and the tiling was done in the Zeiss software immediately after imaging. Due to the large imaging area, four z-slices were taken at each tile across the substrate, in 5 μm increments.

For higher resolution imaging of single colonies, a confocal microscope was instead used (Leica SP5 MP). As only a single colony was being captured per image here, the entire colony was instead captured in the z-stack, taking 0.71 μm increments. The same channels as those mentioned before were chosen, and images were max projected for demonstration purposes.

3.2.3 Immunostaining

For fixing, the cells were first washed with PBS, before being left in PFA (4% v/v) for 10 min. They were washed again with PBS, before being stored in fresh PBS at 4°C until they were ready to be stained, and mounted. The staining of the experiments varied depending on the experiment in question. Primary antibodies were added overnight in blocking buffer (BSA (1% w/v)/Triton X-100 (0.1% v/v) in PBS) at 4°C. Three washing steps were carried out the following day before adding the secondary antibodies, using PBS/BSA (1% w/v)/Triton X-100 (0.1% v/v). The plate was wrapped in foil at room temperature and left for 2 h. Three washing steps were carried out, and then mouse serum (1% v/v) in PBS was added for 1 h. Finally, Sox2 antibody was added in mouse serum (1% v/v) for 2 h. The substrates were then taken and mounted between a glass slide and a coverslip, with mounting media (Fluoromount-G, Thermo Fisher Scientific, cat. no: 00-4958-02). However, the mounting method was later changed, with 8-well plates (ibidi) instead being used with the substrates inverted into the mounting media.

3.2.4 Image analysis

Analysis of imaged neural progenitor cells was carried out using ilastik (University of Heidelberg/European Molecular Biology Laboratory) and CellProfiler (Broad Institute).[155,156] Due to the large amounts of data generated from each substrate, manual annotating and measuring of intensities and colony features was not a feasible approach. The regions of background between cell colonies also needed to be removed from any image analysis, to obtain only data that described the response from cells on the printed patterns. As such, an image analysis pipeline was required, to quantify the response to the printed Shh gradient. The edge regions of substrates often showed disruption and damage, which led to cells aggregating at those points, in particular at the point where the holder contacted the surface during the layer-by-layer process. The Safranin-O staining also showed inconsistencies at the edge regions, with a lower amount of heparin being labelled there. As such, a region of interest was

defined that excluded the edge regions around the entire substrate, to prevent any artefacts being introduced by these factors.

An initial shading correction step was first required. For each tile in the overview image of the substrate, the 488 channel on the widefield microscope had a consistent shading artefact, that was corrected for by applying a pre-determined filter (provided by the imaging suite in Imperial College London, FILM). Once the shading correction was applied, the images were max projected through the 4 z-stack slices (via ImageJ).

The images were then introduced to the ilastik software to carry out labelling of the features present in the images. The Sox2 channel was chosen to train the software to recognise colonies and background in each tile, as well as regions that were slightly out of focus. Sox2 was chosen as this marker was not dependent on the level of Shh pathway activation, and should be present in all neural cells across the DV axis. Initially, hand annotation of the colonies, background and single cells was carried out for the training, before introducing the entire collection of imaged substrates and carrying out an automatic labelling process. From this, binary pixel probability masks were obtained, identifying the various types of features present in each field of view.

CellProfiler was used to segment the four pixel prediction maps by setting a probability threshold of between 0.3 and 0.5 to capture the majority of features in each class. As the imaging was done using a widefield microscope rather than a confocal (widefield was used due to presence of motorised stage, which was needed for tiling of whole substrates) it was not possible to obtain single cell segmentation, due to the convolution of signals from the colony body above and below the focal plane. The morphology and intensity of the subsequent CellProfiler segmented objects were measured. The data from these measurements were exported and analysed using R, with cleaning and thresholding of data being carried out to remove any technical artefacts from the pixel classification or segmentation processes.

3.2.5 Summary of experimental approach

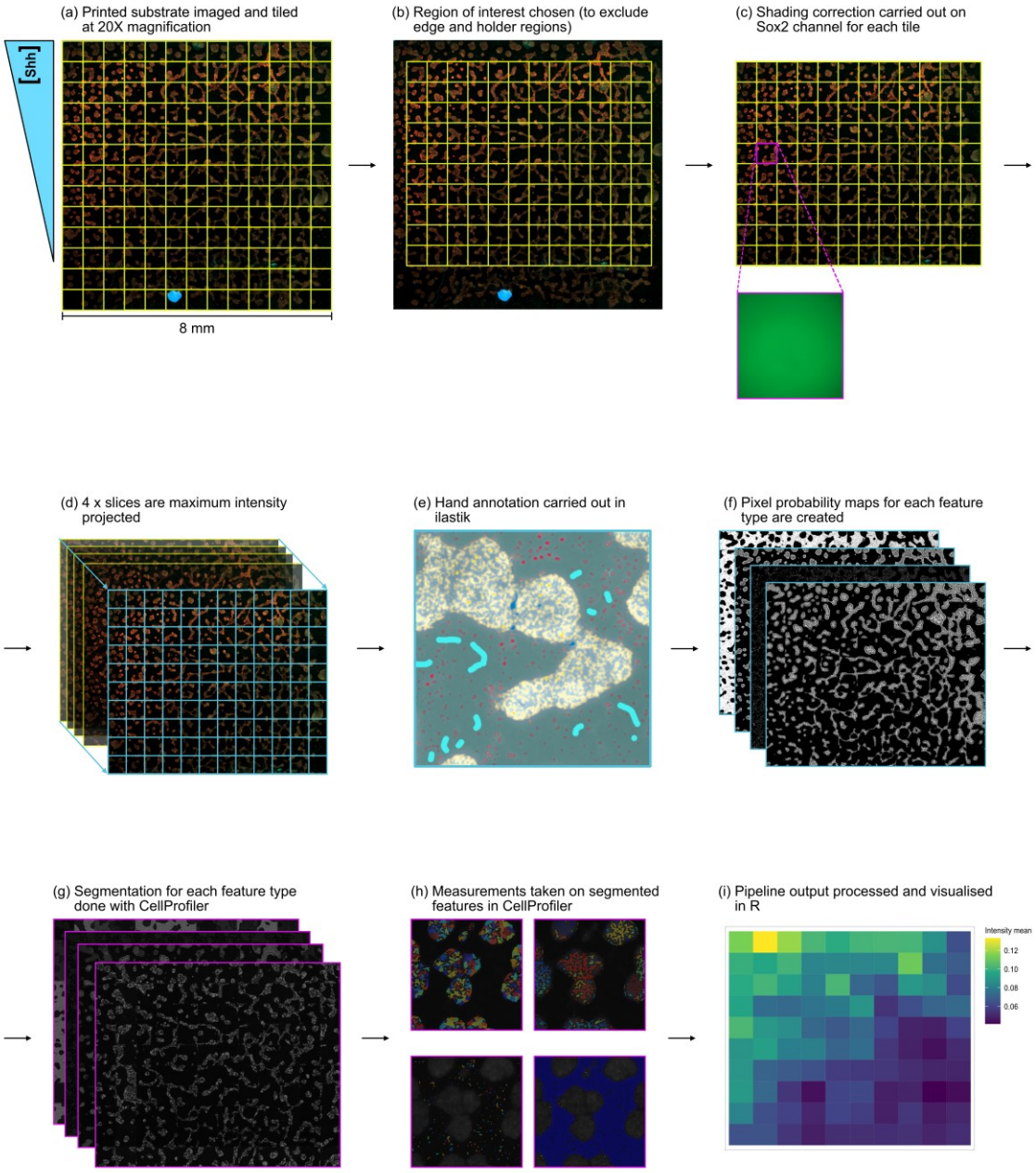


Fig. 3.11: *Overview of the image analysis pipeline to automate data extraction across all gradient substrates. (a) Each substrate across three repeats was imaged and tiled at 20X magnification on the widefield microscope. (b) A uniform region of interest was defined across all substrates, that would exclude the edge regions of each substrate. (c) A shading correction step was carried out using a pre-determined image in the 488 channel. (d) A maximum intensity projection step was carried out across the four slices in each tiled image. (e) Initial hand annotation was carried out on a small number of images, to train the ilastik software to recognise the four different feature types present in the tiled images. (f) Once trained, ilastik was then used to automatically generate pixel probability masks for the four feature types present: large clusters (features within the large colonies of cells), edge regions (regions between those features, usually out of focus), sparse colonies (usually single cells, not connected to any colony or other cells) and background. (g) These pixel probability masks were then used in CellProfiler to segment the various features (single cell segmentation was not achieved). (h) Measurements were taken on the various feature types (e.g. channel intensities, feature area, density) (i) R was used to process and visualise the output data.*

3.3 Results

For all section 3.3 immunofluorescence images, the antibodies used for staining were targeting a subset of the following transcription factors. This was necessary to describe the effectiveness of the printed gradients in modelling the entire DV axis of the neural tube.

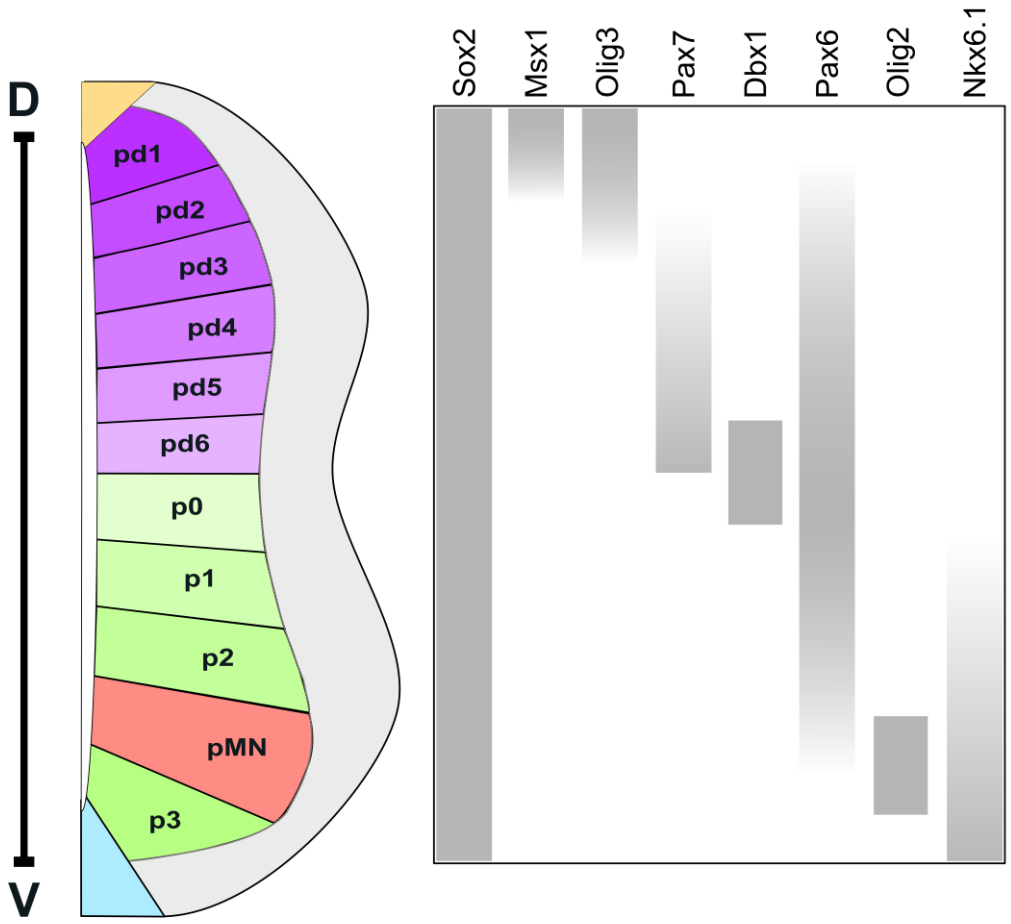


Fig. 3.12: *Part of the transcription factor network of the neural tube, along the dorsal-ventral axis, showing the corresponding locations at which they are present in vivo. This panel of markers was chosen to identify the cell subtypes being generated during printing experiments.*

The mESCs were seen throughout this work to form large colonies on the silicon substrates, rather than single cell layers (see Figure 3.13 for a representative image). This was consistent with the behaviour of this cell line on tissue culture plastic.

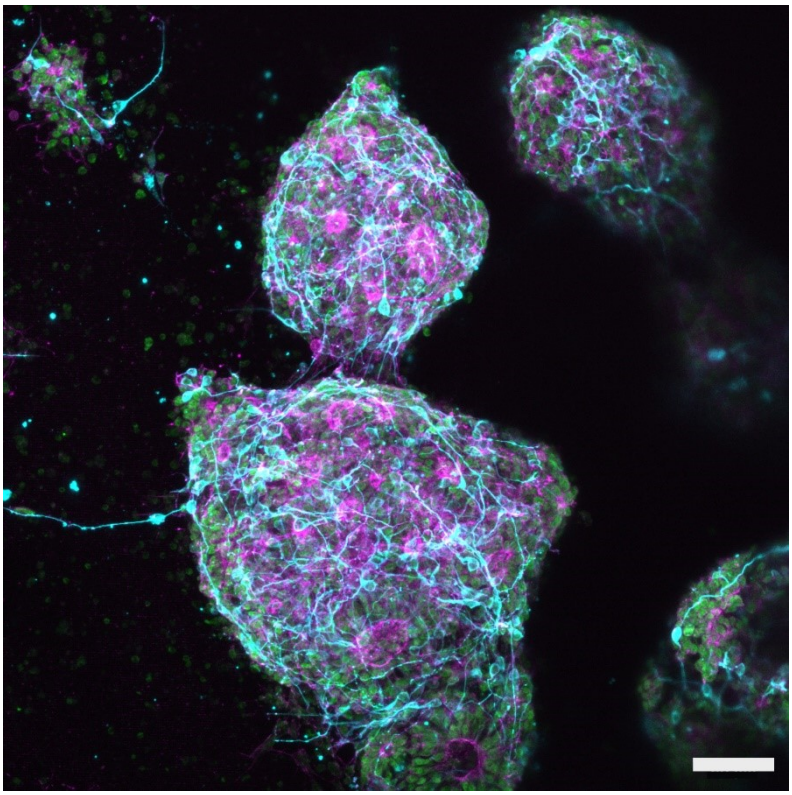


Fig. 3.13: *Representative image of mESC colonies seeded on a nanoneedle substrate, with soluble Shh at a concentration of 5 nM, fixed and stained after 2 days. The formation of axons is evident, with connections forming between cells and across colonies. Cyan = Tuj1, magenta = actin, green = Sox2. Scale bar = 60 μm.*

3.3.1 Initial differentiation of mESCs on substrates

The decision was made to move on to testing the material system in directing the differentiation of mESCs, since ELISA release assays had confirmed morphogens could be maintained on the substrate (section 2.4.1). For initial experiments, standard protocols from the Briscoe Lab were followed, with cells being seeded at day 3 and fixed at day 5 (see section 3.2.1). However, before testing Shh as a surface-bound cue, it was necessary to confirm that cells could survive on the silicon substrates. Initial tests were conducted without the heparin/chitosan bilayers added to the surface, to observe how cells would respond to uncoated silicon.

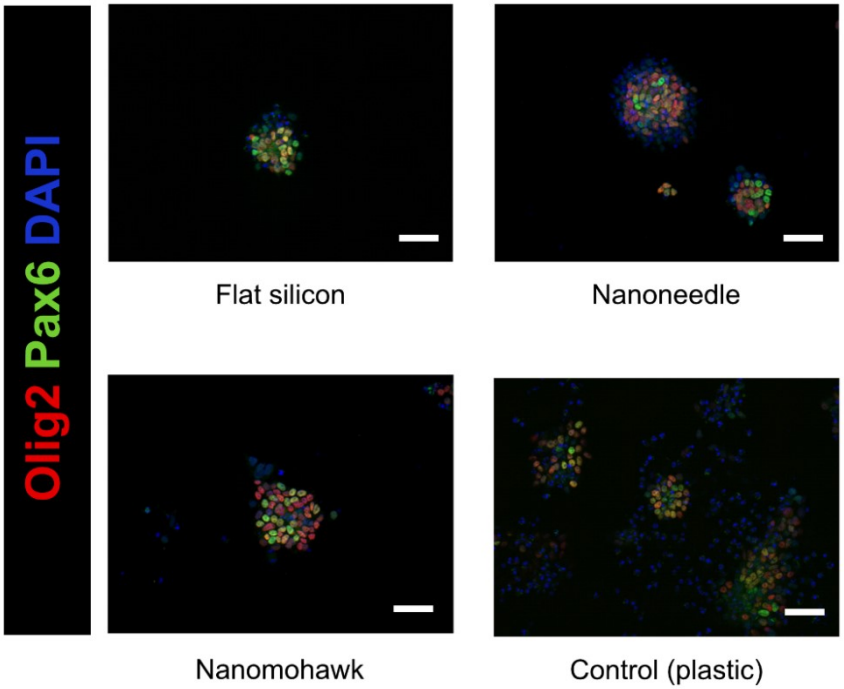


Fig. 3.14: *Differentiations carried out on non-coated silicon substrates, with soluble SAG as a ventralisation cue. Cells were seeded at day 3 and fixed at day 5. No significant difference was noted across the nanoneedle or nanomohawk substrates. However, a lower cell density was noted on the flat silicon substrates. Having been treated with SAG (500 nM) in the media, nuclear Olig2 was observed across all conditions. Scale bars = 50 μm.*

When cells were seeded on the substrates with SAG in the media (soluble SAG was used since this experiment was investigating the response of cells to the uncoated silicon), differentiation was seen to occur (Figure 3.14). The cells on uncoated flat silicon, nanoneedles and nanomohawks (a modified version of the nanoneedles that were initially tested) substrates were seen to behave in much the same way as the tissue culture plastic condition, with colonies of cells present that were Olig2-positive (meaning nuclear Olig2 was present, indicating the presence of ventral motor neuron progenitors). However, the cell density was extremely low across all conditions, particularly for the flat silicon. This indicated that some form of surface treatment would be required to enhance adhesion and proliferation of cells on the surface.

The heparin/chitosan layer-by-layer coatings were subsequently introduced as a means to electrostatically bind the proteins to the surface. Although the chemistry was well documented in literature, it was still necessary to confirm the optimal protein loading concentration that would be carried forward for the printing concentration in future experiments. An investigation into the optimal protein treatment concentration was prepared, with three different concentrations of Shh loaded onto silicon substrates. Shh coatings with concentrations ranging from 50 nM to 200 nM were chosen and generated via incubation overnight. For the control condition, 5 nM Shh was supplemented into the medium (the standard positive control condition used in cell culture as a soluble factor). The concentration was drastically increased in the coatings relative to the control because it was expected that as the protein was localised at the surface, a significantly higher amount would need to be loaded in order to have a similar effective concentration as the soluble protein. Cells were seeded at day 3 on the coated substrates and were fixed and stained for Olig2/Pax6 at day 5.

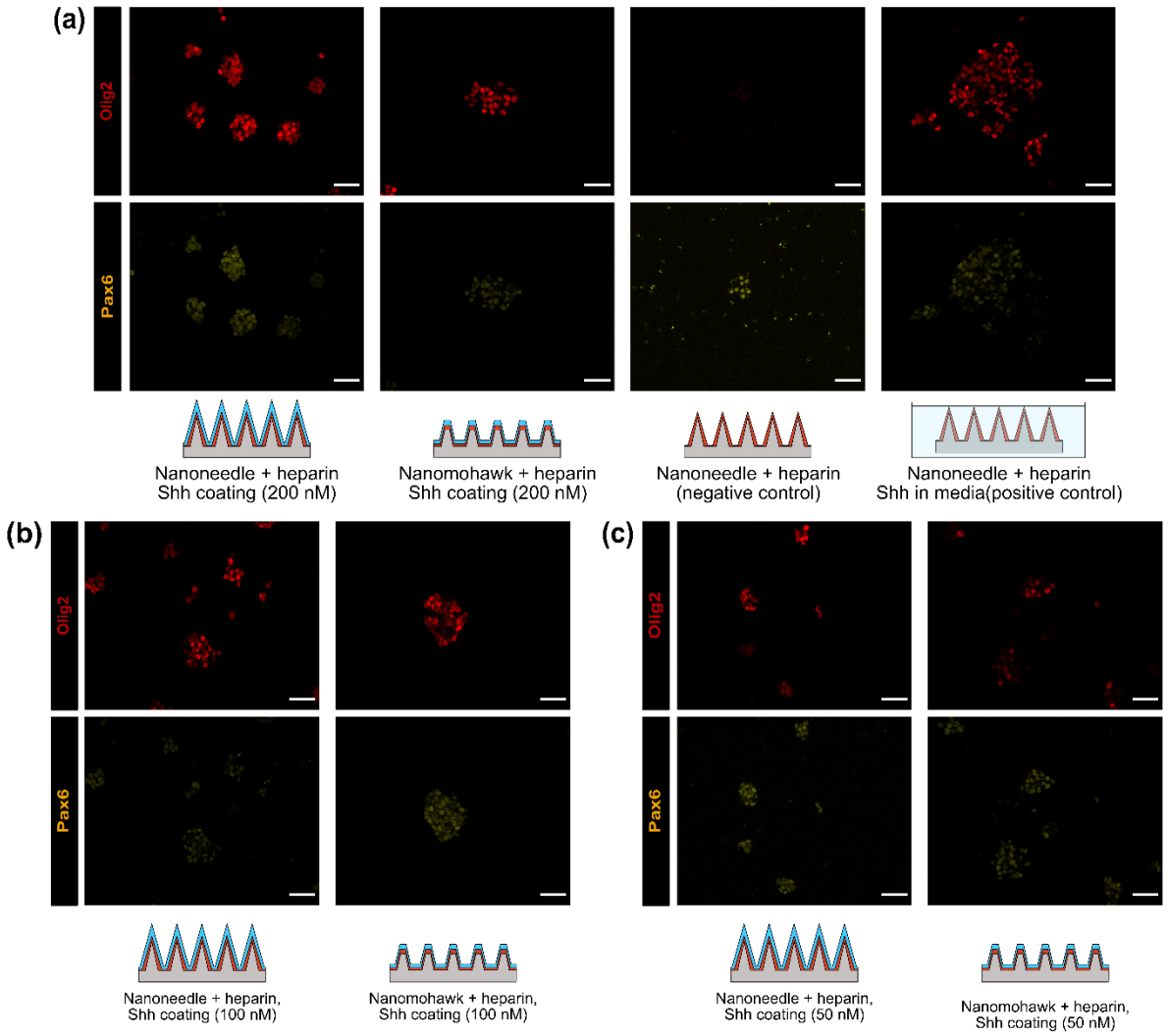


Fig. 3.15: *Shh coating concentration study. All conditions showed a ventral response to the surface bound Shh when seeded at day 3 and fixed at day 5, but the 200 nM coating in (a) was the strongest and most consistent across substrates, relative to (b) 100 nM and (c) 50 nM. As such, 200 nM was chosen as the concentration to be used going forward in the printing of Shh.*

An Olig2 response was seen across all coating conditions, for both nanoneedles and nanomohawks. However, an improved cell density was seen across nanoneedle substrates, and as such these were chosen as the substrate for all future experiments (unless otherwise stated). At 50 nM, an inconsistent Olig2 response was observed (some positive cells in larger colonies, mixed populations of positive/negative cells),

which implied that although the Shh pathway was being activated, it was not particularly efficient. For the 100 nM condition, the response was much stronger, although there was still some inconsistency across colonies on the substrate. The 200 nM coating seemed to give the strongest, most consistent Olig2 response across cell colonies, indicating efficient differentiation of motor neuron progenitors. The response here was a strong indication that the cells would be capable of responding to surface-bound printed proteins. From this data, the Shh concentration of 200 nM was chosen going forward as the bio-ink printing condition, with nanoneedles to be used as the printing substrate.

3.3.2 First inkjet-printed morphogen tests

Inkjet printing of the protein was carried out as described in the methods section, with initial tests being carried out using the Canon printer. For Shh, the protein was made up from a stock solution on the day of printing at 200 nM. The data shown in Figure 3.16 represents a gradient substrate with 10 overprints of Shh (reprints of the same pattern on top), with cells seeded at a density of 1×10^6 cells/well.

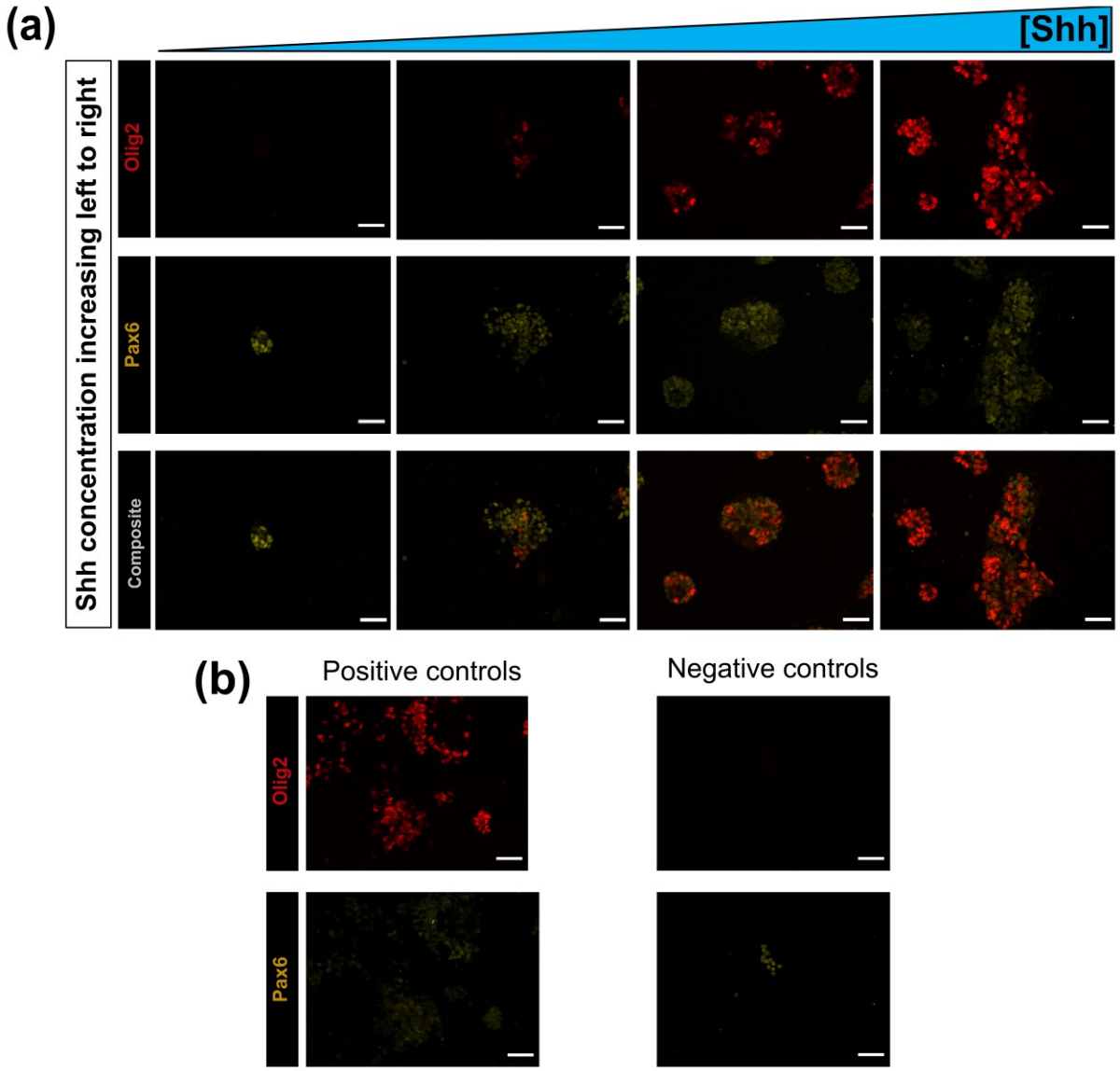


Fig. 3.16: *The first observed response to a printed Shh gradient on nanoneedles (200 nM bio-ink concentration, 10 overprints carried out per substrate using the Canon printer), with cells seeded at day 3 and fixed at day 5. (a) A strong increase in Olig2 signal was seen with increasing effective Shh concentration, indicating the emergence of motor neuron progenitors at higher positions on the gradient. (b) In the positive controls, a similar response was seen to the cells at the high levels of the gradient. Negative controls showed almost no Olig2 signal present beyond some background/debris, while Pax6 was clearly present. Scale bars = 50 μm.*

An increasing Olig2 signal was observed as the position of the cells increased along the gradient. This indicated that as the local Shh concentration increased, the cells responded accordingly. Pax6 was seen to decrease slightly, although it was still present. This was as expected, since it is extremely unlikely that the surface bound Shh would be enough to generate the most ventral subtype, p3 progenitors at this timepoint. All other progenitor cell types would be expected to have some level of Pax6 present, although it would be expected to decrease somewhat as the gradient increased as a result of the increasing ventral character of the cells. If the cells were left for longer on the surface of the substrate, the Pax6 signal strength would be expected to decrease further (this time dependence will be investigated at a later point, section 3.4.3). The presence of nuclear Olig2 indicated that motor neuron progenitors were being generated, a benchmark for a successful spinal cord on-a-chip model. Olig2-positive cells are the second most ventral neuronal subtype in the neural tube. This was the first demonstration of a ventral response to our inkjet-printed gradients, and showed that the protein retained its activity after the printing process with the Canon printer without degradation.

Although this result was promising, the antibody panel of Olig2/Pax6 gave a relatively narrow output for positive ventral responses, and only clarified that motor neuron progenitors were being generated. Ideally, more information on the presence of other ventral progenitor subtypes would be obtained, which are equally as important in developing the spinal cord model. For instance, p2 progenitors might be present also, but do not express Olig2 and so would not be observed. For any comprehensive model of the spinal cord, a larger transcription factor readout would be needed to ensure that neural systems are forming that represent the *in vivo* neural tube.

To improve the breadth of the ventral responses detected in the immunofluorescence imaging, the transcription factor network of the neural tube (Figure 3.12) was again considered. Nkx6.1 was chosen as a candidate transcription factor that would span the ventral third of the neural tube, and so would provide more data on the response of

the cells to the gradient than just Olig2 alone as a ventral readout. To investigate this, gradients of Shh were again printed with the Canon printer (200 nM, 10 overprints). Cells were seeded at day 3 of the differentiation process as before, fixed at day 5 and stained for Pax6 and Nkx6.1.

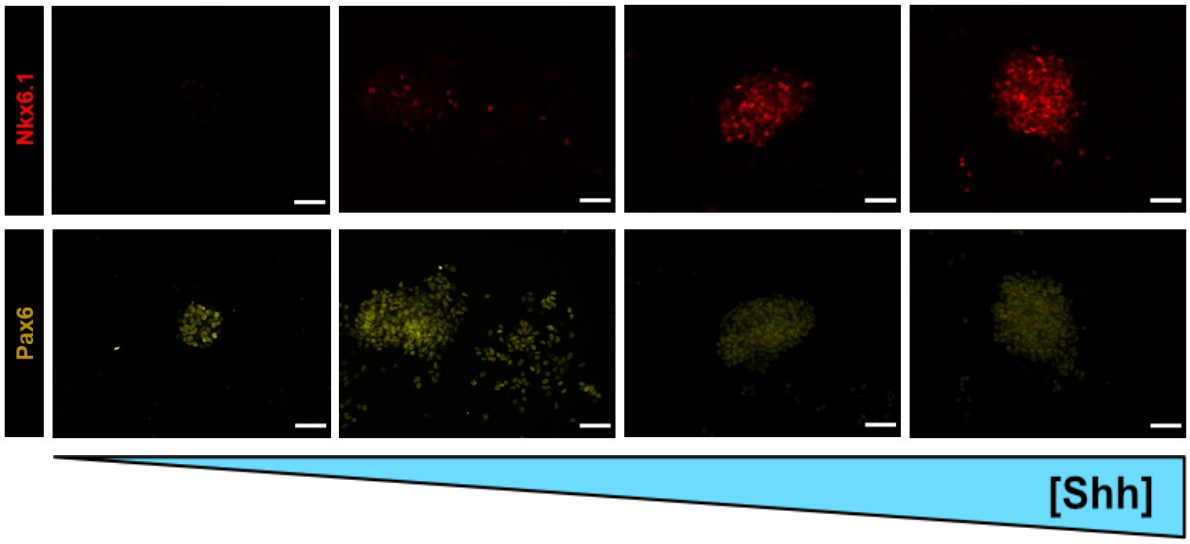


Fig. 3.17: *Response of mESCs to a printed gradient of Shh (200 nM, 10 overprints, Canon printer), with Nkx6.1 used as a ventral marker readout. Cells were seeded at day 3 and fixed at day 5. The ventral signal was slightly more widespread on the gradient than that observed with Olig2 previously, as Nkx6.1 is present in the ventral third of the neural tube (which includes motor neuron progenitors, as well as p2 and p3 progenitors). Scale bars = 50 μm.*

As the presence of Nkx6.1 was providing information on a wider spectrum of ventral neural cell types, this was added to the panel of antibodies for future experiments. By identifying which of Pax6/Olig2/Nkx6.1 were mutually exclusive in each cell colony in immunofluorescence images, it could be determined which ventral progenitor subtypes were present at each point on the gradient. In doing so, it would offer a more complete model of the ventral half of the neural tube, within the limitations of immunofluorescence.

In the above experiments, cells were seeded at a density of 1×10^6 cells per well. However, the cell density and surface coverage were consistently quite low when imaged, which would be an issue for accurately analysing the response to the printed morphogens. A higher density with more complete coverage would give a more continuous response to the printed patterns, and so would give a more robust dataset of the response of the cells on the substrate. As such, seeding density was increased for all experiments from this point to 4×10^6 per substrate (unless otherwise stated).

3.3.3 Changing the seeding timepoint

Along with the seeding density, it was also necessary to consider the potential future experiments where BMP4 and Shh gradients would be combined on a single substrate to map the entire DV axis. Previously, Shh activation was initiated at day 3 of the differentiation and allowed to act for two days before fixing at day 5. However, BMP4 has been shown in the Briscoe lab to initiate dorsal differentiation from day 5 to day 7. This difference in treatment time would cause issues if cells were seeded at day 3, as the dorsal activation would be initiated at the wrong timepoint, and so the formation of the dorsal-ventral axis could not take place correctly. As such, it was necessary to modify the Shh protocol to account for this time difference. Two extra days of maintenance in N2B27 media/retinoic acid were to be added (day 3, day 4) after treatment with bFGF on day 1 and bFGF/CHIR on day 2. Shh activation would then be induced at day 5, and cells would be fixed at day 7. The intention was that the extra days in retinoic acid media would maintain the cells in a neural fate, but would not direct them towards any specific neural subtype. To investigate the impact this change would have on ventral differentiation, tests were carried out in tissue culture plastic, with one and two extra days in RA media both being included. Dorsal markers (Olig3 and Msx1) were included in the antibody panel along with Nkx6.1, to confirm that the extra RA treatment did not induce dorsal fates. Both cell populations were fixed and stained two days after exposure to Shh as before, but in this case the Shh

was spiked into the media, since this was a test of their responsivity and not the surface bound gradients.

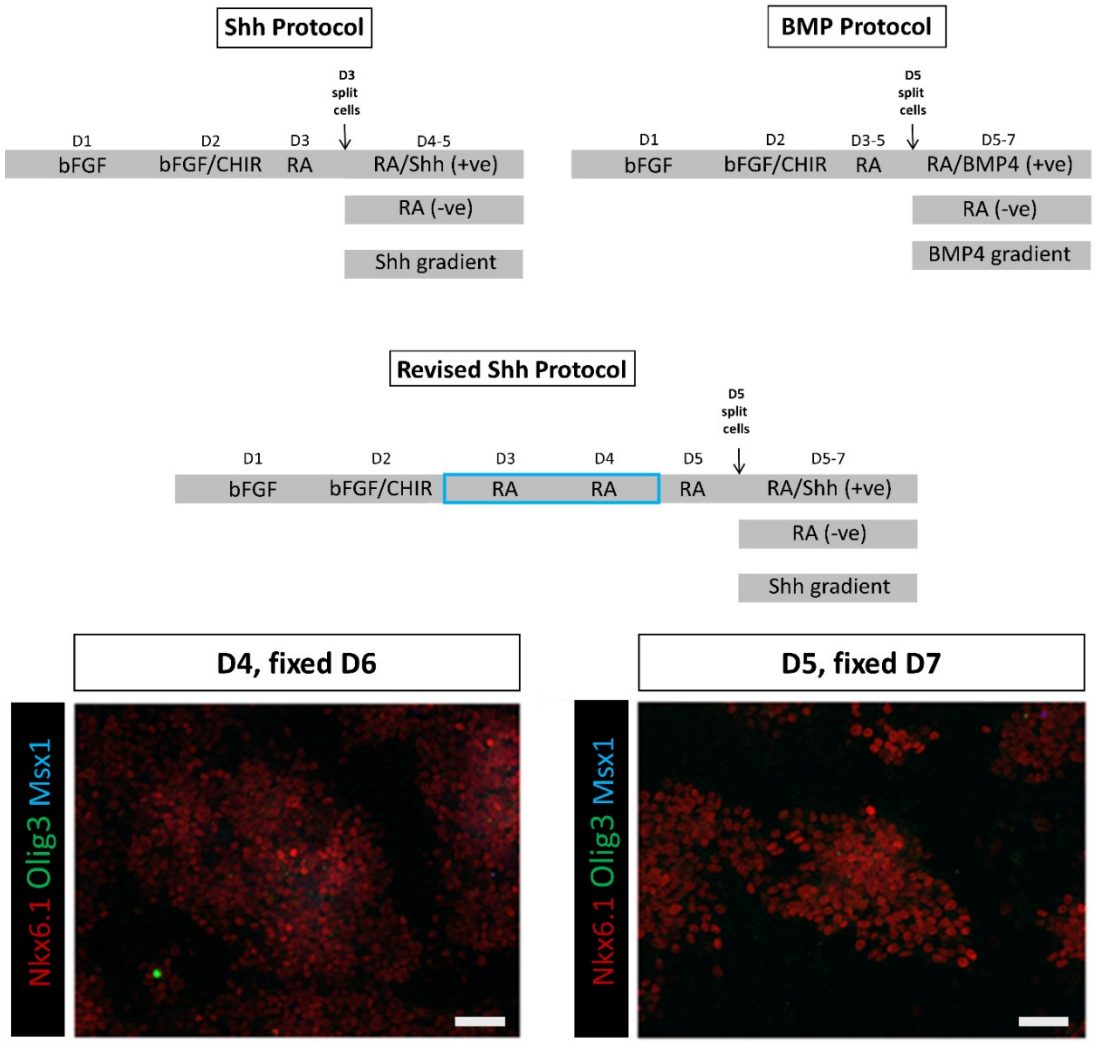


Fig. 3.18: *Revised Shh protocol, to better align with the BMP4 treatment protocol that would be used to induce dorsal fates. Cells are shown with one (left) and two (right) extra days of retinoic acid treatment. D4/D5 refers to the timepoint at which Shh was introduced. Both populations showed strong ventral responses to the Shh treatment (Nkx6.1, red), and the cell density did not seem to be adversely affected by the later treatment compared to previous experiments. No significant amount of dorsal cell types were detected (Olig3, green, and Msx1, blue). Scale bars = 50 µm.*

These data indicated that the extra days of maintenance in N2B27/RA did not adversely affect the differentiation process, and did not seem to prevent the mESCs from gaining ventral character when Shh activation was introduced at day 4 or day 5. This was an extremely important finding, as it confirmed that future experiments could indeed be carried out to map the entire DV axis on a single printed substrate. As such, all future Shh gradient experiments would be carried out with this extended timeline of seeding at day 5 and fixing at day 7 of the differentiation process.

Having expanded the ventral antibody panel to include Nkx6.1, and also having confirmed that cells were responsive to Shh treatment after two extra days in N2B27/RA conditions, a gradient experiment was designed to attempt to recapitulate previous results shown with printed patterns, at this later timepoint. The seeding density was set at 4×10^6 cells per substrate as discussed previously.

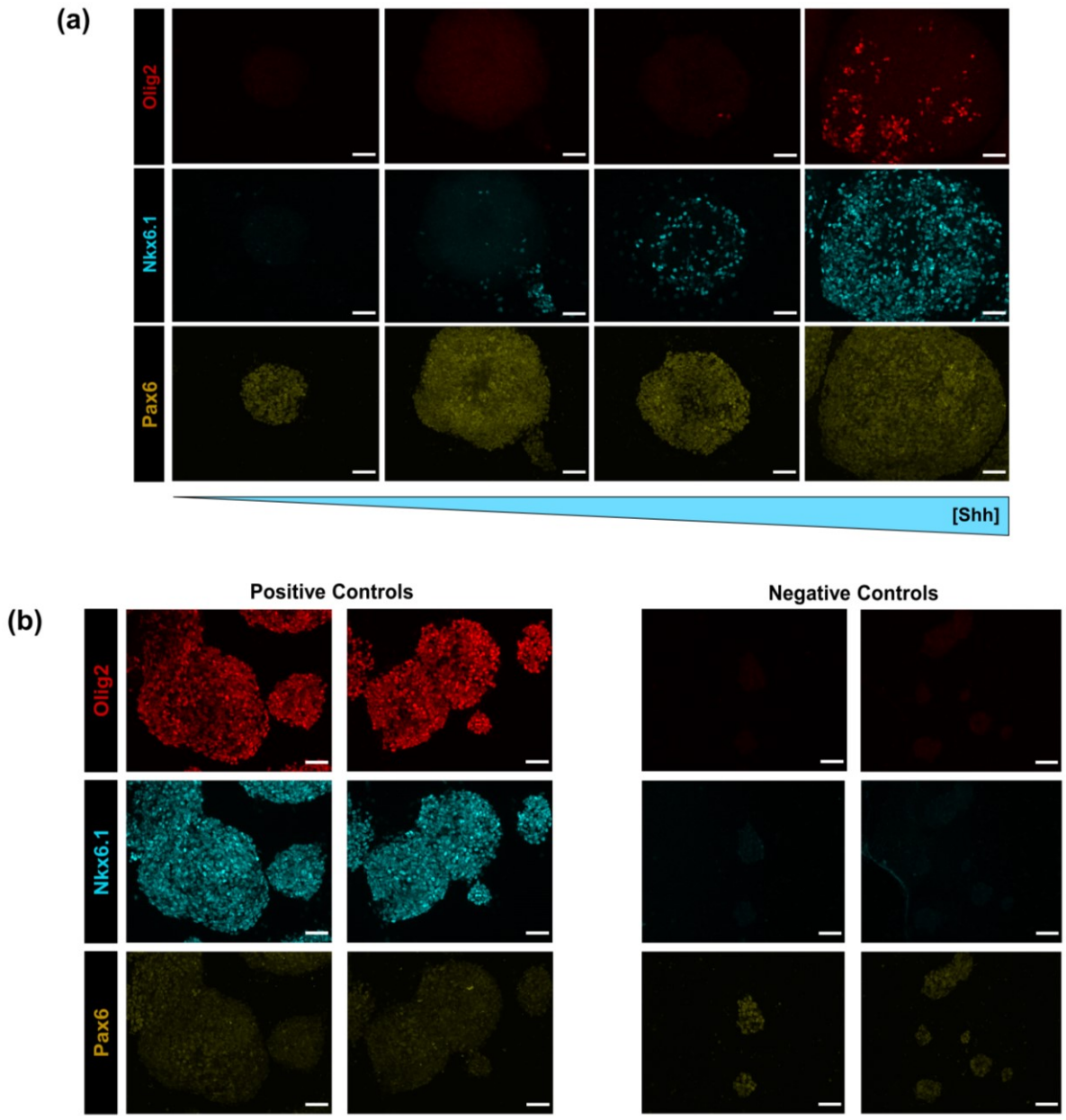


Fig. 3.19: (a) *Response to Shh printed gradient when mESCs were seeded at day 5, and fixed at day 7 of the differentiation process. A strong ventral response is again seen at higher positions of the gradient, with nuclear Nkx6.1 across almost all cells from the midpoint onwards. Olig2 is present, indicating the generation of motor neuron progenitors. Pax6 was not seen to change drastically across the gradient. (b) The positive control showed both Nkx6.1 and Olig2 nuclear signal across most cells, with little Pax6 signal. The negative control showed no presence of ventral markers. Scale bars = 50 μm.*

After staining, the gradient response was again present, with a clear increase in ventral markers as the local effective concentration of Shh increases. Nkx6.1 was widespread at the higher end of the gradient, showing that most cells at that point were p2, motor neuron or p3 progenitors. Olig2 was seen to be present at the high end of the gradient, suggesting that there was a population of motor neuron progenitors present. This is consistent with there being a narrow band of motor neuron progenitors in the neural tube, although the non-uniform nature of the signal may have been because the cells had not been exposed to a sufficient level of Shh activation. A prolonged exposure to the Shh would most likely see an increase in Olig2 signal, and more cross repression of signals such as Pax6, which would indicate the emergence of the most ventral class of cells, p3 progenitors. However, as a model for the ventral neural tube, this was sufficient to show that the printed morphogen platform was viable for generating controlled populations of ventral neural subtypes, with spatial control over the level of ventralisation occurring.

While single field of views can give an indication of the response to a printed gradient, the relatively small number of cells captured per image limits the detail obtained on the neural population as a whole. As such, the mounting method was modified to be suitable for use with the widefield microscope. As this apparatus has a motorised stage and tiling function, an entire substrate could be imaged and stitched to give a more accurate visualisation of the response to printed patterns.

The tiled image below gives a more complete visualisation of the ventralisation occurring in response to the printed Shh gradients. The Nkx6.1 signal emerges slightly before the middle of the printed gradient, which is consistent with the positioning of Nkx6.1 in the ventral neural tube. The density here is also seen to be much improved on previous experiments, indicating that the 4×10^6 seeding density was sufficient to significantly increase surface coverage.

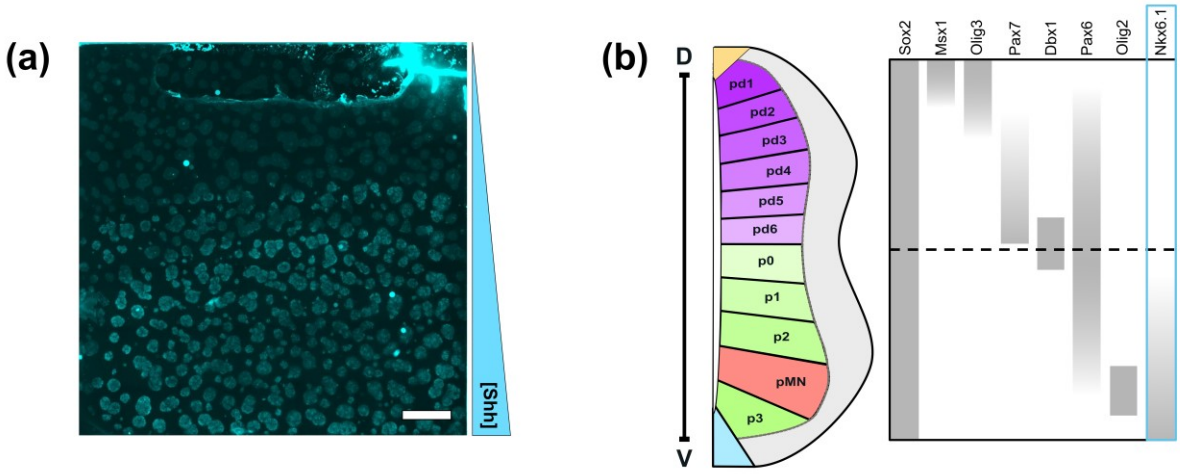


Fig. 3.20: *(a) Tiled image of a representative nanoneedle substrate, with cells seeded on day 5/fixed on day 7 on an Shh gradient (10 overprints of 200 nM Shh bio-ink, with the Canon printer). Cyan = Nkx6.1. The ventral gradient response is seen here to be strong, and to emerge approximately halfway up the gradient pattern. (b) This compares well to the Nkx6.1 transcription factor pattern that would be expected to emerge in the ventral half of the developing neural tube. Scale bar = 1 mm.*

3.3.4 Printer change, linear vs. exponential gradients

At this point in the project, a number of practical and technical challenges in ensuring repeatable prints were encountered with the Canon-printed substrates. The reasons for these issues are discussed in section 2.4.3. These difficulties led to the change to the BioDot AD3220 printing platform, which offered drop-on-demand capabilities and fine control over pattern generation. This led to the introduction of changes to the printing pattern being used. The capability to pattern each location on the substrate individually meant that a sharper gradient could be generated, to illicit a more drastic response from cells seeded on the pattern. For prints using the BioDot printer, the protein was printed at a concetration of 500 nM. All other conditions were maintained from previous experiments, except Pax6 was no longer used (since no significant changes were observed in cells across gradients in previous experiments).

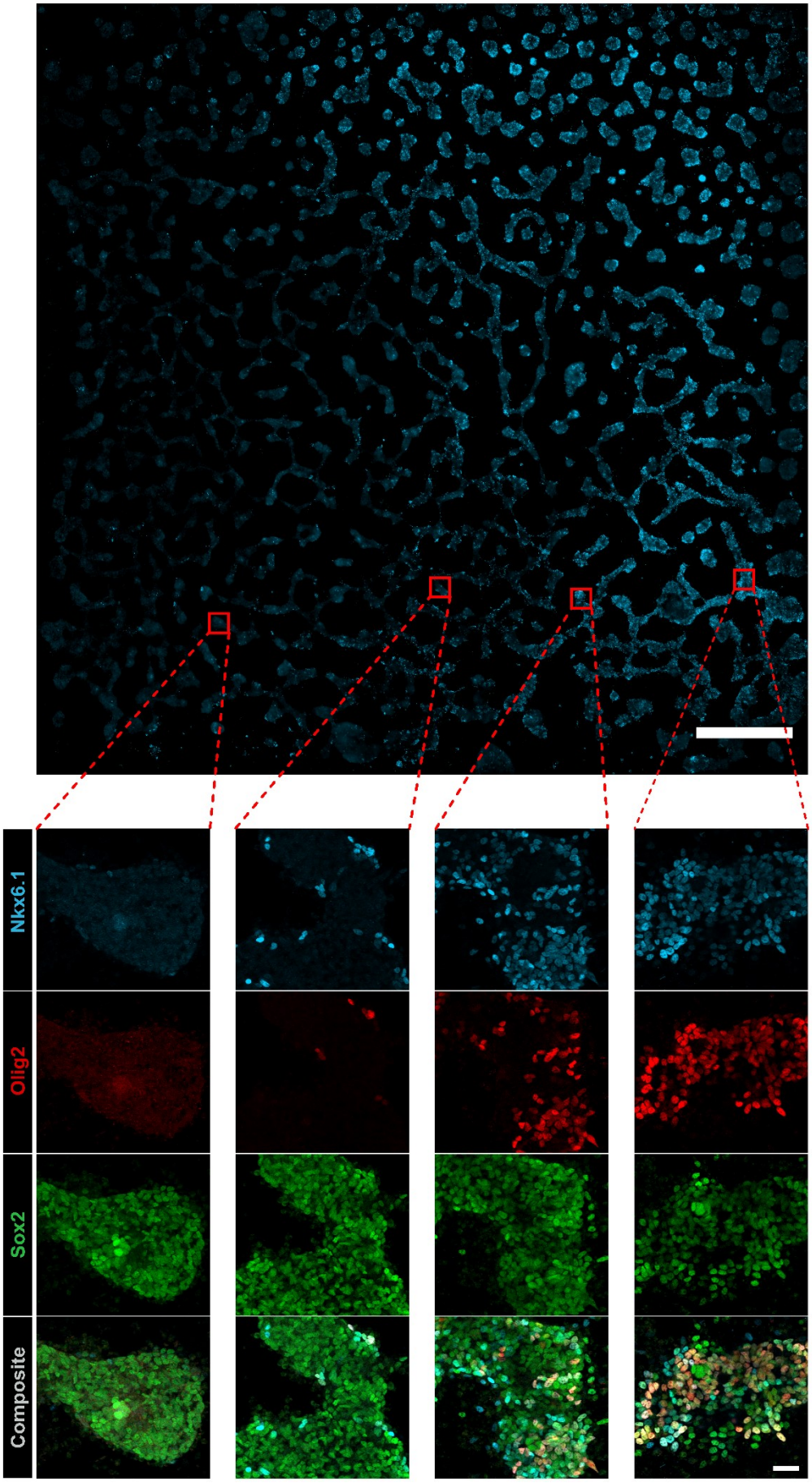

Nkx6.1
Olig2
Sox2
Composite

Fig. 3.21: *(Top) A representative tiled image of a nanoneedle substrate with an exponential Shh gradient, with mESCs seeded at day 5 and fixed at day 7. Nkx6.1 signal (shown in cyan) indicates that there is a clear graded ventralisation present on the substrate as a result of the printed pattern (increasing Shh concentration from left to right). Scale bar = 1 mm. (Bottom) Higher magnification confocal images of individual channels. Ventral markers (Nx6.1, cyan and Olig2, red) further demonstrate the graded response of the cells to the printed Shh. Scale bar = 50 μm.*

Upon imaging, the Nkx6.1 and Olig2 channels showed a clear graded response, with both transcription factors following a similar expression pattern (Figure 3.21). Nkx6.1 appeared to emerge earlier and is slightly more widespread than Olig2, which is to be expected from the transcription factor network of the neural tube *in vivo* (Figure 3.12).

It appeared that there was no obvious saturation of signal at higher regions of the substrate, indicating that 9 drops (maximum number used here, at the high end of the gradient) at a volume of 5 nL per mm^2 was viable for future investigations. There was however a slight drop in the intensity of both ventral markers at the upper end of the gradient. This was likely as a result of the droplet wetting mentioned previously. As the final column of drops had only one neighbouring column, and a region with no printing occurring beside it on the substrate surface, the wetting at this point will have caused slightly less protein to be present at the extreme end of the substrate. As a result of the encouraging data observed from the initial BioDot printer gradient tests, this experimental configuration was carried forward for a larger scale study with the image analysis pipeline.

3.3.5 Imaging pipeline analysis for exponential Shh gradients

Data analysis and visualisation from this section was carried out by Dr Stuart Higgins, with data being adapted as required by the author, unless otherwise stated.

As the immunofluorescence imaging showed an apparent ventral response to the printed exponential Shh gradients, the substrates were subsequently investigated with the image analysis pipeline, to quantify the effect that the printed pattern was having on the cells seeded on the substrates.

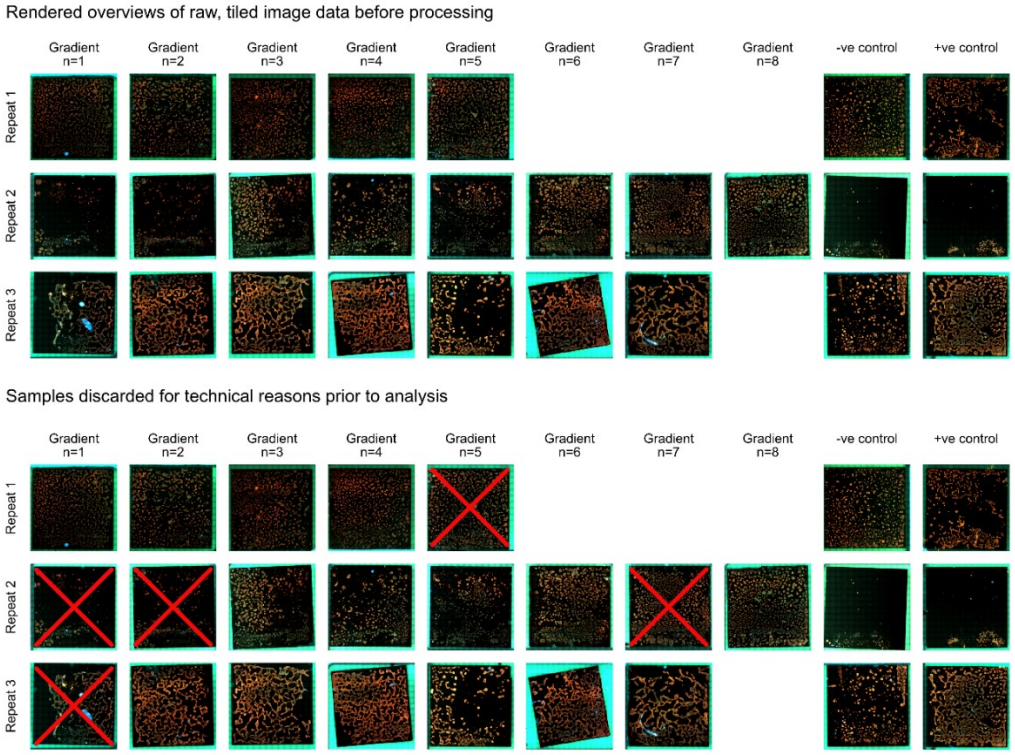


Fig. 3.22: *Overview of total substrate set used in this experiment. Three repeats of n ≥ 5 were initially included, but this was later decreased to n ≥ 4 due to technical issues with some of the substrates. Substrates were discarded as a result of issues with coatings or due to substrate damage, before any analysis or processing was carried out. Figure by Dr Stuart Higgins.*

As an input for the pipeline, each substrate across three repeats was imaged and tiled at 20X magnification on the widefield microscope (Axio Observer, Zeiss), with three

transcription factors being captured: Sox2, Nkx6.1 and Olig2 (Pax7, a midline neural tube marker, was also captured. However, very little nuclear signal was detected across any condition, and so this transcription factor will not be discussed in this work). For the gradient condition, five or more substrates were included in each repeat. Substrates that had technical errors (e.g. handling damage, or poor layer-by-layer coating) were excluded from any downstream analysis. Ultimately, four or more gradient substrates were included for each experimental repeat, plus one positive and one negative control. Figure 3.23 shows examples of the four pixel classes identified in a single field of view imaged during this experiment.

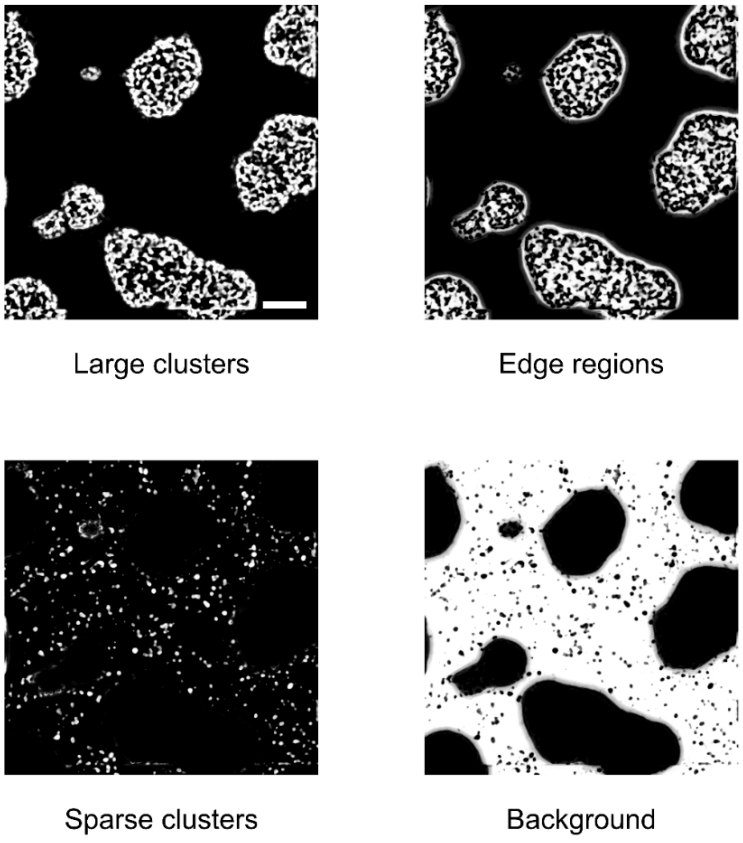


Fig. 3.23: *Representative images of the pixel probability masks generated by ilastik. Four feature classes were identified: large clusters (bright objects within the large colonies), edge regions (regions of diffuse signal between bright objects in the colonies), sparse clusters (mostly individual objects on the substrate surface) and background. Scale bar = 100 µm.*

Data cleaning and processing

Data from each image were rotated to align the gradient axis with the print direction and correct for any rotational offset introduced during the imaging process. Post-rotation another cropping step was performed to create a consistently sized, rectangular field of view across all substrates.

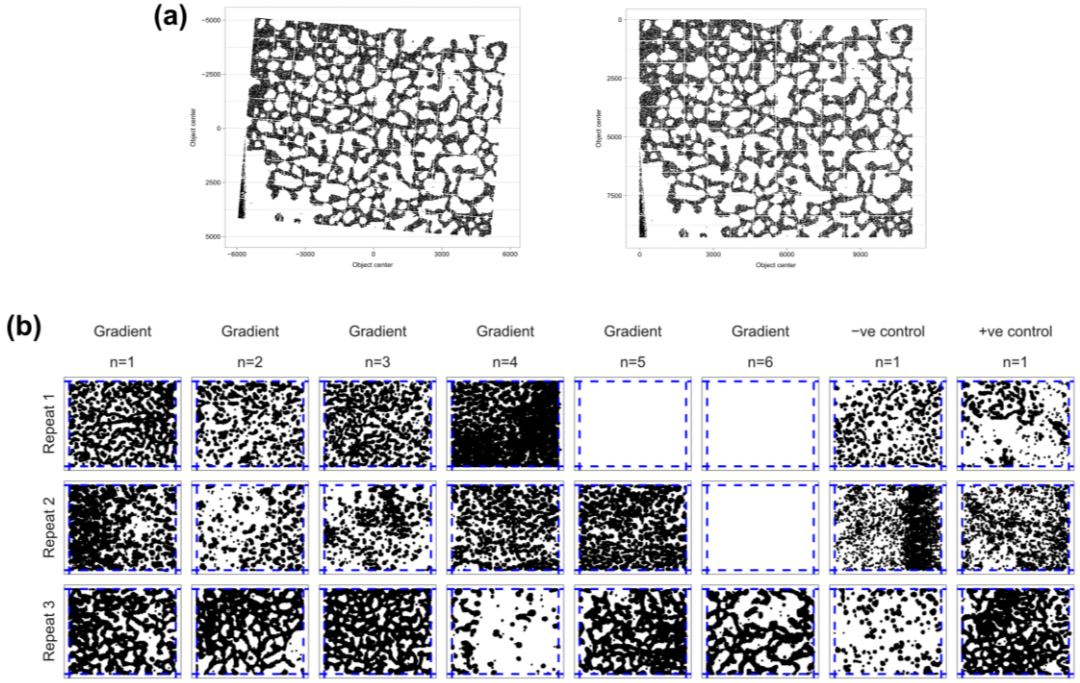


Fig. 3.24: *Representative images from the data cleaning steps of the analysis pipeline. (a) Features defined as large clusters (objects within large colonies) are used as an example here. It was necessary to rotate all the tiled images to ensure that the gradient was increasing from bottom to top of the substrate. A region of interest was then defined to avoid edge regions and the point at which the holder had contacted the surface. (b) This process was repeated for each of the 21 substrates in the dataset, with the region of interest indicated by the blue dashed lines.*

Plots of pooled signal intensities

As a means of summarising the entire dataset of feature types and their responses to the printed exponential gradients, each substrate was initially visualised individually.

The nuclear signal intensity for Olig2, as a motor neuron progenitor marker, is an ideal metric for the effectiveness of the gradient response, since this signal would only be present in the nuclei of motor neuron progenitors, which should occupy a narrow band in the ventral end of the neural tube. A fitted model is shown in the plots in Figure 3.25 through to Figure 3.27, created using the raw mean intensity data to describe the signal intensity of the ventral markers at each point along the gradient.

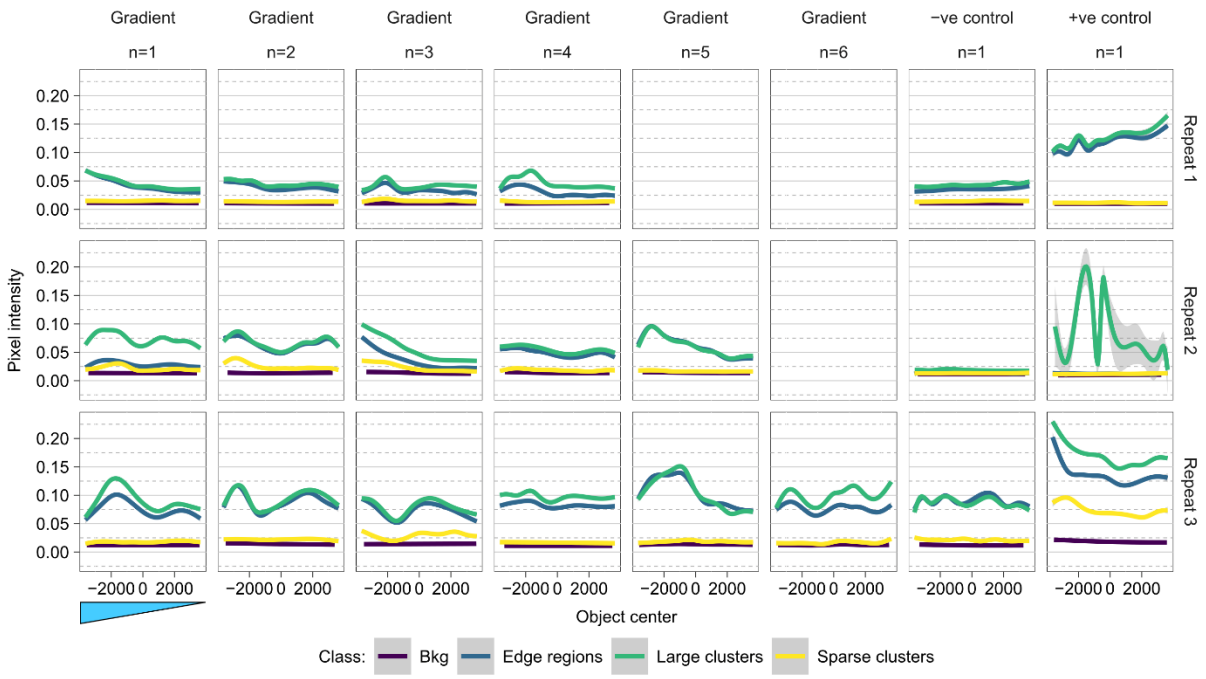


Fig. 3.25: *Model of the mean Olig2 intensity along the printed pattern for each substrate, used to visualise the response of each feature class to the gradients. Gradients are increasing from positive to negative values along the x-axis of each plot. Across almost all conditions, the sparse clusters behaved similarly to the background (Bkg), giving little to no signal. The edge regions (regions between cells in the colonies, out of focus signal) were seen to map closely to the signal in the large cluster features for the most part, while large cluster features gave the largest signal-to-background ratio.*

Across the models for the signal intensities in Figure 3.25, a general gradient trend was observed, although it was noisy and somewhat inconsistent. As the sparse clusters showed a low signal-to-background ratio, the decision was made to remove this

feature class from future discussions for this work. The edge regions (out of focus cells) mapped quite closely to the trend observed in the large cluster features, although the signal-to-background ratio was slightly lower in almost all the datasets. As such, the large clusters were chosen as a descriptor of the gradient response, since they gave the largest intensity and least noise relative to the other feature types.

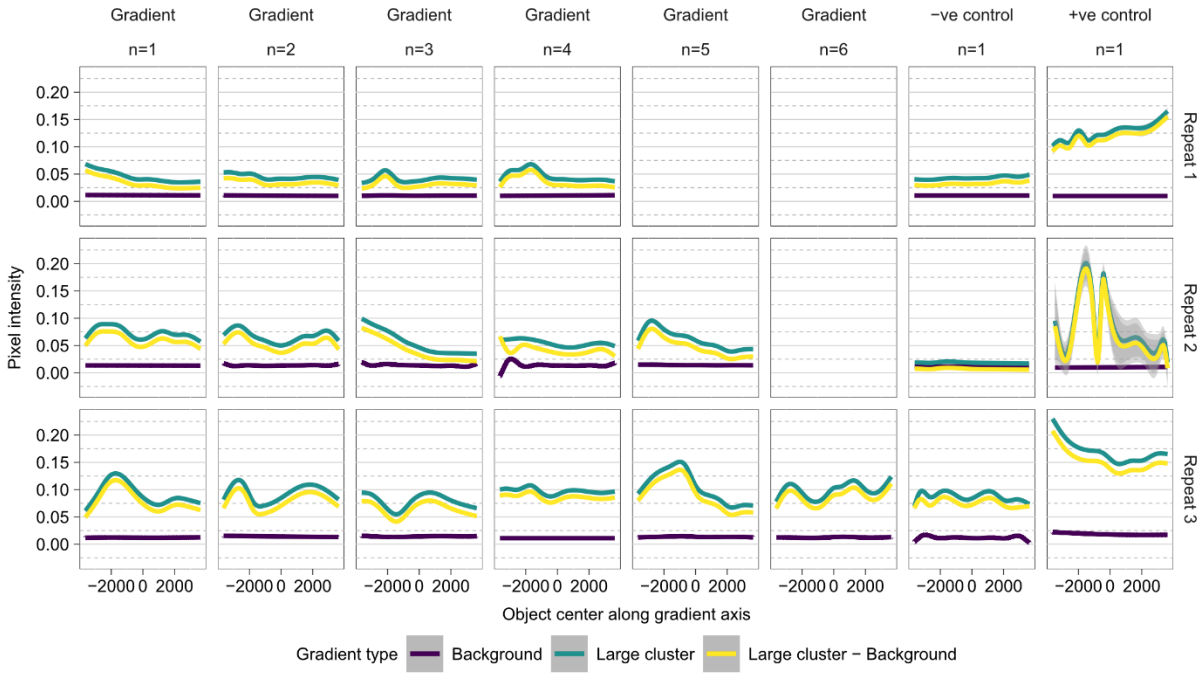


Fig. 3.26: *Model of the mean Olig2 intensity along the printed pattern for each substrate, with and without background subtraction. The background signal did not appear to contribute substantially to the large cluster signal, as seen by the close mapping of the large cluster (green) and large cluster – background (yellow) lines in each plot. Envelope represents a 95% confidence interval from the Olig2 intensity model generated.*

The background appeared to have little impact on the trend in the mean intensity (demonstrated by performing a background subtraction, as shown in Figure 3.26). This indicated that the trend being observed here was indeed as a result of a response to the printed pattern, and was not an inherent artefact present in the imaging. There was a discernible, but relatively inconsistent, increasing gradient in both ventral signals with

increasing Shh concentration. The Olig2 response in general was more pronounced, since Nkx6.1 is present in a range of ventral subtypes, and so should be expected to emerge across a broader range of Shh concentrations than Olig2. As such, the trend of an increase in Olig2 signal at the high end of the gradient on many of the substrates was an indication that the gradient was indeed inducing a spatially resolved differentiation in the cells, although perhaps not in a uniform manner across substrates.

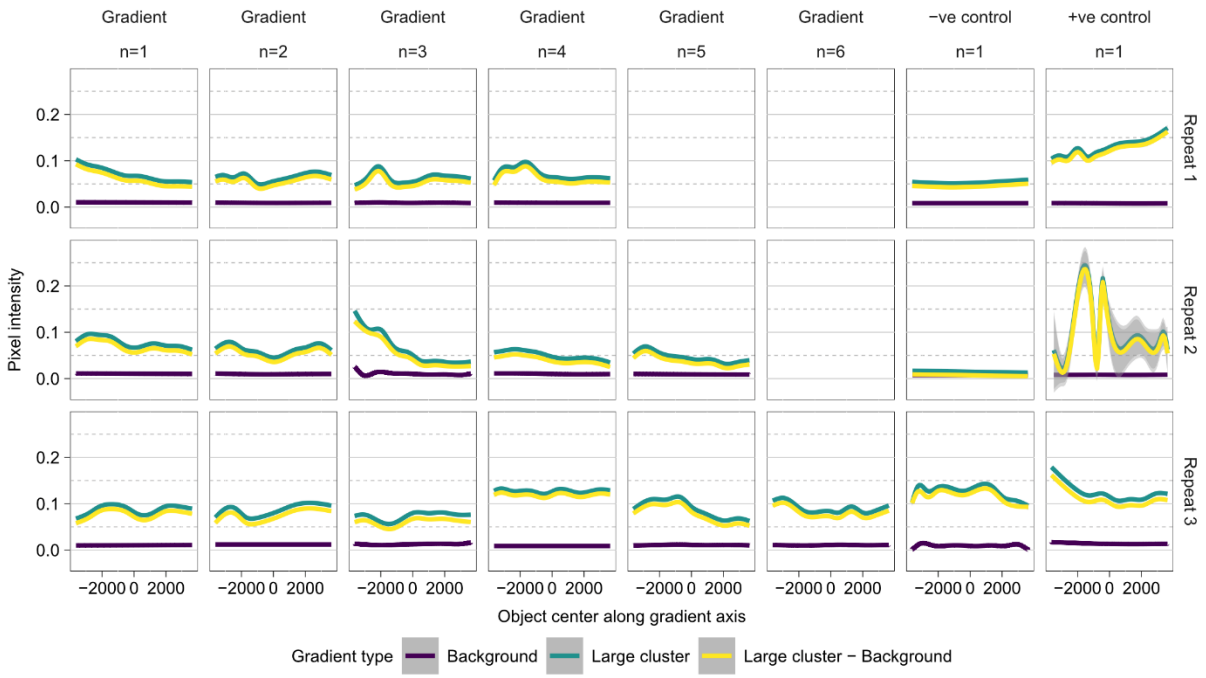


Fig. 3.27: *Model of the mean Nkx6.1 intensity along the printed pattern for each substrate, with background subtraction. The background signal was again not seen to interfere substantially with the large cluster signal here, as demonstrated by the close match between the large cluster (green) and large cluster – background (yellow) lines in each plot. Envelope represents a 95% confidence interval.*

Repeat 1 showed increasing Olig2 signal with increasing Shh concentration across most gradient conditions. The Nkx6.1 signal also increased in gradients 1, 3 and 4, although substrate 2 did not show as pronounced an increase. This, however, was not

necessarily an indication that the ventral response was not occurring. As mentioned previously, Nkx6.1 is present across a range of ventral subtypes, and so the presence of Nkx6.1, combined with an increase in Olig2 as the gradient increased, indicated that this substrate too was consistent with the behaviour expected in the ventral neural tube.

It should be noted that negative control substrates were often seen in previous experiments to have extremely low cell density, which was attributed to the role that Shh plays in proliferation. These issues can clearly be seen in repeat 2, where only a small number of clusters were observed on the negative control (as seen in the overview in Figure 3.22). The positive control too, however, showed low density in repeat 2, which indicated there may have been an issue with the cell seeding or substrate surfaces here, that may also have contributed to the low density in the negative control. The small number of features gave rise to extreme variations in the positive control, as the model was influenced more significantly by each feature. Both the Nkx6.1 and Olig2 signals on the second positive control, however, did exhibit values that were significantly higher than those observed on the gradients.

It was evident that there was a considerable amount of variation in the measurements across most conditions. In particular, repeat 3 showed large variations across the substrates within the experiment, with some (gradients 3, 4 and 6) showing no obvious gradient response. The Nkx6.1 signal across the repeat 3 controls were also very similar in signal strength, which indicated there may have been some amount of ventralisation occurring in the negative control. The Olig2 signal was considerably higher in the positive control, however, suggesting that a larger portion of motor neuron progenitors were being generated. The apparent ventral character present in the negative control, coupled with the inconsistent gradient responses observed, indicated that there may have been an issue with the cell seeding or culture in repeat 3.

To further visualise the gradient responses, 2D heatmaps were generated, by binning the mean intensities of each identified object across all experimental repeats using a 10 × 10 grid.

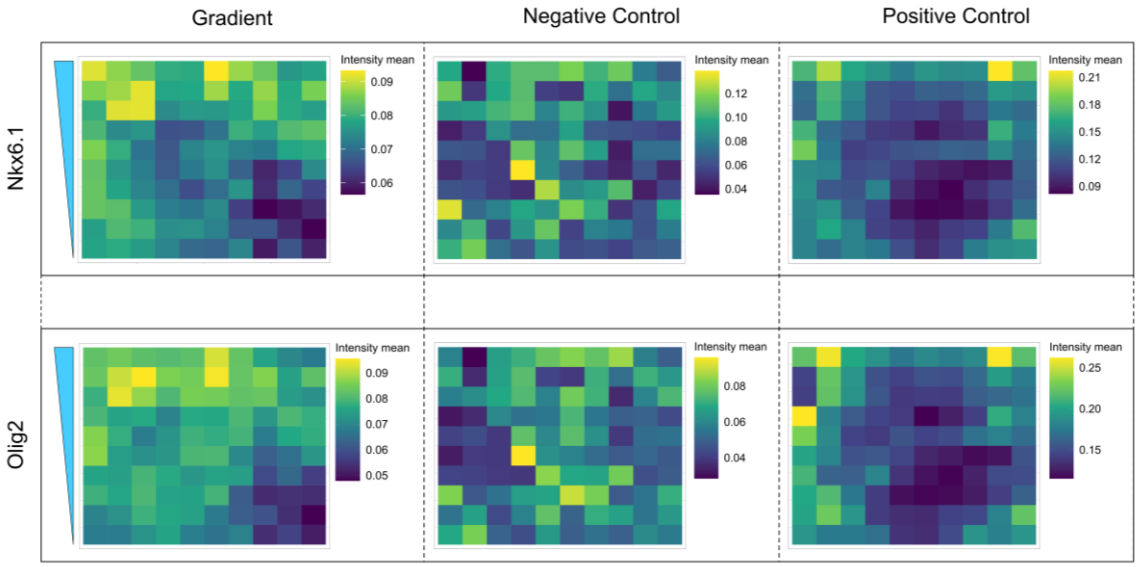


Fig. 3.28: *Mean intensity heatmaps of Nkx6.1 and Olig2, with all substrates across the repeats pooled. Each plot is scaled individually for clarity purposes. Shh concentration increases from bottom to top in the gradient plots.*

In these pooled heatmaps, there is a gradient response apparent in both the Olig2 and Nkx6.1 signals. However, the response is evidently quite noisy and inconsistent. There is also a noticeable difference between the left and right sides of the gradient substrates, suggesting there may have been a printing or wetting artefact influencing the gradient shape being generated on some of the substrates. The variation may also have been a consequence of biological variation from the cells.

The positive controls showed some variation, but the intensity values observed were consistently higher than those present at the highest points of the gradient.

The negative controls, however, showed intensity values that varied considerably between repeats. This was particularly apparent in repeat 3, where mean intensity values were obtained that were comparable to higher regions of the gradients within

that experiment. This is attributed to high levels of cytoplasmic Nkx6.1 and Olig2 in the third negative control. Although these signals were for the most part non-nuclear (and so the cells were Nkx6.1-negative and Olig2-negative), the higher cytoplasmic background still manifested as signal intensity in the analysis process. This resulted in a response being observed in the analysis that was not indicative of the actual level of ventral response (which would be determined by nuclear signal alone).

In the mean intensity plots, it did appear that there was a gradient trend present in the pooled Olig2 and Nkx6.1 signals, suggesting that ventral subtypes, and specifically motor neuron progenitors, were being generated in response to the printed gradients. However, the noisy data, combined with the inconsistency across the same position on the gradient across substrates (higher ventral signals on the left side relative to the right side of the pooled signal), warranted further investigation. To this end, individual heatmaps were generated for each substrate across the repeats using the mean intensity as a binning method.

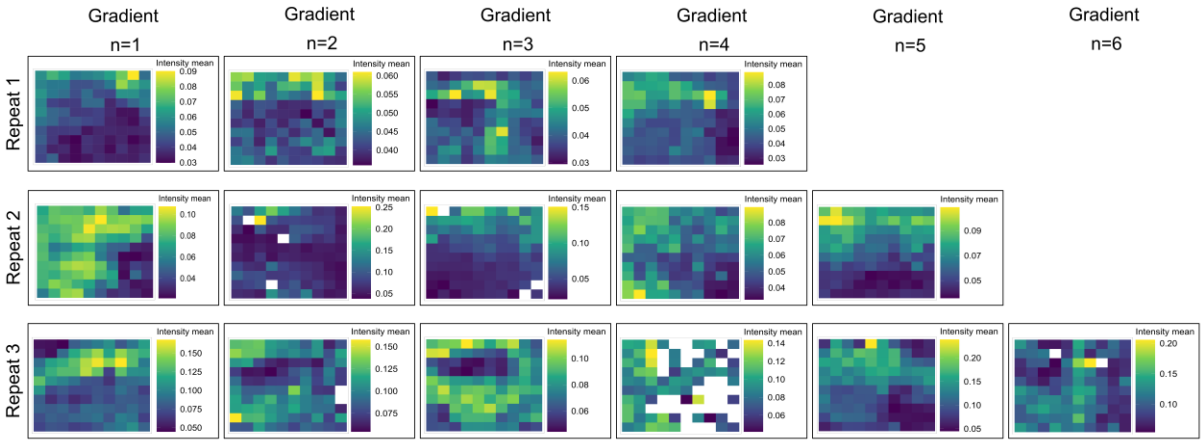


Fig. 3.29: *Binned heatmap plots of the Olig2 mean intensities for each of the gradient substrates across the three repeat experiments. Gradients of Shh are increasing from bottom to top in the printed substrates shown, with each substrate being scaled individually for clarity purposes. White squares indicate regions where no large cluster features were detected on the substrate.*

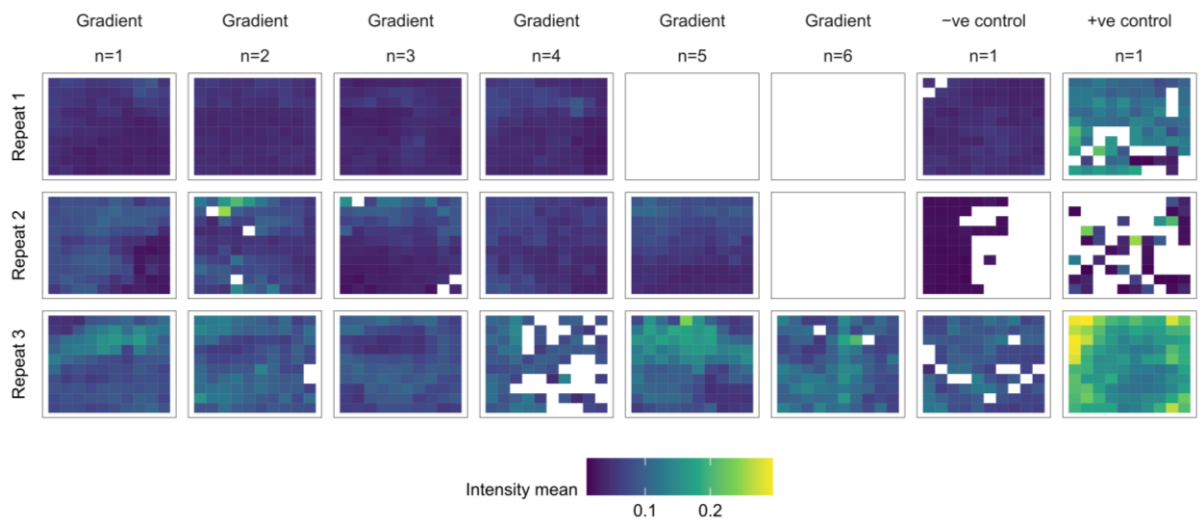


Fig. 3.30: *Binned heatmap plots of the Olig2 mean intensities for each of the substrates, with the control substrates also included. All individual plots here share a universal scale for the intensity mean. White squares indicate regions where no large cluster features were detected on the substrate. Plot generated by Dr Stuart Higgins.*

The inconsistencies in the response are more apparent here, with repeats 1 and 2 showing a trend of increasing Olig2 with increasing Shh, although as in the pooled data, there was significant noise present in the data. Repeat 3, however, was extremely inconsistent, and considerably higher in intensity that the other repeats (as emphasised in Figure 3.30). Of the six printed substrates, only gradients 1 and 5 showed an obvious increase in Olig2 at higher coordinates along the gradient. It was apparent from these individual plots that repeat 3 was influencing the trends in the pooled plots significantly, and was obscuring what was otherwise a relatively consistent ventral response.

Gradient 1 in repeat 2 gives an indication as to the reason for the differences observed between the left and right sides of the pooled gradient data, with a large amount of Olig2 signal observed down the left side of the substrate, even in regions where there should have been little to no Shh present. This was most likely a printing artefact, with the surface wetting properties possibly causing the bio-ink to diffuse across the surface

after printing, and in doing so decreasing the match between the input and output gradient being generated. This may have been as a result of an issue with the individual LbL coating or drying process on this substrate specifically, as the issue is not apparent on most other substrates.

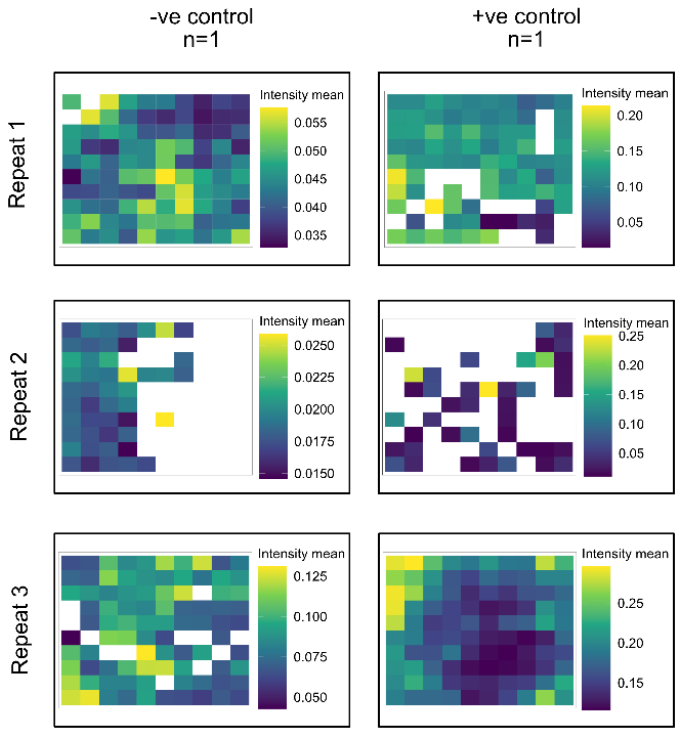


Fig. 3.31: *Binned heatmap plots of the Olig2 mean intensities for the control substrates. White squares indicate regions where no large cluster objects were detected on the substrate. Each substrate is scaled individually, for the purpose of clarity.*

In repeats 1 and 2, the negative controls showed mean intensity values comparable to those seen in the low regions of the printed gradients in their respective repeats, which suggested that the Shh gradient was only causing motor neuron generation at the higher regions as would be expected in the neural tube. This was however not the case in the third repeat, with intensities being observed on the negative control that were similar to those seen at the higher end of the gradients. It should be noted, however, that in the immunofluorescence images taken, little to no nuclear Olig2 was observed in the negative control here. Most of the detected signal was cytoplasmic, and so the

cells would be labelled as Olig2-negative in standard cell culture experiments. This implied that the considerable amount of cytoplasmic signal was influencing the intensities being recorded, and so this further emphasised the limitations of comparing between the controls and gradient substrates in this repeat.

The positive controls across all three repeats were seen to be slightly higher than the mean intensities observed at the upper ends of the gradients. However, both controls in repeat 2 showed extremely low cell density, which as mentioned above, could have been attributed to issues with the cells, the substrate surface or the printed pattern, and limited the amount that could be inferred from the controls.

One factor that was not accounted for in the above plots was the number of features detected per region to be binned. Although the seeding density had been increased drastically for this experiment in the hope of obtaining uniform surface coverage, there were still some substrates that showed lower cell density either in specific regions or across the whole substrate. As there were a much smaller number, features within these low density regions would have contributed considerably more to the mean intensities than features in higher density regions. To investigate the influence of this density issue, a threshold was set to remove any measurements where less than 100 objects were detected in a field of view. The modelled mean intensity plots of the Nkx6.1 signal were again generated as means to visualise this effect.

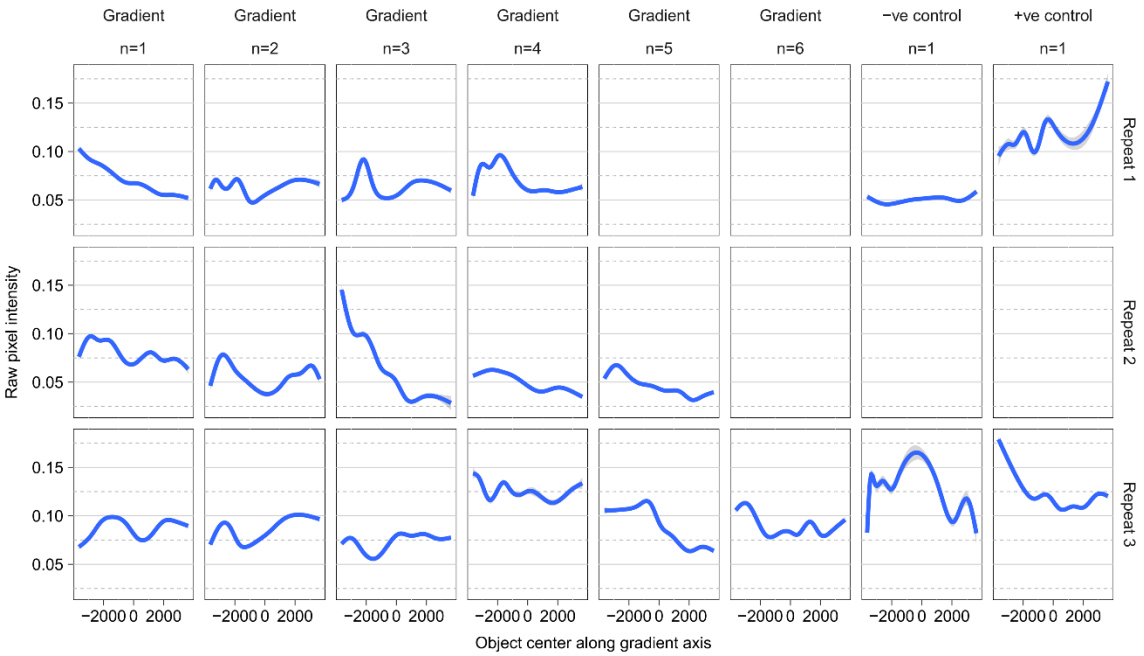


Fig. 3.32: *Plots of the model for the mean Nkx6.1 intensity, with a threshold set to filter out tiles where there are less than 100 features detected. Gradients are again increasing from right to left in each of the gradient substrate plots.*

While this thresholding did not change the general trend observed in any of the conditions, the response in substrates with a graded increasing intensity was seen to become steeper when the feature number was corrected for. Across those conditions, the response was more pronounced than the equivalent plots in Figure 3.27 with no feature number threshold set, indicating that the regions with lower number of objects detected were indeed having a significant impact on the trends observed. However, this increase in the upward trend was not the case across all substrates, with repeat 3 again showing trends that were not consistent with the other two repeats. The Nkx6.1 is seen in gradients 1, 2 and 3 here to decrease as Shh increases. This was however consistent with the trends seen in the plots above without any feature number threshold. The negative control in repeat 3 shows a significant increase in the Nkx6.1 signal, which may have occurred because a majority of the cells were being lost in the threshold here due to the inherently lower density of the negative control. As such, a

few high intensity objects could be influencing the trend observed. These data suggested that the number of features being detected per class was significantly influencing the response observed in the mean intensity, and indicated that further analyses with corrections for cell density may reveal more detailed information on the behaviour of the cells.

It is evident from the above data that a graded differentiation is indeed present across the majority of substrates in response to the printed Shh gradients. However, the response was non-uniform and inconsistent, indicating that further refining of the experimental approach was needed before the platform could confidently be utilised across a range of biological applications. The imaging pipeline may also need to be adjusted to account for the high cytoplasmic signal present in some otherwise transcription factor-negative cells, since this was evidently skewing the data in repeat 3 in particular. Regardless, this was an encouraging proof-of-concept test for the material platform, demonstrating its capability to generate neural ventral patterns on a single substrate, and to model the developing spinal cord. With adjustments to account for wetting issues, and accounting for cell variability between experiments, this platform has significant promise as a tool for investigating developmental and neural conditions.

3.4 Preliminary experiments

3.4.1 Dorsal neural tube modelling

Having confirmed that ventralisation of cells with this platform was possible via printed Shh gradients, another goal was to attempt a similar approach to recreate the dorsal half of the DV neural tube axis in parallel. For this platform to reach its full potential as a model of the early-stage spinal cord, it should be capable of recapitulating the entire dorsal-ventral axis of the neural tube, and be able to generate all the progenitor subtypes contained within. Preliminary experiments have been carried out to investigate whether this will be possible on the material system described above.

BMP4 was chosen as the bio-ink for dorsal gradient generation, since BMP proteins dominate the dorsal neural tube (along with Wnt signalling). Due to its isoelectric point, BMP4 has a positive charge at neutral pH (which is the standard printing condition), and so heparin can also bind it as in the case of Shh. This means that the surface chemistry designed for binding of Shh was also suitable here, and did not need further optimisation or modification. This was of utmost importance, since the final goal was to combine both Shh and BMP4 gradients on a single substrate, and so both proteins would need to be suitable for use with the same surface chemistry via the LbL process.

Before gradients of BMP4 could be considered, the validity of the protein as a soluble factor for generating dorsal subtypes was investigated, as this was a new protocol for the Briscoe lab. Initial tests were carried out on tissue culture plastic, with cells being maintained until days 4 and 5 via the standard protocol, before spiking in BMP4 to the media at 10 ng/mL. Two timepoints were tested, with the initial goal of minimising the time that cells would have to be maintained in RA for ventralisation in the final application (since Shh treatment traditionally occurred at day 3). The transcription factor panel chosen for the preliminary experiment was Msx1/Olig3/Pax6/Nkx6.1. Nkx6.1 was included to visualise whether some ventral cells were generated despite the BMP4 treatment.

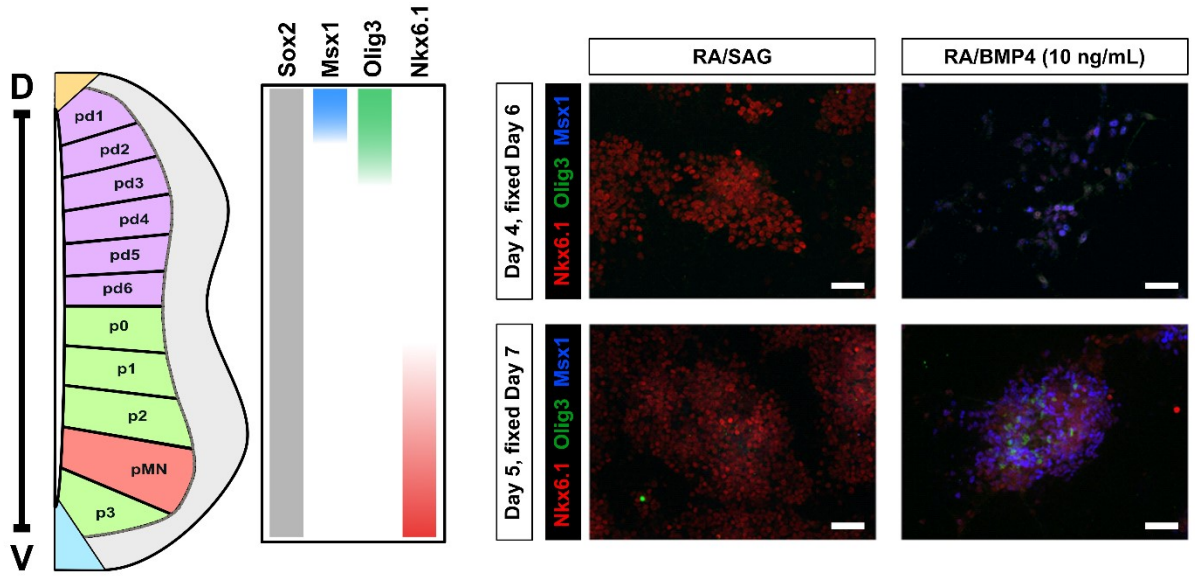


Fig. 3.33: *Initial test of BMP4 as a soluble factor for dorsalisation of mESCs. In both conditions where BMP4 was present, dorsal marker Olig3 and Msx1 were visible after two days of BMP4 treatment. However, Olig3 was not as widespread as might have been expected. This, coupled with further experiments, indicated an issue with the labelling of the Olig3 antibody being used. Some ventral Nkx6.1 signal was present, but this was not nuclear and so was determined to be a cytoplasmic signal. As such, this experiment demonstrated the presence of a dorsal response to soluble BMP4 at 10 ng/mL. Scale bars = 50 µm.*

After two days of BMP4 treatment, both conditions showed positive dorsal responses. The cell density was much improved when BMP4 was introduced at day 5, which was consistent with other protocols. The Msx1 signal was also more widespread, although the Olig3 was not as consistent as would be expected, since it marks a wider range of dorsal cell types than Msx1. This was attributed to issues with the antibody being used, and would be addressed by changing the antibody panel being stained for at a later point. Regardless, this was an encouraging result, and indicated that the revised protocol could indeed generate dorsal interneuron progenitors when required.

Having confirmed that the mESCs were responsive to BMP4 as a soluble factor at day 5, coating tests were then carried out with the protein to confirm that it could interact

with the cells in a similar fashion to the Shh previously shown. This was also an opportunity to optimise the surface loading concentration of the morphogen, to identify the printing concentration to be used in the gradient experiments to follow. In order to achieve this, LbL-coated substrates were incubated at four different BMP4 concentrations in N2B27 media overnight, ranging from 25 ng/mL to 200 ng/mL.

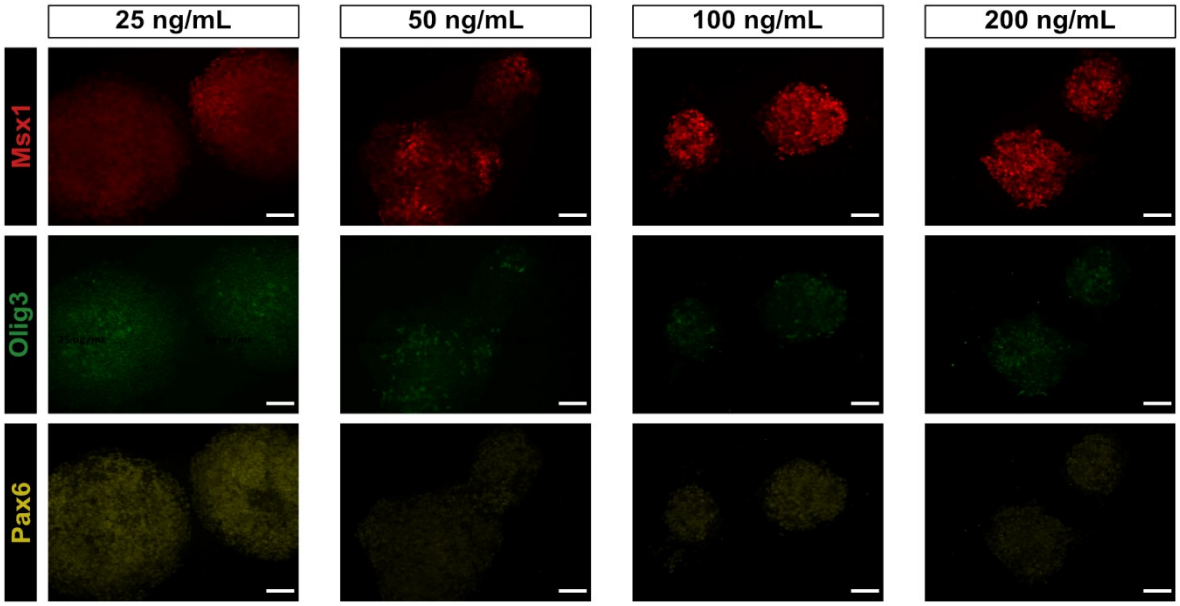


Fig. 3.34: *Concentration studies of BMP4 coatings for directed differentiation of mESCs to dorsal subtypes. The concentrations used ranged from 25 ng/mL to 200 ng/mL. The results shown here, coupled with the previous tests, confirmed that there was an issue with the Olig3 antibody, as only a weak signal was observed at the highest BMP4 condition. The nuclear Msx1 response was minimal at 25 ng/mL, with the strongest Pax6 signal seen here. At 50 ng/mL, a mosaic dorsal response was seen, before almost all cells were positive at both 100 ng/mL and 200 ng/mL. However, the 200 ng/mL coating was seen to provide a more consistent dorsal response, without many mixed cell colonies. It also had the lowest Pax6 signal, indicating that these were the most dorsal cells present across the conditions. As such, this was chosen as the printing concentration to be used going forward. Scale bars = 50 µm.*

A positive dorsal response was seen across all conditions apart from the 25 ng/mL substrates, where mostly background Msx1 signal was observed. At 50 ng/mL, a mosaic response was seen in the Msx1 signal, which improved drastically at 100 ng/mL, and even further at 200 ng/mL. Although both 100 ng/mL and 200 ng/mL gave similar Msx1 signal strength in positive cells, the 100 ng/mL condition generated more mosaic colonies. This, coupled with the lowest Pax6 signal being present, indicated that the 200 ng/mL concentration would be optimal for printing experiments going forward.

As there was an issue with the Olig3 antibody, it was necessary to reconsider the antibody panel being used to map the dorsal neural tube. By considering the dorsal half alone, Dbx1 and Pax7 were chosen to replace Pax6 and Olig3 respectively, since this could more accurately determine which dorsal subtypes were present. Dbx1 should only be present in cells at the midline of the neural tube, with no significant dorsal activation (i.e. at the low end of printed gradients). Pax7 spans the middle of the dorsal half of the neural tube, while Msx1 would be maintained to mark the most dorsal subtypes (i.e. the high end of the gradients). Although antibodies were already available for these transcription factors, it was first necessary to carry out tests in mouse neural tube sections, to confirm that they were behaving as expected.

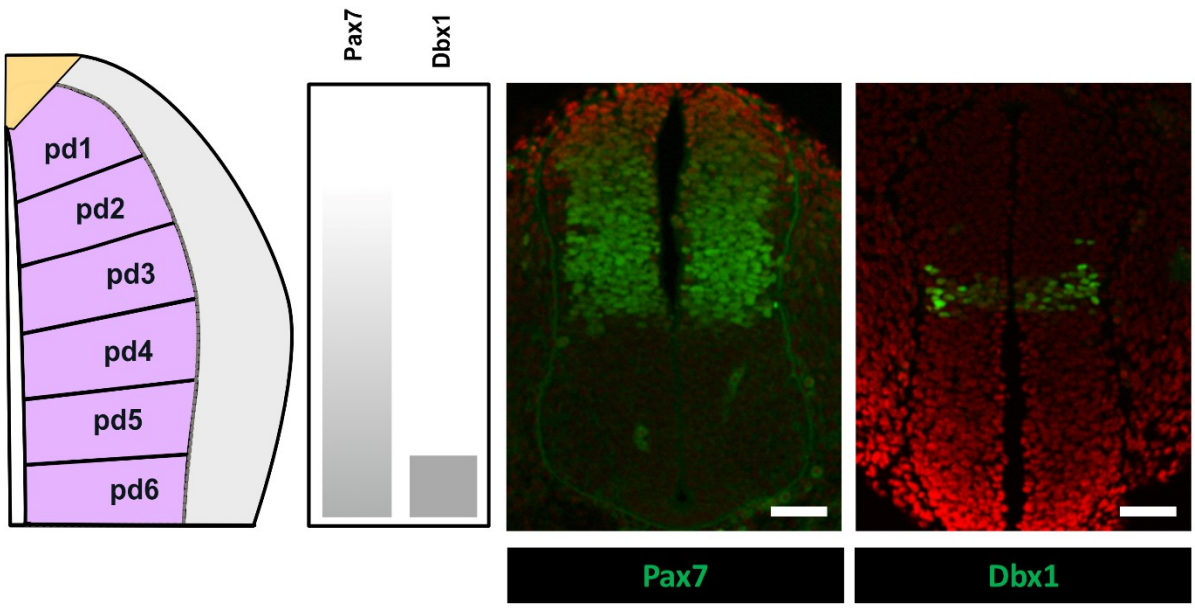


Fig. 3.35: *Testing the Dbx1 and Pax7 antibodies in mouse neural tube sections. Both antibodies behaved as expected, with Pax7 spanning the middle of the dorsal half of the neural tube, and Dbx1 only present at the midline. Neural tube images taken by Dr Despina Stamataki. Scale bars = 50 µm.*

Both antibodies behaved as intended in the mouse neural tube section, with Pax7 signal at its strongest in the middle section of the dorsal half of the neural tube, while Dbx1 was present only at the midline, where little activation of either the dorsal or ventral halves of the neural tube would be present. Going forward, combining these two transcription factors with Msx1 would provide a representative mapping of the entire dorsal half of the neural tube, and would allow identification of the specific subtypes that are present at each point along the printed gradients. For this platform to accurately map the DV axis, both Shh and BMP4 gradients would need to be combined on a single substrate.

3.4.2 Time-dependent ventral response

As well as the dependence on concentration of morphogens, time plays a significant role in which transcription factors emerge across the DV axis of the neural tube. As the

cells progress towards the mature neuron stage, a number of cross-repression interactions occur between the transcription factors to direct the various regions of cells towards their final fate. As this emerges as a result of longer exposure times to Shh, longer seeding times on the substrate surfaces could recapitulate this effect and in doing so, demonstrate the ability to model both the concentration and time dependence of the developing spinal cord.

To investigate this capability, cells were seeded on day 5 as in the above experiments, but were in this case left one extra day until day 8 before fixing. As this was a test of the response over time to Shh while on the substrate, the ventralisation cue here was spiked into the media rather than being surface bound. The cells were stained for Olig2, Sox2 and Nx2.2, which is a marker for the most ventral cells, p3 progenitors. Initially, Olig2 cross-represses Nkx2.2 in the neural tube, and as such, it is not present in the early stages of development. However, as time progresses, this interaction is reversed, with Olig2 then being repressed by the emergence of Nkx2.2. As such, if cells were left for longer on the substrate surface, it would be expected that the presence of Olig2 would be decreased, and Nkx2.2 would begin to emerge.

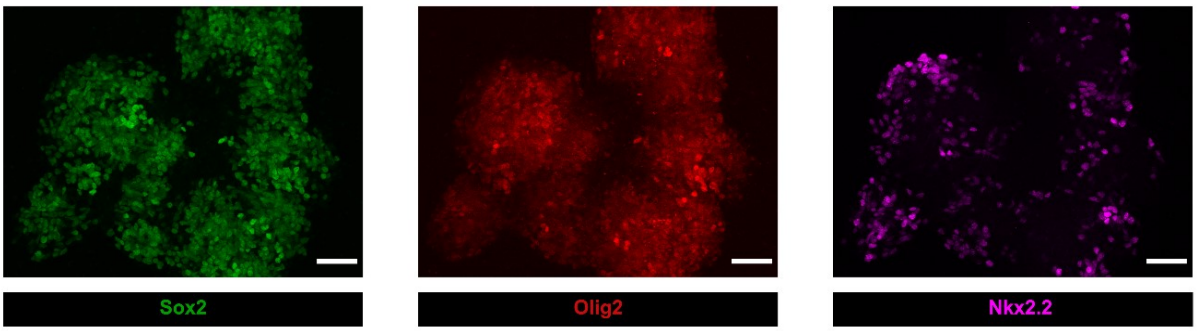


Fig. 3.36: *mESCs seeded at day 5 and fixed at day 8 on nanoneedle substrates, with Shh spiked into the media. Sox2 (green) confirms that the cells are of neural character. The Olig2 signal (red) is seen to mostly be cytoplasmic, with only a small number of nuclei being Olig2-positive. The emergence of Nkx2.2 (magenta) is also apparent, indicating that the cross-repression of Olig2 by Nkx2.2 has begun. Scale bars = 50 µm.*

The Olig2 signal was observed to be mostly cytoplasmic, with only a small number of nuclei being Olig2-positive. Nkx2.2 was present in a number of cells across the substrate, indicating that the cross-repression interaction had begun. This demonstrated the potential for this material platform to also investigate the time-dependence of morphogen action in the neural tube, which would allow more detailed future investigations into the transition from neural progenitors through to mature neurons.

3.4.3 Axonal guidance with nanostructured surfaces

Along with the biochemical guidance offered by the printed patterns, the presence of nanotopographical features on the substrate offers a means to also offer a physical guidance to cells growing on the surface. This has potential applications in modelling of spinal cord injuries, where neurons could be encouraged to grow neurites across the lesion site. This has previously been discussed in the context of nanofibre scaffolds,[44,154] but a similar effect could be achieved through the use of nanostructured substrates. As nanoneedle substrates are manufactured using standard microfabrication and photolithography techniques, the structures on the surface can readily be modified by using a different photomask to create alternative features for the etching process. One such alternative material system previously generated in the Stevens group is a derivative of the nanoneedles known as nanomohawks. These are features of a similar height and sharpness to the nanoneedles, but are elongated into long, ridge-like structures (see Figure 3.38 below). This effectively creates grooves between the structures that could offer an effective contact guidance substrate for the directed elongation of axons and neurites from cells.

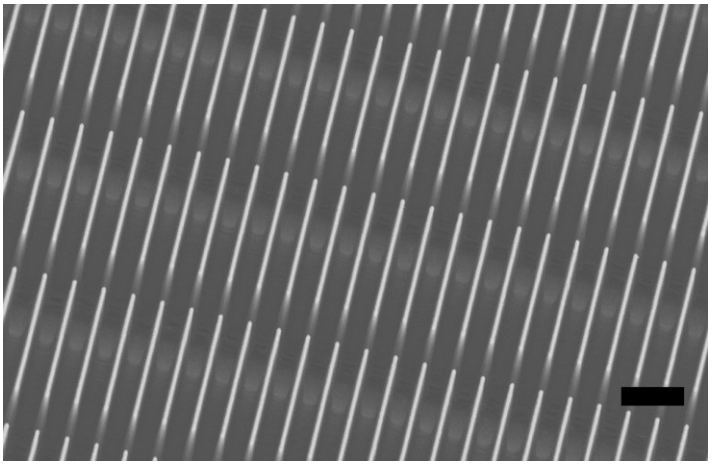


Fig. 3.37: *A nanomohawk substrate, manufactured in a similar way to the nanoneedles from silicon wafers. The structures are elongated relative to the needles, to create 10 µm-long ridge structures. These ridges, and the spaces in between them (2 µm in the image above), could offer ideal contact guidance for the directed growth of axons from neural cells seeded on the substrate. Scale bar = 4 µm. SEM image by Dr Stuart Higgins.*

As the nanomohawk substrates are also manufactured from silicon, the same surface chemistry of the LbL process could be employed to use them as a printing substrate going forward. However, in this instance, a preliminary study was carried out to investigate how the physical structure of the substrate might interfere with cell morphology and axon growth. NMPs were seeded onto a heparin/chitosan-coated nanomohawk substrate at a density of 1×10^6, and after two days were fixed and stained for DAPI/TuJ1. TuJ1 is a protein used as a mature neuron marker that would allow for the visualisation of axon outgrowth from the cell colonies along the nanomohawks.

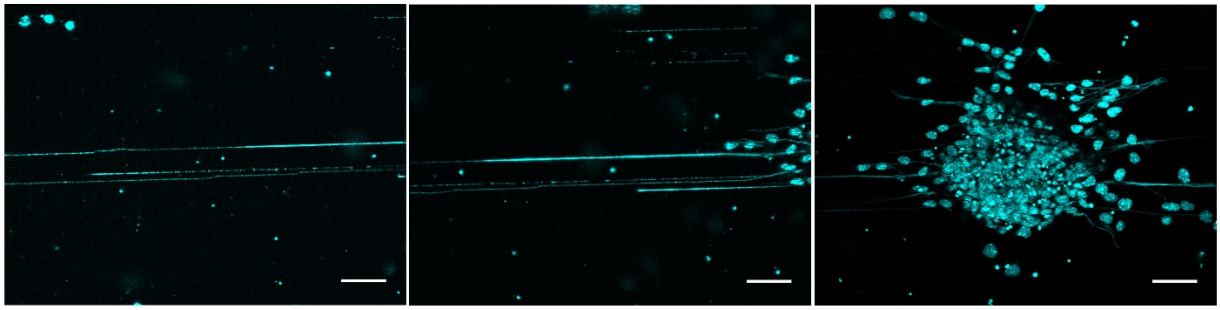


Fig. 3.38: *mESCs seeded on a nanomohawk substrate. Cyan = DAPI/TuJ1 combined stain. The three sequential fields of view here show the axonal outgrowth from one large colonies of cells. Axons were seen to grow lengths of greater than 500 µm, which was significantly larger than the axons that would be observed when cells were seeded on tissue culture plastic. The axons were also seen to be aligned along the direction of the nanomohawk ridges (rows were extending left to right, parallel to the axons seen here), indicating that the process of contact guidance was indeed occurring. Scale bars = 50 µm.*

The axons observed through the TuJ1 staining showed an extreme alignment along the direction of the nanomohawk structures on the substrate (left to right in above images), indicating that contact guidance was indeed occurring. As the gaps between the surface structures was 2 µm, the axons were most likely growing along the tops of the ridges rather than in the spaces between them. The axons extending from the colonies were observed to have lengths in excess of 500 µm, which was significantly longer than axons that would be observed in traditional tissue culture plastic conditions. This suggested that these substrates could have applications in directed growth of axons and nerves, either through the use of ESCs as was the case here, or indeed with spinal cord explant sections as done by Weightman *et al.*[154] This could be combined with inkjet printing of substrates to offer fine control over both the chemical and physical growth conditions that cells or tissue sections experience.

3.5 Discussions and conclusions

In this chapter, the successful recapitulation of the dorsal-ventral axis of the neural tube was achieved *in vitro*. Surface-bound proteins were seen to generate both ventral and dorsal subtypes on substrate surfaces, with an optimum concentration of morphogens being identified. Printed Shh gradients were then used to direct the differentiation of mouse embryonic stem cells into ventral spinal cord progenitor subtypes via the presence of nuclear Olig2 and Nkx6.1, which was the requirement for a preliminary spinal cord-on-a-chip model. Both the Canon and BioDot printers were shown to be capable of printing suitable gradients for cell interfacing, but the BioDot was found to be more consistent and reliable in generating gradients across experiments.

The imaging analysis pipeline confirmed that spatially directed differentiation was indeed occurring. However, it also highlighted the inherent noise and inconsistency in some cell responses to the gradients. In particular, the third repeat experiment showed large variation in the levels of ventral responses observed. This may have been as a result of issues during the coating and printing process, or biological variation within the cells.

The platform could be further expanded for future studies by printing gradients of dorsal cues such as BMP4. A transcription factor panel of Msx1, Pax7 and Dbx1 has been identified as a potential candidate to describe the dorsal response being obtained, and a surface loading concentration of 200 ng/mL was seen to induce a strong dorsal response in preliminary studies. Other dorsal cues such as Wnt proteins could also be considered here, although as BMP4 has already been shown to be effective as a surface coating for this cell type, this should be the initial condition to be tested.

By combining gradients of both Shh and BMP4 on the same substrate, the entire dorsal-ventral axis could be recreated. The readout method for these investigations should be considered, however, since the number of channels that can be imaged

simultaneously in immunofluorescence would not be sufficient to describe the behaviour of all the subtypes present. A description of the transcriptome would be needed, to clarify the cell types that were being generated. The technique described in section 3.4.2 has been developed as a means to enable these future studies, to capture cells from the substrates while maintaining their spatial information. If this were to be achieved, the transcription factor network generated by the printed gradients could be compared to that of the neural tube *in vivo*, and the true potential of this platform could be realised. It is likely that in the current configuration, considerable amounts of noise would be obtained in the transcriptomics data (as seen in the image analysis pipeline output), and as such, further refining of the system is needed before any sequencing is to be carried out. As two of the three repeats in the final study showed a generally ventral response, it was likely that the inconsistencies observed with the third repeat were related to issues within that specific experiment. The capturing of cells via the sectioning described in section 3.4.2 enables immunostaining to be carried out on adjacent slices of cells before sequencing, and so this could be used to confirm that a ventral response had been obtained on the substrate in question before moving forward to the transcriptomics step.

If the platform was shown to accurately generate this transcription factor network, it could potentially be applied to modelling the anterior-posterior axis of the neural tube. This would allow for modelling the development of the brain, and in doing so could be used to investigate the entire early-stage central nervous system. The material system would require little modification, beyond the choice of bio-ink. FGF and Wnt proteins could be used respectively for the two halves of this axis, with both having suitable isoelectric points to bind to the heparin/chitosan bilayers that have been established in this work.

Chapter 4

Spatial patterning of Wnt ligands for cancer investigations

Chapter 4: Spatial patterning of Wnt ligands for cancer investigations

This chapter describes initial investigations into using the printing platforms described previously to study cancer *in vitro*.

Raman spectroscopy was carried out by Dr Vernon Lalone. Plots of Raman spectra were generated by Dr Jelle Penders. Cell seeding was carried out by Dr Lucas Dent and Dr Tomo Higo. Image analysis was carried out by Dr Lucas Dent and the author. The image analysis pipeline was developed by Dr Lucas Dent.

4.1 Introduction

The previous chapter demonstrated the capability of a novel material system to model neural systems *in vitro*. As the strength of this approach lies in the spatial patterning of morphogens and the rapid modification of the platform as required, other biological systems governed by signalling pathways were considered, to further emphasise the potential of this technique.

Cancer is undoubtedly one of the largest challenges facing the field of medicine today, and can loosely be described as the uncontrolled division and growth of cells in the body. In the UK alone, approximately 367,000 new cases are diagnosed each year, while approximately 165,000 people die annually from some form of cancer.[158,159] Although significant progress has been made in recent years in combatting this group of diseases (survival rates have doubled since 1980[160]), it is still the second largest cause of death worldwide.[161] It is clear that new tools and methods are needed to offer further insights into the mechanisms behind this family of diseases. To this end, preliminary studies were carried out to investigate the use of the printing system described previously in modelling cancer biology *in vitro*.

4.1.1 Cancer and signalling pathways

A large challenge associated with overcoming cancer is the fact that each subtype of cancer manifests in extremely different ways, depending on the organ being affected, and indeed varying patient to patient with the same disease. This can be as a result of a genetic predisposition and family history, but other times there is no obvious reason to explain the onset of cancer. Many of the mechanisms behind processes such as migration, proliferation and metastasis remain poorly understood.

The rapid progression of cancerous growth, and difficulty in delivering treatments without causing damage to surrounding tissues and organs contribute to the severity of the disease. As a result of the inherent variation across cancer types, no standardised approach can be applied as a treatment method. Personalised medicine has shown

some promise in allowing for tailored treatment plans for individuals based on their genetic profile and molecular differences between tumours.[162] However, significantly more progress is needed in medical systems worldwide before this approach can be seen as a possible solution to the burden of cancer on society. Another target in recent clinical trials are specific cancer signalling pathways, and their roles in disease progression. Signalling pathways govern standard cellular processes such as differentiation, proliferation and migration in healthy cells. These pathways are vital to healthy development, tissue repair and most other bodily functions. They are extremely complex, consisting of a variety of checkpoint activation and inhibition steps that result in a specific response within the body. If, however, a mutation occurs at some point in the pathway, it can have catastrophic effects. If these pathways could be further investigated in the context of cancer progression, it could potentially inform novel routes forward in cancer therapies. As such, they offer a possible target for treatments that could span a number of cancer types, rather than tailored medications for specific subtypes.

Many different signalling pathways have been implicated in cancer progression, matching the variety in cancer types. One of the most studied of these is the mitogen-activated protein kinase (MAPK) signalling pathway. This pathway is one of the central controlling systems by which cells undergo division and proliferation. The mechanism of action of this pathway occurs in a multi-tiered manner, regardless of the version of the pathway that is acting. A MAPK is phosphorylated by another MAPK kinase (MAPKK), which is itself activated by a MAPKK kinase (MAP3K). The process can often have a further step induced by MAP4K, or a downstream MAPKAPK, although these steps are not always required. This cascade of interactions phosphorylates downstream proteins, introducing signals from the extracellular environment to the inner workings of the cell. This activates processes such as division, differentiation and proliferation.[163,164] Perhaps the most widespread of the MAPK signalling family is the extracellular signal-regulated kinase (ERK) signalling pathway. These proteins are growth factor-activated, and are common across a number of different species, making

them an attractive therapeutic target.[165] The cascade starts by the interacting of a RAS protein (loaded with guanosine triphosphate, GTP) with an activating ligand at the plasma membrane. This causes dimerization of the kinase RAF domain (equivalent of MAP3K here), the subsequent activation of the kinase MEK (MAP2K), and finally the phosphorylation of ERK (MAPK). ERK is the protein that then acts on the various intracellular mechanisms that play a role in the above-mentioned processes.

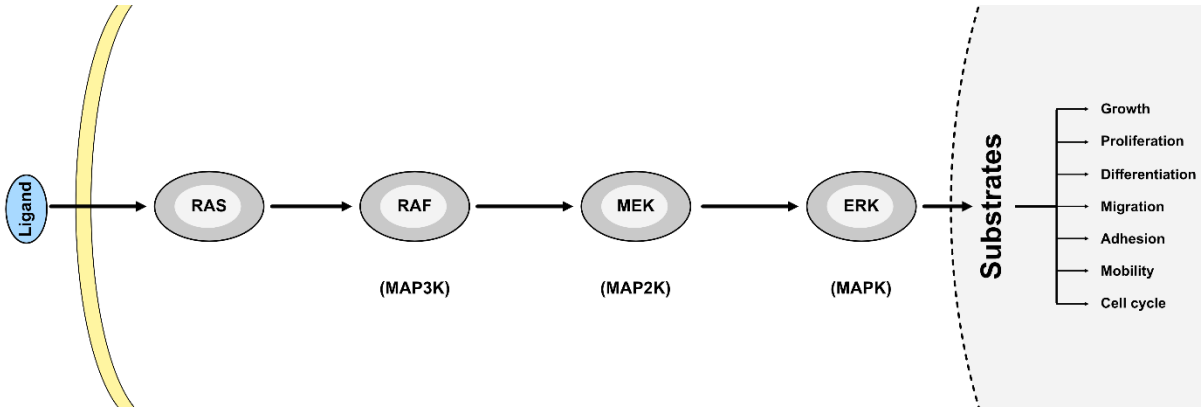


Fig. 4.1: *Schematic of the MAPK signalling pathways, with the ERK pathway being used as an example. An activating ligand (e.g. mitogen, growth factor) at the plasma membrane interacts with the protein RAS. This causes dimerization of the RAF kinase domain (MAP3K equivalent), subsequent MEK activation (MAP2K), and finally ERK phosphorylation (MAPK). The phosphorylated ERK is then free to act on the various intracellular substrates, and in doing so carry out a variety of different roles (some of which are listed here).*

Although a common process in normal, healthy development, this pathway has been a therapeutic target in cancer for a number of years. As it is conserved across species, the translation of animal-to-human research is significantly easier than many other targets, and the breadth of literature and knowledge already available on the pathway enables a range of different approaches. A common mutation in this pathway is at the RAS point (HRAS, KRAS or NRAS, three proteins coded by different RAS genes), present in approximately 30% of cancer types,[166] while mutations in the BRAF gene account

for approximately 8% of cancers.[167] For KRAS mutations, the cancers with highest associated frequencies are pancreas, large intestine and biliary tract. For NRAS, the most common cancers are skin, haematopoietic and lymphoid tissue, and thyroid. Some of the most common HRAS-associated cancers are the salivary gland, cervix and urinary tract. BRAF mutations are often found in skin, large intestine and thyroid cancers.[168] As these various mutations play such a central role in the disease progression, many therapeutic avenues target those points in the pathways as a means to prevent or treat cancer.

Another pathway that is commonly implicated in cancer is the phosphatidylinositol-3-kinase (PI3K)/AKT pathway. As with the MAPK pathway, this plays a role in standard cellular processes such as growth, differentiation and metabolism, and is conserved across most species. However, when aberrant activation or mutations in the signalling cascade occur, it also impacts the survival and proliferation of cancer cells and tissues.[169] The pathway has three key components: PI3K, AKT, and mammalian target of rapamycin (mTOR). The class I PI3Ks are the primary class implicated in cancer.[170] Upon activation of receptors at the cell surface by kinases or growth factors, class Ia PI3K are recruited at the cell membrane, and a sequence of phosphorylation events in the PI proteins are triggered that allow signalling proteins such as phosphoinositide-dependent kinase 1 (PDK1) to attach to the membrane. These signalling proteins then phosphorylate AKT, which in turn acts on a range of downstream targets (one of which is mTOR) that initiate a variety of mechanisms within the cell (apoptosis, cell death, transformation and cell cycle, metabolism). When this pathway is overactivated, those same processes give rise to cancerous growth. Many clinical therapies have been designed using this pathway as a target, primarily through inhibition.

4.1.2 Wnt signalling in cancer

Another important pathway is the family of pathways activated by Wnt ligands, which play a central role in cell growth and proliferation. These are vital for the formation of

a healthy, functional nervous system, as a well as a host of other tissues and systems within the body. However, if these pathways are interrupted or over-activated, it can give rise to unchecked growth of cells in a specific location, a hallmark of cancer development.

Currently, 19 proteins are associated with the Wnt signalling pathway in mammals.[171] This pathway plays a key role in early stage development, in particular as a morphogen acting over distance (such as in neural tube or gut development).[172] There are two distinct branches of the Wnt pathway, commonly known as the canonical and non-canonical pathways. The canonical pathway is dependent on a protein called β-catenin, and is triggered by the binding of Wnt ligands to a receptor complex at the cell surface (which includes transmembrane proteins Frizzled and LRP5/6). Wnt proteins have a hand-like shape, and are believed to bind to Frizzled receptors via the "thumb" and "index finger" branches. When the Wnt pathway is not active, a group of proteins called the β-catenin destruction complex maintains a low cytosolic concentration of the protein (via phosphorylation and subsequent destruction by proteasomes). However, when the binding of a Wnt ligand occurs, LRP5/6 and Frizzled recruit the protein Dishevelled, which in turn recruits axin-GSK3. This then phosphorylates LRP5/6, which allows it to interact with Axin and inhibit the destruction complex to enable the concentration of β-catenin to increase. Once it accumulates, β-catenin is free to translocate to the nucleus, and to interact with transcription factors in order to regulate the transcription of various target genes. However, these target genes are primarily involved in cell proliferation and differentiation, and so in cases of overactive Wnt signalling, poorly controlled proliferation can lead to the development of various types of cancer.

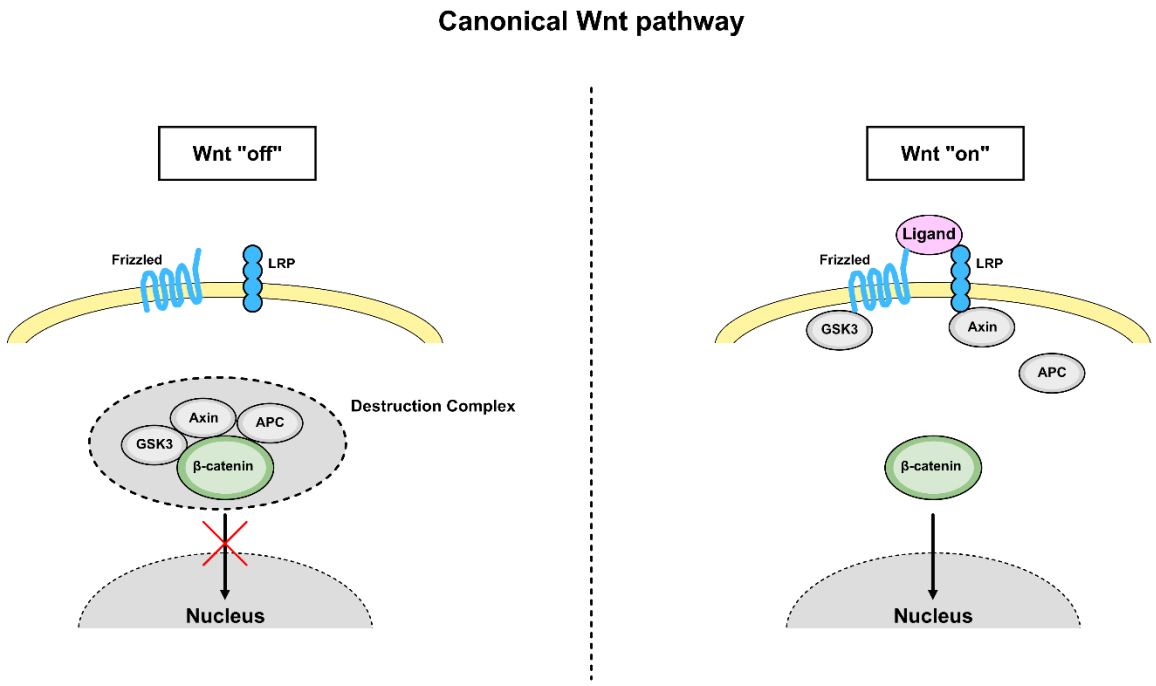


Fig. 4.2: *Schematic of the canonical Wnt signalling pathway. When there is no ligand present and the pathway is in an "off" state, β-catenin translocation is hindered by a group of proteins known as the destruction complex (some of which are shown here). As such, it cannot act in the nucleus to instigate the various aspects of the pathway. However, when a ligand is present, and the pathway is "on", components of the destruction complex are recruited at the plasma membrane due to a number of phosphorylation steps. This then frees β-catenin to translocate into the nucleus and to act on transcription factors there.*

In the non-canonical pathways, the signalling circuits are not dependent on β-catenin, but rather other intracellular factors. The two most studied non-canonical Wnt pathways are the planar cell polarity (PCP) pathway, and the Ca^{2+} pathway. In both cases, binding of Wnt ligands to the Frizzled receptor initiates a series of signalling events that influence different components within the cell. The PCP cascade causes changes in the cytoskeletal arrangement, and further affects the transcription of genes in the nucleus, allowing it to regulate processes such as cell polarity (which plays an important role in morphogenic embryo development, particularly in the neural tube

and gastrulation). The Ca^{2+} pathway similarly influences transcription of genes in the nucleus, but in this case is instead prevalent in cell migration and final cell fate. As such, it is more relevant for the development of diseases, most notably cancer and neural conditions.

When aberrant signalling occurs, it can give rise to a number of unintended biological processes. The Wnt pathway has been strongly implicated in the progression of many cancers, through excessive activation, repression or mutations. Approximately 50% of breast cancers can be linked to the signalling cascade caused by Wnt ligand binding (including many instances of triple-negative breast cancer, which is particularly aggressive).[173,174] In the case of breast cancer, the Wnt pathway has been implicated primarily in metastasis and proliferation, although it most likely plays a number of other roles in parallel.[175,176]

In recent years, it has also been implicated in colorectal cancer (Wnt plays a large role in gut – and so colon – formation).[177] Although the role of Wnt signalling in some cancers has not yet been fully established, for instance with pancreatic adenocarcinoma, evidence is increasingly mounting to suggest that it is indeed playing a role.[178,179] The mutations responsible can occur at any point along the complex sequence of events involved in Wnt signalling, from inhibition of the β-catenin destruction complex to post-transcriptional modifications. Alterations at the gene level can have significant impact on cellular function, and can cause signalling cascades that allow cells to proliferate unchecked. For example, APC is a protein that makes up part of the destruction complex for β-catenin, but has also been strongly linked to colorectal cancer development. If a mutation in the APC gene occurs that inhibits the ability of the complex to degrade the protein, regulation of the cytosolic levels becomes impossible, and overactivation of the Wnt pathway can occur.[180] The link between Wnt and metastasis indicates that this pathway plays a significant role in the cause of secondary cancers after initial diagnosis. In general, Wnt can be implicated in cancers and other diseases that require the pathway for renewal or repair.

However, as disruptions to this pathway seems to be synonymous with the multiple processes that eventually give rise to cancers in the body, it could also offer a route for the development of novel therapeutics. A number of clinical trials have been conducted through the use of pathway antagonists and inhibitors, to elucidate the potential of the Wnt cascade to combat cancer progression.[181] There are three primary methods being employed; inhibition of Porcupine (PORCN, which facilitates Wnt ligand secretion), antagonistic antibodies for Frizzled (FZD) receptors, and specific Wnt ligand antagonists. These have been targeted for a range of cancers, including pancreatic cancer, melanoma, sarcoma and metastatic breast cancer. To date, the furthest a trial has progressed is Phase II – a PORCN inhibitor, and two β-catenin inhibitor drugs. With further tests and development, this pathway could offer an invaluable opportunity to overcome cancers that have traditionally been extremely aggressive and difficult to treat.

Massey *et al.* investigated Wnt signalling pathway dynamics in a number of cellular processes, including during the differentiation of human pluripotent stem cells.[182] This was done through the use of live imaging, observing trends in the amount of nuclear β-catenin over time after treatment with Wnt3a protein. Their focus was on both the concentrations and treatment times that achieved the maximum nuclear signal (and so pathway activation). They investigated a number of different cell types, and observed that the response to Wnt activation varied significantly across different lines.

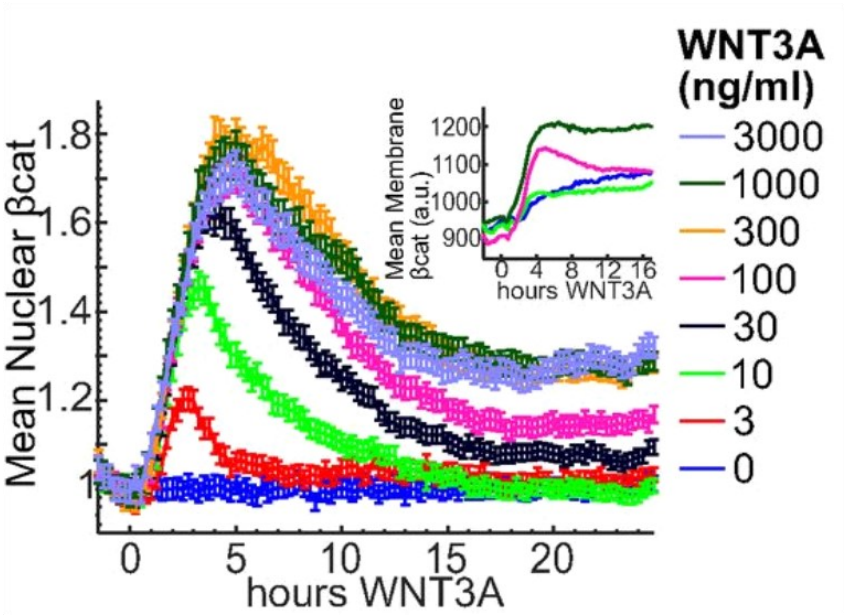


Fig. 4.3: *Response of mESCs to various concentrations of soluble Wnt3a. A peak in nuclear β-catenin was seen in all conditions between 0-6 h, before decreasing drastically. The highest response was seen in the 300 ng/mL treatment condition. Reproduced from Massey et al.*[182]

In human embryonic stem cells (hESCs), the authors found that a peak in pathway activation was obtained at a Wnt3a dose of 300 ng/mL (a range from 0 to 3000 ng/mL was tested). Above this, a saturation was observed in the amount of β-catenin translocating to the nucleus, indicating that in certain instances, increasing the ligand concentration may not increase the response significantly. It was also noted that high doses of exogenous Wnt ligands introduced to the cells completely dominated any endogenous signalling that was occurring in the system. Perhaps of equal significance to the concentration response was the time-dependent signalling dynamics that were exhibited by the cells in response to the presence of Wnt3a. Across all treatment conditions, a peak in the nuclear β-catenin signal was seen between 0 and 6 h after treatment, before decreasing over the subsequent hours.

These data (in particular the time-dependent response) were verified somewhat with those obtained by Reischmann *et al.* in their investigation into the role of Wnt

signalling in HEK293T cell proliferation.[183] Their studies revealed a similar trend with a spike in nuclear β-catenin, but the timescale reported was significantly different. Rather than using live imaging (which allows for continuous imaging), the authors here used western blot analysis at three timepoints – 24 h, 48 h and 72 h. As such, some of the finer grain detail was lost, and so it was reported that the response peaked at 24 h, before falling again at both the 48 and 72 h timepoints. They also investigated a range from 0-200 ng/mL of Wnt3a treatment, and so there may well have been further increases in Wnt signalling at higher treatment concentrations. The cell line under investigation was also different to those used by Massey *et al*.

It should be noted that signalling dynamics in the presence of soluble Wnt ligands could well be drastically different to those in the presence of surface-bound cues, and so these studies should be used as guidelines only for potential materials applications. Also, neither cell line described above were from a cancer, and so should only be used as guides in predicting the behaviour of Wnt signalling in cancer cell lines.

4.1.3 Hedgehog signalling in cancer

Much like Wnt, the Hedgehog (Hh) family of pathways plays a pivotal role in developmental processes (as described in Chapter 3). And, similarly, aberrant signalling cascades can induce unwanted side effects such as developmental disorders, facial and cranial deformities, and indeed cancers. The mechanisms by which Hh signalling plays a role in cancer progression is relatively well understood, and can be divided into three subclasses (Figure 4.4).[184]

Type I cancers are independent of Hh ligands, but are rather caused by mutations that activate the pathway without the need for ligand binding. Mutations in Patched (PTCH1) or Smoothened (SMO) receptors are most often the culprits of this disruption, meaning that no Hh protein is involved, but activation/inhibition steps can still begin the signalling cascade. This Type I activation has been linked to cancers such as basal cell carcinoma and medulloblastomas.[185,186] Type II cancers involve abnormal

activation of the Hh pathway through autocrine signalling (ligands are both produced and bound by the same cell). This autocrine activation has been implicated with prostate, breast, and pancreas cancers among others.[187–189] Type III cancers are the result of paracrine Hh signalling, in which a nearby cell releases Hh ligands that bind to neighbouring cells, and activates the pathway. The ligand can either be released by the cancer cell and bound to a neighbouring stroma cell that instigates a feedback loop with the cancer cell (Type III), or can be released by a neighbouring cell and bound to a cancer cell (Type IIIb). As with Type II, this subtype of cancer has been shown to play a role in pancreatic and prostate cancers.[190,191]

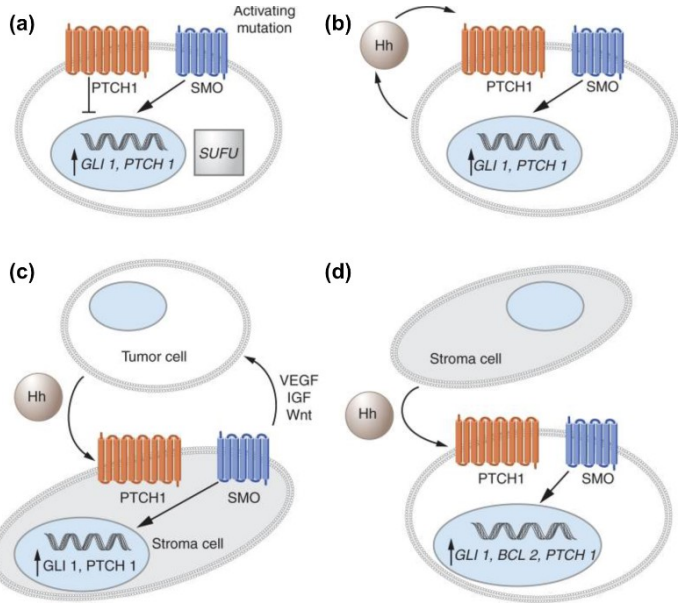


Fig. 4.4: *Schematic showing the four types of Hedgehog signalling associated with cancer development. (a) Type I signalling occurs when a ligand-independent receptor mutation occurs (e.g. Patched, PTCH1, or Smoothened, SMO), allowing for pathway activation without the presence of Hh proteins. (b) Type II activation occurs when a cell binds a ligand that it has itself previously secreted. (c) Type III involves the release of Hh ligands, which bind to nearby stroma cells. These stroma cells are then tied into a feedback loop with the cancer cell, causing activation of various other cascades. (d) Type IIIb signalling describes the instances where stroma cells release Hh ligands that bind to nearby cells, and activate the signalling pathway. Reproduced from Gupta et al.* [184]

Understanding how these Hh-associated cancers can arise provides a route towards developing targeted therapies for specific disease types. For instances where mutations in the pathway cause increased proliferation (e.g. Type I), Hh small molecule antagonists or blockers could be used to inhibit the signalling process. Similarly, where inter-cell signalling is playing a role in cancer progression, inhibition of the pathway could slow or indeed prevent the process from occurring. Many small molecules have been designed that can target receptors such as SMO that are vital checkpoints in the Hh pathway.[192] Although it would also be possible to target PTCH1 receptors using agonists to prevent activation of the signalling cascade, most attempts at clinical Hh targeting have centred around SMO inhibiting. Drugs such as Vismodegib, Sonidegib and Glasdegib have previously been employed in clinical trials to varying degrees of success, with many reaching Phase II/III. In one trial, Vismodegib has reached Phase IV for the treatment of periocular basal cell carcinoma.[193]

While these trials with the above-mentioned pathways are extremely promising, and may well present as viable treatment options in the future, a number of aspects of these pathways and their roles remain unclear. Progress is being made through the use of standard *in vitro* methods, but the process could be assisted by more effective engineering tools, to accelerate the screening and prototyping process. A finer control over local concentrations and activation/inhibition patterns *in vitro* would allow for bespoke experimental conditions for the specific cell-drug interaction being interrogated. Tools that provide these capabilities could shed further light on the role of these pathways in cancer progression, and could inform other trials and investigations towards novel therapeutics.

The role that signalling pathways play in cancer progression is evident from the above-mentioned studies. The next sections describe preliminary studies into the printing of cancer-relevant ligands for cell interfacing *in vitro*. A tool that exerts influence over these pathways in a spatially controlled manner could be a powerful asset for

researchers attempting to tackle the challenge of cancer development and progression.

4.2 Materials and methods

4.2.1 Substrate preparation and inkjet printing of Wnt3a

All nanoneedle substrates used in this chapter were coated with heparin/chitosan bilayers via the layer-by-layer process, as described in section 2.3.2.

Wnt3a (cat. no: 1324-WN, R&D Systems) was made up at the required bio-ink concentration in PBS/BSA (0.1% w/v, cat.no: 9048-46-8, Sigma-Aldrich), and printed using either the Canon or BioDot printers as described in sections 2.4.2 and 2.4.4 respectively.

4.2.2 Cell culture

Mouse melanoma cell lines (MEL10s and 19398s) were cultured in Dulbecco's modified eagle's medium/F-12 (cat. no: 11320033, Gibco/Thermo Fisher Scientific), supplemented with primocin (0.002% v/v) and fetal bovine serum (10% v/v, Gibco/Thermo Fisher Scientific). Human melanoma cells (WM266.4s) were cultured in Dulbecco's modified eagle's medium/F-12, supplemented with penicillin/streptomycin (1% v/v, cat. no: 15140122, Gibco/Thermo Fisher Scientific) and fetal bovine serum (10% v/v, Gibco/Thermo Fisher Scientific).

MEL10s were seeded at a density of 1.5×10^5 per substrate, while 19398s were seeded at a density of 1×10^5. WM266.4s were seeded at a density of 1.28×10^4 per substrate (to match density used by Hansel *et al.)*[100]. Where necessary, interferon gamma (cat. no: 315-05, Peprotech) was introduced 24 h after seeding at a concentration of 100 U/mL, with both MEL10s and 19398s being fixed after 48 h on the substrates using paraformaldehyde (4% v/v, cat. no: 7732-18-5, Thermo Fisher Scientific). WM266.4s were fixed at either 6 h or 48 h timepoints as needed. Primary antibodies were made up at a 1:1000 dilution in PBS/BSA (0.5% w/v)/Triton-X (0.01% v/v, cat. no: HFH10,

Thermo Fisher Scientific). Substrates were incubated overnight at 4°C, before being washed with PBS and adding the secondary antibodies, made up at 1:1000 dilution in PBS/BSA (0.5% w/v). Secondary antibody incubation was carried out for 2 h at room temperature, before washing again and mounting for imaging.

4.2.3 Imaging

Imaging was carried out on an Axio Observer widefield microscope (Zeiss) as described in section 3.2.2. For higher magnification imaging, a spinning disk confocal microscope (3i) was used at a 20X magnification, with the substrates again being tiled.

4.2.4 Image analysis

To analyse the response of these cells to printed Wnt patterns, a method to automate segmentation and feature extraction was developed using ilastik and CellProfiler, in a similar manner to the method described in Chapter 3.[155,156] Each substrate was imaged and tiled into one composite image. For the initial approach, the whole region (8 x 8 mm) was then divided into a grid of 5 rows and columns (see Figure 4.20 (a)) for analysis (later modified to a larger grid).

ilastik was again used to create pixel probability masks for both the nuclei (DAPI) and cell body (actin) of the WM266.4s on the substrate (see Figure 4.20 (b)). From there, CellProfiler was used to segment the features and to extract intensity values for each channel to be analysed.

4.3 Results

The goal of this piece of work was to carry out proof-of-concept investigations into the use of the printing platform for studying cancer biology *in vitro*. Along with the importance of signalling pathways, there is increasing evidence that cell shape plays a significant role in cancer invasiveness and progression.[194,195] Due to their topographies,

the nanoneedle substrates were seen as an ideal candidate to exert both physical and biochemical influence over cell shape, along with their capabilities as a printing substrate. Initial studies aimed to clarify the effect of the Wnt gradients on both pathway activation, and also, in conjunction with the surface topography, on cell morphology. To this end, interferon-gamma (IFNG) was included in some conditions as a soluble factor, a cytokine with potential therapeutic applications that has previously been shown to alter cell shape.[196] Before using Wnt proteins as the bio-ink for pathway activation, efforts were made to characterise small molecule pathway activators and inhibitors using Raman spectroscopy.

4.3.1 Characterisation of Wnt activators/inhibitors via Raman spectroscopy

In the context of Wnt signalling, there is a range of small molecules that have been designed to target various aspects of the pathway for therapeutic and research applications. A collaborating group from the University of Oslo (the Krauss lab, part of the Hybrid Technology Hub) provided a number of small molecule candidates for Wnt activation and inhibition, with the hope of printing them for cell interfacing applications. As Wnt pathways play a role in almost every biological process, from developmental neural differentiation to cancer progression, this was seen as a powerful tool in adding to the potential of the platform.

These molecules were not fluorescent, and so Raman spectroscopy was used to characterise them. Spectra were captured as described in section 2.3.3. In total, 6 small molecules were analysed. The molecules supplied were CHIR99021 (activator), IWR-1, XAV939, MIX17, LGK974 and G007-LK (inhibitors). The XAV939 sample was analysed in solid powder form, while the others were in DMSO solution (at a concentration of 10 mM) as provided. In this instance, samples were placed on a glass slide for analysis, and had not been printed. It was hoped that, by obtaining spectra at the maximum possible concentration before printing, reference data could then be generated for later experiments. However, both CHIR99021 and IWR-1 did not provide usable Raman

spectra (signals were not detected due to large amounts of background fluorescence). The other spectra are shown below in Figure 4.5.

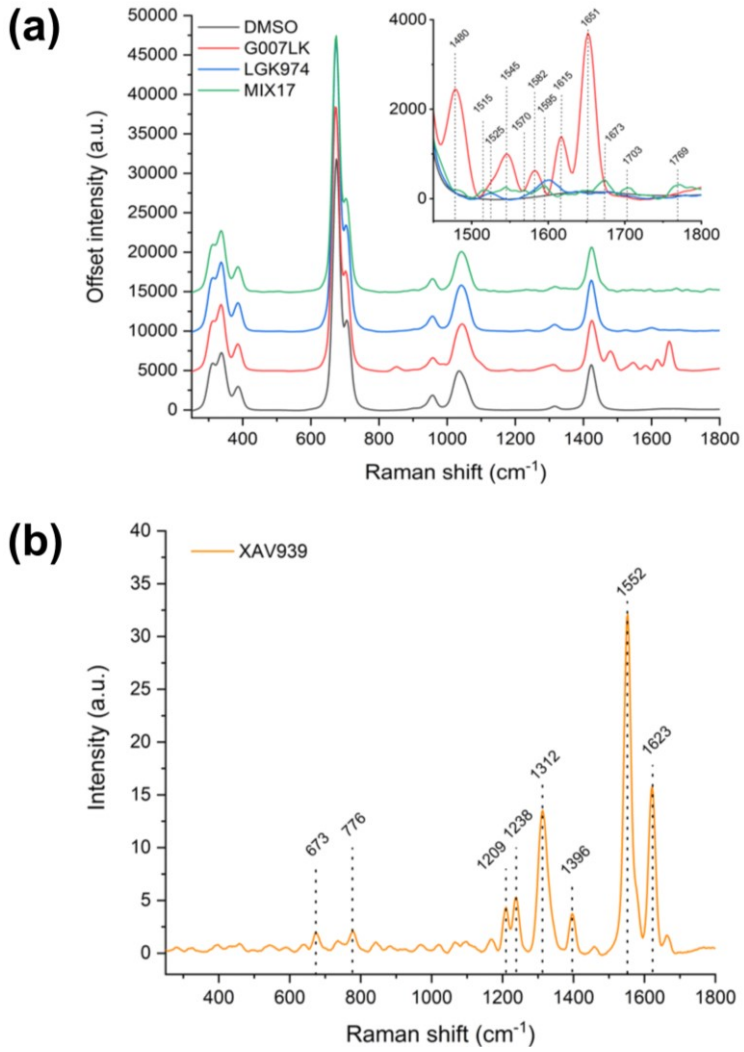


Fig. 4.5: *Raman spectra from the various small molecule Wnt activators/inhibitors provided by the Krauss lab. In (a), the spectra of samples dissolved in DMSO are shown with DMSO reference (black), G007LK (red), LGK974 (blue), and MIX17 (green). (b) shows the spectrum for the dry powder XAV939 (orange). The MIX17 and LGK974 showed no distinct differences in their spectra relative to the DMSO solvent. The G007-LK showed a series of peaks in the 1450-1700 wavenumber region that were not present in the case of DMSO (inset image in (a)). The XAV939 showed the most unique spectrum, which is to be expected as this sample was analysed in solid form. Spectra captured by Dr Vernon Lalone, plots by Dr Jelle Penders. Peak assignments in Table 2 and Table 3 (appendix).*

The MIX17 and LGK974 did not exhibit any changes in their spectra relative to the control, indicating that Raman spectroscopy would be not a viable method for detecting them. Of the molecules analysed, only two showed significant differences in their spectra relative to the DMSO solvent – XAV939 and G007-LK. The small differences observed with G007-LK, however, were present here at a concentration of 10 mM. For any printing application, this would be decreased significantly, and so would most likely not be detectable at printing concentrations. The XAV939 molecule did produce a unique spectrum, although this was taken in solid state. While the XAV939 would most likely be detectable on substrates after printing (with optimisation), it is an extremely hydrophobic molecule, and so could not be printed in aqueous solvents. As described previously, the Canon printer is not capable of printing organic solvents due to the large amounts of plastic internal parts it contains. As the BioDot AD3220 printer had not yet been obtained at this point in the project, it was decided that the better course of action would be to pursue the printing of Wnt proteins. By printing proteins in both project branches, the challenge of using organic solvents was removed, and the entire platform could readily be applied to either application with minimal changing of components.

Having decided that Wnt proteins would be used for pathway activation, a suitable cell line was then needed that would respond to the printed gradients, and would be amenable to processing via an automated image analysis pipeline.

All experiments in the following sections of this chapter are carried out on nanoneedle substrates, unless otherwise stated.

4.3.2 Finding the optimal candidate cell lines to investigate Wnt signalling

MEL10 melanoma cells

The first cell line investigated were MEL10s (mouse melanoma cells). They were chosen as a candidate due to their tendency to not form colonies, but to remain as single cells, which would facilitate the automated image analysis process. These cells also possess

the ability to form protrusions, which was expected to be enhanced by the contact guidance provided by the nanoneedle substrates. As such, any changes in cell morphology would be more pronounced, to indicate the role that the gradients might play in the behaviour of cancer cells.

At this point, the Canon printer was still in use, with 15 overprints of the bio-ink being carried out in all experiments in this section. Cells were seeded as described in section 4.2.2 above, and were treated with one of three nanoneedle substrate conditions: a printed Wnt3a gradient (1 µg/mL), the same gradient with IFNG introduced (100 U/mL) as a soluble factor, or with Wnt3a as a soluble factor in the media (1 µg/mL).

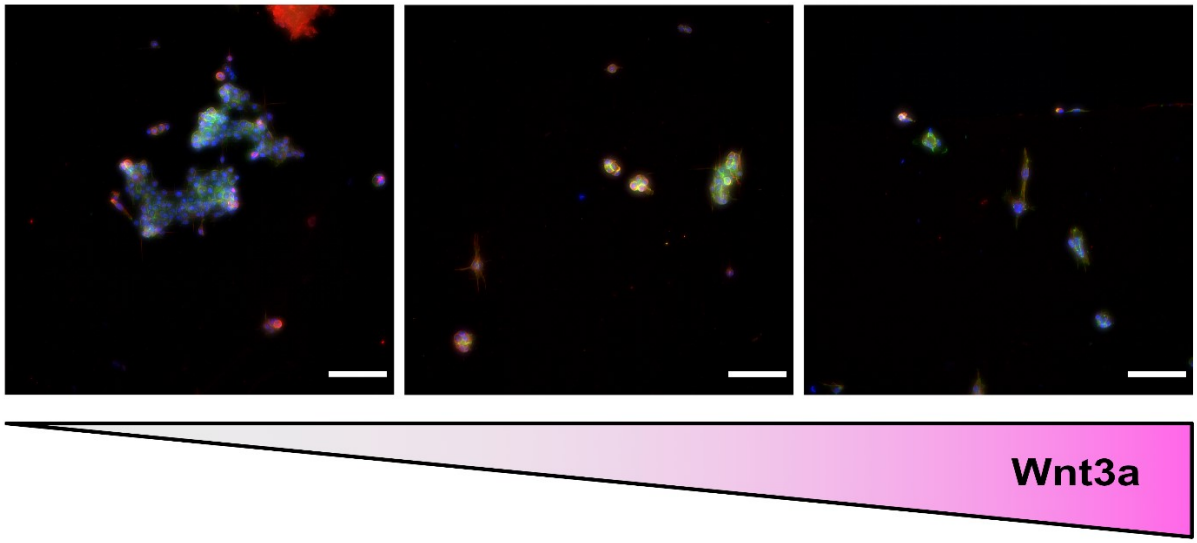


Fig. 4.6: *Representative fields of view of MEL10 cells, seeded on a Wnt3a gradient (1 µg/mL), with protein concentration increasing from left to right. Cells were generally rounded up, although more protrusions were seen at the higher Wnt3a concentration region. Blue = Hoescht, green = tubulin and red = phalloidin. Scale bars = 100 µm.*

A clear decrease in cell density was noted as Wnt3a concentration increased. The cells did not seem to spread or form protrusions when just Wnt3a was present, and in general were rounded up, often in colonies. This may have been caused by the Wnt3a concentration being in the wrong range – studies have previously been carried out to investigate effective concentration ranges *in vitro* for specific cell types. While the

studies of Massey *et al.* and Reischmann *et al.* are only somewhat comparable to these experimental conditions (different cell line and surface bound vs. soluble factor), they indicated that there may be a saturating effect at certain concentrations.[182,183] The decreasing cell density response suggested that the Wnt3a gradient was indeed present and active. The lack of protrusion formation and directionality was further summarised by visualising the distribution of protrusion directions across the gradient, with low to high referring to the three fields of view shown in Figure 4.6. It should be noted that these descriptions of directionality were carried out for the single images shown above, and not all cells across the substrate. As such, the number of cells being analysed was relatively low, in particular in low density regions.

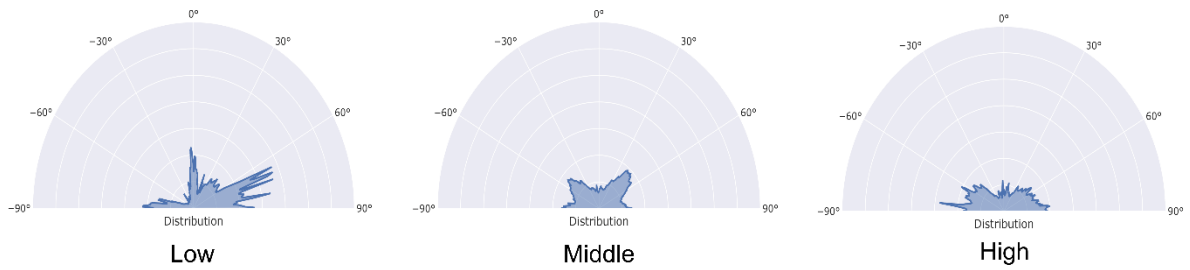


Fig. 4.7: *Distributions of protrusion directions from the MEL10 cells seeded on a Wnt3a gradient. 0° indicates protrusions going from right-to-left, while 90°/-90° indicates protrusions going from bottom-to-top. Low, middle and high refer to the three fields of view shown in Figure 4.6.*

The distribution of protrusions in the presence of a Wnt3a gradient alone (Figure 4.7) appeared to be random, with little to no interaction with the substrate surface occurring in both the low and high images (rows and columns of needles go from left-to-right and top-to-bottom in all images, allowing for slight rotations during mounting). In the middle region, some alignment was seen at 45°/-45°, suggesting that the substrate may have been rotated in this image. The alignment shown here most likely was as a result of the few single cells observed that did appear to form

protrusions (Figure 4.6, middle), although most cells were seen to be rounded up in the image. The cell density was also quite low in this condition, which may also have contributed to the lack of an obvious alignment response. To clarify whether the lack of interaction and morphological changes was due to the protein concentration being too low, a control condition was tested with Wnt3a included instead as a soluble factor.

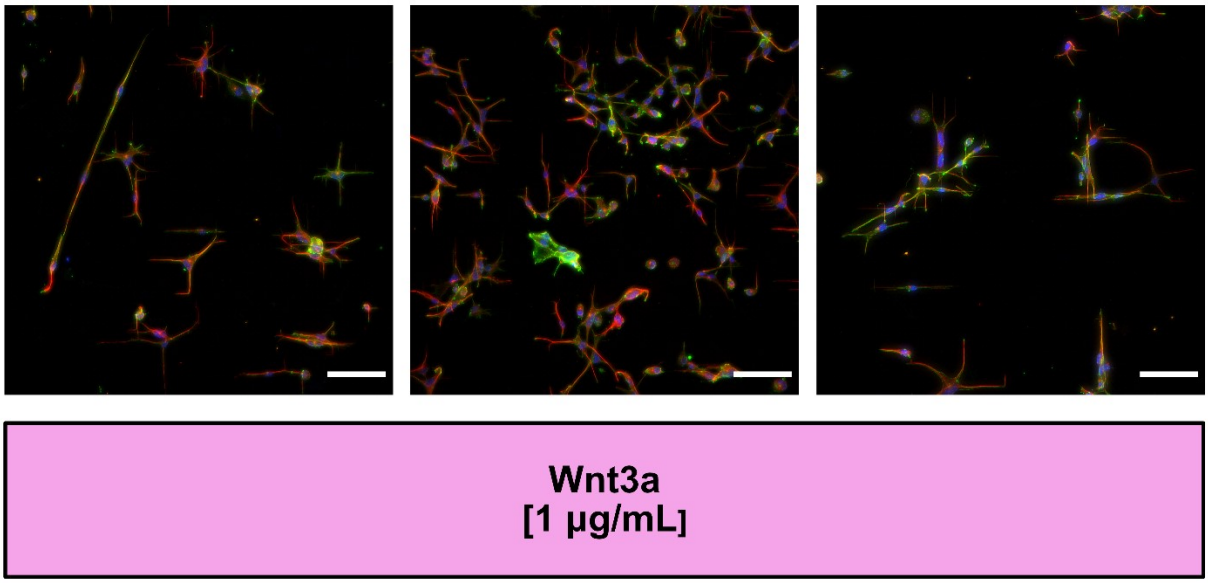


Fig. 4.8: *Representative fields of view of MEL10 cells, seeded on a nanoneedle substrate with soluble Wnt3a (1 µg/mL). Cells were seen to produce significantly more protrusions than those in the presence of a gradient, suggesting that the printed protein bio-ink concentration in Figure 4.6 was too low. Blue = Hoescht, green = tubulin, red = phalloidin. Scale bars = 100 µm.*

When Wnt3a was present as a soluble factor, the cells spread more and formed protrusions, which were not seen when Wnt3a was present as a surface-bound gradient. This supports the hypothesis that the printed concentration range was not sufficient to induce morphological changes, as the local concentration at the surface would be much lower than in this instance where the soluble factor was present. The plots in Figure 4.9 again describe the cell directionality seen in the respective fields of view in Figure 4.8.

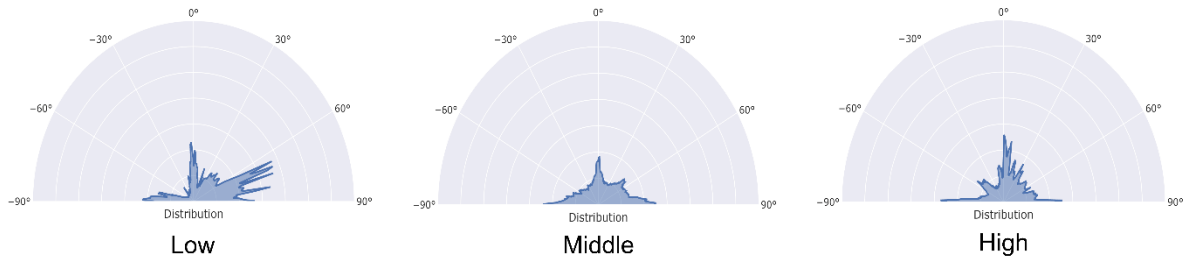


Fig. 4.9: *Distributions of protrusion directions from the MEL10 cells seeded with Wnt3a in the culture media (1 µg/mL). 0° indicates protrusions going from right-to-left or left-to-right, while 90° indicates protrusions going from bottom-to-top, and -90° indicates top-to-bottom.*

A larger number of protrusions were seen in this condition, with some alignment along the nanoneedle structures also occurring. However, there was still a considerable number of cells that were not aligning with the topographies. These data suggested that the Wnt3a was indeed playing a role in changing the cell morphology, but not all cells were being influenced in their directionality by the substrate topography. To clarify whether it would be possible to induce more cell-surface interaction, cells were seeded again onto a Wnt3a gradient, and IFNG was added into the media at a concentration of 100 U/mL.

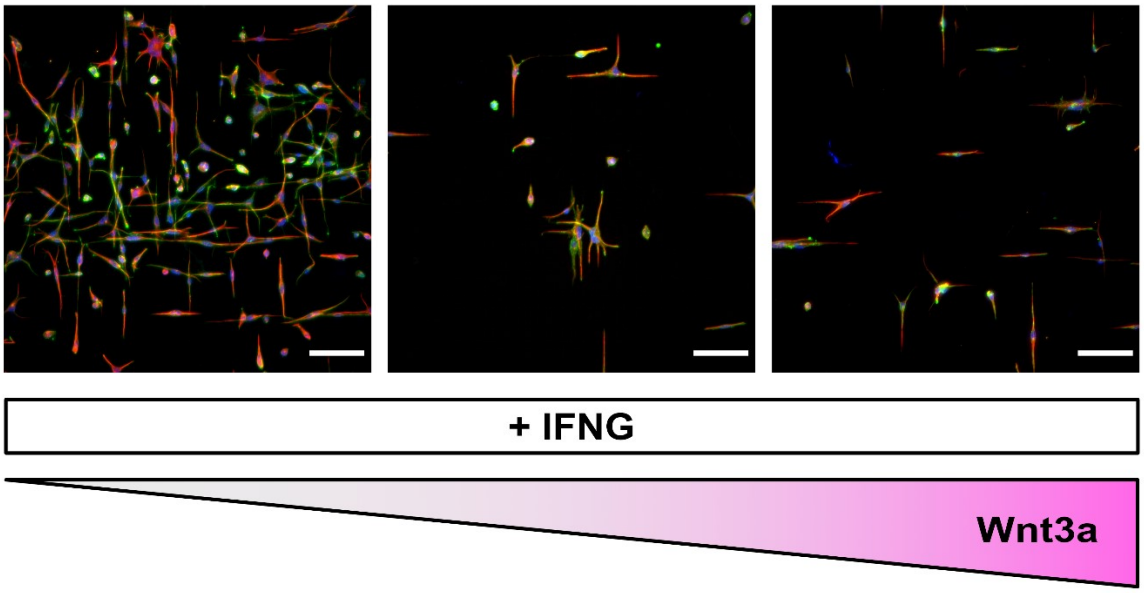


Fig. 4.10: *Representative fields of view of MEL10 cells, seeded on a nanoneedle substrate with a Wnt3a gradient (1 µg/mL), and IFNG (100 U/mL) added as a soluble factor. Cell density was again seen to decrease as Wnt3a concentration increased, and a large number of protrusions and elongation in the cells was observed. Blue = Hoescht, green = tubulin and red = phalloidin. Scale bars = 100 µm.*

Again, the cell density was seen to decrease as the Wnt3a concentration increased, indicating that the density was inversely proportional to the local concentration on the surface. In this instance, however, a clear difference was observed in cell morphology. The cells were no longer grouped in colonies and rounded, but were spreading and forming protrusions more readily across the chip. The cell directionality plots below refer to the images in Figure 4.10.

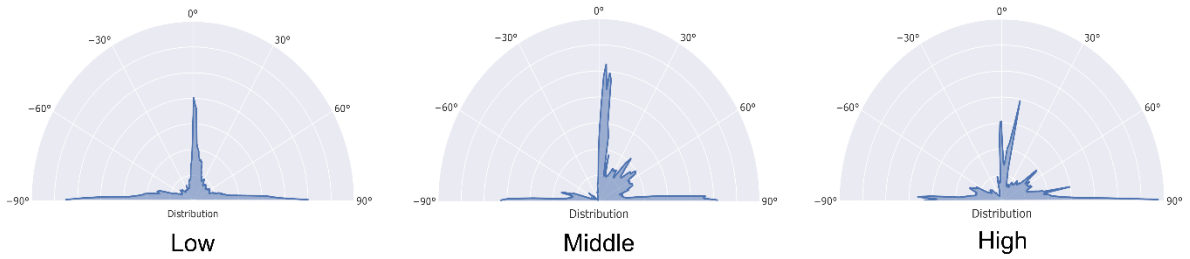


Fig. 4.11: *Distributions of protrusion directions from the MEL10 cells seeded on a Wnt3a gradient, with IFNG in the culture media.*

The cells in this condition also showed considerable alignment along the rows and columns of the needles, which was not seen in the presence of soluble Wnt3a alone. This indicated that there was indeed some interaction between the Wnt pathway and the response to IFNG in the cells, as the gradient and other surface chemistry was identical to the first condition. There was a decrease in this alignment along the nanoneedles as the local Wnt3a concentration increased. While not definitive, this initial exploration yielded results that warrant further investigations into the interaction between Wnt signalling and the role of IFNG. Unfortunately, further attempts to culture MEL10 cells proved unsuccessful, with large amounts of cell death and poor surface coverage observed across a number of attempts. As the goal of this project was the development of a high throughput tool for *in vitro* investigations, this cell line was evidently not suitable for future investigations. As such, a new cell line was chosen to further investigate the interaction between the substrates, Wnt signalling and IFNG.

19398 melanoma cells

In the place of the MEL10s, 19398 (NRAS-mutated mouse melanoma) cells were chosen to offer further insights into the interactions previously discussed. All seeding and printing conditions were kept constant, to minimise the differences between this and the previous experiment. Again, both Wnt3a gradient and Wnt3a/IFNG conditions

were tested. However, an extra control was included here with both Wnt3a and IFNG as soluble factors. Also, the immunostaining approach was altered slightly. In the previous work with MEL10s, the decreasing cell density as the Wnt3a gradient increased suggested Wnt signalling was indeed influencing cell behaviour. However, as there was no marker included to visualise pathway activation, limited conclusions could be drawn beyond the morphological changes. To overcome this, a β-catenin antibody was included. As described in section 4.1.2, β-catenin should translocate to the nucleus upon Wnt pathway activation, and so this was seen as a necessity for quantifying the response to the printed Wnt3a gradient. Hoescht was used as a nuclear stain, along with actin to visualise the cell body.

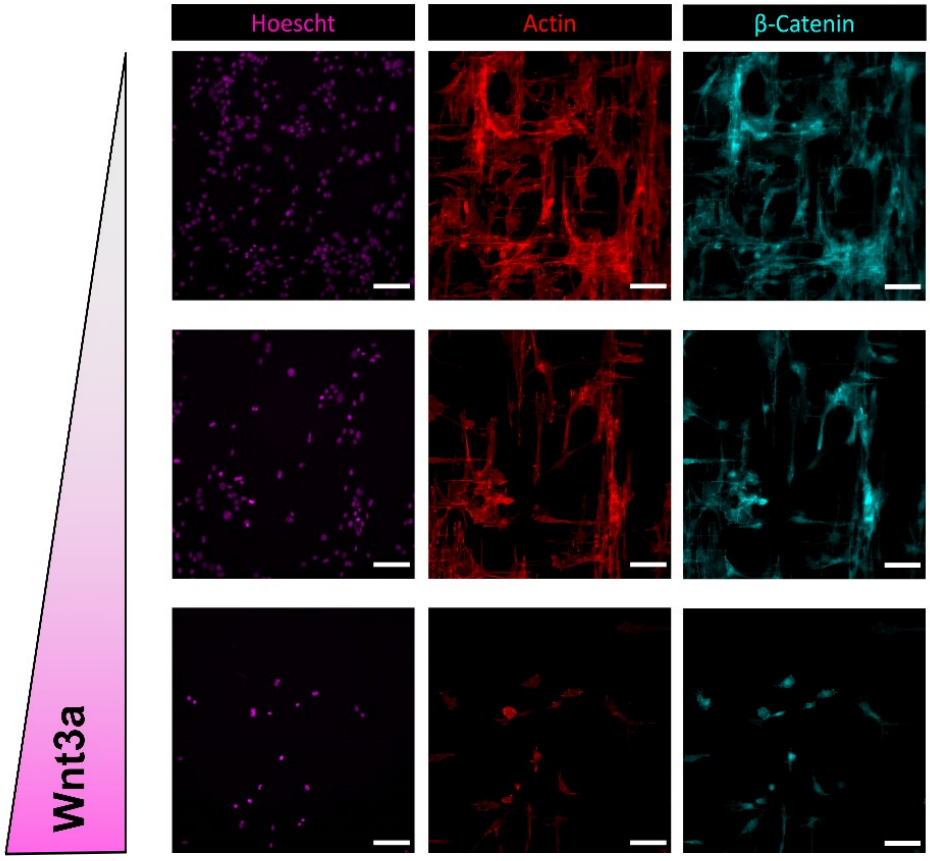


Fig. 4.12: *19398 cells seeded on a Wnt3a gradient printed at a concentration of 1 µg/mL. Individual fields of view representing the response along the gradient (increasing Wnt3a concentration from top to bottom) are shown. Magenta = Hoescht, red = actin, cyan = β-catenin. Scale bars = 100 µm.*

There was no apparent nuclear translocation of β-catenin to the nucleus in the cells along the Wnt3a gradient. However, these cells were seen to form large, dense colonies across the substrate surface, making it difficult to resolve the nuclei of single cells. There was again a decrease in cell density as the Wnt3a concentration increased, as was the case with the MEL10 cells. This further indicated that the printed Wnt3a was playing a role in cell proliferation and perhaps migration, but was not sufficient for translocation, and so pathway activation, to occur.

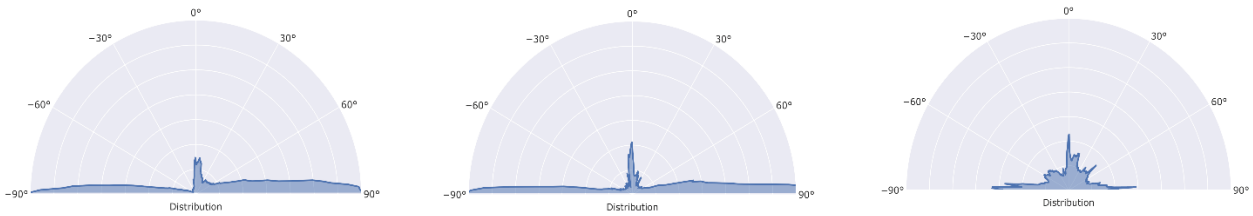


Fig. 4.13: *Distributions of protrusion directions from the 19398 cells seeded on a Wnt3a gradient (1 µg/mL).*

Some alignment of the cells was seen along the needles in this condition, particularly at the low and middle points of the gradient. The lower density and more rounded cells at the high regions most likely contributed to the less pronounced physical guidance occurring here.

It was hoped that the positive control condition, with Wnt3a in the media, would give a more obvious nuclear translocation of β-catenin. In this condition, cells were seeded onto LbL-coated substrates with Wnt3a in the media at a concentration of 1 µg/mL.

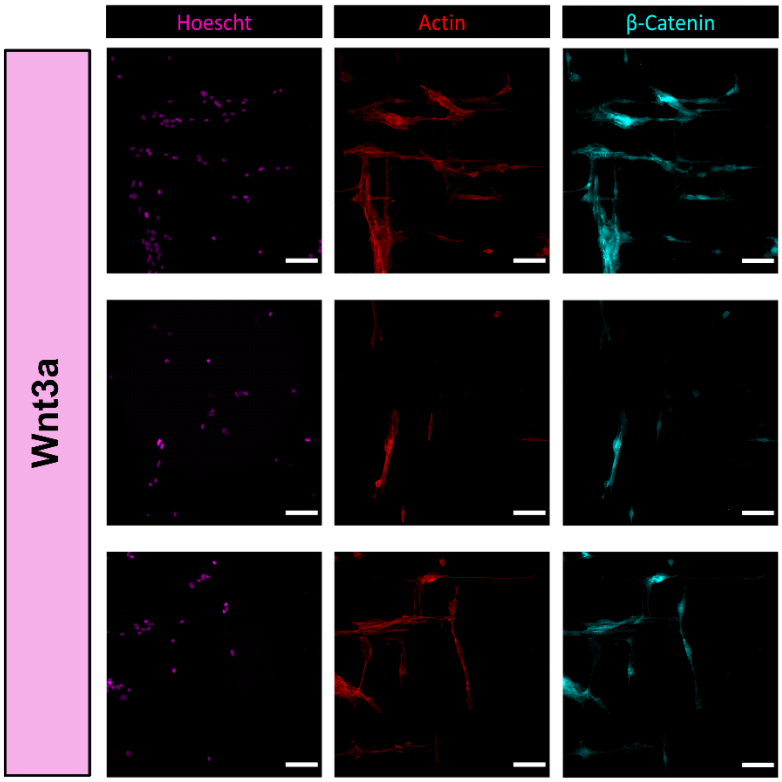


Fig. 4.14: *19398 cells on the control chip with Wnt3a (1 µg/mL) introduced as a soluble factor. Individual fields of view representing the response on the Wnt3a control chip are shown. Magenta = Hoescht, red = actin, cyan = β-catenin. Scale bars = 100 µm.*

There was also very little discernible nuclear β-catenin in this condition, with most of the signal appearing to be cytoplasmic. However, the dense colonies formed by the cells again made this difficult to discern from the immunofluorescence images. If the signal were mostly cytoplasmic, it would indicate that this cell line might not be responsive to Wnt ligands, even at these high soluble concentrations.

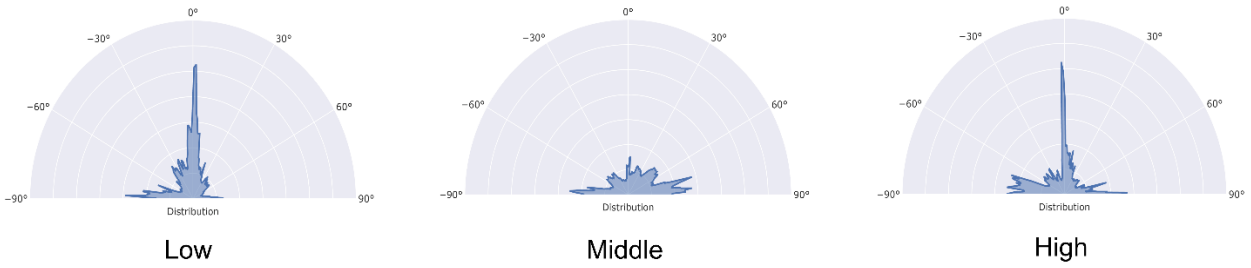


Fig. 4.15: *Distributions of protrusion directions from the 19398 cells seeded in the soluble Wnt3a control condition (concentration of 1 µg/mL).*

The protrusions of the cells also showed variation in this condition (Figure 4.15). However, the cell density was seen to be extremely low, which was consistent with the low density at high regions of the printed gradients, further emphasising the inverse relationship between cell density and ligand presence.

In the case of the MEL10 cells, the introduction of IFNG was seen to drastically increase the alignment of the cell protrusions along the needles. This cytokine was again included here with the 19398s, to investigate whether the same effect would be seen on the cell directionality.

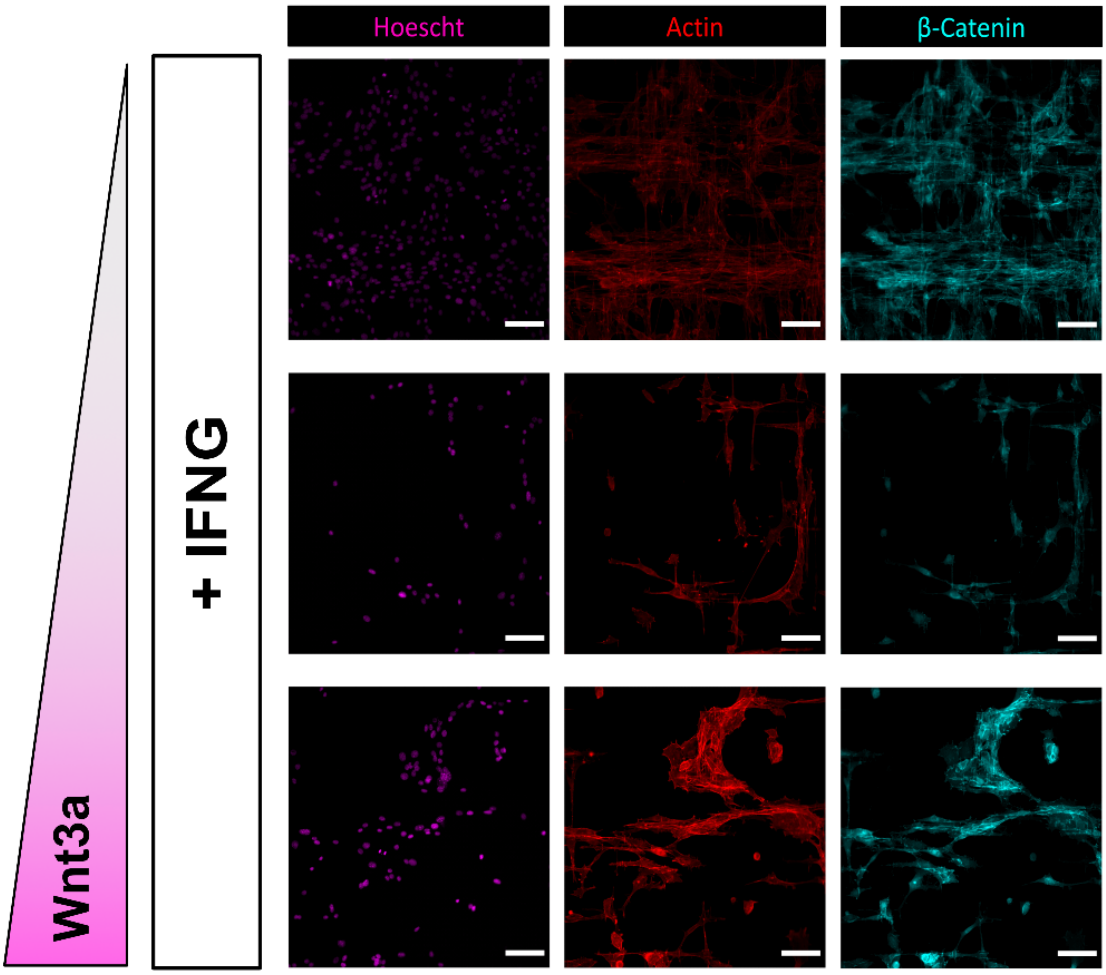


Fig. 4.16: *19398 cells on the control chip with Wnt3a gradient (1 µg/mL). Individual fields of view representing the response on the Wnt3a control chip are shown. Magenta = Hoescht, red = actin, cyan = β-catenin. Bright β-catenin signal was observed in many of the higher gradient regions, but was not definitively nuclear. Scale bars = 100 µm.*

The difference between the Wnt3a gradient and Wnt3a gradient/IFNG conditions was less pronounced in the case of the 19398 cells than they were with the MEL10s. Low regions of Wnt3a again showed the highest cell density, although there was a slightly higher density in general observed here. Again, no obvious nuclear translocation of β-catenin was occurring. While there was some brighter β-catenin signal at the higher points of the gradient, the dense colonies formed by the cells made it difficult to conclude whether the signal was nuclear or cytoplasmic.

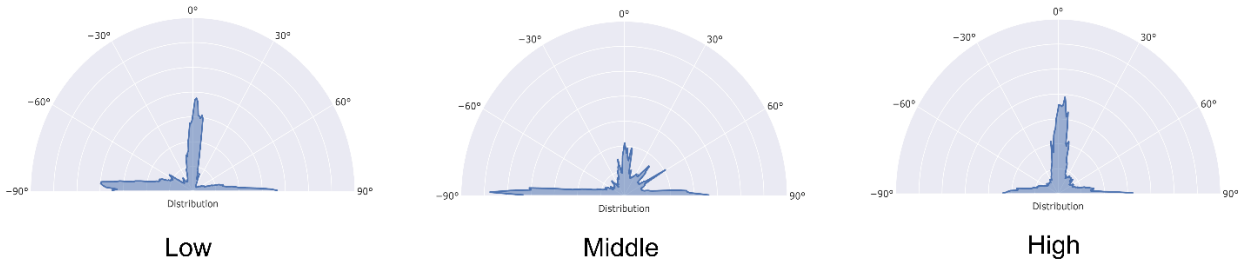


Fig. 4.17: *Distributions of protrusion directions from the 19398 cells seeded on a Wnt3a gradient (1 µg/mL), with soluble IFNG (100 U/mL).*

Little difference was observed here in the alignment, relative to the Wnt3a gradient alone (Figure 4.17). There was a slightly more directional growth of cells at the higher region of the gradient, although as the density was considerably higher here, limited conclusions could be drawn about the role that IFNG was playing.

It was clear that both cell lines investigated up to this point had their limitations. The MEL10s showed promising alignment and protrusion formation, as well as decreasing cell density with the increasing gradient. However, they were extremely difficult to culture reproducibly on the substrates, with extreme variation in the number of cells observed on substrates across experiments. This indicated that they would not be a suitable candidate for the proof-of-concept tests to be carried out here. The 19398 cells showed a similar decreasing density with increasing Wnt3a concentration, including in the control condition. This suggested that the presence of Wnt ligands was playing a role in cell proliferation, which could have applications for investigating therapeutic cancer targets. However, no clear nuclear β-catenin was observed across all conditions with the 19398s, as a result of the overly dense colonies formed by the cells. This behaviour would make automated feature segmentation (and so quantification) challenging, which would limit the use of the platform for high throughput image analysis.

The IFNG treatments had shown some interesting data, that warrant further investigation. However, the response to printed Wnt3a was not yet clear, and so it was

decided to focus on a new cell line and Wnt3a printing alone, to fully clarify the role that the printed protein might play in cell behaviour. Once this behaviour is better understood, the interaction of IFNG and Wnt ligands will again be explored. This point in the project also coincided with the transiton from the Canon printer to the BioDot printer.

4.3.3 A new candidate cell line for spatially resolved Wnt3a response.

The above experiments indicated that a new cell line was required, that would enable quantification of the nuclear to cytoplasmic ratio of β-catenin. This would allow the gradient response to be described quantitatively, and would also allow faster analysis to be carried out for future experiments. As the MEL10s and 19398s each showed limitations in their use for this project, other cell lines were considered. WM266.4 cells are human melanoma cells with a BRAF mutation. They usually have a broad, flat shape when cultured on tissue culture plastic (see Figure 4.18 for representative cell shapes. Note: small amount of debris seen in the Hoescht channel).

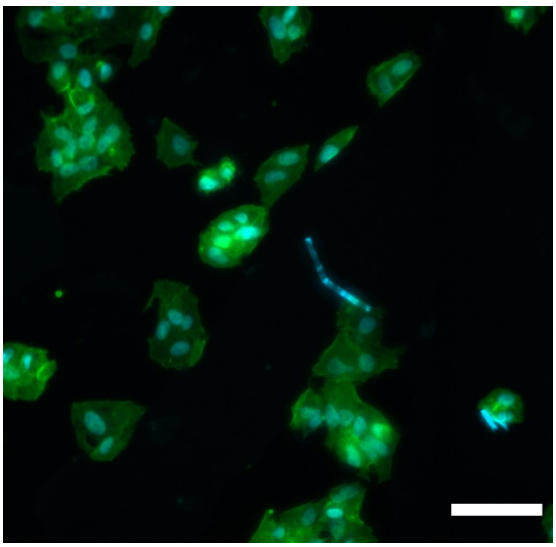


Fig. 4.18: *Representative image showing the broad, flat shape of WM266.4 human melanoma cells on tissue culture plastic, displaying very few protrusions or spindle-like shapes. Cyan = Hoescht, Green = Actin. Scale bar = 100 µm.*

As such, it was hoped that the morphogen-printed nanotopographical substrates might have considerable morphological influence on the cell shape. Previous studies also indicated that these cells do not have high levels of inherent β-catenin signalling, which would allow for changes in signalling due to the gradient to be more pronounced.[197] Although Wnt signalling is lower in WM266.4s than other cell lines, it still plays a significant role in their proliferation and cell-cycle progression.[198]

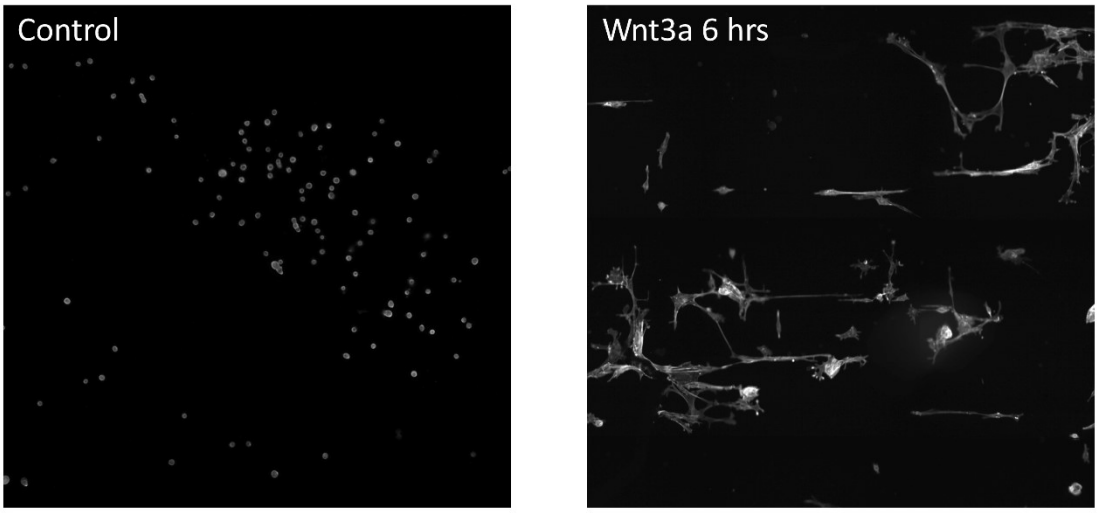


Fig. 4.19: *WM266.4 cells on nanoneedles when no Wnt ligand is present (left) and cells that have been treated with Wnt3a (1 µg/mL) for a period of 6 h. The cells were rounded up without the presence of a Wnt ligand. In contrast, when Wnt3a was present, the cells formed considerably more protrusions. Grey = actin.*

When the WM266.4 cells were seeded on negative control nanoneedles (substrates coated in heparin/chitosan bilayers from the LbL process but no Wnt ligand), they tended to round up and did not at all aggregate. However, when Wnt3a ligand was present (as either a soluble or surface bound factor), significant morphological changes were seen (Figure 4.19). In some cells, protrusions were seen to form along the rows and columns of the needles. The fact that these cells were less inclined to form large aggregations meant that the analysis process would also be much easier, should a response to the printed Wnt ligands be observed.

4.3.4 Initial investigations and pipeline development

The image analysis pipeline was developed as described in Chapter 3. ilastik provided pixel probability masks for the feature types (in this instance there were three features: the nucleus, from DAPI staining; the cell body, from actin; and the background). CellProfiler was then used for segmentation and measurements of the features that ilastik had designated. For analysis, each substrate was initially divided into a 5 × 5 grid, and each tile was analysed individually. Images were initially taken on the Axio observer widefield microscope (Zeiss). It should be noted that the resolution of these initial images made resolving the nuclear/cytoplasmic ratio of β-catenin difficult. As such, later experiments were imaged on the spinning disk confocal microscope (3i).

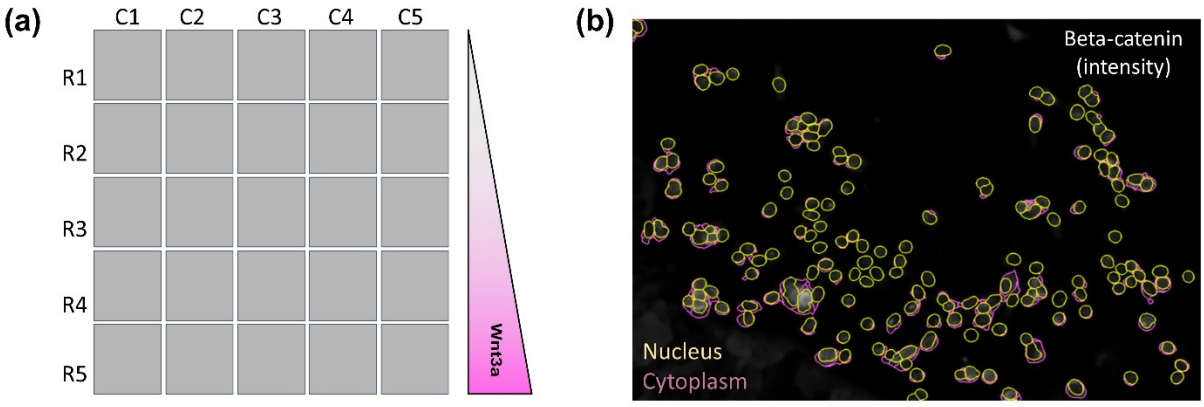


Fig. 4.20: *A schematic of the image analysis pipeline. (a) The tiled image of the nanoneedle substrates was divided into a grid of 5 rows and 5 columns, with Wnt3a concentration increasing from R1 to R5. (b) ilastik was then used to carry out segmentation to generate nuclear (DAPI or Hoescht) and cell body (actin) masks. CellProfiler was then applied in conjunction with these masks to segment and extract data on the various channels present in each experiment. The cells in this instance were quite rounded up, leading to little distinction between the nucleus and cytoplasm. Figure adapted from Dr Lucas Dent.*

With the pipeline in place, an initial experiment was planned with the WM266.4 cells. Three conditions were included in the first gradient experiment: negative control

nanoneedles (only coated in heparin/chitosan), a positive control with Wnt3a added to the media at 300 ng/mL, and the Wnt3a gradient (printed at a concentration of 1 µg/mL on the BioDot). Cells were seeded on the substrate for 6 h before fixing and staining.

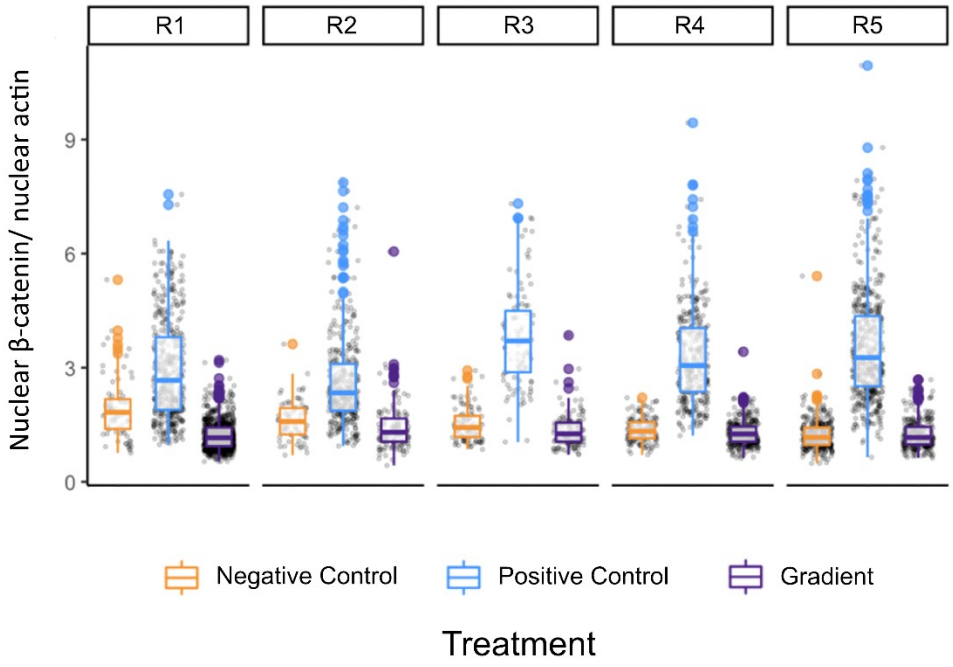


Fig. 4.21: *Response of WM266.4 cells to Wnt3a after 6 h. The ratio of mean nuclear β-catenin to mean nuclear actin is shown. No obvious gradient was observed, but an increased nuclear signal was seen in the positive control. Wnt3a concentration is increasing from tile R1 to tile R5 in the gradient condition. Box edges refer to the interquartile range (IQR), while the central bar within the box represents the median value for each condition. Box whiskers extend 1.5 × IQR for each condition. Figure adapted from Dr Lucas Dent.*

In Figure 4.21 and Figure 4.22, the nuclear β-catenin was normalised to nuclear actin signal, since the widefield microscope did not give high enough resolution in this instance to resolve the nuclear/cytoplasmic ratio of β-catenin. Form the mean nuclear β-catenin, there was no obvious gradient response at the 6 h timepoint, indicating that the printed Wnt3a was not inducing β-catenin translocation in the WM266.4s.

However, the positive control cells did show an increase in the nuclear β-catenin relative to the other conditions, indicating that this cell line was indeed responsive to exogenous Wnt signalling. This suggested that either the Wnt3a bio-ink concentration was too low to induce translocation, or the treatment time was too short for the surface-bound Wnt3a.

As indicated by Massey *et al.,* both the concentration and the treatment time play a significant role in the amount of nuclear β-catenin observed.[182] The authors observed a peak in the signal in their system by the 6 h timepoint, before seeing a drop off in the subsequent hours. It should be noted that the signalling dynamics in the soluble ligand condition are expected to be quite different to those in the surface-bound ligand, along with the fact that a different cell line was used, and so these results should be used as guidelines only. It is likely that cells would require significantly longer on gradient substrates to elicit a similar response to those observed in the positive control substrates. As such, a 48-h timepoint was also included in this preliminary experiment.

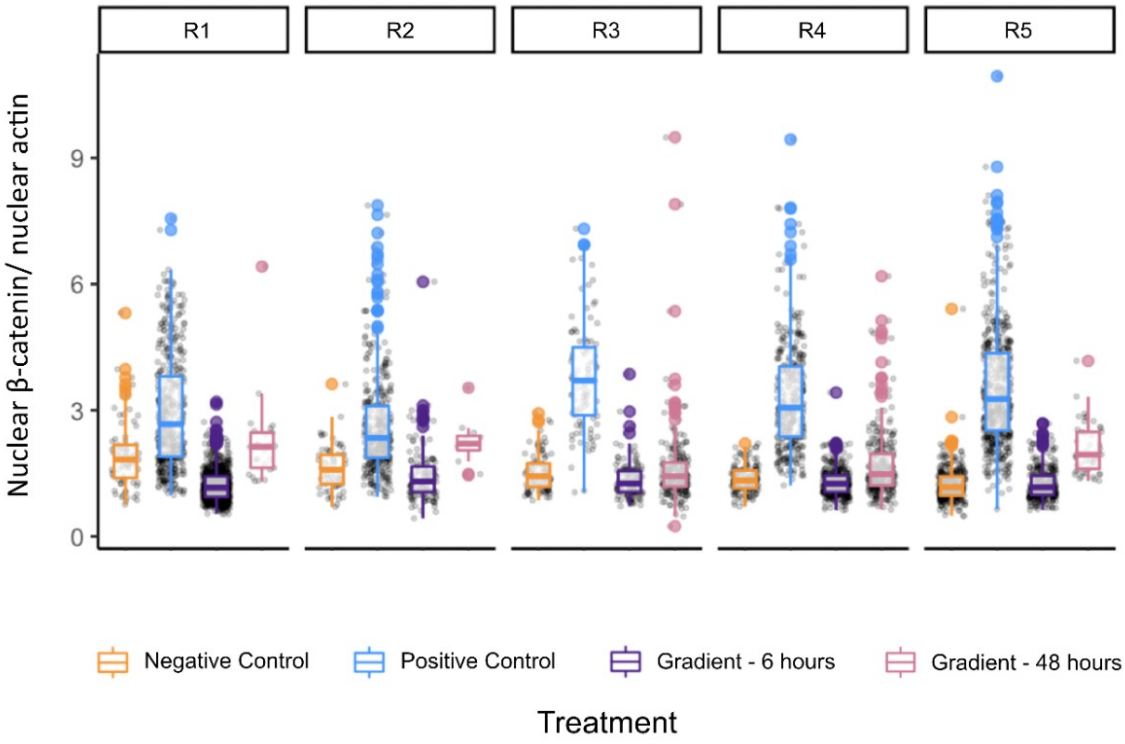


Fig. 4.22: *The response of WM266.4 cells seeded on printed Wnt gradients, with the 48 h timepoint included. The nuclear β-catenin signal is normalised to the nuclear actin in each image. As before, Wnt3a concentration is increasing from tile R1 to tile R5. Box edges refer to the interquartile range (IQR), while the central bar within the box represents the median value for each condition. Box whiskers extend 1.5 × IQR for each condition. Figure adapted from Dr Lucas Dent.*

There was again no obvious gradient response in Figure 4.22, with the positive control cells being considerably higher than those at any point along the gradient substrates. However, an increase in the nuclear β-catenin was seen at all points along the gradient at 48 h relative to the 6 h timepoint. This indicates that the length of time the cells spend on the gradient does play a role in the response observed, but that the effective local concentration of the printed ligand would need to be significantly higher to observe nuclear translocation.

This initial study, although not demonstrating a gradient response, was useful in determining that this cell line was suitable for follow-up investigations due to their

sensitivity to exogenous Wnt3a. It also gave an indication of the lower range of the ligand concentration that would be needed to induce translocation as a surface-bound cue. It was evident that for future experiments, the ligand concentration needed to be increased. As such, a second experiment was carried out with the WM266.4 cells, with the bio-ink concentration being increased from 1 µg/mL to 4 µg/mL.

4.3.5 β-catenin response at higher printed Wnt3a concentrations

The above experiment was again repeated, with WM266.4 cells being seeded on Wnt3a gradients for 6 h, before fixing and staining. However, in this instance, the concentration of the bio-ink was increased to 4 µg/mL.

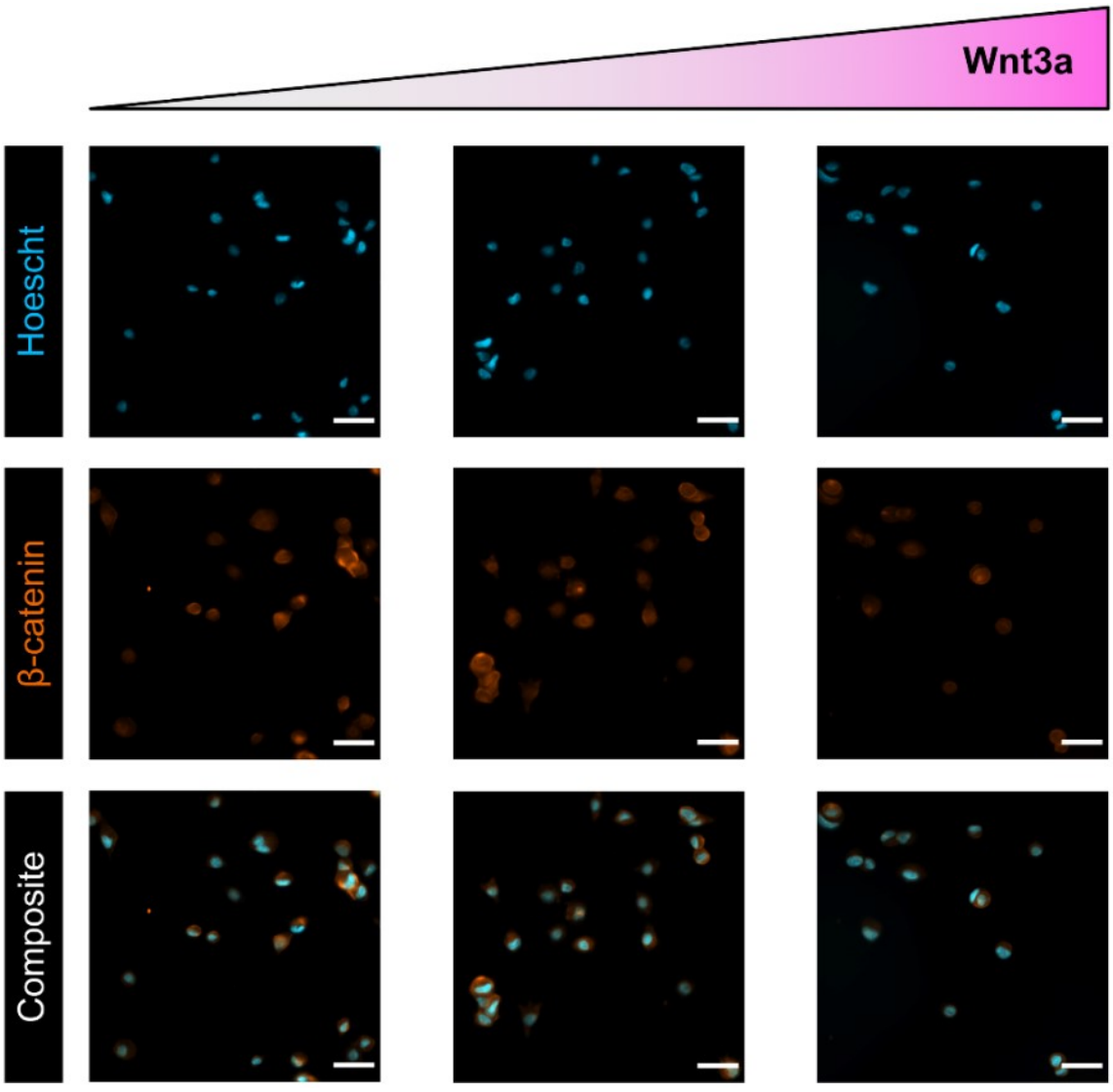


Fig. 4.23: *Representative fields of view along a chip that has been printed with a Wnt3a gradient (4 µg/mL), with WM266.4s seeded for 6 h. Nuclear β-catenin was observed in most cells at the high region of the gradient, indicating that this concentration and timepoint were sufficient for Wnt pathway activation. Cyan = Hoescht, orange = β-catenin. Scale bars = 50 µm.*

As can be seen in Figure 4.23, there was a significant amount of β-catenin translocation occurring across the substrate. This indicated that printed gradients of Wnt3a could successfully activate the Wnt pathway on a timescale comparable to that reported by Massey *et al.*[182] However, there was comparable amounts of translocation occurring at the middle and low regions of the gradient to that of the high region. This suggested that the bio-ink concentration of 4 µg/mL was possibly too high, causing activation even in regions where there was a relatively small amount of protein printed. By combining this data with those collected from the previous experiment (where Wnt3a was printed at a concentration of 1 µg/mL), an upper and lower limit of the required protein for activation was obtained.

It was also observed that the cells in general were quite rounded up on the chips in this experiment, although some did show protrusion formation. This may have been as a result of the relatively short time that the cells were seeded for before fixing and staining, although similar inconsistencies had been noted in previous experiments.

Having determined that 1 µg/mL and 4 µg/mL bio-ink concentrations gave the lower and upper ranges of nuclear β-catenin response, a gradient of Wnt3a was then printed at 2.5 µg/mL. As the cells were seen to respond after 6 h in the previous experiment, this timepoint was maintained here. For the analysis, the entire substrate was split into the individual tiled fields of view, rather than the 5 × 5 grid used in previous visualisations. From this point on, substrates were imaged on the spinning disk confocal microscope, to better resolve the nucleus and cytoplasm of cells.

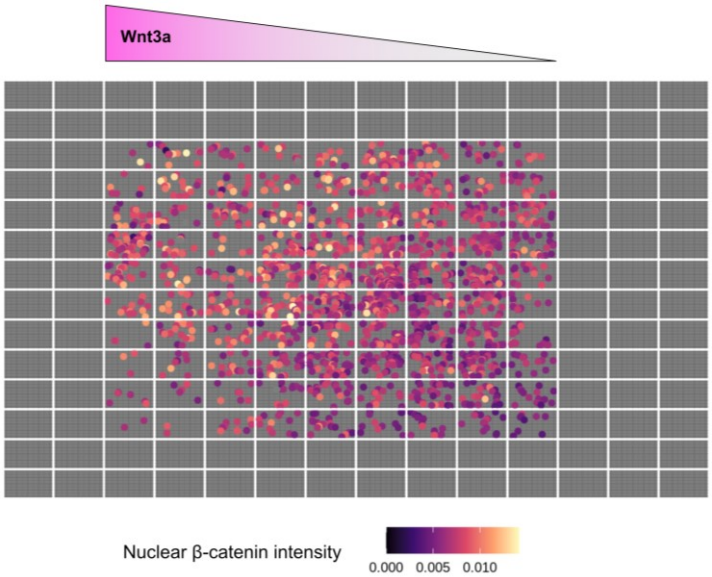


Fig. 4.24: *Heatmap of the mean nuclear β-catenin, with WM266.4 cells seeded on a Wnt3a gradient (2.5 µg/mL). Each datapoint represents a single nucleus. Figure adapted from Dr Lucas Dent.*

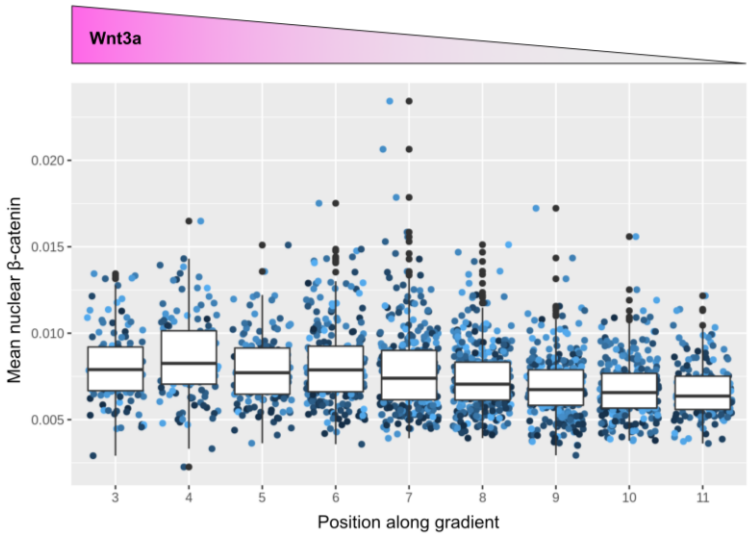


Fig. 4.25: *Box plot showing mean nuclear β-catenin in WM266.4 cells seeded on a Wnt3a gradient (2.5 µg/mL). Column numbers refer to the columns in Figure 4.24. Box edges refer to the interquartile range (IQR). The central bar within the box represents the median value for each condition. Box whiskers extend 1.5 × IQR for each condition. Figure adapted from Dr Lucas Dent.*

In Figure 4.24, the mean nuclear β-catenin on a printed gradient substrate is visualised in an overview heatmap format, while Figure 4.25 shows the same substrate as a binned boxplot for the mean nuclear β-catenin. An increase in this signal was indeed seen as the gradient concentration increased. This was encouraging, as it further confirmed that the printed Wnt3a gradients were indeed active, and were interacting with cells seeded on them to activate the signalling pathway.

What was also apparent was the decreasing cell density along the gradient, with far fewer features detected by the pipeline at higher Wnt3a concentrations. This aligned well with the observations from previous experiments and cell lines, further indicating that Wnt3a was playing a central role in cell proliferation, and validated that this gradient system could be applied for cell proliferation studies. Both of these facts were strong indications that this platform has potential as a tool for *in vitro* cancer studies.

However, the ratio of nuclear to cellular β-catenin also needed to be considered, since this translocation occurs as a result of the pathway activation. As such, there should be the same increase in this ratio as the position along the gradient increased. The confocal microscope enabled resolving of both the nucleus and the cytoplasm, even in the case of rounded up cells.

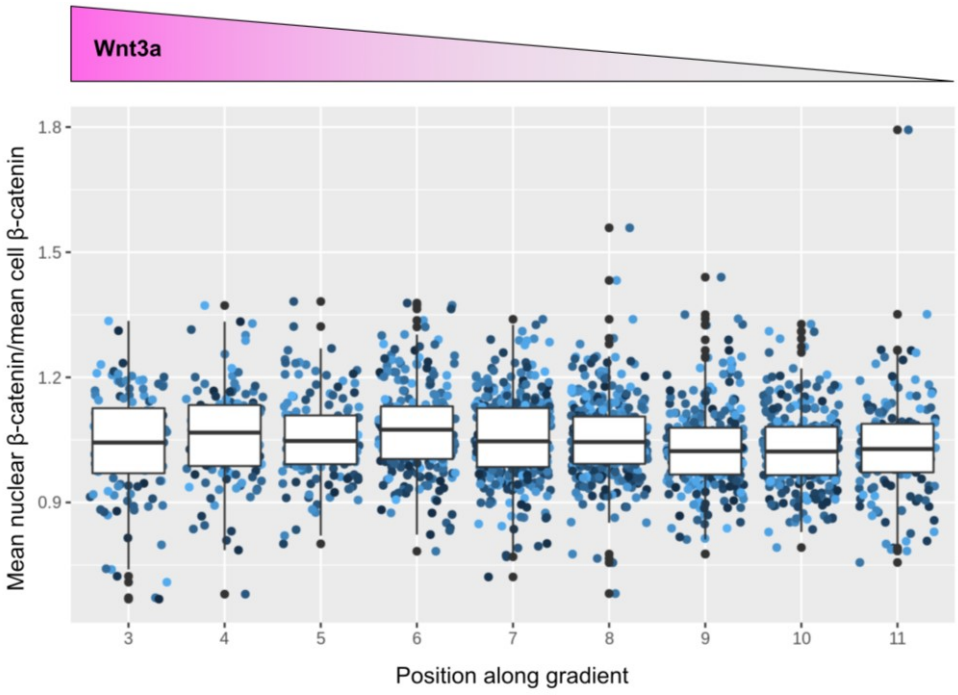


Fig. 4.26: *Box plot showing the mean ratio of nuclear to cell β-catenin in WM266.4 cells seeded on Wnt3a gradient 1 (2.5 µg/mL). Each datapoint represents a single nucleus. Box edges refer to the interquartile range (IQR), while the central bar within the box represents the median value for each condition. Box whiskers extend 1.5 × IQR for each condition. Figure adapted from Dr Lucas Dent.*

The same trend from Figure 4.25 was observed when the ratio of mean nuclear to cellular β-catenin signal was calculated, although the response was seen to be relatively weak (Figure 4.26).

While these data were encouraging as to the ability of this platform to be utilised for future investigations into signalling pathways in cancer, there still existed considerable noise and inconsistency in the system. As seen from the investigations in Chapter 3, the printing system does not produce uniform responses across the entire gradient, possibly as a result of wetting or cell seeding artefacts. While data from the substrate shown above suggested a graded response in nuclear β-catenin, other substrates from the same experiment did not show the same (Figure 4.27 and Figure 4.28 highlight these differences in responses).

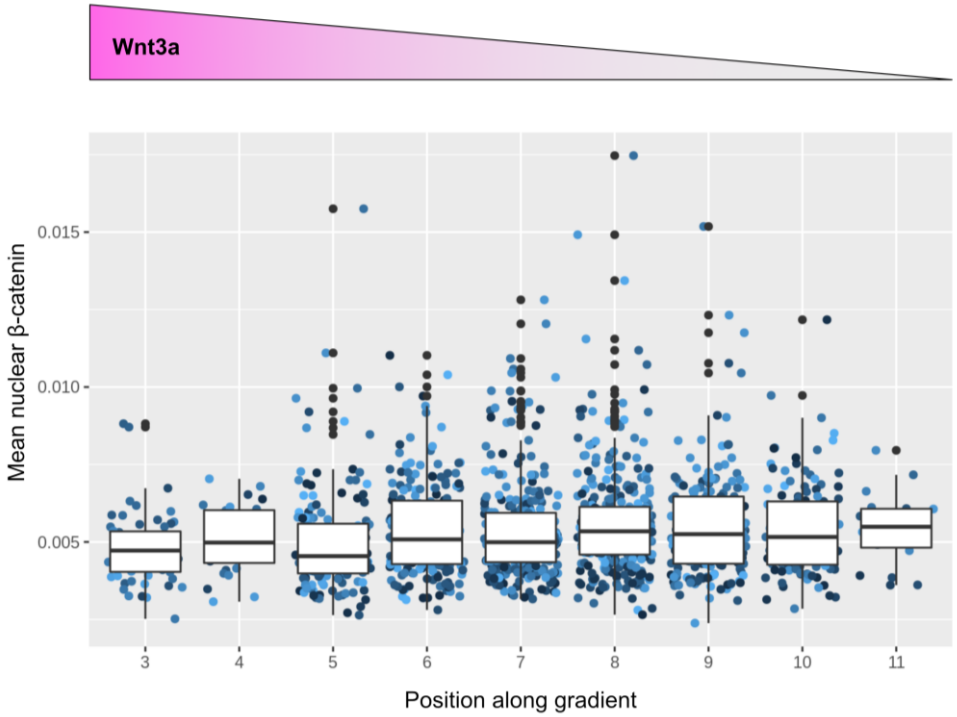


Fig. 4.27: *Box plot showing the mean ratio of nuclear to cell β-catenin in WM266.4 cells seeded on a second Wnt3a gradient (2.5 µg/mL), within the same experiment as that shown in Figure 4.25. The variation across substrates within printing batches is apparent. Each datapoint represents a single nucleus. Box edges refer to the interquartile range (IQR), while the central bar within the box represents the median value for each condition. Box whiskers extend 1.5 × IQR for each condition. Figure adapted from Dr Lucas Dent.*

For both the nuclear β-catenin (Figure 4.27) and nuclear/cellular ratio of β-catenin (Figure 4.28 below), no gradient was observed on this second substrate. It should be noted that the cell density was considerably lower on this substrate than in the condition discussed in Figures 4.24-4.26. This suggested that as in the spinal cord model from Chapter 3, there were some inconsistencies in the system that needed to be overcome before this platform could be expected to produce reproducible results.

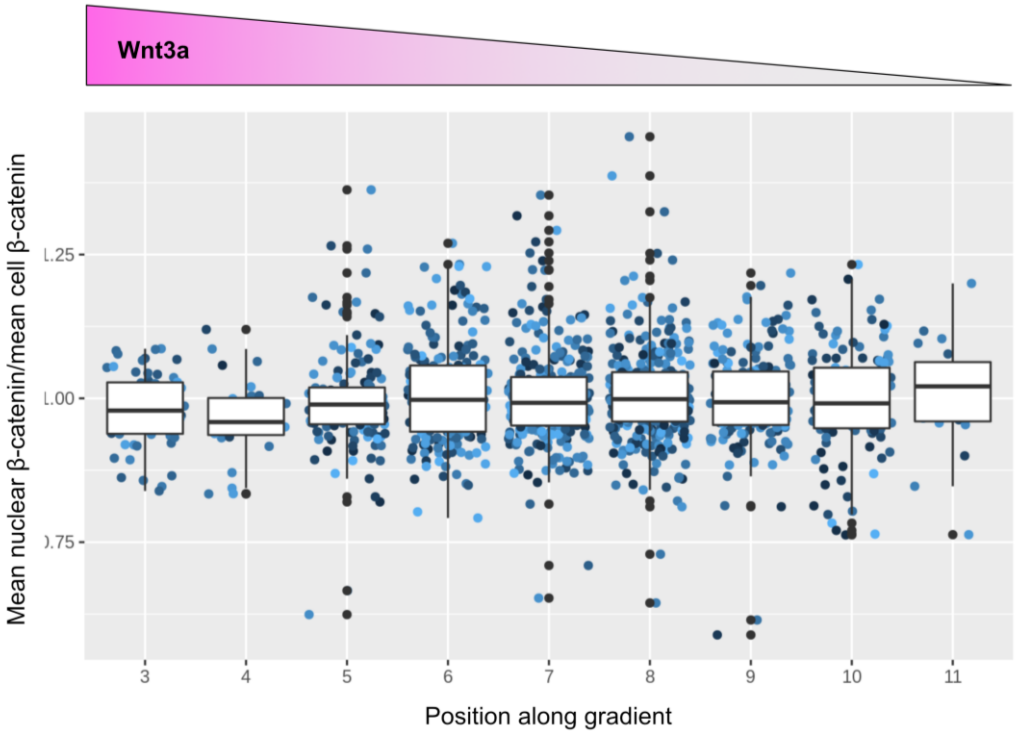


Fig. 4.28: *Box plot showing the mean ratio of nuclear to cell β-catenin in WM266.4 cells seeded on a second Wnt3a gradient (2.5 µg/mL). Each datapoint represents a single nucleus. Box edges refer to the interquartile range (IQR), while the central bar within the box represents the median value for each condition. Box whiskers extend 1.5 × IQR for each condition. Figure adapted from Dr Lucas Dent.*

4.4 Discussions and future work

The preliminary experiments described above succeeded in identifying a candidate cell line that was responsive to Wnt signalling, and could be used to investigate the application of printed morphogen patterns in cancer investigations.

MEL10 mouse melanoma cells showed strong morphological and cell density changes in the presence of Wnt3a ligands. This cell line also showed increased directionality when exposed to both Wnt3a and IFNG, which could potentially be leveraged to better understand the role that interferons might play in novel cancer therapeutics. However, difficulty in culturing the MEL10 cells limited the throughput of the technique considerably.

19398 mouse melanoma cells also showed a decreasing density with increasing Wnt3a concentration. This indicated that the Wnt3a signalling pathway was playing a central role in proliferation of these cancer cells, which could have potential applications as a therapeutic target for the slowing of cancer progression. However, the 19398s did not show any definitive nuclear translocation of β-catenin when exposed to surface-bound or exogenous Wnt3a. The large, dense colonies of cells formed on the substrates also made quantifying the response (via immunofluorescence) challenging. An ideal cell candidate would form less colonies and more single cell layers, which would allow for clearer visualisation of the nucleus and cytoplasm of each cell.

This was achieved with the WM266.4 human melanoma cells. While their morphological changes were seen to be inconsistent, the separation obtained between cells on the substrate enabled the development of an image analysis pipeline to quantify the levels of nuclear β-catenin, which was used a metric here for Wnt3a pathway activation. A concentration range was identified that induced translocation in the cells, although again this was not as consistent as would be needed for reproducible results. While this was a promising demonstration of the capabilities of this material system in cancer biology, more refining of the method is needed before an effective *in vitro* platform can be realised. A sharper increase in the printed morphogen might illicit a more contrasting response between the higher and lower regions of the gradient, which could readily be achieved using the drop-on-demand capabilities of the BioDot printer.

While the WM266.4s did show a response to both the printed and exogenous Wnt3a, the shape of the cells was seen to be inconsistent across substrates. Some cells did form protrusions and elongated cell bodies, while others were rounded and did not appear to interact with the surface topography significantly. Future investigations could explore the mechanisms determining the morphologies observed in these cells in response to both the gradient and the surface topography, along with the fixing

timepoint. Once the cause of these differences was identified, IFNG could again be introduced to the experimental design to further explore its therapeutic potential.

Other morphogen bio-inks could also be considered. As discussed in section 4.1.3, hedgehog signalling plays a central role in the development and progression of many cancers. Previous work described in Chapter 3 has already detailed the printing of Shh patterns for cell interfacing, which could be applied here in place of Wnt3a. However, consideration would be needed for the cancer type and cell line that would be a suitable model for investigating this signalling pathway *in vitro*. Printing of interferons, small molecules or other bio-active compounds could also be utilised, should a different target or application be considered.

Chapter 5

Conclusions and future work

Chapter 5: Conclusions and future work

Spatial patterns of bioactive molecules play a central role in biological systems across all scales, from early-stage embryo processes to entire tissues and organs. While many engineering approaches have been presented to investigate the generation of morphogen and small molecule gradients for *in vitro* modelling, current methods all have associated limitations. Simple 2D coatings offer facile and rapid cell culturing, but are hindered by the lack of spatial control that can be exerted, preventing them from creating bespoke local environments on the same substrate. They also lack the dimensionality of the environment that would be experienced by cells *in vivo*. 3D scaffolds offer an alternative method that more accurately maps the architecture of biological systems, such as the extra cellular matrix. By generating hydrogel structures from various natural or synthetic molecules, and functionalising the surfaces as required, tailored systems can be designed to recapitulate complex biological systems *in vitro*.[42,52] However, the challenge of presenting surface-bound factors in a spatially resolved manner remains. Some attempts have been made to generate gradient-patterned gels, although this configuration is not feasible for all applications.[54] The inherent 3D structure of gel systems also prevents a top-down approach such as inkjet printing from being used to deposit bio-inks for pattern generation. Early stage studies with organoids have shown some promise in recreating neural systems *in vitro*, but are still limited by the long culture times and relatively low throughput that they provide.[147,150]

Microfluidic systems have shown considerable potential as an engineering platform for pattern generation. The use of dynamic, flow-based gradients enables the constant presentation of nutrients, growth factors and other bioactive molecules to cells in culture. This allows for both 2D and 3D cell and tissue patterning, and has been applied across a range of research areas, including in neural development and in cancer.[56,70] As manufacturing methods advance, this may become one of the primary techniques for interrogating complex biological systems. However, microfluidic devices are

currently limited by the relatively low throughput and complexity of fabrication, with systems proving difficult to modify beyond the addition of a different solution into the inlets. Polymer casting has decreased the cost of these devices considerably, and undoubtedly this will decrease further as more advancements are made.

Until these challenges are overcome, however, it is clear that there exists an opportunity for a novel platform that presents patterned biomolecules at the cell-material interface. As described in the previous chapters, inkjet printing has been shown in the past to be a valuable tool in influencing cell behaviour, through the controlled deposition of bio-inks.[76,83] While this technique has been used in preliminary studies, it is apparent that there is still significant potential to expand its capabilities further. This has possible applications in stem cell therapy, where the generation of controlled subpopulations of cell types could prove invaluable. It also could enable the investigation of complex gradient-patterned biological systems *in vitro*, that might otherwise prove challenging to model.

5.1 Material system development

In chapter 2, the development of a material platform was described that built upon the previously developed silicon nanoneedle platform in the Stevens group.

A number of functionalisation methods were considered for cell interfacing applications with this system. By leveraging electrostatic binding via the layer-by-layer technique, a method was identified that would enable the binding of proteins and other bioactive molecules, without causing significant changes to the functionality of the molecule in question. Through the use of scanning electron microscopy, contact angle measurements, Safranin-O staining, X-ray photoelectron spectroscopy and atomic force microscopy, the addition of heparin/chitosan bilayers onto the surface was confirmed. The Safranin-O staining did highlight some inconsistencies in the coating at the edge regions of the substrates. This was most likely as a result of wetting/drying artefacts during the coating process, which was carried out by

sequential submerging of the substrate in the charged materials. Although further steps could be taken to control the wetting and drying of substrates, for the scope of this work the layer-by-layer approach was effective in binding the proteins required. For future applications of the platform, other charged polymers could be considered for inclusion in the bilayer, should further functionality be required. Composite materials could readily be introduced by mixing solutions before the coating step, enabling more targeted coatings to be generated.

Inkjet printing was then investigated as a means to pattern bio-relevant molecules. Although small molecule pathway activators and inhibitors were initially considered, the decision was eventually made to focus solely on the patterning of proteins for directing cell behaviour. By maintaining one bio-ink type across all applications within this work, the modular nature of the material system was maintained. Antibody staining of the protein patterns generated by the Canon and BioDot printers showed that gradients could be readily generated, and further cell interfacing experiments described in chapters 3 and 4 confirmed that the proteins being printed retained their activity after deposition.

Although the BioDot proved to be a reliable method for pattern generation, some challenges remain. Slight inconsistencies in the pattern generated were observed, with dark spots at the positions that droplets impacted the surface. A more homogenous, reproducible gradient could improve the consistency of response observed in cells seeded on the substrates. Modifications to the time between droplet deposition during prints could overcome this issue, although a small number of drying artefacts are an inherent limitation of the printing approach. For applications where a more significant increase in bio-ink concentration is required, the pattern could be altered to create a sharper profile by increasing the number of drops drastically along the pattern (as demonstrated by the use of an exponential-like pattern in this work). Multiplexing of inks is also an exciting opportunity for modelling neural network

formation, particularly in the neural tube, where both the dorsal and ventral halves are patterned by opposing gradients.

5.2 Inkjet printing for the modelling of developing neural systems

Chapter 3 described the generation of a spinal cord model through the use of inkjet printed Shh gradients. The neural tube was an ideal candidate for proof-of-concept investigations with this material system, due to the central role that gradients play in the early-stage embryo. Optimal protein concentration for the generation of ventral subtypes was shown with both the Canon and BioDot printers, and an image analysis pipeline was developed to interrogate the response observed in embryonic stem cells seeded on the patterns.

Ventral subtypes were indeed seen to emerge, with the presence of transcription factors such as Olig2 and Nkx6.1 confirming the cell types being generated. The generation of motor neuron progenitors was particularly encouraging, as this was seen as one of the primary benchmarks for a successful spinal cord model *in vitro*. However, while the generation of ventral subtypes was occurring, the image analysis pipeline highlighted considerable amounts of noise and variation within the system. Some biological variation is inherent in all systems where inter- and intra-cell signalling are taking place, but this inconsistency is the main limiting factor in realising the potential of this material system. As mentioned in section 5.1, challenges in reproducibility of gradient generation were present, which was detrimental to the cell interfacing applications described herein. More consistency or a more efficient quality control process would be needed, before this tool could confidently be applied to other biological areas. As the main method to confirm the presence of the printed gradient was by seeding cells and observing their response, the throughput of the technique was being hindered (since cell culture experiments usually take weeks to generate output data).

One potential solution would be to carry out immunostaining of representative gradient substrates on the day of printing, to obtain a view of the patterns being generated. This would however require excess substrates to be coated for each experiment, and once stained, these substrates could not be used for cell culture. As such, they could only ever be used as guides for the quality of pattern being generated, without allowing for visualisation of the actual gradients that cells would experience. Alternatively, an antibody for the printed gradient could be used in the staining process after cells have been seeded, to visualise the printed protein in the regions between cells. However, the small amounts of protein release during culture (as shown by the ELISA assay in section 2.4.1), along with the interactions of cells at the surface, would undoubtedly disrupt the protein pattern somewhat. Also, the use of an antibody for the bio-ink would decrease the number of transcription factors that could be investigated during immunofluorescence imaging, which is traditionally limited by the number of channels available.

Regardless, as a proof-of-concept study, the generation of ventral subtypes demonstrated the potential of inkjet printing as a means to model the complex neural systems that form in the embryo, and could potentially offer an alternative to the burden of animal research in this field. In the future, once the printing approach has been further refined for reproducibility, further investigations into dorsal patterning could be carried out. Initial investigations described here have identified both suitable antibodies and BMP4 bio-ink concentrations for the generation of dorsal subtypes. By combining both ventral and dorsal cues on the same substrate, the entire dorsal-ventral axis of the neural tube could be modelled. If successful, this would have considerable potential in developmental biology labs, with applications across drug development and neural systems research. However, with the complexity of the neural tube, a more detailed readout to immunofluorescence would be required. A method has been developed and optimised to carry out spatially resolved transcriptomics, as described in the appendix, section 6.1. This would enable the entire transcription factor network of the spinal cord model to be identified, and could provide a more accurate

comparison to the neural tube *in vivo*. The platform could also readily be expanded to investigate the anterior-posterior axis of the neural tube. Rifes *et al.* have previously demonstrated that microfluidic gradient systems can be utilised to pattern neural cells towards different cell types in the developing brain.[56] A similar approach could be employed here, with printing of morphogens such as Wnt3a enabling anterior-posterior patterning.

5.3 Inkjet printing for investigating cancer development and progression

Chapter 4 described the application of the material system in preliminary *in vitro* cancer studies. The ease of modification of the platform was demonstrated here, as only the bio-ink of choice and cell type required altering from the configuration used in Chapter 3. A number of cell lines were investigated, to determine an optimal candidate line for emphasising the capabilities of inkjet printing in cancer research.

Across all cell lines, an inverse relationship between cell density and Wnt3a concentration was observed, with the gradient appearing to inhibit cell proliferation. Further investigation is needed, but if this behaviour was shown to be consistent across cell lines, this could prove to be a valuable tool in investigating novel therapeutics for the slowing of cancer progression.

The MEL10 mouse melanoma cells also showed interesting morphological changes in certain conditions. Printed Wnt3a gradients did not appear to play a role in the cell morphology, although the bio-ink concentration (1 µg/mL) was most likely too low. Soluble Wnt3a induced considerable amounts of protrusion formation in the cells, and some alignment was seen along the surface topographies. This behaviour became more pronounced in the presence of the cytokine interferon-gamma. However, difficulties were encountered in culturing this cell line reproducibly, and so further investigations into the role of Wnt3a and interferon-gamma was not possible. As such, alternative cell lines were considered.

19398 mouse melanoma cells demonstrated more reproducible culturing on the nanoneedle substrates. For this experiment, β-catenin antibodies were also included to visualise its translocation upon pathway activation. However, these cells did not exhibit any observable response to either the printed or soluble Wnt3a, suggesting that this line may not be responsive to Wnt3a signalling. The large, dense colonies formed by the cells also made analysis of the nuclear/cytoplasmic ratio of the β-catenin challenging, limiting the throughput and applications of the system.

Finally, WM266.4 human melanoma cells were identified as a promising candidate for these proof-of-concept experiments. This line had inherently low levels of Wnt signalling occurring, which suggested that they would be more responsive to changes induced by printed patterns.[197] They were also seen to remain as single cells on the substrate after seeding, and did not tend to form large colonies as in the case of the 19398s. This made them more amenable to high throughput image analysis, which would greatly enhance the potential of the platform. The WM266.4 cells exhibited similar density behaviour in response to Wnt3a concentration, and in some instances did exhibit a graded nuclear β-catenin signal in response to the printed gradient (concentrations from 1 μg/mL to 4 μg/mL were investigated). However, the response was not consistent, with substrates within the same experiment often exhibiting differing behaviour. The shape of the cells was also varied, with some rounding up and others forming large protrusions in the presence of Wnt3a. This may have been as a result of the time allowed for culturing, with most cells being fixed at the 6 h or 48 h timepoints. Longer culturing might encourage the formation of more protrusions and adhesions at the surface, although the time-dependence of β-catenin should also be considered.

Chapter 4 successfully identified a candidate cell line that could be used to determine the effectiveness of printed morphogen gradients in cancer research. Further experiments might investigate the effect of culture time on cell morphology, and could

also elucidate further the role of the Wnt3a concentration in the nuclear/cytoplasmic β-catenin ratio (as demonstrated by Massey *et al.*[182]).

Beyond the resolving of these inconsistencies within the material system and cell culture, the applications of this system for investigating cancer *in vitro* are extensive. A small number of cell lines were investigated here, but this could be greatly expanded to identify a library of candidate lines that might be suitable. The bio-ink being printed could readily be modified, with Shh being a strong candidate for future studies. The printing of this protein has already been demonstrated in Chapter 3, and the pathway has been implicated in a host of cancers.[188] The printing of small molecules and therapeutic agents could also enable concentration studies to be carried out on single substrates, which could greatly accelerate the screening of novel treatment candidates. The ability to tailor the microenvironment that cancer cells experience offers a unique opportunity to target specific aspects of signalling pathways in cancer, and could have a significant impact on the field.

5.4 Perspective

This thesis has demonstrated the potential of materials that present biochemical patterns at the cell-material interface. Both neural systems and cancer behaviour have been modelled, utilising the inherent ease of modification of the system to readily investigate contrasting biological processes.

These initial studies highlight the potential of this approach as a tool towards the better understanding of biological systems that are otherwise challenging to model *in vitro*. The capability to pattern bio-relevant molecules can be leveraged across a range of applications, and it is hoped that this may have a profound impact on the field of biomaterial design as a whole.

Chapter 6: Appendix

6.1 Spatially resolved transcriptome analysis

While immunofluorescence is an informative technique to provide information of specific behaviours within cells, it is somewhat limited by the number of channels that can be stained for simultaneously. As a result of overlapping excitation/emission profiles of various fluorophores, only a small number of target transcription factors could be labelled and identified in images on the widefield or confocal microscopes. Ideally, another technique would be used in parallel to provide finer detail on the response within neural cells to the printed gradients. This technique should provide transcriptome-level information through RNA sequencing, to provide a clear comparison between the cells seeded on substrates and those in the neural tube *in vivo*. In order for this platform to have the potential to replace *in vivo* studies, it would need to recapitulate the transcription factor network of the neural tube reliably and reproducibly. In the current state of the platform, further refinement is needed before this is possible. However, steps have been taken to prepare a workflow for this eventual application.

Standard spatial transcriptomics approaches involve the use of microarray oligonucleotide or DNA substrates to capture RNA from tissue sections. In this case, however, this is extremely challenging as the cells are seeded onto the silicon substrate and cannot readily be removed without losing their coordinates along the printed gradient. Instead, a method was needed to maintain the cells in their position, and to carry out spatially resolved capture for later RNA isolation and sequencing. This was achieved by fixing the cells in optimal cutting temperature compound (OCT), to create a large mould that contained all the colonies from across the substrate. This block of OCT could then be sectioned using a microtome, and a laser capture microdissection apparatus used to isolate cells from specific regions of the gradient for sequencing. Proof-of-concept attempts using H&E staining showed that the cells could indeed be fixed and sectioned in this way, to capture the entire substrate surface in single slices

of approximately 10 µm thickness. Initial quality control steps indicated that, when isolated using laser capture microdissection, RNA of sufficient quantity and quality was obtained to carry out sequencing of the transcriptome present in cells across the gradients. As such, once the final configuration of the platform has been optimised, this method can be applied to further support the data seen by immunofluorescence imaging, and to draw more detailed comparisons with the transcription factor network of the neural tube, which has already been sequenced extensively.[157]

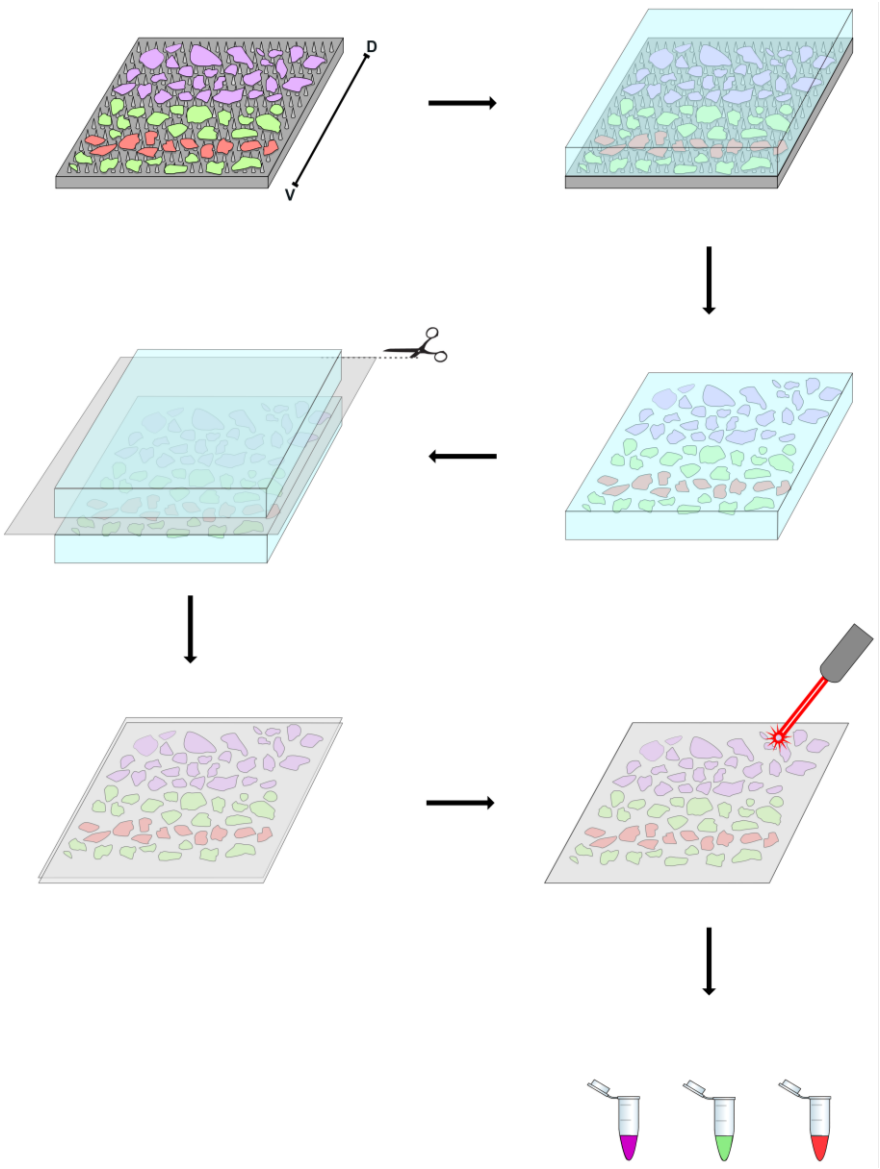


Fig. 6.1: *Approach for carrying out transcriptome analysis of cells on substrates, while maintaining their spatial coordinates along the gradient. Initially, the cells are fixed in an OCT block, which its then sectioned using a microtome. This produces 10-15 μm thickness slices through the colonies of neural cells, that can then be isolated using laser capture microdissection. The isolated populations of cells from specific regions of the gradient can then be pooled and sequenced to describe the transcription factor network present in the cells, and to draw comparisons with the transcriptome of the neural tube.*

6.2 Raman spectra peaks for Wnt activators/inhibitors, Figure 4.5.

Table 2 (a): *Raman peak assignments for Figure 4.5 (a), small molecule targets for the Wnt pathway dissolved in DMSO. Peak assignments by Dr Jelle Penders.*

Raman shift of peak (cm^{-1})	
1480	C=N stretch
1515	C=C in ring
1525	C=C
1545	C=N, C=C in ring
1570	C=N in ring
1582	C=C stretch
1595	Amide, C=O
1615	C=C in ring
1651	C=N, C=C stretch
1673	Amide
1703	Amide
1769	C=O stretch

Table 2 (b): *Raman peak assignments for Figure 4.5 (b), XAV939 in dry powder form. Peak assignments by Dr Jelle Penders.*

Raman shift of peak (cm^{-1})	
673	C-S, C=N in ring
776	C-F, Pyrimidine ring mode
1209	C=C in ring
1238	C-N stretch
1312	C-N in ring
1396	CH_2 in ring
1552	C=C in ring
1623	C=C in ring

References

1. Macklis, J. D., Sidman, R. L. & Shine, H. D. Cross-linked collagen surface for cell culture that is stable, uniform, and optically superior to conventional surfaces. *Vitr. Cell. Dev. Biol.* **21**, 189–194 (1985).

2. Leschik, J., Stefanovic, S., Brinon, B. & Pucéat, M. Cardiac commitment of primate embryonic stem cells. *Nat. Protoc.* **3**, 1381–1387 (2008).

3. Kleinman, H. K. & Martin, G. R. Matrigel: Basement membrane matrix with biological activity. *Semin. Cancer Biol.* **15**, 378–386 (2005).

4. Gandhi, N. S. & Mancera, R. L. The Structure of Glycosaminoglycans and their Interactions with Proteins. *Chem. Biol. Drug Des.* **72**, 455–482 (2008).

5. Morla, S. Glycosaminoglycans and Glycosaminoglycan Mimetics in Cancer and Inflammation. *Int. J. Mol. Sci.* **20**, 1963 (2019).

6. Baldwin, A. D. & Kiick, K. L. Polysaccharide-modified synthetic polymeric biomaterials. *Biopolymers* **94**, 128–140 (2010).

7. Jakša, G., Štefane, B. & Kovač, J. Influence of different solvents on the morphology of APTMS-modified silicon surfaces. *Appl. Surf. Sci.* **315**, 516–522 (2014).

8. Qiao, B., Wang, T.-J., Gao, H. & Jin, Y. High density silanization of nano-silica particles using γ-aminopropyltriethoxysilane (APTES). *Appl. Surf. Sci.* **351**, 646–654 (2015).

9. Gong, Y. *et al.* Layer-by-layer assembly of chondroitin sulfate and collagen on aminolyzed poly(l-lactic acid) porous scaffolds to enhance their chondrogenesis. *Acta Biomater.* **3**, 677–685 (2007).

10. Krishnamoorthy, M., Hakobyan, S., Ramstedt, M. & Gautrot, J. E. Surface-Initiated Polymer Brushes in the Biomedical Field: Applications in Membrane Science, Biosensing, Cell Culture, Regenerative Medicine and Antibacterial Coatings. *Chem. Rev.* **114**, 10976–11026 (2014).

11. Guzmán, E., Rubio, R. G. & Ortega, F. A closer physico-chemical look to the Layer-by-Layer electrostatic self-assembly of polyelectrolyte multilayers. *Adv. Colloid Interface Sci.* **282**, 102197 (2020).

12. Lvov, Y., Ariga, K., Ichinose, I. & Kunitake, T. Assembly of Multicomponent Protein Films by Means of Electrostatic Layer-by-Layer Adsorption. *J. Am. Chem. Soc.* **117**, 6117–6123 (1995).

13. Ahmed, E. M. Hydrogel: Preparation, characterization, and applications: A review. *J. Adv. Res.* **6**, 105–121 (2015).

14. Gyles, D. A., Castro, L. D., Silva, J. O. C. & Ribeiro-Costa, R. M. A review of the designs and prominent biomedical advances of natural and synthetic hydrogel formulations. *European Polymer Journal* **88**, 373–392 (2017).

15. Freudenberg, U., Liang, Y., Kiick, K. L. & Werner, C. Glycosaminoglycan-Based Biohybrid Hydrogels: A Sweet and Smart Choice for Multifunctional Biomaterials. *Adv. Mater.* **28**, 8861–8891 (2016).

16. Sargeant, T. D., Desai, A. P., Banerjee, S., Agawu, A. & Stopek, J. B. An in situ forming collagen–PEG hydrogel for tissue regeneration. *Acta Biomater.* **8**, 124–132 (2012).

17. Hadjipanayi, E., Mudera, V. & Brown, R. A. Close dependence of fibroblast proliferation on collagen scaffold matrix stiffness. *J. Tissue Eng. Regen. Med.* **3**, 77–84 (2009).

18. Willits, R. K. & Skornia, S. L. Effect of collagen gel stiffness on neurite extension. *J. Biomater. Sci. Polym. Ed.* **15**, 1521–1531 (2004).

19. Hosseinkhani, H. *et al.* Engineering Three-Dimensional Collagen-IKVAV Matrix to Mimic Neural Microenvironment. *ACS Chem. Neurosci.* **4**, 1229–1235 (2013).

20. Farrukh, A. *et al.* Bifunctional Hydrogels Containing the Laminin Motif IKVAV Promote Neurogenesis. *Stem Cell Reports* **9**, 1432–1440 (2017).

21. Yin, Y. *et al.* Pentapeptide IKVAV-engineered hydrogels for neural stem cell attachment. *Biomater. Sci.* **9**, 2887–2892 (2021).

22. Republished with permission of John Wiley & Sons - Books , from Sun, W. *et al.* Viability and neuronal differentiation of neural stem cells encapsulated in silk fibroin hydrogel functionalized with an IKVAV peptide. *J. Tissue Eng. Regen. Med.* **11**, 1532–1541 (2017); permission conveyed through Copyright Clearance Center,Inc.

23. Yao, L. *et al.* The effect of laminin peptide gradient in enzymatically cross-linked collagen scaffolds on neurite growth. *J. Biomed. Mater. Res. Part A* **92A**, 484–492 (2010).

24. Itoh, S. *et al.* Synthetic collagen fibers coated with a synthetic peptide containing the YIGSR sequence of laminin to promote peripheral nerve regeneration in vivo. *J. Mater. Sci. Mater. Med.* **10**, 129–134 (1999).

25. Kaiser, A., Kale, A., Novozhilova, E. & Olivius, P. The Effects of Matrigel® on the Survival and Differentiation of a Human Neural Progenitor Dissociated Sphere Culture. *Anat. Rec.* **303**, 441–450 (2020).

26. Cavo, M. *et al.* A new cell-laden 3D Alginate-Matrigel hydrogel resembles human breast cancer cell malignant morphology, spread and invasion capability observed "in vivo". *Sci. Rep.* **8**, 5333 (2018).

27. Republished with permission of John Wiley & Sons - Books, from Uemura, M. *et al.* Matrigel supports survival and neuronal differentiation of grafted embryonic stem cell-derived neural precursor cells. *J. Neurosci. Res.* **88**, 542–551 (2010); permission conveyed through Copyright Clearance Center,Inc.

28. Hachim, D., Whittaker, T. E., Kim, H. & Stevens, M. M. Glycosaminoglycan-based biomaterials for growth factor and cytokine delivery: Making the right choices. *J. Control. Release* **313**, 131–147 (2019).

29. Kfoury, G. *et al.* Alginate Sulfate Substrates Control Growth Factor Binding and Growth of Primary Neurons: Toward Engineered 3D Neural Networks. *Adv. Biosyst.* **4**, 2000047 (2020).

30. Jeon, O., Powell, C., Solorio, L. D., Krebs, M. D. & Alsberg, E. Affinity-based growth factor delivery using biodegradable, photocrosslinked heparin-alginate hydrogels. *J. Control. Release* **154**, 258–266 (2011).

31. Si, J., Yang, Y., Xing, X., Yang, F. & Shan, P. Controlled degradable chitosan/collagen composite scaffolds for application in nerve tissue regeneration. *Polym. Degrad. Stab.* **166**, 73–85 (2019).

32. Karumbaiah, L. *et al.* Chondroitin Sulfate Glycosaminoglycan Hydrogels Create Endogenous Niches for Neural Stem Cells. *Bioconjug. Chem.* **26**, 2336–2349 (2015).

33. Wang, X., He, J., Wang, Y. & Cui, F.-Z. Hyaluronic acid-based scaffold for central neural tissue engineering. *Interface Focus* **2**, 278–291 (2012).

34. Wang, T.-W. & Spector, M. Development of hyaluronic acid-based scaffolds for brain tissue engineering. *Acta Biomater.* **5**, 2371–2384 (2009).

35. Pan, L., Ren, Y., Cui, F. & Xu, Q. Viability and differentiation of neural precursors on hyaluronic acid hydrogel scaffold. *J. Neurosci. Res.* **87**, 3207–3220 (2009).

36. Republished with permission of Elsevier Science & Technology Journals, from Hou, S. *et al.* The enhancement of cell adherence and inducement of neurite outgrowth of dorsal root

ganglia co-cultured with hyaluronic acid hydrogels modified with Nogo-66 receptor antagonist in vitro. *Neuroscience* **137**, 519–529 (2006); permission conveyed through Copyright Clearance Center,Inc.

37. Younesi, M., Donmez, B. O., Islam, A. & Akkus, O. Heparinized collagen sutures for sustained delivery of PDGF-BB: Delivery profile and effects on tendon-derived cells In-Vitro. *Acta Biomater.* **41**, 100–109 (2016).

38. Hachim, D. *et al.* Distinct release strategies are required to modulate macrophage phenotype in young versus aged animals. *J. Control. Release* **305**, 65–74 (2019).

39. Walthers, C. M., Lyall, C. J., Nazemi, A. K., Rana, P. V & Dunn, J. C. Y. Collagen and heparan sulfate coatings differentially alter cell proliferation and attachment in vitro and in vivo. *TECHNOLOGY* **04**, 159–169 (2016).

40. Habuchi, H. *et al.* Structure of a heparan sulphate oligosaccharide that binds to basic fibroblast growth factor. *Biochem. J.* **285**, 805–813 (1992).

41. Kreuger, J., Salmivirta, M., Sturiale, L., Giménez-Gallego, G. & Lindahl, U. Sequence Analysis of Heparan Sulfate Epitopes with Graded Affinities for Fibroblast Growth Factors 1 and 2 *. *J. Biol. Chem.* **276**, 30744–30752 (2001).

42. Murphy, A. R., Laslett, A., O'Brien, C. M. & Cameron, N. R. Scaffolds for 3D in vitro culture of neural lineage cells. *Acta Biomater.* **54**, 1–20 (2017).

43. Mammadov, B., Sever, M., Guler, M. O. & Tekinay, A. B. Neural differentiation on synthetic scaffold materials. *Biomater. Sci.* **1**, 1119–1137 (2013).

44. Adapted with permission from Patel, S. *et al.* Bioactive Nanofibers: Synergistic Effects of Nanotopography and Chemical Signaling on Cell Guidance. *Nano Lett.* **7**, 2122–2128 (2007), American Chemical Society.

45. Farzamfar, S. *et al.* Poly-lactic Acid/Gelatin Nanofiber (PLA/GTNF) Conduits Containing Platelet-Rich Plasma for Peripheral Nerve Regeneration. *Int. J. Heal. Stud. Vol. 3, Issue 2, 2017* (2017). doi:10.22100/ijhs.v3i2.236

46. Zeng, C.-G., Xiong, Y., Xie, G., Dong, P. & Quan, D. Fabrication and evaluation of PLLA multichannel conduits with nanofibrous microstructure for the differentiation of NSCs in vitro. *Tissue Eng. Part A* **20**, 1038–1048 (2014).

47. Kuriakose, A. E., Hu, W., Nguyen, K. T. & Menon, J. U. Scaffold-based lung tumor culture on porous PLGA microparticle substrates. *PLoS One* **14**, e0217640 (2019).

48. Nune, M., Krishnan, U. M. & Sethuraman, S. PLGA nanofibers blended with designer self-assembling peptides for peripheral neural regeneration. *Mater. Sci. Eng. C* **62**, 329–337 (2016).

49. Hwang, C. M., Kim, S. K., Kim, J. H., Khademhosseini, A. & Lee, S. H. Differentiation of human neural progenitor cells on PLGA microfibers. in *2009 IEEE 35th Annual Northeast Bioengineering Conference* 1–2 (2009). doi:10.1109/NEBC.2009.4967758

50. Munoz-Pinto, D. J. *et al.* Inorganic–organic hybrid scaffolds for osteochondral regeneration. *J. Biomed. Mater. Res. Part A* **94A**, 112–121 (2010).

51. Soman, P. *et al.* Cancer cell migration within 3D layer-by-layer microfabricated photocrosslinked PEG scaffolds with tunable stiffness. *Biomaterials* **33**, 7064–7070 (2012).

52. Lampe, K. J., Mooney, R. G., Bjugstad, K. B. & Mahoney, M. J. Effect of macromer weight percent on neural cell growth in 2D and 3D nondegradable PEG hydrogel culture. *J. Biomed. Mater. Res. Part A* **94A**, 1162–1171 (2010).

53. Lampe, K. J., Kern, D. S., Mahoney, M. J. & Bjugstad, K. B. The administration of BDNF and GDNF to the brain via PLGA microparticles patterned within a degradable PEG-based hydrogel: Protein distribution and the glial response. *J. Biomed. Mater. Res. Part A* **96A**, 595–607 (2011).

54. Li, C. *et al.* Buoyancy-Driven Gradients for Biomaterial Fabrication and Tissue Engineering. *Adv. Mater.* **31**, 1900291 (2019).

55. Demers, C. J. *et al.* Development-on-chip: in vitro neural tube patterning with a microfluidic device. *Development* **143**, 1884 LP – 1892 (2016).

56. Republished with permission of Springer Nature BV, from Rifes, P. *et al.* Modeling neural tube development by differentiation of human embryonic stem cells in a microfluidic WNT gradient. *Nat. Biotechnol.* **38**, 1265–1273 (2020); permission conveyed through Copyright Clearance Center,Inc.

57. Keenan, T. M. & Folch, A. Biomolecular gradients in cell culture systems. *Lab Chip* **8**, 34–57 (2008).

58. Homan, K. A. *et al.* Bioprinting of 3D Convoluted Renal Proximal Tubules on Perfusable Chips. *Sci. Rep.* **6**, 34845 (2016).

59. Li, X., Valadez, A. V, Zuo, P. & Nie, Z. Microfluidic 3D cell culture: potential application for tissue-based bioassays. *Bioanalysis* **4**, 1509–1525 (2012).

60. Tehranirokh, M., Kouzani, A. Z., Francis, P. S. & Kanwar, J. R. Microfluidic devices for cell cultivation and proliferation. *Biomicrofluidics* **7**, 51502 (2013).

61. Yadavali, S., Jeong, H.-H., Lee, D. & Issadore, D. Silicon and glass very large scale microfluidic droplet integration for terascale generation of polymer microparticles. doi:10.1038/s41467-018-03515-2

62. Golozar, M. *et al.* Fabrication of high-quality glass microfluidic devices for bioanalytical and space flight applications. *MethodsX* **7**, 101043 (2020).

63. Becker, H. & Locascio, L. E. Polymer microfluidic devices. *Talanta* **56**, 267–287 (2002).

64. Chung, B. G. *et al.* Human neural stem cell growth and differentiation in a gradient-generating microfluidic device. *Lab Chip* **5**, 401–406 (2005).

65. Park, J. Y. *et al.* Differentiation of Neural Progenitor Cells in a Microfluidic Chip-Generated Cytokine Gradient. *Stem Cells* **27**, 2646–2654 (2009).

66. Choi, J. *et al.* Wnt5a-mediating neurogenesis of human adipose tissue-derived stem cells in a 3D microfluidic cell culture system. *Biomaterials* **32**, 7013–7022 (2011).

67. Mattei, F. *et al.* A multidisciplinary study using in vivo tumor models and microfluidic cell-on-chip approach to explore the cross-talk between cancer and immune cells. *J. Immunotoxicol.* **11**, 337–346 (2014).

68. Businaro, L. *et al.* Cross talk between cancer and immune cells: exploring complex dynamics in a microfluidic environment. *Lab Chip* **13**, 229–239 (2013).

69. Agliari, E. *et al.* Cancer-driven dynamics of immune cells in a microfluidic environment. *Sci. Rep.* **4**, 6639 (2014).

70. Bischel, L. L., Beebe, D. J. & Sung, K. E. Microfluidic model of ductal carcinoma in situ with 3D, organotypic structure. *BMC Cancer* **15**, 12 (2015).

71. Han, J., Jung, Y., Jun, Y., Park, S. & Lee, S. Elucidating molecular mechanisms of acquired resistance to BRAF inhibitors in melanoma using a microfluidic device and deep sequencing. *Genomics Inform.* **19**, e2–e2 (2021).

72. Bai, J., Tu, T.-Y., Kim, C., Thiery, J. P. & Kamm, R. D. Identification of drugs as single agents or in combination to prevent carcinoma dissemination in a microfluidic 3D environment. *Oncotarget* **6**, 36603–36614 (2015).

73. Morita, N., Khalate, A. A., Buul, A. M. va. & Wijshoff, H. Inkjet Printheads. *Fundamentals of Inkjet Printing* 57–92 (2016). doi:https://doi.org/10.1002/9783527684724.ch3

74. Sirringhaus, H. & Shimoda, T. Inkjet Printing of Functional Materials. *MRS Bull.* **28**, 802–806 (2003).

75. Evans, S. E. *et al.* 2D and 3D inkjet printing of biopharmaceuticals – A review of trends and future perspectives in research and manufacturing. *Int. J. Pharm.* **599**, 120443 (2021).

76. Miller, E. *et al.* Inkjet Printing of Growth Factor Concentration Gradients and Combinatorial Arrays Immobilized on Biologically-Relevant Substrates. *Comb. Chem. High Throughput Screen.* **12**, 604–618 (2009).

77. Phillippi, J. A. *et al.* Microenvironments Engineered by Inkjet Bioprinting Spatially Direct Adult Stem Cells Toward Muscle- and Bone-Like Subpopulations. *Stem Cells* **26**, 127–134 (2008).

78. Borchers, K. *et al.* Ink Formulation for Inkjet Printing of Streptavidin and Streptavidin Functionalized Nanoparticles Ink Formulation for Inkjet Printing of Streptavidin and Streptavidin Functionalized Nanoparticles. **2691**, (2011).

79. Dalilottojari, A. *et al.* Porous Silicon-Based Cell Microarrays: Optimizing Human Endothelial Cell-Material Surface Interactions and Bioactive Release. *Biomacromolecules* **17**, 3724–3731 (2016).

80. Fox, C. B. *et al.* Picoliter-volume inkjet printing into planar microdevice reservoirs for low-waste , high-capacity drug loading. 9–16 (2017). doi:10.1002/btm2.10053

81. Roth, E. A. *et al.* Inkjet printing for high-throughput cell patterning. *Biomaterials* **25**, 3707–3715 (2004).

82. Ilkhanizadeh, S., Teixeira, A. I. & Hermanson, O. Inkjet printing of macromolecules on hydrogels to steer neural stem cell differentiation. *Biomaterials* **28**, 3936–3943 (2007).

83. Guo, J. *et al.* Coding Cell Micropatterns Through Peptide Inkjet Printing for Arbitrary Biomineralized Architectures. *Adv. Funct. Mater.* **28**, 1800228 (2018).

84. Higgins, S. G. *et al.* High-Aspect-Ratio Nanostructured Surfaces as Biological Metamaterials. *Adv. Mater.* **32**, 1903862 (2020).

85. Aryal, M. *et al.* Imprinted large-scale high density polymer nanopillars for organic solar cells. *J. Vac. Sci. Technol. B Microelectron. Nanom. Struct.* **26**, 2562–2566 (2008).

86. Chou, S. Y., Krauss, P. R. & Renstrom, P. J. Imprint of sub-25 nm vias and trenches in polymers. *Appl. Phys. Lett.* **67**, 3114 (1995).

87. Xie, C., Lin, Z., Hanson, L., Cui, Y. & Cui, B. Intracellular recording of action potentials by nanopillar electroporation. *Nat. Nanotechnol.* **7**, 185–190 (2012).

88. Hanson, L., Lin, Z. C., Xie, C., Cui, Y. & Cui, B. Characterization of the cell-nanopillar interface by transmission electron microscopy. *Nano Lett.* **12**, 5815–5820 (2012).

89. Kim, S.-M. *et al.* Strong contact coupling of neuronal growth cones with height-controlled vertical silicon nanocolumns. *Nano Res.* **11**, 2532–2543 (2018).

90. Shalek, A. K. *et al.* Nanowire-Mediated Delivery Enables Functional Interrogation of Primary Immune Cells: Application to the Analysis of Chronic Lymphocytic Leukemia. (2012).

91. Adapted with permission from Chiappini, C. *et al.* Biodegradable nanoneedles for localized delivery of nanoparticles in vivo: Exploring the biointerface. *ACS Nano* **9**, 5500–5509 (2015), American Chemical Society.

92. Zhu, X. *et al.* Dense diamond nanoneedle arrays for enhanced intracellular delivery of drug molecules to cell lines. *J. Mater. Sci.* **50**, 7800–7807 (2015).

93. Republished with permission of Springer Nature BV, from Chiappini, C. *et al.* Biodegradable silicon nanoneedles delivering nucleic acids intracellularly induce localized in vivo neovascularization. *Nat. Mater.* **14**, 532–539 (2015); permission conveyed through Copyright Clearance Center,Inc.

94. Gopal, S. *et al.* Porous Silicon Nanoneedles Modulate Endocytosis to Deliver Biological Payloads. *Adv. Mater.* **31**, 1806788 (2019).

95. Whitehead, K. A., Langer, R. & Anderson, D. G. Knocking down barriers: Advances in siRNA delivery. *Nat. Rev. Drug Discov.* **8**, 129–138 (2009).

96. Wang, Y. *et al.* Poking cells for efficient vector-free intracellular delivery. *Nat. Commun.* **5**, 1–9 (2014).

97. Republished with permission of John Wiley & Sons - Books, from Zhu, X. *et al.* Diamond-Nanoneedle-Array-Facilitated Intracellular Delivery and the Potential Influence on Cell Physiology. *Adv. Healthc. Mater.* **5**, 1157–1168 (2016); permission conveyed through Copyright Clearance Center,Inc.

98. Chen, X. *et al.* A diamond nanoneedle array for potential high-throughput intracellular delivery. *Adv. Healthc. Mater.* **2**, 1103–1107 (2013).

99. Yang, Y. *et al.* Fabrication of arrays of high-aspect-ratio diamond nanoneedles via maskless ECR-assisted microwave plasma etching. *CrystEngComm* **17**, 2791–2800 (2015).

100. Hansel, C. S. *et al.* Nanoneedle-Mediated Stimulation of Cell Mechanotransduction Machinery. *ACS Nano* **13**, 2913–2926 (2019).

101. Seong, H. *et al.* Size-Tunable Nanoneedle Arrays for Influencing Stem Cell Morphology, Gene Expression, and Nuclear Membrane Curvature. *ACS Nano* **14**, 5371–5381 (2020).

102. Chang, S.-C., Mulloy, B., Magee, A. I. & Couchman, J. R. Two distinct sites in sonic Hedgehog combine for heparan sulfate interactions and cell signaling functions. *J. Biol. Chem.* **286**, 44391–44402 (2011).

103. Rubin, J. B., Choi, Y. & Segal, R. A. Cerebellar proteoglycans regulate sonic hedgehog responses during development. *Development* **129**, 2223–2232 (2002).

104. Kovarova, M. Isolation and characterization of mast cells in mouse models of allergic diseases. *Methods Mol. Biol.* **1032**, 109–119 (2013).

105. Wan, H., Chen, H., Chu, Y., Ju, X. & Jiang, H. Structure characterization and optical properties investigation of the four main components of the classical phenazinium dye Safranin O. *Analyst* **144**, 7149–7156 (2019).

106. Hornbeck, P. V *et al.* PhosphoSitePlus, 2014: mutations, PTMs and recalibrations. *Nucleic Acids Res.* **43**, D512-20 (2015).

107. O'Rahilly, R. Early human development and the chief sources of information on staged human embryos. *European Journal of Obstetrics and Gynecology and Reproductive Biology* **9**, 273–280 (1979).

108. Gerri, C., Menchero, S., Mahadevaiah, S. K., Turner, J. M. A. & Niakan, K. K. Human Embryogenesis: A Comparative Perspective. *Annu. Rev. Cell Dev. Biol. 2020* **36**, 411–440 (2020).

109. Mikawa, T., Poh, A. M., Kelly, K. A., Ishii, Y. & Reese, D. E. Induction and patterning of the primitive streak, an organizing center of gastrulation in the amniote. *Dev. Dyn. an Off. Publ. Am. Assoc. Anat.* **229**, 422–432 (2004).

110. Grapin-Botton, A. & Melton, D. A. Endoderm development: From patterning to organogenesis. *Trends in Genetics* **16**, 124–130 (2000).

111. Ferretti, E., Hadjantonakis, A.-K., Wickströ, S. A. & Yang, Y. Mesoderm specification and diversification: from single cells to emergent tissues. *Curr. Opin. Cell Biol.* **61**, 110–116 (2019).

112. Sasai, Y. & De Robertis, E. M. Ectodermal patterning in vertebrate embryos. *Developmental Biology* **182**, 5–20 (1997).

113. Sadler, T. W. Embryology of neural tube development. *Am. J. Med. Genet. Part C Semin. Med. Genet.* **135C**, 2–8 (2005).

114. Nikolopoulou, E., Galea, G. L., Rolo, A., Greene, N. D. E. & Copp, A. J. Neural tube closure: cellular, molecular and biomechanical mechanisms. *Development* **144**, 552–566 (2017).

115. Takata, N., Sakakura, E., Eiraku, M., Kasukawa, T. & Sasai, Y. Self-patterning of rostral-caudal neuroectoderm requires dual role of Fgf signaling for localized Wnt antagonism. doi:10.1038/s41467-017-01105-2

116. Briscoe, J. & Small, S. Morphogen rules: design principles of gradient-mediated embryo patterning. *Development* **142**, 3996–4009 (2015).

117. Choudhry, Z. *et al.* Sonic hedgehog signalling pathway: a complex network. *Ann. Neurosci.* **21**, 28–31 (2014).

118. Briscoe, J. & Thérond, P. P. The mechanisms of Hedgehog signalling and its roles in development and disease. *Nat. Rev. Mol. Cell Biol.* **14**, 416–429 (2013).

119. Massagué, J. TGFβ signalling in context. *Nat. Rev. Mol. Cell Biol.* **13**, 616–630 (2012).

120. M Memet Özek, Giuseppe Cinalli, Wirginia Maixner. *Spina Bifida: Management and Outcome*. (Springer Science & Business Media, 2008).

121. NINDS, NIH. Spina Bifida Fact Sheet. *21-NS-309* (2021). Available at: https://www.ninds.nih.gov/Disorders/Patient-Caregiver-Education/Fact-Sheets/Spina-Bifida-Fact-Sheet. (Accessed: 27th May 2021)

122. Nakano, K. K. Anencephaly: A Review. *Dev. Med. Child Neurol.* **15**, 383–400 (1973).

123. Obeidi, N., Russell, N., Higgins, J. R. & O'Donoghue, K. The Natural History of Anencephaly. *Prenat. Diagn.* **30**, 357–360 (2010).

124. Siffel, C., Wong, L.-Y. C., Olney, R. S. & Correa, A. Survival of infants diagnosed with encephalocele in Atlanta, 1979-98. *Paediatr. Perinat. Epidemiol.* **17**, 40–48 (2003).

125. NINDS, N. Hydranencephaly Information Page. (2019).

126. Blom, H. J., Shaw, G. M., den Heijer, M. & Finnell, R. H. Neural tube defects and folate: case far from closed. *Nat. Rev. Neurosci.* **7**, 724–731 (2006).

127. Pitkin, R. M. Folate and neural tube defects. *Am. J. Clin. Nutr.* **85**, 285S-288S (2007).

128. MS Society. MS in the UK. *MS Prevalence Report* 1 (2020). Available at: https://www.mssociety.org.uk/care-and-support/resources-and-publications/publications-search/ms-in-the-uk. (Accessed: 27th May 2021)

129. Qureshi, M., Schoenfeld, D. A., Paliwal, Y., Shui, A. & Cudkowicz, M. E. The natural history of ALS is changing: Improved survival. *Amyotroph. Lateral Scler.* **10**, 324–331 (2009).

130. Marigo, V. *et al.* Cloning, Expression, and Chromosomal Location of SHH and IHH: Two Human Homologues of the Drosophila Segment Polarity Gene Hedgehog. *Genomics* **28**, 44–51 (1995).

131. Greene, N. D. E. *et al.* Differential Protein Expression at the Stage of Neural Tube Closure in the Mouse Embryo *. *J. Biol. Chem.* **277**, 41645–41651 (2002).

132. Greene, N. D. E. & Copp, A. J. Development of the vertebrate central nervous system: formation of the neural tube. *Prenat. Diagn.* **29**, 303–311 (2009).

133. Ybot-Gonzalez, P., Cogram, P., Gerrelli, D. & Copp, A. J. Sonic hedgehog and the molecular regulation of mouse neural tube closure. *Development* **129**, 2507–2517 (2002).

134. Republished with permission of The Company of Biologists Ltd, from Exelby, K. *et al.* Precision of tissue patterning is controlled by dynamical properties of gene regulatory networks. *Development* **148**, (2021); permission conveyed through Copyright Clearance Center,Inc.

135. Verrier, L., Davidson, L., Gierliński, M., Dady, A. & Storey, K. G. Neural differentiation, selection and transcriptomic profiling of human neuromesodermal progenitor-like cells in vitro. *Development* **145**, (2018).

136. Bragina, O. *et al.* Smoothened agonist augments proliferation and survival of neural cells. *Neurosci. Lett.* **482**, 81–85 (2010).

137. Sinha, S. & Chen, J. K. Purmorphamine activates the Hedgehog pathway by targeting Smoothened. *Nat. Chem. Biol.* **2**, 29–30 (2006).

138. Stanton, B. Z. & Peng, L. F. Small-molecule modulators of the Sonic Hedgehog signaling pathway. *Mol. Biosyst.* **6**, 44–54 (2010).

139. Xiong, F. *et al.* Specified neural progenitors sort to form sharp domains after noisy Shh signaling. *Cell* **153**, 550–561 (2013).

140. Gouti, M. *et al.* In vitro generation of neuromesodermal progenitors reveals distinct roles for wnt signalling in the specification of spinal cord and paraxial mesoderm identity. *PLoS Biol.* **12**, e1001937 (2014).

141. Liem, K. F., Jessell, T. M. & Briscoe, J. Regulation of the neural patterning activity of sonic hedgehog by secreted BMP inhibitors expressed by notochord and somites. *Development* **127**, 4855–4866 (2000).

142. Lippmann, E. S. *et al.* Deterministic HOX Patterning in Human Pluripotent Stem Cell-Derived Neuroectoderm. *Stem Cell Reports* **4**, 632–644 (2015).

143. Barberi, T. *et al.* Neural subtype specification of fertilization and nuclear transfer embryonic stem cells and application in parkinsonian mice. *Nat. Biotechnol.* **21**, 1200–1207 (2003).

144. Yan, Y. *et al.* Directed Differentiation of Dopaminergic Neuronal Subtypes from Human Embryonic Stem Cells. *Stem Cells* **23**, 781–790 (2005).

145. Bagley, J. A., Reumann, D., Bian, S., Lévi-Strauss, J. & Knoblich, J. A. Fused cerebral organoids model interactions between brain regions. *Nat. Methods* **14**, 743–751 (2017).

146. Liu, F. *et al.* Advances in Cerebral Organoid Systems and their Application in Disease Modeling. *Neuroscience* **399**, 28–38 (2019).

147. Republished with permission from Springer Nature BV, from Lancaster, M. A. *et al.* Cerebral organoids model human brain development and microcephaly. *Nature* **501**, 373–379 (2013) permission conveyed through Copyright Clearance Center,Inc.

148. Lancaster, M. A. & Knoblich, J. A. Generation of cerebral organoids from human pluripotent stem cells. *Nat. Protoc.* **9**, 2329–2340 (2014).

149. Meinhardt, A. *et al.* 3D Reconstitution of the Patterned Neural Tube from Embryonic Stem Cells. *Stem Cell Reports* **3**, 987–999 (2014).

150. Ranga, A. *et al.* Neural tube morphogenesis in synthetic 3D microenvironments. *Proc. Natl. Acad. Sci.* **113**, E6831 LP-E6839 (2016).

151. Velasco, S. *et al.* Individual brain organoids reproducibly form cell diversity of the human cerebral cortex. *Nature* **570**, 523–527 (2019).

152. Bonnici, B. & Kapfhammer, J. P. Spontaneous regeneration of intrinsic spinal cord axons in a novel spinal cord slice culture model. *Eur. J. Neurosci.* **27**, 2483–2492 (2008).

153. Republished with permission of Elsevier Science & Technology Journals, from Heidemann, M., Streit, J. & Tscherter, A. Functional regeneration of intraspinal connections in a new in vitro model. *Neuroscience* **262**, 40–52 (2014); permission conveyed through Copyright Clearance Center,Inc.

154. Republished with permission of Elsevier Science & Technology Journals, from Weightman, A. P., Pickard, M. R., Yang, Y. & Chari, D. M. An in vitro spinal cord injury model to screen neuroregenerative materials. *Biomaterials* **35**, 3756–3765 (2014) ; permission conveyed through Copyright Clearance Center,Inc.

155. Berg, S. *et al.* ilastik: interactive machine learning for (bio)image analysis. *Nat. Methods* **16**, 1226–1232 (2019).

156. Stirling, D. R. *et al.* CellProfiler 4: improvements in speed, utility and usability. *BMC Bioinformatics* **22**, 433 (2021).

157. Delile, J. *et al.* Single cell transcriptomics reveals spatial and temporal dynamics of gene expression in the developing mouse spinal cord. *Development* **146**, (2019).

158. Cancer incidence statistics | Cancer Research UK. Available at: https://www.cancerresearchuk.org/health-professional/cancer-statistics/incidence#heading-Zero. (Accessed: 5th January 2021)

159. Cancer mortality statistics | Cancer Research UK. Available at: https://www.cancerresearchuk.org/health-professional/cancer-statistics/mortality#heading-Zero. (Accessed: 5th January 2021)

160. Cancer survival statistics | Cancer Research UK. Available at: https://www.cancerresearchuk.org/health-professional/cancer-statistics/survival#heading-Zero. (Accessed: 5th January 2021)

161. Plummer, M. *et al.* Global burden of cancers attributable to infections in 2012: a synthetic analysis. *Lancet Glob. Heal.* **4**, e609–e616 (2016).

162. Krzyszczyk, P. *et al.* The growing role of precision and personalized medicine for cancer treatment. *Rev. Technol. l Vol.* **6**,

163. Keshet, Y. & Seger, R. The MAP Kinase Signaling Cascades: A System of Hundreds of Components Regulates a Diverse Array of Physiological Functions BT - MAP Kinase Signaling Protocols: Second Edition. in (ed. Seger, R.) 3–38 (Humana Press, 2010). doi:10.1007/978-1-60761-795-2_1

164. Guo, Y.-J. *et al.* ERK/MAPK signalling pathway and tumorigenesis. *Exp. Ther. Med.* **19**, 1997–2007 (2020).

165. Lavoie, H., Gagnon, J. & Therrien, M. ERK signalling: a master regulator of cell behaviour, life and fate. *Nat. Rev. Mol. Cell Biol.* **21**, 607–632 (2020).

166. Khan, A. Q. *et al.* RAS-mediated oncogenic signaling pathways in human malignancies. *Semin. Cancer Biol.* **54**, 1–13 (2019).

167. Sanchez-Vega, F. *et al.* Oncogenic Signaling Pathways in The Cancer Genome Atlas. *Cell* **173**, 321-337.e10 (2018).

168. Santarpia, L., Lippman, S. M. & El-Naggar, A. K. Targeting the MAPK-RAS-RAF signaling pathway in cancer therapy. *Expert Opin. Ther. Targets* **16**, 103–119 (2012).

169. Yang, J. *et al.* Targeting PI3K in cancer: mechanisms and advances in clinical trials. *Mol. Cancer* **18**, 26 (2019).

170. Liu, P., Cheng, H., Roberts, T. M. & Zhao, J. J. Targeting the phosphoinositide 3-kinase pathway in cancer. *Nat. Rev. Drug Discov.* **8**, 627–644 (2009).

171. Mikels, A. J. & Nusse, R. Wnts as ligands: Processing, secretion and reception. *Oncogene* **25**, 7461–7468 (2006).

172. Cadigan, K. M. & Nusse, R. Wnt signaling: A common theme in animal development. *Genes and Development* **11**, 3286–3305 (1997).

173. Zhan, T., Rindtorff, N. & Boutros, M. Wnt signaling in cancer. *Oncogene* **36**, 1461–1473 (2017).

174. Xu, X., Zhang, M., Xu, F. & Jiang, S. Wnt signaling in breast cancer: biological mechanisms, challenges and opportunities. *Molecular Cancer* **19**, 1–35 (2020).

175. Wang, X. *et al.* PAF-Wnt signaling-induced cell plasticity is required for maintenance of breast cancer cell stemness. *Nat. Commun.* **7**, 1–13 (2016).

176. Jiang, S. *et al.* WNT5B governs the phenotype of basal-like breast cancer by activating WNT signaling. *Cell Commun. Signal.* **17**, 109 (2019).

177. Nie, X., Liu, H., Liu, L., Wang, Y. D. & Chen, W. D. Emerging Roles of Wnt Ligands in Human Colorectal Cancer. *Frontiers in Oncology* **10**, 1341 (2020).

178. Zeng, G. *et al.* Aberrant Wnt/β-catenin signaling in pancreatic adenocarcinoma. *Neoplasia* **8**, 279–289 (2006).

179. Sano, M. *et al.* Activation of WNT/β-Catenin Signaling Enhances Pancreatic Cancer Development and the Malignant Potential Via Up-regulation of Cyr61. *Neoplasia (United States)* **18**, 785–794 (2016).

180. Polakis, P. Wnt signaling in cancer. *Cold Spring Harb. Perspect. Biol.* **4**, 9 (2012).

181. Jung, Y. S. & Park, J. Il. Wnt signaling in cancer: therapeutic targeting of Wnt signaling beyond β-catenin and the destruction complex. *Experimental and Molecular Medicine* **52**, 183–191 (2020).

182. Massey, J. *et al.* Synergy with TGFβ ligands switches WNT pathway dynamics from transient to sustained during human pluripotent cell differentiation. *Proc. Natl. Acad. Sci. U. S. A.* **116**, 4989–4998 (2019).

183. Reischmann, P., Fiebeck, J., von der Weiden, N. & Müller, O. Measured Effects of Wnt3a on Proliferation of HEK293T Cells Depend on the Applied Assay. *Int. J. Cell Biol.* **2015**, 928502 (2015).

184. Gupta, S., Takebe, N. & Lorusso, P. Targeting the Hedgehog pathway in cancer. *Therapeutic Advances in Medical Oncology* **2**, 237–250 (2010).

185. Dahmane, N., Lee, J., Robins, P., Heller, P. & Ruiz I Altaba, A. Activation of the transcription factor Gli1 and the sonic hedgehog signalling pathway in skin tumours. *Nature* **389**, 876–881 (1997).

186. Taylor, M. D. *et al.* Mutations in SUFU predispose to medulloblastoma. *Nat. Genet.* **31**, 306–310 (2002).

187. Karhadkar, S. S. *et al.* Hedgehog signalling in prostate regeneration, neoplasia and metastasis. *Nature* **431**, 707–712 (2004).

188. Kubo, M. *et al.* Hedgehog signaling pathway is a new therapeutic target for patients with breast cancer. *Cancer Res.* **64**, 6071–6074 (2004).

189. Thayer, S. P. *et al.* Hedgehog is an early and late mediator of pancreatic cancer tumorigenesis. *Nature* **425**, 851–856 (2003).

190. Nolan-Stevaux, O. *et al.* GLI1 is regulated through Smoothened-independent mechanisms in neoplastic pancreatic ducts and mediates PDAC cell survival and transformation. *Genes Dev.* **23**, 24–36 (2009).

191. Fan, L. *et al.* Hedgehog signaling promotes prostate xenograft tumor growth. *Endocrinology* **145**, 3961–3970 (2004).

192. Gallinari, P., Filocamo, G., Jones, P., Pazzaglia, S. & Steinkühler, C. Smoothened antagonists: A promising new class of antitumor agents. *Expert Opinion on Drug Discovery* **4**, 525–544 (2009).

193. Xie, H., Paradise, B. D., Ma, W. W. & Fernandez-Zapico, M. E. Recent Advances in the Clinical Targeting of Hedgehog/GLI Signaling in Cancer. *Cells* **8**, 394 (2019).

194. Baskaran, J. P. *et al.* Cell shape, and not 2D migration, predicts extracellular matrix-driven 3D cell invasion in breast cancer. *APL Bioeng.* **4**, 26105 (2020).

195. Stylianou, A., Gkretsi, V. & Stylianopoulos, T. Transforming growth factor-β modulates pancreatic cancer associated fibroblasts cell shape, stiffness and invasion. *Biochim. Biophys. Acta - Gen. Subj.* **1862**, 1537–1546 (2018).

196. Klinker, M. W., Marklein, R. A., Lo Surdo, J. L., Wei, C.-H. & Bauer, S. R. Morphological features of IFN-γ-stimulated mesenchymal stromal cells predict overall immunosuppressive capacity. *Proc. Natl. Acad. Sci.* **114**, E2598--E2607 (2017).

197. Arozarena, I. *et al.* In melanoma, beta-catenin is a suppressor of invasion. *Oncogene* **30**, 4531–4543 (2011).

198. Shami Shah, A., Cao, X., White, A. C. & Baskin, J. M. PLEKHA4 Promotes Wnt/β-Catenin Signaling–Mediated G1–S Transition and Proliferation in Melanoma. *Cancer Res.* **81**, 2029 LP – 2043 (2021).